Origin of the oldest (3600–3200 Ma) cratonic core in the Western Dharwar Craton, Southern India: Implications for evolving tectonics of the Archean Earth

M. Jayananda, Martin Guitreau, K.R. Aadhiseshan, T. Miyazaki, S.L. Chung

▶ To cite this version:

M. Jayananda, Martin Guitreau, K.R. Aadhiseshan, T. Miyazaki, S.L. Chung. Origin of the oldest (3600–3200 Ma) cratonic core in the Western Dharwar Craton, Southern India: Implications for evolving tectonics of the Archean Earth. Earth-Science Reviews, 2023, 236, pp.104278. 10.1016/j.earscirev.2022.104278 . hal-04012947

HAL Id: hal-04012947

https://uca.hal.science/hal-04012947

Submitted on 23 Sep 2023

Origin of the oldest (3600-3200 Ma) cratonic core in the Western Dharwar Craton, Southern India: Implications for evolving tectonics of the Archean Earth

M. Jayananda[1*]., Martin Guitreau[2], K.R. Aadhiseshan[1]., T. Miyazaki[3]., S.L. Chung[4,5]

[1] *Centre for Earth, Ocean & Atmospheric Sciences, University of Hyderabad, Gachibowli, Hyderabad -500 046, India*

[2] *Laboratoire Magmas et Volcans, CNRS-UMR6524, IRD-UMR163, OPGC, Université Clermont Auvergne, F-63178 Aubière, France*

[3] *Research Institute for Marine Geodynamics (IMG), Japan Agency for Marine-Earth Science and Technology (JAMSTEC), Yokosuka, Japan*

[4] *Institute of Earth Sciences, Academia Sinica, Taipei 11529, Taiwan, China*

[5] *Department of Geosciences, National Taiwan University, Taipei, Taiwan, China*

[*] *Corresponding author: mjayan.geol@gmail.com*

Contents:

Abstract

This contribution presents a comprehensive synthesis on the origin of oldest (3600-3200 Ma) cratonic core in the Western Dharwar Craton (WDC), Southern India based our new field, geochronologic, elemental and Nd-Hf isotopes data on the Holenarsipur greenstone belt and adjacent granitoids combined with published record on the stratigraphically equivalent greenstone belts in the same region. Our study shows that the oldest cratonic core in the WDC formed through assembly of different tectonic units close to 3200 Ma. These tectonic units include microcontinental remnants with oceanic plateaus, oceanic island arcs and preserved oceanic crust similar to modern oceanic crustal section close to a spreading center. Isotopic age data for these greenstone sequences (detrital zircons -3600-3230 Ma; volcanics 3384-3200 Ma) and adjoining granitoids (3430-3400 and 3350-3270 Ma with remnants of older 3600-3500 Ma gneisses) indicate that a large part of the old TTG-type granitoids in the WDC is either coeval to or slightly younger than associated greenstone units. The final stage of assembly of these tectonic elements into cratonic framework through horizontal motion of intervening oceanic crust and eventual slab breakoff is marked by the formation of ca. 3200 Ma trondhjemite magmas, emplacement of which into the lower crust caused partial convective overturn of the crust, thereby leading to the development of dome and keel patterns followed by metamorphism and cratonization of the WDC crust at 3100 Ma. Our study strongly suggests that the tectonic environments in which Archean cratons formed require some sort of horizontal motion but not necessarily modern plate tectonics. However, vertical addition of juvenile crust in hotspot environments associated with mantle plumes played a major role in building of early crustal nuclei. The model proposed for the formation of the cratonic core in the western

Dharwar craton is compatible with observations made globally in most of the Paleoarchean cratons.

Key words: Archean tectonics; Dharwar Craton; TTGs; Komatiites; U-Pb zircon ages; Sm-Nd and Lu-Hf isotopes; Whole rock geochemistry.

1. Introduction

The origin of Archean cratons is one of the major research themes in solid earth sciences as they are known for great economic mineral potential as well as provide important insights into the early earth dynamics, redox evolution of ocean-atmospheric system and emergence of biosphere (Hashizume et al., 2016; Johnson et al., 2017; Catling and Zahnle, 2020; Windley et al., 2021; Bosak et al., 2021; Korenaga, 2021). Archean cratons differ from their present-day counterparts by exhibiting strong dichotomous lithological assemblages made of greenstone belts (ultramafic-mafic and felsic volcanic rocks together with detrital and chemical sedimentary rocks) and adjacent granitoids (dominantly made of TTGs; tonalite-trondhjemite-granodiorite, e.g., Anhaeusser, 2014). The tectonic context of formation of both lithological assemblages and the processes responsible for their spatial association are still disputed (e.g., Smithies et al., 2019; Adams et al., 2012; Moyen and Martin, 2012; Kaczmarek et al., 2016; Bedard, 2018; Wyman, 2018). Several studies argue for horizontal motion of lithospheric plates initiated between 3200 Ma and 2500 Ma (e.g., Gerya, 2014; Cawood et al., 2018; Wiemer et al., 2018) whereas others presented evidence for craton specific Eoarchean horizontal tectonics (Polat et al., 1998, 2015; Kusky and Polat, 1999; Komiya et al., 2015; Hastie and Fitton, 2019; Nutman et al., 2021; Garde et al., 2020; Roman and Arndt, 2020; Korenaga, 2021; Kusky et al., 2021; Windley et al., 2021; Grocolas et al., 2022; Sotiriou et al., 2022). Alternative models involve stagnant crustal lid with periodic mantle overturn resulting in mantle upwelling, in turn, generating komatiitic to basaltic volcanism forming volcanic plateaus which were subsequently remelted to form felsic crust with eventual delamination of garnet-rich residue (e.g., Bedard, 2018). Recently proposed models on Archean tectonics involve stagnant lid, crustal drips, and horizontal motion of stagnant lid (Bedard, 2006, 2018; Rozel et al., 2017; Moyen and Laurent, 2018; Johnson et al., 2018; Nebel et al., 2018). Part of the uncertainty regarding the tectonic setting of Archean continent formation relies on when plate tectonics began on the planet Earth, which is currently an unsolved issue and subject of much discussion (e.g., Turner et al., 2020; Korenaga, 2013, 2021; Windley et al., 2021). Addressing this issue is crucial as it bears on the thermal and chemical evolution of the early earth, the formation of habitable continents and the emergence of biosphere.

The western Dharwar craton is an ideal target for studying the evolving early earth dynamics, continental growth and craton formation partly because it forms a wide time and tectonic window with a preserved crustal record of 3450 – 2600 Ma (Jayananda et al., 2018) with remnants as old as of 3600 Ma and isotopic evidence for even older fractionation events at 3800 Ma (Meen et al., 1992; Nutman et al., 1992; Jayananda et al., 2015; Guitreau et al., 2017; Ravindran et al., 2020). The oldest (ca.3600-3300 Ma) preserved TTGs - greenstone assemblages are located in the vicinity of Holenarsipur greenstone belt (HGB) correspond to a cratonic core which was intruded by 3200 Ma diapiric trondhjemites (e.g., Naqvi and Rogers, 1987; Meen et al., 1992;Jayananda et al., 2008, 2015, 2019; Guitreau et al., 2017;Ravindran et al., 2020) coinciding with the development of regional dome and keel structures (Bouhallier et al., 1993,1995; Chardon et al., 1996). Furthermore, 3600-3200 Ma detrital zircon record together with 3400-3200 TTG- greenstone volcanic assemblages also preserved in the regions adjoining to Holenarsipur greenstone belt (see fig.2) which include Nuggihalli, Kalyadi, Jayachamaraja Pura (J.C. Pura), Banasandra, Nagamangala, southern margin of the Bababudan basin and western margin of the Chitradurga greenstone belt (Nutman et al., 1992;

Ramakrishnan et al., 1994; Hokada et al., 2013; Lancaster et al., 2015; Wang et al., 2020; Jayananda et al., 2008, 2016, 2020; Ravindran et al., 2020).

However, the mechanisms and tectonic context(s) of crust formation and craton building mechanisms in the oldest crustal nuclei of the WDC remain debated and have been the subjects of much discussion (Kunugiza et al., 1996; Choukroune et al., 1997; Chadwick et al., 2000; Jayananda et al., 2008, 2015; Naqvi et al., 2009; Guitreau et al., 2017; Patra et al., 2020; Ranjan et al., 2020; Panicker et al., 2021). The greenstone sequences and the adjoining granitoids of TTG affinity have been interpreted as oceanic plateau and island arc (Jayananda et al., 2008, 2015, 2016; Peucat et al., 1995), flat subduction of plume-fed oceanic plateau crust (Naqvi et al., 2009), or remnants of migrating oceanic crust from mid-ocean ridge to trench (Kunugiza et al., 1996). The WDC is considered to be a collage of different stratigraphic units wherein geological (Swami Nath and Ramakrishnan, 1981; Naqvi, 1983), strain fabrics data (Bouhallier et al., 1993,1995; Chardon et al., 1996,1998,2008), petrological, elemental and isotopic data have been published (Meen et al., 1992;Peucat et al., 1993, 1995; Naqvi et al., 2009; Jayananda et al., 2008, 2013a, 2015; Guitreau et al., 2017; Dasgupta et al., 2019; Wang and Santosh, 2019; Ranjan et al., 2020). The Holenarsipur greenstone belt and adjacent granitoids (TTG-type Peninsular gneisses) have long been considered as early Precambrian crustal nuclei (Radhakrishna and Naqvi., 1986). Komatiite-dominated volcanic sequences stratigraphically equivalent to the Holenarsipur greenstone belt can be found in 3400-3200 Ma Nuggihalli, Kalyadi, J.C. Pura, Ghattihosahalli, Banasandra and Nagamangala greenstone belts (Chadwick et al., 1981; Swami Nath and Ramakrishnan, 1981; Venkata Dasu et al., 1991; Jayananda et al. 2008, 2016, 2020). However, spatial link between greenstone volcanism and adjoining granitoids formation, mantle evolution and continental growth, evolving tectonics and craton building processes are still largely conjectural. No major multidisciplinary approach has been initiated to address the origin of the oldest cratonic core in the WDC. Therefore, the older greenstone sequences (Sargur Group) and their adjoining granitoids (TTGs) form a most relevant target to address evolving early earth dynamics, mantle evolution, continental growth and origins of cratonic cores worldwide.

Here, we present a comprehensive synthesis based on multidisciplinary approach that involves our new field, petrological, and geochemical data (whole-rock elemental and Sm-Nd isotope data as well as U-Pb zircon ages coupled with *in-situ* Lu-Hf isotope data) in combination with published data for the Holenarsipur greenstone belt and adjacent granitoids (TTG-type Peninsular gneisses) and diapiric trondhjemite plutons as well as published record from the other stratigraphically equivalent Sargur Group greenstone belts and their spatially associated granitoids of TTG-affinity forming cratonic core in the WDC (see fig.1 and 2a). We address the origin of komatiite-dominated greenstone volcanic rocks, TTG-type granitoids and diapiric trondhjemites as well as the formation of the oldest cratonic core in the WDC through assembly of micro-blocks and, in turn, bring constraints on the early earth geodynamics and origin of Archean protocontinents.

2. Regional geological and tectonic framework

The Dharwar craton (**Fig.1**) preserves a large tilted section of Archean continental crust displaying progressive transition from lower to upper continental crust from south to the north, respectively, forming a wide time (3600-2500 Ma) window to early earth evolution (e.g., Naqvi and Rogers, 1987; Jayananda et al., 2018). This feature is unique to the WDC and makes it a prime target to address crust formation processes, continental growth, mantle evolution, craton building mechanisms and evolving tectonics of the Archean Earth. The craton comprises three major lithological assemblages which include voluminous 3450-3200 Ma granitoids of essentially TTG-affinity with much older (>3600 Ma) remnants, 2700-2600 Transitional TTGs, two distinct groups of volcanic-sedimentary greenstone successions (>3200 Ma Sargur Group and 3000-2600 Ma Dharwar Supergroup) and 3000-2520 Ma calc-alkaline to potassic plutons (Jayananda et al 2018, 2019 and references therein). The Dharwar craton has been divided into two sub-blocks (western and eastern Dharwar) based on the nature and abundance of greenstones as well as the age of surrounding granitoids of TTG affinity, potassic granite plutons, crustal thickness, and thermal records. The steep mylonitic shear zone along the eastern margin of the Chitradurga greenstone belt (**Fig. 2**) has been considered as the fundamental dividing line between these two cratonic blocks (Swami Nath et al., 1976) and a paleosuture (Naqvi, 1985). Recent tectonic fabric data, metamorphic record, geochronological, elemental and Nd isotope data show that the Dharwar craton contains three blocks (western, central, and eastern) with independent thermal records and accretion histories (Peucat et al., 2013; Jayananda et al., 2018). The western block has the oldest preserved TTG-greenstone associations (3450-3200 Ma) with evidence for even older remnants (ca.3600 Ma; Meen et al., 1992; Nutman et al., 1992; Bidyananda et al., 2011; Guitreau et al., 2017; Ravindran et al., 2020) and two thermal events (3100 Ma and 2500 Ma; Jayananda et al., 2013a, 2015; Dasgupta et al., 2019). In contrast, the central block has a mixture of old (3360-3000 Ma) and young (2700-2520 Ma) which was involved in three thermal events (ca.3200 Ma, 2620 Ma and 2510 Ga; Jayananda et al., 2013a). Finally, the eastern block is mainly made of young crust of 2700 -2530 Ma that recorded only one thermal event close to 2510 Ma (Peucat et al., 2013). On the cratonic scale, tectonic fabrics mapping, and kinematic analysis reveal dome and basin patterns in the western block with widely spaced shear zones (Bouhallier et al.,1995; Chardon et al., 2008), whereas the central and eastern blocks have spectacular flat fabrics linked to lateral constrictional flow of hot orogenic crust with closely spaced shear zone network (Chardon et al., 2011). Recent strain fabric data in combination with metamorphic facies, age zonation patterns, Sm-Nd isotopes, and strong seismic reflectivity pointed towards Neoarchean craton formation through assembly of the three crustal blocks through westward convergence of oceanic lithosphere along the eastern margin of the Chitradurga greenstone belt (Chadwick et al., 2000; Chardon et al., 2011; Vijaya Rao et al., 2015; Jayananda et al., 2013b, 2018, 2020).

The Holenarsipur greenstone belt (HGB) and adjacent granitoids are considered to be the oldest Archean crustal nucleus in the Dharwar craton (Radhakrishna and Naqvi, 1986). Several studies on tectono-stratigraphy, strain patterns, metamorphic record, geochemistry and the tectonic processes have significantly contributed to our fundamental understanding of crustal architecture of the Hassan-Gorur-Holenarsipur region (Chadwick et al., 1978; Ramakrishnan and Viswanatha, 1981; Naqvi, 1981; Hussain and Naqvi,1983; Naqvi et al., 2009; Bouhallier et al., 1993,1995; Chardon et al., 2008; Jayananda et al., 2013a, 2015; Dasgupta et al., 2019). Despite many studies, the stratigraphy of the Holenarsipur greenstone belt and its temporal relationship with the surrounding granitoids (TTGs) is still debated. Ramakrishnan and Swami Nath (1981) reported two distinct volcanic-sedimentary supracrustal sequences comprising older Sargur Group (>3200 Ma) in the south and younger Bababudan Group (<3000 Ma) to the north separated by the Tattekere conglomerate (e.g., Chatterjee and Das, 2004). On the contrary, Naqvi (1981) argued that the Tattekere conglomerate does not mark the separation between two stratigraphic sequences as cross-bedded quartzite between two stratigraphic sequences itself does not form a proof for time break. Based on the map patterns, Naqvi (1981) and Hussain and Naqvi (1983) have proposed that supracrustal rocks predate the surrounding Peninsular gneisses while isotopic age data from Monrad, (1983) and Meen et al., (1992) concluded that Peninsular gneisses are older. Zircon U-Pb dating from felsic volcanic flow from higher stratigraphic level of ‘so called’ younger northern Bababudan Group, yielded an age of 3298 ±7 Ma (Peucat et al., 1995), indicating that the entire Holenarsipur greenstone belt is ca.3300 Ma old, which in turn coeval with adjoining TTGs (Jayananda et al., 2015; Guitreau et al., 2017). According to Drury et al. (1987), the crustal architecture of the Holenarsipur belt was shaped by large mushroom-type fold interferences and earlier recumbent isoclinal folds refolded into upright folds. Subsequent strain fabrics mapping and kinematic analysis by Bouhallier et al. (1993,1995) revealed classical crustal-scale dome and keel patterns, typical of Archean cratons, wherein low density orthogneisses define circular to elliptical domes whilst high-density greenstone sequences form keel structures (Gorman et al., 1978). Between the interfering dome and keel structures, areas of foliation triple points contain either ascending trondhjemite magma injections or down-going high density ultramafic—mafic volcanic rocks which define vertical tectonites (Bouhallier et al., 1993). However, recent phase equilibrium and mechanical modelling have argued that sagduction was unlikely to have operated in the Archean (Miocevich et al., 2022). The HGB was considered to have originated by migration of an oceanic crust from a spreading centre to a trench forming an accretionary complex (Kunugiza et al., 1996).

Volcanic-sedimentary sequences stratigraphically equivalent to the Holenarsipur greenstone basin are preserved in the adjacent regions like the Nuggihalli, Kalyadi, J.C. Pura, Ghattihosahalli, Banasandra and Nagamangala belts (see fig.2a). These greenstone belts also preserve voluminous komatiite-komatiitic basalt with minor basaltic rocks and interlayered sedimentary rocks (Jayananda et al., 2008, 2016; Maya et al., 2017; Tushipokla and Jayananda, 2013). Published magmatic and detrital zircon ages together with Sm-Nd whole-rock isochrons reveal major episodes of crust formation during 3600-3200 Ma (Meen et al., 1992; Nutman et al., 1992; Peucat et al., 1995; Hokada et al., 2013; Jayananda et al., 2008, 2015, 2019; Wang and Santosh, 2019). They form an extension of oldest cratonic nuclei preserved in the Holenarsipur region. The cratonic core in the WDC experienced greenschist to amphibolite facies metamorphism that affected the whole Dharwar craton close to 2500 Ma with an earlier thermal event ca. 3100 Ma (Bouhallier, 1995; Jayananda et al., 2013a 2015; Dasgupta et al., 2019).

3. Lithological assemblages, field relationships and petrography

The cratonic core in the WDC (**Fig.2a**) comprises the komatiite dominated Sargur Group volcanic-sedimentary greenstone sequences and adjoining granitoids (TTGs) which, in turn, were intruded by ca. 3200 Ma diapiric trondhjemites. It shows classical dome and keel patterns typical of oldest cratonic cores in the Archean cratons (Bouhallier et al., 1993, 1995; Choukroune et al., 1995; Chardon et al., 1996, 1998, 2008). The Holenarsipur greenstone belt together with other stratigraphically equivalent volcanic-sedimentary sequences found in the J.C.Pura, Nuggihalli, Kalyadi, Banasandra and Nagamangala greenstone belts and adjoining TTGs form the cratonic core in the Western Dharwar Craton (Chardon, 1997; Ramakrishnan et al., 1994; Nutman et al., 1992; Meen et al., 1992; Peucat et al., 1995; Guitreau et al., 2017; Jayananda et al., 2008, 2015; Hokada et al., 2013; Bidyananda et al., 2016; Lancaster et al., 2015;Wang and Santosh, 2019). Here we present our new field data on the Holenarsipur greenstone belt and adjacent granitoids together with published data of the other stratigraphically equivalent greenstone belts (Swami Nath and Ramakrishnan, 1981; Radhakrishna, 1983) in the cratonic core and their adjacent granitoids of TTG-affinity.

The Holenarsipur greenstone belt (**Fig. 2b**) and surrounding granitoids (TTGs) display complex internal architecture (Naqvi, 1981; Ramakrishnan and Viswanatha, 1981; Bouhallier et al., 1993, 1995; Choukroune et al., 1995, 1997). The volcano-sedimentary greenstone sequence comprises abundant ultramafic assemblages (komatiite to komatiitic basalts), amphibolite with interlayered northwest – southeast trending quartzite-conglomerate and pelites in the central part separating the greenstone into three units. Banded Iron Formations (BIFs) are confined to the summits of the north - south trending eastern most part of the greenstone belt (**Fig.2c**). Diapiric trondhjemites (3230-3170 Ma; Jayananda et al., 2015; Guitreau et al., 2017) intruded the greenstone sequences and adjoining granitoids whilst 3150

Ma granite veins intrude the TTG gneisses in the Southwestern part. Minor anorthosite (3240 Ma; Panicker et al., 2021) intrude the greenstone sequences in the south-eastern part.

Our extensive field work revealed the composite nature of the Holenarsipur greenstone belt which comprises three distinct tectonic units identified based on distinct lithological assemblages and their corresponding tectonic features. We labelled these units Southwestern, Northcentral, and Eastern blocks (**see fig.2b, c**) and describe them below.

3.1 Southwestern block

The southwestern block (**see fig.2b)** comprises dominant metamorphosed ultramafic (serpentinite ±olivine bearing dunite, serpentine-talc-tremolite schist, talc-chlorite schist, actinolite-tremolite schist) with minor mafic volcanic rocks (plagioclase-chlorite-actinolite-hornblende schist) associated with sedimentary rocks (conglomerate, quartzite, garnet-mica-staurolite-kyanite bearing pelites) and surrounding gneisses (granitoids of TTG affinity).

The ultramafic-mafic rocks are found as either large discontinuous bands or dismembered outcrops distributed within the TTG-gneisses (**Fig. 3.1a**). Their contacts with adjacent granitoids (TTG-type gneisses) and sedimentary rock sequences are tectonized. In the southernmost part, the ultramafic rocks are found as numerous dismembered fragments or outcrops. A gradual increase in their abundance can be followed from disrupted fragments in the southernmost part to continuous outcrops to the northern part of the southwestern block. These ultramafic rocks were disrupted and fragmented probably during the intrusion of trondhjemite magmas. They occasionally show crude pillow structure with chilled margins which indicate their eruption in a marine environment (**Fig. 3.1b**). The ultramafic rocks are medium to fine grained containing serpentine-talc-tremolite or tremolite-actinolite, and their primary mineralogy is nearly absent except for remnants of olivine and/or clinopyroxene rarely preserved in a few samples (**Fig. 4.1a**). The mafic rocks are found as large discontinuous outcrops or continuous bands which do not show contact with ultramafic units. They are medium- to fine-grained with abundant actinolite, tremolite, minor plagioclase with rare hornblende. This mineralogy developed during post-magmatic hydrothermal alteration or metamorphism. These ultramafic-mafic assemblages together with granitoids (TTG- gneisses) are bounded by southeast to northwest trending shallow water sedimentary successions (conglomerate-quartzite-pelites) which define the northern limit of the southwestern block (**see fig. 2c**). Among the sedimentary sequences, conglomerates contain rounded to stretched ellipsoidal quartz pebbles embedded in quartz-rich matrix (**Fig. 3.1c**) and quartzites are often fuchsite-bearing and display ripple marks (**Fig. 3.1d**) and crossbedding (**Fig.3.1e**) characteristic of shallow shelf environment. Pelites comprise diverse assemblages including garnet-biotite, garnet-biotite-muscovite-kyanite, garnet-biotite-staurolite-kyanite bearing assemblages (**Fig.3.1f**) indicating that equilibration took place at 4-7 kbars and ~550^{o}C (Bouhallier, 1994; Dasgupta et al., 2019). Detrital zircons from garnet-mica-kyanite-bearing pelites yielded ages ranging from 3560 to 3230 Ma (Nutman et al., 1992). The contact between the ultramafic-mafic rocks and adjoining granitoids are tectonized. The dominant ultramafic with minor mafic rock assemblages with crude pillows point to a possible oceanic plateau.

The adjacent granitoids of TTG affinity comprise several associations of grey to dark grey granodioritic to tonalitic gneisses containing the remnants of whitish grey granite to trondhjemite, intermediate to mafic layers. The older remnants of whitish grey granite to trondhjemite are found as fragments within tonalite or granodiorite layers (**Fig.3.1g**). They contain quartz, plagioclase (An_{10-12}), minor microcline, biotite and occasional primary muscovite. The dark grey tonalite layers are abundant and often show diffusive contacts with granodiorite suggesting their coeval nature. Tonalite contains quartz, plagioclase (An_{15-26}), minor microcline, hornblende, biotite with accessory zircon, apatite, titanite and opaques. The voluminous grey granodiorite contains older remnants of biotite-rich mafic enclaves

(**Fig.3.1h**). They have quartz, plagioclase (An_{16-22}), microcline, biotite in their mineral assemblage. Both tonalite and granodiorite were intruded by veins of trondhjemite which are often folded (**Fig.3.1i**). These trondhjemite veins contain quartz, sodic plagioclase (An_{10-13}), minor microcline, biotite and rare muscovite. Late (3150 Ma; Jayananda et al., 2015) granodiorite to granite veins and/or dykes intrudes TTGs. Trondhjemite injects into the gneisses and form vertical tectonites at foliation triple points (**Fig.3.1j**).

3.2 **Northcentral block**

The greenstone sequence of the Northcentral block is surrounded by TTG-type granitoids and trondhjemite intrusions on its northern and western margins. This greenstone unit was probably dismantled into two fragments (**see fig.2b**) during trondhjemite (Halekote-type) intrusion. The greenstone assemblages comprise ultramafic to mafic volcanic rocks with minor felsic pyroclastic flows and interlayered sedimentary rocks (garnet-chlorite-chloritoid-bearing pelite). Ultramafic-mafic rocks erupted in marine environment as revealed by flow top pillow breccias (**Fig. 3.2a).** They show constrictional fabrics forming vertical tectonites at foliation triple junctions developed at the junction of interfering rising gneiss domes and down going ultramafic volcanics (Bouhallier et al., 1993). The ultramafic volcanic rocks contain serpentine-talc-tremolite or talc-tremolite-actinolite or talc-chlorite whilst mafic volcanic rocks exhibit actinolite-tremolite with minor plagioclase or actinolite-hornblende-plagioclase in the mineral assemblage (**Fig. 4.1b, c**). Felsic volcanic rocks (quartz- sodic plagioclase - minor k-feldspar-biotite) are confined to the southwestern margin of Northcentral block. This felsic volcanic unit corresponds to higher stratigraphic levels that comprises pyroclastic flows erupted in sub-aerial conditions as revealed by blue quartz phenocrysts, medium grained matrix and tiny fine-grained angular rock fragments within fine grained ash (**Fig. 3.2b**). Chlorite-chloritoid-garnet-bearing pelitic sedimentary rocks (**Fig. 3.2c**) are found along the southern-margin close to the contact with the Southwestern block. The mineralogy of these chloritoid-bearing pelitic rocks imply ultramafic to mafic provenance and deposition in an oceanic environment far from a sizable continent. The dominant ultramafic-mafic assemblages with minor felsic volcanic rocks and associated chloritoid-chlorite-bearing pelite rocks point to an ocean island arc spatially associated with a volcanic plateau.

The greenstone volcanic rocks show the imprints of contact metamorphism along their boundary with ca. 3200 Ma diapiric Halekote-type trondhjemite as revealed by large randomly oriented crystals of actinolite, tremolite and hornblende in mafic-ultramafic volcanic rocks (**Fig.3.2d**). Numerous quartz-veins with large tourmaline crystals also injected into the greenstone volcanic sequences along the contact zone with diapiric trondhjemite.

The granitoids around the Northcentral block is dominantly coarse- to medium- grained dark grey tonalitic to grey granodioritic gneisses defining the domal pattern (Bouhallier et al., 1993). These gneisses are traversed by medium-grained whitish grey trondhjemite veins and highly coarse-grained pegmatites. The contacts between greenstone and granitoids (TTG-type) are tectonized. The tonalitic gneisses contain quartz, plagioclase (An_{17-25}), biotite, minor microcline with biotite and hornblende whilst granodiorite has quartz, plagioclase (An_{15-20}), microcline and biotite with common accessory phases such as zircon, apatite, titanite and opaques.

3.3 Eastern block

The eastern block forms a thin (500 m to 3 km width) elongated band that runs for about 60 km in north-south direction (**see fig. 2b**). The eastern block and adjacent granitoids (TTG-type) experienced strong deformation associated with regional shortening that affected the whole Archean crust in the Dharwar craton close to 2500 Ma (Bouhallier et al., 1993). In the northern part of the Holenarsipur greenstone belt, an E-W road cut displays a complete section of volcano-sedimentary sequence characteristic of the Eastern block (**Fig.3.3a**). From east to west, the greenstone sequence begins with pillowed mafic-ultramafic rocks with chilled margins followed by phyllite, chert layers, BIFs, several fine-grained sheeted mafic dykes, plagiogranite, gabbros to layered gabbros, fine-grained ultramafic rocks to medium-grained peridotite to the westernmost part (**Fig.3.3b**). Further west, peridotitic rocks show tectonic contacts with the adjacent granitoids of TTG affinity. The pillowed ultramafic rocks contain serpentine-talc-tremolite, talc-tremolite-actinolite or talc-chlorite whilst mafic volcanic rocks display chlorite-actinolite-plagioclase in the mineral assemblages. The gabbros and layered gabbros show plagioclase-hornblende with remnants of clinopyroxene. The plagiogranite exhibit dominant sodic plagioclase with minor quartz and rare biotite. The medium-grained peridotitic ultramafic rocks in the western margin contain serpentine with remnants of olivine, serpentine-talc-tremolite in their mineralogical assemblage. Immediately south of the road cut, a thin band of intraformational conglomerate interlayered with phyllite and BIFs was documented by Swami Nath and Ramakrishnan (1981). The conglomerate contains flat to angular pebbles of chert, fuchsite-bearing quartzite, and mafic volcanic rocks with greywacke matrix suggest fragmentation within the basin without much transportation. The southern part of the eastern block corresponds to deeper levels that exhibit serpentine-talc-tremolite and actinolite-hornblende schist (**Fig. 4.1d**) as well as gabbro-anorthosite, plagiogranite, and peridotitic rocks along an east-west section. These field evidence include rock sequences like peridotite-foliated gabbro - plagiogranite - sheeted dykes-pillowed ultramafic volcanics with chert and BIFs along E-W cross-sections at different crustal levels which suggest that the eastern block could probably correspond to a titled and deformed panel of preserved oceanic crust close to an oceanic spreading centre (**Fig. 3.3b, c**).

The granitoids (TTG-gneisses) adjoining to the eastern block comprise dark grey tonalitic to grey granodioritic gneisses, which contain thin whitish trondhjemite veins along steep foliation. These TTG-type granitoids are traversed by strong transcurrent ductile to brittle-ductile shears which locally reoriented foliation and lineation (Bouhallier et al., 1993). The tonalite has quartz, plagioclase (An_{19-27}), traces of microcline, hornblende, biotite whilst granodiorite contain quartz, plagioclase (An_{14-20}), subordinate microcline, biotite, occasional hornblende, and common accessory minerals such as zircon, apatite, titanite and opaque phases. Whitish grey trondhjemite veins are found along the steep foliation of tonalitic to granodioritic gneisses contain minor quartz and abundant sodic plagioclase (An_{10-12}), minor microcline with rare biotite and muscovite.

3.4 Diapiric trondhjemite intrusions

Diapiric trondhjemites intruded as plutons at the contact zone between the three greenstone units and the TTG-type granitoids (**see fig.2b, c**) but they also occur as veins and sheets (often folded) within the adjoining TTGs away from main intrusions. They also define foliation triple points at junctions of interfering dome-keel structures forming vertical tectonites (**see fig.3.1j**). These diapiric trondhjemite intrusions are dominantly homogeneous coarse-grained trondhjemite with minor granite in their core. They have quartz, plagioclase (An_{10-12}), minor microcline, biotite with or without muscovite, accessory zircon, titanite and Fe-Ti oxides. Detailed tectonic fabric analysis reveals that the intrusion of diapiric trondhjemites shaped the fundamental architecture of the preserved crustal panel in the Holenarsipur greenstone belt (Bouhallier et al., 1993).

3.5 Lithological assemblages along the contact zone of the three tectonic units

The contact zone between the three tectonic units is key to understand the crustal architecture, tectonic relationships between the three greenstone units. Distinct sedimentary assemblages are found along the northern and southern margin of the contact zone between southwestern and northcentral block (**see fig. 2b-c**). Along the northern limit of the southwestern block, thick quartzite with crossbedding (**see fig. 3.1e)** and ripple marks (**see fig. 3.1d**), following quartz-pebble conglomerate (**see fig. 3.1c**), mark a shallow shelf environment. These quartzite-conglomerate layers are followed by quartz-mica-kyanite-staurolite-garnet-bearing pelite (**see fig. 3.1f**) which spatially associated with ultramafic rocks and granitoids (TTGs) suggesting a mixed provenance. On the contrary mineralogy (chlorite-chloritoid-garnet) and major element composition of the pelite unit interlayered with greenstone volcanic rocks (Bouhallier, 1995) along the south-eastern margin of the northcentral block (**see fig. 2c**) suggests its derivation from dominant ultramafic-mafic source. Within the eastern block, close to the contact with the northcentral block (**see fig.2b**), a polymict conglomerate with sparse angular fragments of greenstone volcanic rocks/sedimentary rocks in clay matrix (Ramakrishnan and Viswanatha, 1981) indicate local fragmentation within the oceanic basin. The contact zone of the three blocks is marked by the intrusion of diapiric trondhjemites wherein numerous quartz veins that contain large crystals of tourmaline injected into volcanic-sedimentary sequences. The origin of tourmaline-bearing quartz veins is probably linked to the volatile-rich fluid flow associated with the intrusion of ca. 3200 Ma diapiric trondhjemite as also suggested by Rogers et al. (1986). To summarize, the observed field relationships along the contact zone imply that these three greenstone units representing three tectonic units probably originated in distinct settings and their juxtaposition coincided with the formation of diapiric trondhjemites.

3.6 Stratigraphically equivalent greenstone belts and adjacent granitoids rocks in the cratonic core

The stratigraphically equivalent greenstone sequences to the Holenarsipur greenstone belt include Nuggihalli, Kalyadi, J.C. Pura, Ghattihosahalli, Banasandra and Nagamangala greenstone belts (**see fig. 2a**). These greenstone belts are surrounded by ca.3350-3300 Ma granitoids rocks which were intruded by ca. 3200-3150 Ma diapiric trondhjemites, as well as 3000 Ma and 2600 Ma potassic granites (Meen et al., 1992; Chardon, 1997; Jayananda et al., 2006, 2019; Ao et al., 2021).

3.6.1 The Nuggihalli greenstone belt

The Nuggihalli greenstone belt is an elongated NNW-SSE trending volcano-sedimentary sequence that extend about 50 km from Kempinakote in the south to Arsikere in the north (Jafri et al., 1983). The greenstone belt is surrounded by granitoids which comprise TTG-type banded to migmatitic gneisses, and their contacts have been tectonized. Nuggihalli greenstone stratigraphically correlates with the Holenarsipur greenstone belt (Swami Nath and Ramakrishnan, 1981). It is difficult to establish relationships among the lithologies as lithological assemblages were disrupted during strong shear deformation. The dominant lithological sequences include metamorphosed ultramafic rocks (peridotite, serpentinite and dunite with chromite layers, talc-tremolite schists; **Fig. 5.1a**), mafic rocks (gabbros and garnet-amphibolite), anorthosites, granite veins (plagiogranite?) and titaniferous magnetite. Metasedimentary rocks such as fuchsite-bearing quartzite, garnet-mica (± kyanite or staurolite) metapelite were documented in central and northern part within granitoids (Swami Nath and Ramakrishnan, 1981; Jafri et al., 1983). The ultramafic rocks can be found as lenses and elongated bodies throughout the belt. Peridotitic komatiites with chromite layers are well preserved at Jambur, Nuggihalli, Tagadur, Byrapur and Bhaktarahalli chromite mines. On a regional scale, the greenstone belt defines NNW trending fabrics and was affected by strong shear deformation. Whole-rock Sm-Nd isotope data of Nuggihalli volcanic rocks together with data from the adjoining Kalyadi belt define an imprecise regression age of 3284 ± 310 Ma (Jayananda et al., 2008). The Nuggihalli greenstone belt was equilibrated in greenschist to amphibolite facies. An increase of metamorphic grade can actually be followed from south to north as documented by Jafri et al. (1983). The lithological association of dominant ultramafic-mafic volcanic rocks with chromite layers, gabbro-anorthosites and granite (plagiogranite?) injections point to a preserved section of oceanic crust close to spreading centre. The komatiites contain serpentine, tremolite, talc, actinolite, chlorite (**Fig. 5.2a**), chromite with rare olivine and enstatite (Jayananda et al., 2008).

3.6.2 Kalyadi greenstone belt

The volcanic-sedimentary sequences in the Kalyadi region crop out as several large discontinuous boudins or small 1-2 km bands within the TTG-type granitoids which in turn intruded by diapiric trondhjemites. The contacts between the greenstone sequences and surrounding TTGs are tectonized. Late potassic granites (ca. 2620 Ma Arsikere-Banavara plutons) are intrusive into the Kalyadi greenstone belt and adjoining TTGs (Meen et al., 1992; Jayananda et al., 2006). The greenstone sequences are dominated by komatiitic volcanic rocks which include serpentinite, serpentine-talc-tremolite and talc-chlorite schists (**Fig. 5.2b)**. Minor amphibolites and hornblende schists are associated with ultramafic rocks (**Fig.5.1b**). Nodular structures found in komatiite comprise spherical nodules with 1-2 cm diameter surrounded by fine grained matrix (Jayananda et al., 2008). The minor sedimentary assemblages include cherty quartzites and metapelites interlayered with volcanic rocks (Subba Rao and Naqvi, 1999) and immediately north fuchsite-bearing quartzite that contain chromitite layers (Swami Nath and Ramakrishnan, 1981). The abundant komatiites and associated minor sedimentary rocks point to their eruption in a marine environment representing a possible section of volcanic plateau fragment spatially associated with an oceanic spreading centre.

Published U-Pb zircon age for the granitoids adjacent to the Kalyadi greenstone belt is rather scanty. However, Meen et al (1992) have estimated an age of 3390 Ma for the magmatic protoliths of low-Rb gneisses south of the Kalyadi belt. U-Pb zircon ages of tonalitic to granodioritic gneisses northeast of the Kalyadi belt indicate 3310-3205 Ma (Chardon, 1997) whilst detrital zircons from chromite-bearing fuchsite indicate 3230 Ma (Nutman et al., 1992), and directly ~30 km to the west, granitoids of TTG-affinity in the southern boundary of Bababudan basin provide an age range of 3350-3270 Ma (Jayananda et al., 2015).

3.6.3 J.C. Pura greenstone belt

The J.C. Pura greenstone belt preserves voluminous fresh ultramafic volcanic sequences of komatiite and komatiitic basalt composition which are interlayered with minor cherty quartzites (Venkata Dasu et al., 1991; Ramakrishnan et al., 1994; Jayananda et al 2008, 2016). Komatiites form spectacular pillows, pillow breccias and flowtop breccia with chilled margins (Jayananda et al., 2016). Crude spinifex structures were also documented (Venkata Dasu et al., 1991). Thick flows (70-90 m) of undifferentiated komatiites form prominent ridges around Rampura-Sasivala region. These rocks originated as long drawn lava lobes and lava sheets spread over tens of metres (Jayananda et al., 2016). The lithological association of voluminous komatiite, komatiitic basalts and minor basalt with flowtop pillow breccias (**Fig. 5.1c & d**) imply their eruption in marine environment possibly as an oceanic plateau. Komatiites define an Sm-Nd whole-rock regression age of 3384 ± 200 Ma (Jayananda et al., 2008) whilst detrital zircons from associated quartzites yield an age 3230 Ma (Ramakrishnan et al., 1994). Komatiites contain serpentine, serpentine-talc-tremolite, talc-chlorite with accessory chromite and spinel. Remnants of olivine are found in serpentine-rich layers (**Fig. 5.2c)**. The adjacent granitoids defines circular to sub-circular domes (Chardon et al., 1996) and provide U-Pb zircon ages of 3315-3217 Ma (Chardon, 1997; Jayananda unpublished data) whilst trondhjemite to granodioritic intrusions into the TTG-type granitoids indicate U-Pb zircon ages close to 3198 Ma (Chardon, 1997).

3.6.4 Ghattihosahalli greenstone belt

The Ghattihosahalli belt forms a small and elongated band along the western boundary of the ca. 2700 Ma Chitradurga greenstone belt. Komatiites are the most abundant lithologies which are associated with minor amphibolites, fuchsite-bearing quartzites which are interbedded with barite layers (Radhakrishna and Srinivasaiah, 1974). These komatiites occur as bouldery outcrops on the hill to the south of Kummanghatta and occasionally show relict spinifex texture (Viswanatha et al 1977). Petrographic study reveals abundant serpentine (>90%) in the majority of samples and serpentine-talc-tremolite in a few samples (**Fig. 5.2d)**. The dominant komatiitic volcanic rocks together with fuchsite-bearing quartzite and barite layers point to remnants of an oceanic plateau.

The granitoids adjacent to the Ghattihosahalli belt comprises banded dark grey tonalitic to grey granodiorite with several leucocratic aplitic veins along the foliation. SIMS U-Pb zircon ages provide ages of 3318 ± 15 Ma to 3259 ± 7 Ma for the TTG-type granitoids which in turn intruded by 3000 Ma potassic Hosdurga granite (Jayananda et al. in prep).

3.6.5 Banasandra greenstone belt

The Banasandra greenstone belt is located on the southwestern margin of the Chitradurga greenstone belt (**see fig. 2a**). This belt occurs as a NW-SE trending bands which comprises well-preserved voluminous peridotitic komatiites around Banasandra, Kodihalli and Kunikenahalli (Srikantia and Bose, 1985). These komatiites are fine-grained forming pillow breccias or flowtop breccias (Jayananda et al., 2016) in the south near Kunikenahalli and display spectacular spinifex structures (**Fig.5.1e**) to the north close to Kodihalli village (Jayananda et al., 2008, 2016). Pillow breccias and flowtop breccias are considered to underlie the spinifex (Srikantia and Bose, 1985). The studied komatiites consist of serpentine (cumulate), serpentine-talc-tremolite, talc-tremolite and talc-chlorite in mineral assemblages (**Fig. 5.2e)**. Serpentine-tremolite-talc and talc-chlorite assemblages indicate low grade metamorphism under greenschist facies conditions. The discontinuous outcrop patterns together with dominant komatiite volcanic rocks, which form spectacular pillow breccia and a spinifex texture, imply that Banasandra komatiites correspond to possible remnants of an oceanic plateau.

The adjacent granitoids are dominantly dark grey banded tonalitic to granodioritic gneisses which are intruded by whitish grey trondhjemite. Zircons from tonalitic to granodioritic layers indicate U-Pb ages of 3310 ± 15 Ma and 3210 ± 10 Ma (Jayananda et al., 2019). All of which, in turn intruded by ca. 3000 Ma high-K granite plutons (Jayananda et al., 2019; Ao et al., 2021).

3.6.6 Nagamangala greenstone belt

The Nagamangala greenstone belt is located in the easternmost part of the WDC (**see fig. 2a**) and it extends about 30 km from Nelligere in the north to Honnakere in the south (Srikantia and Venkataramana, 1989). The greenstone belt is surrounded by ca. 3300-3200 Ma granitoids, all of which were intruded by ca. 3000 Ma potassic plutons (Jayananda et al., 2019). The preserved volcanic rocks include abundant ultramafic rocks of komatiite affinity with minor basalts which are interlayered with sedimentary rocks (**Fig. 5.1f**) (pelite-quartzite-carbonate). The ultramafic rocks display spinifex and pillow structures whilst mafic rocks forming pillows with chilled margins (Devapriyan et al., 1994; Tushipokla and Jayananda, 2013). The ultramafic volcanic rocks contain serpentine-tremolite-talc and tremolite-actinolite whilst mafic volcanic rocks exhibit actinolite-hornblende-plagioclase assemblage (**Fig. 5.2f)**. The lithological associations of dominant ultramafic to minor mafic volcanic rocks show pillow structures with interlayered quartzite and pelite which possibility imply an eruption in marine environments alike oceanic plateaus. Mineral assemblages indicate greenschist to lower amphibolite layers metamorphic conditions (Tushipokla and Jayananda, 2013).

The surrounding granitoids comprise strongly banded tonalitic to granodiorite which contain trondhjemite veins along the foliation which are often boudinaged (**Fig. 6.1a-f**). The gneisses are affected by strong deformation associated with regional shortening and steep foliation. Zircons from tonalitic to granodioritic grey gneisses yield U-Pb zircon ages of 3205 ± 5 to 3310 ± 10 Ma (Jayananda et al., 2019) whilst high-potassic plutons emplaced along TTG - greenstone contact zone provide U-Pb zircon ages of 2989-2974 Ma and 2620-2600 Ma (Jayananda et al. 2006, 2019).

To summarize stratigraphically equivalent Sargur Group (ca.3400-3200 Ma) greenstone volcanic sequences in the cratonic core are dominated by komatiite-komatiitic basalts with minor basaltic rocks. The primary mineralogy of volcanic rocks is absent (except rare olivine and orthopyroxene) and observed mineralogy developed during hydrothermal alteration and low-grade metamorphism. The volcanic rocks are interlayered with shallow water shelf sedimentary sequences like quartzite-pelite-carbonate-BIFs. The contacts between greenstone sequences and adjoining granitoid rocks are tectonized. Our field observations combined with published tectonic fabrics analyses in the WSW-ENE crustal corridor in the cratonic core (Bouhallier et al., 1993, 1995; Chardon et al., 1996, 1998, 2008) reveal dome and keel architecture with major shear zones traverse the eastern block of the Holenarsipur, Nuggihalli-Kalyadi, and Nagamangala greenstone belts (**Fig. 6.1g**).

3.7 Structural patterns

Dome and basin structures are a fundamental feature of TTG-greenstone terranes of many oldest Archean cratons (Gorman et al., 1978; Bouhallier et al., 1993; Chardon et al., 1996, 2009; Choukroune et al., 1995, 1997; Rey et al., 2003; Whitney et al 2004). These dome and basin patterns were observed in different spatial scales and their origin have been attributed to various processes operated in diverse tectonic settings (Bouhallier et al., 1995; Collins et al., 1998; Hamilton, 1998; Kusky et al., 2021; Zulauf et al., 2019). Structural studies and seismic tomographic data on the western Dharwar craton reveal a first order cratonic internal architecture that comprises thick crust (40-45 km) with dome and basin patterns and crustal scale shear zone network (Drury and Holt, 1980; Chadwick et al., 1978, 1981; Gupta et al., 2003; Bouhallier et al., 1995; Chardon et al., 1998, 2008). Detailed structural analysis based on combined satellite-based remote sensing data (Spot and LANDSAT image analysis) together field-based strain fabrics measurements in the cratonic core reveal crustal scale dome and basin patterns bounded by widely spaced shear zone network (Bouhallier et al., 1995; Chardon et al., 1996, 2008; Choukroune et al., 1997). In the NE part of the cratonic core, a detailed structural analysis involving strain fabrics measurements and kinematic analysis around the ca.3400 Ma J.C. Pura greenstone belt and ca.3300 Ma adjacent granitoids indicate the development of diapiric structures due to vertical displacements of high-density greenstone volcanics associated with gravitational instabilities (Chardon et al., 1996). This diapiric event is possibly linked to the emplacement of trondhjemite to granodiorite plutons close to 3200-3150 Ma (Meen et al.,1992; Chardon, 1997; Jayananda et al., in prep.). Foliation trajectories together with strain variation and kinematic analysis of the Holenarsipur greenstone belt and adjoining granitoid gneisses reveal that two deformation events have shaped the crustal architecture of the region. Kinematic indicators along the contact between greenstone and gneisses indicate downward displacement of high-density greenstone assemblages relative to granitoids (Bouhallier et al., 1993). The regional diapiric event is contemporaneous with the intrusion of ca.3200 Ma Halekote trondhjemite which produced circular to elliptical domes surrounded by greenstone sequences. The foliation triple points marked by vertical tectonics developed at junction of converging lineation associated with interfering domes and keel pattern (Bouhallier et al., 1993; Choukroune et al., 1997).

Sinistral ductile shearing affected the eastern block (**see fig.2b**) of the Holenarsipur belt and adjacent gneisses which is interpreted as a result of vertical movements linked to body forces with minor horizontal shortening (Bouhallier et al. 1993). Further to the south in Gundlupet region, Bouhallier et al (1995) presented a 3D geometrical information of diapiric structures from a tilted crust in the WDC corresponding to various depths developed elliptical gneiss domes and greenstone keel with foliation triple points at the junction of converging lineation (Bouhallier et al., 1995; Choukroune et al., 1997).

In summary our field observations together with published strain fabrics data including foliation trajectories and kinematic indicators in the WSW – ENE corridor of the cratonic core (**Fig. 6.1g**) reveal circular to elliptical dome-keel patterns (Bouhallier et al., 1993,1995; Choukroune et al., 1997; Chardon et al., 1996, 2008). Kinematic indicators reveal downward displacement of high-density greenstone with respect to adjacent low-density TTG-type granitoids. Foliation triple points defined by vertical tectonites are associated with regions of subsidence of high-density greenstone assemblages. These dome and basin structures are also compatible with experimental analogue modelling (Bouhallier et al., 1995). Late transcurrent shear zones are confined to the eastern boundary Holenarsipur and further south to the Gundlupet region and Banasandra and Nagamangala greenstone belts (**see fig. 2**) which partly reorient the foliation and lineation of dome-keel patterns (Bouhallier et al., 1995; Chardon et al., 2008). The dome and keel patterns of the cratonal core are compatible with the dome and basin structures documented in the cratonal cores in the East Pilbara and Kaapvaal cratons (Anhaeusser, 2014; Collins et al., 1998; van Kranendonk et al., 2015).

4. Metamorphic record

Metamorphic pressure-temperature history of the cratonic core in WDC is poorly known except for a few studies by Bouhallier (1995), Jayananda et al (2013a) and Dasgupta et al (2019) on the Holenarsipur region. Studies on the regional metamorphism of the WDC reveal a progressive increase in metamorphic grade from north to south (Raase et al., 1986; Jayananda et al., 2013a, 2020 and references therein). Mineral assemblages (chlorite-actinolite-tremolite-serpentine or chlorite-actinolite-garnet) in the remnants of the Sargur Group greenstones from the southern margin of the Bababudan basin indicate greenschist facies (Chadwick et al., 1981) whilst garnet-staurolite-kyanite-chloritoid-bearing pelites in the Holenarsipur region indicate amphibolite facies conditions (Bouhallier et al., 1995; Dasgupta et al., 2019). Further south in the Sargur-Gundlupet region hornblende-clinopyroxene bearing mafic rocks and appearance of orthopyroxene in migmatitic gneisses marks amphibolite to granulite facies transition (Bouhallier et al., 1995; Jayananda et al., 2013a). The documented progressive increase of metamorphic grade from north to south is related to the end Archean (ca.2500 Ma) tectonothermal event ("hot orogen") that affected the whole Archean crust of the Dharwar craton (Peucat et al., 2013; Chardon et al., 2011; Jayananda et al., 2013a, 2018). Evidence for an earlier episode of metamorphism close to ca. 3100 Ma is preserved in the Holenarsipur region (Jayananda et al., 2013a, 2015; Dasgupta et al., 2019). To summarize, the cratonic core in WDC was affected by two major thermal events during ca. 3100 Ma and 2500 Ma (Jayananda et al., 2013a; Dasgupta et al., 2019). The 3100 Ma event was immediately preceded by a major tectono-magmatic event marked by the intrusion of hot trondhjemite magmas, partial convective overturn of mid to lower crust, and formation of dome-keel pattern.

5. Analytical methods

5.1 Elemental geochemistry

We present new major and trace elements data for the Holenarsipur greenstone volcanic rocks (Supplementary Table 1), spatially associated granitoids (TTG-type gneisses) and diapiric trondhjemites (Supplementary Table 2), as well as new LA-ICP-MS U-Pb zircon ages (Supplementary Table 3) together with *in-situ* LA-MC-ICP-MS Lu-Hf (Supplementary Table 4) isotope data for zircons from the adjoining granitoids. Our new Nd isotope data for the greenstone assemblages of the Holenarsipur greenstone belt presented in Supplementary Table 5. Published data of the stratigraphically equivalent greenstone belts and their adjoining granitoids also in the cratonic core have been compiled and also presented in Supplementary Tables 1 -5 (Bhaskar Rao et al., 1992, 2008; Monrad, 1983; Peucat et al., 1993; Chardon, 1997; Guitreau et al., 2017; Jayananda et al., 2008, 2015, 2016, 2019; Naqvi et al., 2009; Tushipokla and Jayananda, 2013; Maya et al., 2017; Mukherjee et al., 2012; Ranjan et al., 2020; Patra et al., 2020; Panicker et al., 2021).

The least altered samples were selected for elemental and Nd isotope analysis. Rocks were chipped into smaller pieces and powdered using a jaw-crusher (tungsten carbide jaws) and agate mill to obtain fine powder. A total of 65 samples (51 greenstone volcanic rocks and 14 granitoid samples) were selected for major and trace element measurements. Major elements were analyzed by automated XRF (Pan Analytical Axios Model PW4400/40). The precision for major elements is as follows: 1% for SiO_2, 1.5-3% for Al_2O_3, 2-3% for Fe_2O_3, 10% for MnO, 1-3% for MgO, 2-5% for CaO, 1.5-3% for Na_2O, 2.5% for K_2O, 2-5% for TiO_2, and 5% for P_2O_5. Trace elements for granitoid samples were analysed at National Geophysical Research (NGRI) Hyderabad using HR-ICPMS Nu instruments AttoM. Granitoid samples were dissolved using Microwave acid digestion method (Model MARS-5, CEM corporation, USA) at CSIR-NGRI (Hyderabad) which involves dissolution of 0.05g finely powdered (~200 ASTM mesh) sample in a PFA lined vessel using electronic grade HF and analytical grade HNO_3 in 7:3 proportion. The operating parameters of the microwave digestion system are optimally chosen to ramp and hold the processing time to get clear solutions. Rh-103 is used as an internal standard and 0.02% solution of matrix matched geological reference material is used as calibration standard. The data obtained for trace elements generally have a precision better than 5% (RSD) and comparable accuracy. Trace element concentrations for granitoids were determined by using Perkin Elmer SCIEX ELAN DRC II at CSIR-NGRI following the procedures described by Balaram and Gnaneswar Rao (2003).

Trace element concentrations for the Holenarsipur volcanic rocks were analyzed at Department of Geosciences, National Taiwan University by quadrupole inductively coupled plasma–mass spectrometry (ICP-MS). About 50 mg sample powders were dissolved in an equal mixture of sub-boiling distilled HF and HNO_3 in a Teflon high-pressure bomb on a hot plate for 48 hours. The dissolved samples were then evaporated to dryness, refluxed with 6 N HNO_3, and reheated close dryness. Then samples were re-dissolved in 2 mL of 3N HNO_3 in high-pressure bombs for an additional 24 h to ensure complete dissolution of refractory minerals. After dissolution, the samples were diluted with Milli-Q water (18.2 mega-ohm) to a final dilution factor of 2000.

5.2 *Whole-rock Sm-Nd isotopes*

Sm-Nd isotope analysis were performed at JAMSTEC (Japan) and Institute of Earth Sciences and Academia Sinica (Taipei). At JAMSTEC, chemical separation procedures for Sm-Nd purification were done using an AG50W-X8 cation ion exchange resin (Bio Rad, California, USA), along with Sr-spec and Ln-spec resins (Eichrom Tec. Inc., Illinois, USA). After the initial separation, using 1 mL of AG50W-X8 resin, Nd was purified using 0.05 mL of Sr-spec resin, 0.3 mL of Ln-spec resin, and 1 mL of Ln-spec resin, respectively. Parts of the column separation procedures were conducted with a fully automated open-column chemical separation system named COLUMNSPIDER (Miyazaki et al., 2018), developed by JAMSTEC and HOYUTEC Co., Ltd. (Kawagoe, Japan). The total procedural blanks for Nd, and Hf were <69, 8 pg. The Nd isotope ratios were measured with a Triton thermal ionization mass spectrometer (TIMS; Thermo-Finnigan, Bremen, Germany) at JAMSTEC. The measured Nd isotope ratios were normalized to a ^{146}Nd/^{144}Nd value of 0.7219 to correct for mass fractionation. The mean value obtained by repeated analyses of the JNdi-1 standard was 0.512097 ± 0.000009 (2SD, n = 14) which is consistent with the consensus value of 0.512115 ± 0.000007 (Tanaka et al., 2000).

The analytical procedure at the Institute of Earth Sciences, Academia Sinica (Taipei) involved dissolution of approximately 100 mg of whole-rock powder using a mixture of HF-HNO_3-$HClO_4$ in a Teflon beaker at 145°C for seven days. Sample dissolution procedures were repeated to ensure the total dissolution of the refractory phases in the samples. REEs were separated using polyethylene columns with a 5 ml resin bed of AG 50W-X8, 200 to 400 mesh. Neodymium was separated from other REEs using polyethylene columns with a Ln resin as a cation exchange medium. Nd was loaded with H_3PO_4 on a Rhenium double filament. The ^{143}Nd/^{144}Nd ratios were normalized to ^{146}Nd/^{144}Nd = 0.7219. ^{143}Nd/^{144}Nd isotope ratios were measured using a Finnigan Triton TIMS at the Institute of Earth Sciences, Academia Sinica, Taipei. JMC Nd standard yielded a ^{143}Nd/^{144}Nd of 0.511816 ± 12 (2s, n = 101) consistent with the consensus value of JMC standard 0.511812±7 (Jahn et al., 2009). The Chondritic Uniform Reservoir (CHUR) composition used to calculate ε_{Nd} values is ^{143}Nd/^{144}Nd = 0.512630 and ^{147}Sm/^{144}Nd = 0.1960 (Bouvier et al., 2008), the ^{147}Sm decay constant is 0.00654 Ga^{-1} (Begemann et al., 2001). Depleted mantle (DM) values used in the calculation of T_{DM} model ages are ^{143}Nd/^{144}Nd = 0.51315 and ^{147}Sm/^{144}Nd = 0.2137 (De Paolo, 1981).

5.3 *Zircon U-Pb geochronology by LA-ICP-MS*

Zircon U–Pb geochronology by LA-ICP-MS was performed at Laboratoire Magmas et Volcans (LMV), Université Clermont Auvergne, Clermont-Ferrand (France) using a Resonetics Resolution M-50 laser-ablation system coupled to a Thermo Element XR. Operating conditions are presented in the Supplementary Table 6. We have handpicked euhedral, clear zircon crystals without visible inclusions as much as possible and mounted them in epoxy. These zircon mounts were further polished and imaged by cathodoluminescence (CL) and/or back-scattered-electrons (BSE) using a Jeol JSM-5910LV scanning electron microscope at LMV. CL/BSE images were acquired using an acceleration voltage of 15 kV. Internal zircon texture was used to select crystals with least radiation damage for U–Pb dating and target most pristine-looking zones (relatively bright zones with fine oscillatory zoning in CL; Corfu et al., 2003). LA-ICP-MS analyses were carried out using the zircon standard 91500 (1065 Ma: Wiedenbeck et al. 1995) for external normalization and AS3 (1099 Ma: Paces & Miller 1993) and Plešovice (337 Ma: Sláma et al. 2008) for data quality control. Zircon U-Pb data were processed using the GLITTER software (Van Achterberg et al. 2001), age calculations were done using a present-day $^{238}U/^{235}U$ of 137.818 (Hiess et al., 2012) and decay constants of $1.55125.10^{-10}$, $9.8485.10^{-10}$, and $4.9475.10^{-11}$ $year^{-1}$ for ^{238}U, ^{235}U and ^{232}Th, respectively (Jaffey et al., 1971; LeRoux and Glendenin, 1963). Finally, data were plotted using Isoplot version 3.75 by Ludwig (2008). Zircon reference materials AS3 and Plešovice analyzed during our LA-ICP-MS sessions returned Concordia ages of 1098.2 ± 2.6 Ma (2SE, MSWD = 0.68) and 337.6 ± 1.1 Ma (2SE, MSWD = 0.70), respectively, which are in excellent agreement with ages provided in Paces and Miller (1993) (1099 Ma) and in Sláma et al. 2008 (337 Ma).

5.4 Zircon Lu-Hf isotope geochemistry by LA-MC-ICPMS

Lu-Hf isotope measurements were conducted at LMV using a Resonetics Resolution M-50 laser-ablation system coupled to a Thermo Neptune Plus MC-ICP-MS (LA-MC-ICP-MS; see Supplementary Table 6). Methods and operating conditions are presented in further detail in Guitreau et al. (2017, 2019). Isotopic ratios of ^{173}Yb/^{171}Yb normalized to the value of 1.132685 (Chu et al., 2002) and ^{179}Hf/^{177}Hf normalized to the value of 0.7325 (Stevenson and Patchett 1990) were used to determine Yb and Hf instrumental mass biases. Lu fractionation was assumed to follow that of Yb (Fisher et al., 2014). Values of 0.79618 for ^{176}Yb/^{173}Yb (Chu et al., 2002) and 0.02655 for ^{176}Lu/^{175}Lu (Fisher et al., 2014) were used to correct data for the isobaric interferences of ^{176}Yb and ^{176}Lu on ^{176}Hf. Natural zircon 91500 (Blichert-Toft, 2008) and Mud Tank (Woodhead and Hergt, 2005) together with the MUN artificial zircon reference materials (Fisher et al., 2011) were measured multiple times during LA-MC-ICP-MS analyses in order to monitor instrumental fractionation and check data quality. Lu-Hf isotope analyses were done on top of zones with coherent U-Pb systematics that were identified during the U-Pb isotope analyses in order to acquire linked information. Time-resolved signals were carefully monitored throughout each and every analysis to minimize issue of domain mixing and grain heterogeneities. We have used the ^{176}Lu decay constant value of Scherer et al. (2011) and Söderlund et al. (2004), which is $1.867.10^{-11}$ year^{-1} to calculate initial Hf isotopic compositions. Uncertainties associated with the radiogenic-ingrowth correction were propagated using the algorithms of Ickert (2013). ε_{Hf} values were calculated using CHUR values provided in Iizuka et al. (2015). Results on standards and unknowns are available in supplementary Table 4. The synthetic MUN-0 zircon, which contains no measurable quantities of REE, gave an instrumental-fractionation-corrected ^{176}Hf/^{177}Hf slightly different from that published in (Fisher et al., 2011) which was used to correct all other zircon reference materials by external normalization. All data were acquired over two separate measurement sessions. For the first session, MUN-1, MUN3, 91500, and Mud Tank gave respective present-day

^{176}Hf/^{177}Hf of 0.282124 ± 0.000029, 0.282127 ± 0.000034, 0.282315 ± 0.000057, and 0.282511 ± 0.000023 (Supplementary Table 4), which are consistent with published values of 0.282135 ± 0.000007 for MUN zircons (Fisher et al., 2011), 0.282308 ± 0.000006 for 91500 (Blichert-Toft, 2008), and 0.282507 ± 0.000006 for Mud Tank (Woodhead and Hergt, 2005). Measured ^{176}Lu/^{177}Hf and ^{176}Yb/^{177}Hf were also consistent with the range provided in corresponding references. For the second session, MUN-1, MUN-3, MUN-4, 91500, and Mud Tank gave respective present-day ^{176}Hf/^{177}Hf of 0.282131 ± 0.000027, 0.282126 ± 0.000027, 0.282126 ± 0.000043, 0.282296 ± 0.000021, 0.282512 ± 0.000022, which are also consistent with published values (Supplementary Table 4). The same is true for measured ^{176}Lu/^{177}Hf and ^{176}Yb/^{177}Hf.

6. Geochemistry of the greenstone volcanic rocks

6.1 Major elements

The volcanic rocks of the Holenarsipur greenstone belt are dominantly ultramafic with minor mafic composition. The volcanic rocks of the three blocks in the Holenarsipur greenstone belt show a wide range of elemental compositions. The distinction between the komatiites and komatiitic basalts in the three blocks is based on their respective MgO contents (Arndt and Nisbet, 1982).

The volcanic rocks of the southwestern block are komatiitic (SiO_2 = 44.3-47.9 wt.% and MgO = 21.4-29.7 wt.%) except two samples that display komatiitic basalt composition (SiO_2 = 48.5-49.1 wt.%; MgO = 15.9-15.6 wt.%). Both komatiite and komatiitic basalts exhibit high CaO/Al_2O_3 (1.06-1.59) and low Al_2O_3/TiO_2 (7.7-14.7) values.

Among 20 analyzed samples of volcanic rocks from the northcentral block, five samples show komatiite composition (SiO_2 = 45.1-47.9 wt.%; MgO = 17.9 -23.9 wt.%) whilst 14 samples have komatiitic basalt chemistry (SiO_2 = 47.4-49.3 wt.%; MgO = 16.6-10.3 wt.%), one sample show basaltic affinity (SiO_2 = 50.6 wt.%; MgO = 9.8 wt.%) and another one is felsic (SiO_2 = 68.6 wt.%; MgO = 1.47 wt.%; Na_2O = 3.47 wt.%; K_2O = 1.47 wt.%). These volcanic rocks (felsic volcanic excluded) display significant variation in CaO/Al_2O_3 (1.32-1.09) and Al_2O_3/TiO_2 (7.7 – 12.5) values.

Among 21 samples analyzed from the eastern block, eighteen samples are volcanic rocks and three samples are gabbro to plagiogranite. Volcanic rocks comprise 12 samples of komatiites (SiO_2 = 42.7-48.0 wt.%; MgO = 35.5-18.0 wt.%), 6 samples of komatiitic basalt to high-Mg basalts (SiO_2 = 48.5- 50.2 wt.%; MgO=17.3-9.4 wt.%), 2 samples of gabbro (SiO_2 = 48.7-48.8 wt.%; MgO = 6.73-6.89 wt.%) and one plagiogranite sample (SiO_2 = 69.7 wt.%; MgO = 0.95 wt.%; Na_2O = 6.39 wt.%; K_2O = 0.60 wt.%). The komatiites show higher CaO/Al_2O_3 (1.42-1.04 wt.%), but conversely low Al_2O_3/TiO_2 (7.9 to 15.3 except one sample that has higher value of 20.5), compared to komatiitic basalts which exhibit high CaO/Al_2O_3 (1.04-1.11) and low Al_2O_3/TiO_2 (7.92 to 9.42).

Published data on volcanic assemblages from the other stratigraphically equivalent greenstone belts in the cratonic core (Subba Rao and Naqvi, 1999; Jayananda et al., 2008, 2016; Mukherjee et al., 2012; Tushipokla and Jayananda, 2013; Maya et al., 2017; Patra et al., 2020) reveal voluminous komatiite and komatiitic basalts displaying large variation in major and trace element compositions. Among the greenstone volcanic rocks, the Nuggihalli samples display a narrow range of SiO_2 = 41.3-42.5 wt.% with MgO = 33.0-35.0 wt.% but significant variation in CaO/Al_2O_3 (1.19-0.61) and Al_2O_3/TiO_2 (9.8-21.0) whilst the Kalyadi samples exhibit large variation in SiO_2 (38.9-50.3 wt.%) and MgO (22.9-32.97 wt.%) as well as CaO/Al_2O_3 (1.32-0.84) and Al_2O_3/TiO_2 (12.38-23.48). The J.C. Pura volcanic rocks also display significant variation in SiO_2 (42.12-50.63 wt.%; but most samples show less than 46.0 wt.% SiO_2) and MgO (10.8-42.20 wt.%; most samples show >30 wt.% MgO) as well as CaO/Al_2O_3 (2.45-0.70) and Al_2O_3/TiO_2 (6.2-22.5). On the contrary, the Ghattihosahalli samples are characterized by a narrow range of SiO_2 (42.0-42.4 wt.%; MgO (39.2- 41.3 wt.%), CaO/Al_2O_3 (1.34-1.32) and Al_2O_3/TiO_2 (5.0). The Banasandra komatiites also display a narrow compositional range of SiO_2 (41.5-46.8 wt.%), high MgO (30.4-42.4 wt.%) and CaO/Al_2O_3 (0.64-1.25) and Al_2O_3/TiO_2 (6.75-18.48). The Nagamangala volcanic rocks also exhibit a narrow range of compositions (SiO_2 = 40.5-44.0 wt.%; MgO = 28.8-35.8 wt.%), CaO/Al_2O_3 (1.18-0.67) and Al_2O_3/TiO_2 (11.37-19.96).

In summary, the volcanic assemblages from the three blocks of the Holenarsipur greenstone belt show variations in major element characteristics wherein the southwestern block shows komatiite with minor komatiitic basalt whilst the northcentral block reveals abundant komatiitic basalts with komatiite, and the eastern block contains komatiite, minor basalt intruded by sheeted dykes, gabbro and plagiogranite. The volcanic sequences from other greenstone belts are dominantly komatiite to komatiitic basalt in composition with significant variations in major element contents. The majority of studied komatiite and komatiitic basalts flows show characteristics similar to the Al-depleted Barberton komatiites and komatiitic basalts with CaO/Al_2O_3 >1 and Al_2O_3/TiO_2 <18 whilst other samples show Al-undepleted [CaO/Al_2O_3 <1.0; Al_2O_3/TiO_2 >18.0] character of Munro-type (Arndt, 2003).

Major element data for volcanic rocks of the Holenarsipur greenstone belt together with volcanic rocks of the Nuggihalli, Kalyadi, J.C. Pura, Ghattihosahalli, Banasandra and Nagamangala greenstone belts projected on the triangular plots of Al_2O_3-Fe_2O_3+TiO_2-MgO (after Jensen, 1976 modified by Viljoen et al., 1982) and CaO-MgO-Al_2O_3 (Viljoen et al., 1982) reveal komatiite to komatiitic-basalt composition except few samples extending into the tholeiitic field (**Fig.7.1a, b**). On the Al_2O_3 versus FeO/(FeO+MgO) versus binary plot (after Viljoen et al., 1982) the volcanic rocks of the southwestern block of the Holenarsipur belt plot on the Barberton komatiite field whilst majority of the samples from the northcentral block fall within the Barberton komatiitic basalt field except few samples (**Fig.7.1c**). The eastern block samples together with samples from other greenstone belts plot on the Barberton komatiite field and extending into the komatiitic basalt field. About 70% of the studied volcanic rocks show characteristics similar to the Al-depleted Barberton komatiites and komatiitic basalts whilst remaining samples show Al-undepleted character (**Fig.7.1c**) of Munro-type (Arndt, 2003).

On Harker binary plots, major element oxides plotted against MgO define moderate to strong correlations for greenstone volcanic rocks of the three blocks of the Holenarsipur belt together with volcanic rocks of other equivalent greenstone belts (**Fig.7.1d**) which suggest an olivine ± orthopyroxene control. However, some minor differences in correlations and/or compositions can be seen locally (e.g., TiO_2 vs. MgO in J.C Pura).

6.2 Trace elements

The volcanic rocks from the Holenarsipur and other equivalent greenstones from the cratonic core show a wide range of trace element concentrations. Among the Holenarsipur volcanic rocks, komatiites and komatiitic basalts of the southwestern block exhibit high Ni (900-1983 ppm except for two samples with 368 and 492 ppm) and Cr (1011-3005 ppm) contents whereas the northcentral block komatiitic basalts and komatiites show low to high Ni (381-1204 ppm) and Cr (941-2167 ppm) concentrations. On the contrary, the eastern block komatiites display moderate to very high Ni contents (796 to 2786 ppm) except for two komatiitic basalts that have lower values of 399 and 486 ppm.

The komatiites of the Nuggihalli belt are characterized by high Ni (1544-1960 ppm) and Cr (2702-4400 ppm) concentrations, whilst the Kalyadi komatiites show moderate to high Ni (3145-3177 ppm) and Cr (1969-3597 ppm) contents. In contrast, the J.C. Pura volcanic rocks display large variations in Ni content (600-3064 ppm with exception of a few basaltic samples that have less than 500 ppm), and Cr (800-5649 ppm with a few samples less than 700 ppm). The Ghattihosahalli komatiites exhibit the highest Ni contents (3145-3147 ppm) but conversely low Cr (1208-1338 ppm) among ultramafic volcanic rocks of the region, whilst the Banasandra komatiites show high Ni concentrations (1313-2619 ppm) with a large variation in Cr (1614-2494 ppm). The Nagamangala komatiites are characterized by high Ni (1121-1590 ppm) with a wide range of Cr contents (1294-3860 ppm).

When projected against MgO in Harker's binary diagrams, petrogenetically significant trace elements show strong to poorly fractionated trends of the studied volcanic rocks (**Fig.7.1e**). The greenstone volcanic rocks in the cratonic core show significant variations in the REE and other incompatible element abundances. The studied komatiites and komatiitic basalts from the three blocks of the Holenarsipur belt exhibit large variations in REE contents. Samples from the SW block form two groups (low- and high-REE; **Fig.7.2a, c**). The low REE samples (ΣREE = 4.4-19.2 ppm; MgO = 25.1-29.7 wt.%) exhibit flat REE patterns with variable $(Gd/Yb)_N$ values of 0.53-1.86 (**see fig.7.2a**). On primitive-mantle normalized multi-element diagrams (Sun and McDonough, 1989), these samples display either positive or no Zr-Ti anomalies without any Hf anomalies whilst all samples show slight positive Y anomalies (**Fig.7.2b**). The high REE samples (ΣREE = 20.6-66.7 ppm; MgO = 15.6-29.5) show fractionated REE with $(Gd/Yb)_N$ of 1.22-2.29 (**see fig.7.2c)** with two samples displaying negative Eu anomalies. On the contrary, the high ΣREE komatiites show either slightly positive or no significant Nb anomalies associated with negative Zr, Hf, Ti and Y anomalies on primitive-mantle normalized multi-element diagrams (**Fig.7.2d**). Two samples exhibit negative Nb anomalies coupled with mild positive Zr, Hf and Y anomalies on multi-element diagrams (**see fig.7.2d**).

Komatiites from the northcentral block (MgO = 17.9-23.9 wt.%) with low to high ΣREE (14.6 -59.1 ppm) show flat to moderately fractionated REE patterns with three samples having negative Eu anomalies (**Fig.7.2e**). On the other hand, komatiitic basalts contain moderate to high ΣREE (31.2-138.0 ppm; MgO = 10.3-16.6 wt.%) and display flat to moderately fractionated REE patterns (**Fig.7.2g**) with one sample displaying a negative Eu anomaly. On primitive-mantle normalized multi-element diagrams, both komatiites (**Fig.7.2f**) and komatiitic basalts (**Fig.7.2h**) exhibit negative Nb anomalies with slight positive to negative Zr, Hf, Ti, Y anomalies. The felsic volcanic sample shows [high SiO_2 = 68.65 wt.%, Al_2O_3 = 14.94 wt.%, MgO = 1.29 wt.%, and Na_2O = 3.17 wt.%] high total REE (392 ppm) content and poorly fractionated REE patterns [$(La/Yb)_N$ = 2.47], as well as a slightly negative Eu anomaly (**see fig.7.2g**). The samples display either negative or no significant Nb, Zr, Hf, Ti and Y anomalies on primitive-mantle normalized multi-element diagram.

The eastern block volcanic rocks are mainly komatiitic with a few samples displaying basaltic compositions, and their REE contents reveal two groups (i.e., low- and high-REE). The low ΣREE group (4.4-18.4 ppm with MgO = 22.8-30.9 wt.%) is characterized by flat and poorly to moderately fractionated REE patterns [$(Gd/Yb)_N$ = 0.41-1.38] with two samples showing negative Eu anomalies (**Fig.7.2i**). On PM-normalized multi-element diagrams, no significant Nb, Zr and Hf anomalies but positive Ti anomalies and variable Y anomalies (either positive, negative or no anomaly; **Fig.7.2j**). The high ΣREE (48.4-294.8 ppm) group (MgO = 17.0-30.4 wt.%) exhibits fractionated REE patterns $(Gd/Yb)_N$ =1.16-1.96; **Fig.7.2k**) coupled with positive Nb anomalies and negative Zr, Hf and Ti anomalies (**Fig.7.2l**) on multi-element diagrams. Two samples of gabbro intruded into the komatiite to basaltic volcanic rocks in the eastern block show low total REE contents (34.4-44.3 ppm), LREE depletion and poorly fractionated REE patterns with $(Gd/Yb)_N$ values ranging from 0.92 to 1.05 (**Fig.7.2i**). A plagiogranite unit injected into the volcanic sequence and gabbro shows low total REE content (41.7 ppm) with poorly fractionated REE pattern and $(La/Yb)_N$ value of 5.66 (**see fig.7.2i**).

Komatiites from the Nuggihalli greenstone belt exhibit sub-chondritic to low total REE concentrations (ΣREE = 4.2-30.9 ppm) and display poor to moderately fractionated REE patterns [$(Gd/Yb)_N$ = 0.43-1.24] with one sample showing negative Eu anomaly (**Fig.7.3a**). On PM normalized multi-element plot, two samples show positive Zr, Ti and Y anomalies whilst one sample shows negative Zr, Ti and Y anomalies (**Fig.7.3b**). Komatiites of the Kalyadi greenstone belt also display sub-chondritic to moderate total REE contents (ΣREE = 2.7-52.0 ppm) with poorly to moderately fractionated REE patterns [$(Gd/Yb)_N$ = 0.62-1.48] except for one sample that shows negative Ce anomaly (**Fig.7.3a**). On the PM normalized multi-element diagram, three samples exhibit positive Zr and Ti anomalies, but two samples show positive Y anomalies and one sample show negative Nb, Zr and Ti anomalies (**see Fig.7.3b**).

The komatiite and komatiitic basalts of the J.C Pura greenstone belt exhibit large variations in REE abundances (Jayananda et al., 2008, 2016) wherein samples of komatiite flows (<35 wt.% MgO) exhibit low to moderate REE (ΣREE = 14.1-45.9 ppm) whilst the cumulate layers (>35 upto 43 wt.%) contain very low to sub-chondritic REE concentrations (3.6-12.1 ppm). The samples of komatiite flows show uniform patterns with flat to moderately fractionated REE patterns [$(Gd/Yb)_N$ = 0.98-1.85)] except few samples displaying negative Eu anomalies (**Fig.7.4a**). On PM normalized multi-element diagrams, they exhibit strong negative Zr, Hf, Ti and Y anomalies with positive Nb anomalies (**Fig.7.4b**). The cumulate layers show flat to moderately fractionated REE patterns with [$(Gd/Yb)_N$ = 0.65-1.66)] with two samples showing either positive or negative Eu anomalies (**Fig.7.4c).** On PM normalized multi-element plots, these cumulate layers show slight positive Nb and Y anomalies but significant negative Hf and positive Ti anomalies with a few samples showing no or very faint anomalies (**Fig.7.4d**). The J.C. Pura komatiitic basalts display poor to moderately fractionated REE patterns ([$(Gd/Yb)_N$ = 0.66-1.48] whilst on the PM normalised multi-element diagram they exhibit negative Nb, Zr, Hf, and Y anomalies (**Fig.7.4e,f).**

The Ghattihosahalli komatiites have very low REE concentrations (ΣREE = 9.76-9.81 ppm) and show fractionated REE patterns with $(Gd/Yb)_N$ = 2.26-2.52 (**Fig.7.5a**). On PM normalized multi-element diagrams, they show slight negative Nb and Th anomalies with strong negative Hf anomalies (**Fig.7.5b**). The Banasandra komatiites exhibit sub-chondritic to low total REE contents (3.5-12.2 ppm) and show poorly to moderately fractionated REE patterns [$(Gd/Yb)_N$ = 0.99-1.90)] (**Fig.7.5c**). On PM normalized multi-element diagrams, these komatiites display positive Nb and Ti anomalies associated with negative Hf anomalies (**Fig.7.5d**). The Nagamangala komatiites and komatiitic basalts contain low to moderate total REE contents (9.2-51.0 ppm), and exhibit poorly to moderately fractionated REE [$(Gd/Yb)_N$= 0.59-2.57)] (**Fig.7.5e**). On PM normalised multi-element plot, these samples show slight negative Nb but strong negative Hf anomalies (**Fig.7.5f**).

When projected on $(Gd/Yb)_N$ versus Al_2O_3/TiO_2 and CaO/Al_2O_3 plots, data for komatiite and komatiitic basalts from all three blocks of the Holenarsipur greenstone belt, together with volcanic rocks of other greenstone belts from the cratonic core form an ellipse that overlaps fields corresponding to Barberton and Abitibi-type komatiites. About 70% of data fall in the field defined by Barberton komatiites and the remaining samples plot in the field of Abitibi-type komatiites (**Fig.7.6a, b**).

6.3 Sm-Nd isotope geochemistry

Our new Sm-Nd isotope data for the Holenarsipur greenstone belt along with the published data for other greenstone belts (Jayananda et al., 2008; Mukherjee et al., 2012; Maya et al., 2017; Patra et al., 2020) are presented in the Supplementary Table 5. The komatiite and komatiitic basalts from all the greenstone belts in the cratonic core show significant variations in $^{147}Sm/^{144}Nd$ and $^{143}Nd/^{144}Nd$ values. Among the Holenarsipur volcanic rocks, komatiite and komatiitic basalts from the southwestern block displays a well-defined positive correlation (R^2 = 0.99) between present-day $^{147}Sm/^{144}Nd$ and $^{143}Nd/^{144}Nd$ that show a range of respectively, 0.1137-0.2105 and 0.510971-513037. The higher the Nd and Sm concentrations, the lower the

^{147}Sm/^{144}Nd. The slope of this correlation translates into a Sm-Nd regression age of 3118 ± 168 Ma that gives an initial ^{143}Nd/^{144}Nd of 0.50870 ± 0.00021, which translates into an initial ε_{Nd} of +2.1 ± 4.1 at 3118 Ma.

Volcanic rocks from the eastern block exhibit positively correlated (R^2 = 0.85) ^{147}Sm/^{144}Nd and ^{143}Nd/^{144}Nd (present-day) ranging from, respectively, 0.1318-0.2211 and 0.511482-0.513980. The higher Nd and Sm concentrations, the lower ^{147}Sm/^{144}Nd. Sm-Nd regression for Eastern block volcanic rocks give an imprecise age of 3043 ± 428 Ma and an initial ^{143}Nd/^{144}Nd of 0.50876 ± 0.00037, which translates into an initial ε_{Nd} of +1.4 ± 7.3 at 3043 Ma.

Volcanic rocks from the northcentral block present weakly correlated (R^2 = 0.62) ^{147}Sm/^{144}Nd and ^{143}Nd/^{144}Nd (present-day) that range from, respectively, 0.1695-0.2139 and 0.512127-0.513119. If the Sm-Nd correlation is converted into a regression age, it gives 2578 ± 763 Ma associated with an initial ^{143}Nd/^{144}Nd of 0.5094 ± 0.0013, which translates into an initial a ε_{Nd} of +2.0 ± 2.3 at 2578 Ma that is comparable with the Sm-Nd whole rock isochron age 2620±55 Ma documented by Drury et al (1987). However, our ^{147}Sm/^{144}Nd and ^{143}Nd/^{144}Nd data for komatiites and komatiitic basalts from all the three blocks of the Holenarsipur belt together with published data for komatiites (Jayananda et al., 2008) from other stratigraphically equivalent greenstone belts in the cratonic core yield a regression age of 3356 ± 68 Ma for the komatiite volcanism in the Holenarsipur belt which is associated with an initial ^{143}Nd/^{144}Nd of 0.50843 ±0.00027 that translates into an initial ε_{Nd} of +2.9 ± 5.3 at 3356 Ma. Our data exhibit some consistency with published Sm-Nd isotope data for WDC komatiites (Jayananda et al., 2008) because they follow the main ^{147}Sm/^{144}Nd-^{143}Nd/^{144}Nd correlation that provided an age of 3352 ± 110 Ma.

The volcanic rocks of other greenstone belts in the cratonic core display large variations in ^{147}Sm/^{144}Nd, ^{143}Nd/^{144}Nd and $\varepsilon_{Nd(T)}$. The Nuggihalli and Kalyadi volcanic rocks exhibit high

$^{147}Sm/^{144}Nd$ and $^{143}Nd/^{144}Nd$ values with $\varepsilon_{Nd(T)}$ signatures (Jayananda et al 2008; Mukherjee et al., 2012; Patra et al, 2020) ranging from +1.3 to +5.4 except for three samples that have negative signatures (i.e., -1.4 to -3.6). These Sm-Nd data suggest their origin from variably depleted mantle reservoirs with possible traces of crustal contamination or influence of secondary processes. The moderate to high $^{147}Sm/^{144}Nd$ (0.1851 – 0.2194) and $^{143}Nd/^{144}Nd$ (0.511569 to 0.513203), and $\varepsilon_{Nd(T)}$ of +1.2 to +2.6 for the J.C. Pura komatiites can be attributed to their origin from moderately depleted mantle reservoirs. The Ghattihosahalli samples display relatively narrow range of $^{147}Sm/^{144}Nd$ (0.1493 – 0.1686) and $^{143}Nd/^{144}Nd$ (0.511859 to 0.512159) values and $\varepsilon_{Nd(T)}$ from +2.8 to +5.3 indicating depleted mantle reservoirs. In contrast, Banasandra komatiites show large variations in $^{147}Sm/^{144}Nd$ (0.1224 – 0.2431) and $^{143}Nd/^{144}Nd$ (0.511174 to 0.514037) with $\varepsilon_{Nd(T)}$ from +1.1 to +5.1 suggesting their origin from variably depleted mantle reservoirs.

6.4 Timing of greenstone volcanism (ca.3400-3200 Ma)

The time frame of greenstone volcanism in the cratonic core is poorly constrained as precise and accurate geochronological data are rather scanty. Most direct geochronological information pertaining to greenstone volcanism have been obtained using whole-rock Sm-Nd isotope system or through U-Pb dating of zircons from interlayered felsic volcanic units (e.g. Peucat et al., 1995). Dating komatiite assemblages is challenging due to their unusually low Nd contents coupled with the effects of metamorphism and hydrothermal alteration processes which affected the Sm-Nd isotope system. Drury et al. (1987) presented a Sm-Nd whole-rock isochron age of 2620 ± 55 Ma for the mafic volcanic rocks from the “so called” younger Dharwar Supergroup of the Holenarsipur belt (Swami Nath and Ramakrishnan, 1981) corresponding to northcentral block of the present study. In contrast, Peucat et al (1995) obtained U-Pb zircon age of 3298 ± 7 Ma for felsic volcanic flow from the same younger

Dharwar Supergroup (Swami Nath and Ramakrishnan, 1981) and concluded that the entire Holenarsipur belt belongs to the older Sargur Group. Our new U-Pb zircon age of 3305 ± 10 Ma (**Fig.7.8m**) from the same felsic volcanic flow also confirms the age obtained by Peucat et al (1995). Further, $^{147}Sm/^{144}Nd$ and $^{143}Nd/^{144}Nd$ data for komatiites and komatiitic basalts from the three blocks of the Holenarsipur belt together with published data for komatiites from other stratigraphically equivalent greenstone belts from the cratonic core yield an isochron age of 3356 ± 68 Ma. Our data exhibit some consistency with published Sm-Nd isotope data of komatiites (Jayananda et al., 2008) because they follow the main $^{147}Sm/^{144}Nd$-$^{143}Nd/^{144}Nd$ correlation that provided an age of 3352 ± 110 Ma based on 16 samples from the J.C. Pura, Nuggihalli, Kalyadi, Ghattihosahalli and Banasandra greenstone belts. The J.C. Pura komatiites alone define a Sm-Nd whole-rock isochron age of 3384 ± 200 Ma (MSWD = 1.8). Published Sm-Nd data for komatiites from Nuggihalli and adjoining Kalyadi greenstone belt (Jayananda et al., 2008; Mukherjee et al., 2012; Patra et al., 2020) together define a whole-rock isochron age of 3207 ± 89 Ma (initial $^{143}Nd/^{144}Nd = 0.00012$; MSWD=4.3) which is similar to the ages obtained for these belts 3284 ±310 Ma (MSWD 3.7; this work and Jayananda et al 2008) as well as recent Sm-Nd and Lu-Hf isochron ages of komatiites and komatiitic basalts from the north-eastern part of Bababudan basin (Ravindran et al., 2021). Sm-Nd isotope data for peridotite-pyroxenite-anorthosite-gabbro from the Nuggihalli belt yielded a whole-rock isochron age of 3125 ± 120 Ma (Mukherjee et al., 2012). The Banasandra komatiites define a Sm-Nd whole-rock isochron age of ca. 3150 Ma (Maya et al., 2017). Although other workers (Mukherjee et al., 2012; Maya et al., 2017) have obtained Sm-Nd whole-rock isochron ages of 3150 Ma for the Nuggihalli and Banasandra greenstone belts, they are within the limits of Sm-Nd and Lu-Hf whole-rock isochron results considering their elevated analytical uncertainties. Our new Sm-Nd isotope data of the komatiites and komatiitic basalts from the three blocks of the Holenarsipur greenstone belt together with published data define a whole-rock isochron age of 3356 ± 68 Ma for the widespread komatiite volcanism in the cratonic core.

On the other hand, komatiite and komatiitic basalts from the Nuggihalli, Kalyadi, J.C. Pura, Ghattihosahalli and Banasandra greenstone belts exhibit wide ranges of ^{147}Sm/^{144}Nd values which is reflected in their LREE contents (Jayananda et al.,2008; Mukherjee et al., 2012; Maya et al., 2017; Patra et al., 2020). Twenty-one samples from different greenstone belts (excluding Holenarsipur) define a whole-rock isochron age of 3330 ± 210 Ma. Whole-rock isochrons calculated for the komatiite and komatiitic basalts of individual greenstone belts (Jayananda et al., 2008; Mukherjee et al., 2012; Patra et al., 2020; Maya et al. 2017; this study) exhibit similar initial Nd isotope compositions which suggest a genetic link. Sargur Group greenstones could, hence, have been erupted within short-time intervals in which case Sm-Nd age dispersion would be due to secondary (post-crystallization) processes. Alternatively, greenstone volcanic assemblages emplaced over a long time period and the range of ~210 Ma indicates an actual time span over which greenstone volcanic rocks formed, hence, essentially between 3400 and 3200 Ma concurrently with WDC granitoids formation (Peucat et al., 1993; Jayananda et al., 2015; Guitreau et al., 2017; Ranjan et al., 2020; Bidyananda et al., 2016).

7. Geochemistry of granitoids (TTG-type gneisses) and diapiric trondhjemites

7.1 Zircon U-Pb geochronology

Our new U-Pb zircon data on granitoids, felsic volcanic flow of the Northcentral block and a plagiogranite from Eastern block together with published ages on the gneisses adjacent to the Holenarsipur greenstone belt presented in the Supplementary Table 3. Furthermore, CL images (**Fig. 7.7a-c**) of the studied zircons and U-Pb concordia presented in **Fig. 7.8a-n**. Our new zircon age data together with published U-Pb zircon ages of the gneisses and trondhjemite intrusions of the cratonic core (Peucat et al., 1993; Jayananda et al., 2015, 2019; Ranjan et al., 2020) are described in the following section.

Zircon crystals from the sample 18HP23 commonly exhibit fine oscillatory zoning (**Fig. 7.7c**) with various degrees of radiation damage accumulation. Th/U ratios are essentially within magmatic values (0.01-0.81 with an average of 0.45) and U concentrations are low to very high (177-1419 ppm with an average of 668 ppm). U-Pb data display various degrees of discordance but align along a single Discordia line with an upper-intercept represented by concordant analyses giving a Concordia age of 3430 ± 7 Ma (2 SE; **Fig.7.8a**) that we interpret as that of 18HP23 crystallization. One concordant analysis returned an age of 3500 ± 12 Ma (2 SE) which we interpret as an inherited crystal because the core of this zircon looks distinct from the rest of the crystal which has fine oscillatory zoning.

Most zircon crystals from the sample 18HP24a exhibit fine oscillatory or convolute zoning (**Fig. 7.7c**) with evidence for local radiation damage accumulation. Th/U ratios vary between 0.21 and 1.24 with an average of 0.74, hence, within magmatic values. U concentrations are low to very high because they vary between 55 and 1497 ppm with an average of 524 ppm. U-Pb data are variably discordant but align along a single Discordia line that intercepts the Concordia at an age of 3431 ± 8 Ma (2 SE) given by concordant analyses. This age is interpreted as that of crystallization of 18HP24a (**Fig.7.8b**).

Zircon crystals from the sample 18HP10b, which is a mica-rich enclave, provided three concordant ages of 3468 ± 17 Ma, 3271 ± 11 Ma, and 3166 ± 9 Ma (**Fig.7.8c**). These zircon crystals show bright fine oscillatory zoning with darker zones due to radiation damage accumulation (**Fig. 7.7c**). Th/U ratios vary between 0.05 and 0.58 with an average of 0.44, hence, within magmatic values, and U concentrations are very low to high (12-868 ppm; average 245 ppm).

The sample 18HP05 yielded very few zircon crystals of acceptable quality for U-Pb dating. We, therefore, report results for four crystals that exhibit oscillatory zoning with oval resorption patterns underlined by thin bright zones (**Fig. 7.7b**). Many crystals have accumulated large degrees of radiation damage. Th/U ratios vary between 0.59 and 0.87, hence, clearly within the magmatic range and U concentrations are low (83-431 ppm). U-Pb data are limitedly discordant and align along a single discordia line consistent with the concordia age of 3341 ± 9 Ma (2 SE; **Fig.7.8d**) given by the concordant data. This age is interpreted as the crystallization age of the sample 18HP05.

Zircon crystals from the sample 18HP01a exhibit various internal textures from bright and fine oscillatory zoning to dark patchy domains (**Fig. 7.7a**). Only best-looking domains were analysed and returned Th/U ratios from 0.04 to 1.37, with the majority being around the average value of 0.55. Uranium concentrations are very low to high (34-713 ppm) with an average of 221 ppm. U-Pb data are variably discordant and do not align along a single Discordia line but define a fan shape that converges towards concordant data indicating a Concordia age of 3319 ± 7 Ma (2 SE; **Fig.7.8e**). This age is interpreted as that of magmatic crystallization of the sample 18HP01a.

Zircon crystals from the sample 18HP01c are commonly dark in CL images and have broad zoning and stubby habit (**Fig. 7.7a**). Th/U ratios are consistent between crystals from this population (0.22-0.77) and so are U concentrations (281-757 ppm: average 501 ppm). U-Pb data are variably discordant but most concordant data record a concordia age of 3311 ± 10 Ma (2 SE; **Fig.7.8f**), assumed to be that of magmatic crystallization of the sample 18HP01c.

Zircon crystals from the sample 18HP03a have either fine oscillatory zoning or broad dark zoning (**Fig.7.7a**) with various evidence for advanced radiation damage accumulation. Th/U ratios are mostly high and vary between 0.40 and 1.81 (average of 0.94). Uranium concentrations are essentially low (27-295 ppm). U-Pb data are variably discordant and do not align along a single discordia but converge towards concordant data that give a concordia age of 3320 ± 8 Ma (2 SE; **Fig.7.8g**), interpreted as that of magmatic crystallization of the sample18HP03a.

Zircon crystals from sample 18HP03b commonly display fine oscillatory zoning although effects of radiation damage are also visible in some portions of the crystals (**Fig. 7.7a**). Th/U are commonly alike magmatic values (0.24-0.77) except for 2 crystals (0.05 and 1.12) and U concentrations are very variable (86-2940 ppm). U-Pb data show great dispersion, but some concordant data provide a Concordia age of 3320 ± 8 Ma (2 SE; **Fig.7.8h**) that is thought to be that of igneous crystallization of the sample 18HP03c.

Zircon crystals from the sample 18HP04a are generally dark in CL images but show fine oscillatory zoning (**Fig. 7.7a, b**). Th/U ratios fall within magmatic values because they range from 0.43 to 0.91. Uranium concentrations are low to moderate (209-764 ppm; average = 418 ppm). U-Pb data distribute close to the Concordia curve and most concordant data give an age of 3304 ± 8 Ma (2 SE; **Fig.7.8i**) which is assumed to be that of crystallization.

Zircon crystals from the sample 18HP04b exhibit fine oscillatory zoning as well as sector zoning (**Fig. 7.7b**). Their Th/U vary between 0.48 and 1.32 with an average of 395 whereas U concentrations are generally moderate (253-568 ppm). U-Pb data show complex characteristics in Concordia plot that returned two concordant clusters at 3292 ± 9 Ma (2 SE) and 3339 ± 8 Ma (**Fig.7.8j**). We interpreted the first age as that of magmatic crystallization and the second one as zircon inheritance.

Zircon crystals from the sample 18HP07 commonly have simple fine oscillatory zoning (**Fig. 7.7b**) despite some crystals having obvious signs of advanced radiation damage. Th/U are essentially within magmatic values (0.07-0.73) and U concentrations are very variable (179-1185 ppm). U-Pb data essentially align along a single discordia which upper-intercept correspond to concordant data that provided a concordia age of 3429 ± 9 Ma (2 SE; **Fig.7.8k**), assumed to be that of 18HP07 crystallization.

Zircon crystals from the sample 18HP15a are characterized by fine oscillatory zoning (**Fig. 7.7c**) and Th/U between 0.14 and 0.77, which corresponds to magmatic values. Their U contents are low to very high because they vary from 216 to 1773 ppm with an average of 575 ppm. With the exception of a few datapoints, U-Pb data align along a single discordia line with an upper-intercept that coincides with most concordant data at 3429 ± 11 Ma (2 SE; **Fig.7.8l**), most likely indicative of the time of igneous crystallization.

The sample 18HP13 yielded very poor-quality zircons except for one that we analysed multiple times. This crystal revealed a simple oscillatory zoning (**Fig. 7.7c**), consistent Th/U (0.24-0.71) and U concentrations (43-281 ppm). U-Pb data are either concordant or limitedly discordant all consistent with an age of 3305 ± 10 Ma (2 SE; **Fig.7.8m**).

The few zircon crystals that we managed to recover from sample 18HP39 show fine oscillatory zoning (**Fig. 7.7c**) and generally simple textures. Their Th/U are magmatic (0.35-0.82) and U concentrations variable (180-1001 ppm). U-Pb data gave a coherent age of 3347 ± 11 Ma (2 SE) that we interpret as that of crystallization (**Fig.7.8n**).

Published U-Pb zircon age data on the granitoids and detrital zircons from the cratonic core around Holenarsipur-Gorur, southern margin Bababudan basin, the J.C. Pura and Bellur-Nagamangala regions reveal that their magmatic protoliths formed during 3600-3200 Ma (Nutman et al., 1992; Meen et al., 1992; Peucat et al., 1993; Bidyananda et al., 2016; Jayananda et al., 2015; Ranjan et al., 2020; Ao et al., 2021). The oldest zircon xenocrysts from trondhjemitic gneiss in the Hassan-Gorur region indicate 3610 Ma (Guitreau et al., 2017) whilst detrital zircons from pelitic sedimentary rocks in the same region provide ages of 3560-3500 Ma (Nutman et al., 1992; Ranjan et al., 2022). More recent U-Pb zircon ages of the granitoids (TTGs) reveal 3350-3270 Ma for formation of their magmatic precursors (Jayananda et al., 2015; Ranjan et al., 2020). Northeast of the Holenarsipur greenstone belt, detrital zircons from quartzite in the J.C Pura greenstone belt and pelites from the western boundary of the Chitradurga greenstone belt provided U-Pb ages of 3400 - 3200 Ma (Ramakrishnan et al., 1994; Hokada et al., 2013; Lancaster et al., 2015; Wang and Santosh, 2019). South of the Holenarsipur, in the Kabini dam area, older detrital zircons from paragneiss also indicate U-Pb ages of 3400 - 3200 Ma (Bidyananda et al., 2016).

7.2 Major episodes of granitoid crust formation

U-Pb zircon ages of the present study together with published ages for the granitoids of the WDC show three major stages of felsic crust formation marking episodic continental growth during Paleoarchean (Peucat et al., 1993; Jayananda et al., 2015; Guitreau et al., 2017; Ranjan et al., 2020).

The granitoids in the southwestern block adjoining to the Holenarsipur greenstone belt emplaced during three major events. Zircon xenocrysts from the trondhjemite (Guitreau et al. 2017) together with ages of zircon xenocrysts from this study indicate U-Pb ages of 3610-3500 Ma corresponding to the earliest event (Guitreau et al., 2017). U-Pb zircon data for the tonalitic to granodioritic gneisses record a second episode at 3470-3400 Ma whilst several U-Pb zircon ages for tonalitic to the granodioritic gneisses indicate a major crust building event during the time interval 3350-3270 Ma. Our new zircon U-Pb ages for the gneisses adjoining to the northcentral block provided ages of 3429 ± 9 Ma and 3429 ± 11 Ma, respectively (**see fig.7.8k, l**) without any identified inherited cores. Recent U-Pb zircon dating of the granitoids close to our sampled locations (**see fig. 2b**) revealed magmatic crystallization events of their precursors at 3361 ± 25 Ma, 3339 ± 23 Ma and 3302 ± 44 Ma (Ao et al., 2021). Although stratigraphic relationships between the greenstone sequences of the northcentral block and surrounding granitoids (gneisses) remain uncertain due to commonly tectonized contacts, greenstone volcanism and surrounding granitoid formation may be sub-contemporaneous whereas 3305 ± 10 Ma (**see fig.7.8m**) pyroclastic rhyolite flows may represent a terminal stage of greenstone volcanism in the northcentral block.

In the eastern block, zircons from the plagiogranite interlayered with gabbroic rocks in the northern roadcut yielded a U-Pb age of 3347 ± 11 Ma (**see fig.7.8n**) which coincides with imprecise Sm-Nd whole rock isochron age and of 3345 ± 111 Ma defined for the associated komatiites and komatiitic basalts. Published U-Pb zircon ages for tonalitic gneiss from the western margin of the eastern block indicate ages of 3276 ± 5 Ma (Jayananda et al., 2015) and 3289 ± 6 Ma (Ranjan et al., 2020). Thus, the eastern granitoids are slightly younger than adjoining greenstone in which the plagiogranite injected into komatiitic to basaltic volcanic rocks defined an age of 3347 ± 11 Ma (**see fig.7.8n**).

Diapiric trondhjemites intrude into the volcanic assemblages of all the three blocks of the Holenarsipur greenstone belt and post-date the formation of granitoids. Published U-Pb zircon and titanite ages together with new data from the present study indicate 3230-3177 Ma with xenocrysts and inherited cores up to 3350 Ma (present study; Peucat et al., 1993; Jayananda et al., 2015; Guitreau et al., 2017; Ranjan et al., 2020).

Published U-Pb zircon ages for the granitoids adjacent to the J.C. Pura greenstone belt indicate U-Pb zircon ages of 3315-3270 Ma (Chardon, 1997) whilst Pb-Pb ages of feldspar separates from gneisses around the North-eastern part of the Holenarsipur belt and the Kalyadi greenstone belt provide ages 3350 Ma with an inherited component as old as 3800 Ma (Meen et al., 1992). Zircon crystals from granitoids gneisses along the western margin of the Chitradurga and Nagamangala belts provides U-Pb and Pb-Pb ages ranging from 3315 to 3270 Ma (Taylor et al., 1984, 1988; Ravindran et al., 2020; Jayananda et al., 2019). On the other hand, the granitoids in the southern and eastern margin of the Bababudan belt indicate U-Pb zircon ages of 3350-3200 Ma with inherited crystals as old as 3600-3800 Ma (Peucat et al., 1993; Jayananda et al., 2015; Bidyananda et al., 2016).

Diapiric trondhjemite plutons intruding the TTG-type granitoids adjoining to the J.C Pura greenstone belt indicate an age of 3158 ± 9 Ma (Ao et al., 2021) which coincides with a U-Pb zircon age of 3198 ± 26 Ma obtained from aplitic dykes that intruded the TTG-type granitoids (Chardon, 1997).

7.3 Elemental geochemistry

The granitoids adjacent to the three greenstone units of the Holenarsipur greenstone belt comprises heterogeneous association of grey gneisses with a TTG affinity. The gneisses in the vicinity of the southwestern block are composite and comprise 3500-3431 Ma granite, granodiorite, trondhjemite with minor tonalite, together with abundant 3350-3270 Ma tonalite to granodiorite, all of which in turn are intruded by 3230-3177 Ma diapiric trondhjemite plutons (this study; Jayananda et al., 2015; Ranjan et al., 2020). Inherited zircon xenocrysts from the present study indicate 3500 Ma, which is consistent with previous studies documented zircon ages of 3610 Ma (Guitreau et al., 2017). Granitoids adjoining to the southwestern block exhibits a wide range of compositions (SiO_2 = 64.1 - 79.7 wt.%, Al_2O_3 =10.7 - 17.3 wt.% with a few mafic-rich layers displaying low SiO_2 in the range 52.0 - 60.6 wt.%). wt.%wt.%

In an Ab-An-Or triangular diagram (O'Connor's, 1965; fields after Barker, 1979), gneisses from the southwestern block plot on the trondhjemite, tonalite with a few samples extending into granite field (**Fig.7.9a**). These rocks can be further sub-divided into two major age groups: a younger 3350-3270 Ma group and an older 3500-3431 Ma group. The younger 3350-3271 Ma granitoids are dominantly tonalite to granodiorite with quartz, sodic plagioclase (An_{14-25}), minor K-feldspar, biotite, and occasional hornblende. They display variable Al contents (<14.55 to 17.30 wt.% Al_2O_3) and poorly to highly fractionated REE [$(La/Yb)_N$=8.51-33.74)] patterns (**Fig.7.10a**) with negative Ba, Nb, Ta, and Ti anomalies but variable Sr anomalies (**Fig.7.10b**) on multi-element diagrams. One biotite-rich mafic enclave (SiO_2 = 51 wt.%) with high total REE content (1154 ppm) display highly fractionated REE [$(La/Yb)_N$ = 44.5) with negative Nb-Ta-Ba-Sr but positive Y anomaly on multi-element diagrams (figure not shown). In contrast the older (3500-3430 Ma) gneisses are dominantly trondhjemite to granite with quartz, sodic plagioclase (An_{10-14}), minor K-feldspar, biotite with occasional primary muscovite. They exhibit higher SiO_2 contents (>73 wt.%), lower Al_2O_3 (<13.0 wt.%) but conversely higher Fe_2O_3 (0.4 - 4.8 wt.%) and MgO (0.43 to 1.43 wt.%). These older granitoids show low Ba-Sr, total REE (378-1211 ppm) with weakly to moderately fractionated REE patterns [$(La/Yb)_N$ = 3.24-20.0)], with strong negative Eu anomalies (**see fig.7.10c**), but negative Ba, Nb, Ta, Sr, and Ti anomalies associated with positive Zr and Hf anomalies (**see fig.7.10d**).

The TTG-type granitoids (3430 Ma) spatially associated with the northcentral block are tonalite-trondhjemite-granite in composition and contain quartz, sodic plagioclase (An_{10-19}), minor K-feldspar, biotite with occasional hornblende. They exhibit high SiO_2 (71-74 wt.%), low to high -Al (13.30-15.56 wt.%), low to moderate Ba, Sr, total REE (46-185 ppm), and poorly to moderately fractionated REE (**Fig.7.10e**) patterns [$(La/Yb)_N$ = 1.06 -19.1]. They also show variable Eu anomalies (Eu/Eu* = 0.41 to 1.93) with negative Ba, Nb, Ta, Ti but negative to positive Sr anomalies on multi-element diagrams (**Fig.7.10f**).

Granitoids from around the eastern block contain quartz, sodic plagioclase (An_{15-23}), minor K-feldspar, biotite and hornblende in mineral assemblages. Published data (Jayananda et al., 2015; Ranjan et al., 2020) for gneisses adjoining to the eastern block reveal younger ages of 3289-3276 Ma corresponding to a terminal event of TTG-type granitoids formation. The of studied samples have low-Al concentrations (<14.0 wt.%) except few samples show high-Al content (14.0 to 16.34wt.%) correlated with the SiO_2 content (64.14 to 70.0 wt.%) with the exception of one sample that has 73.11 wt.% SiO_2. The low-Al samples have high-SiO_2 concentrations (73-76 wt.%), higher Fe_2O_3 and MgO, and they display low Ba-Sr, ΣREE (48-132 ppm), with poorly fractionated (**Fig.7.10g**) REE patterns [$(La/Yb)_N = 9.62$-14.09] and variable Eu (Eu/Eu* = 0.77-1.07) anomalies. These samples are also characterized by negative Ba, Nb, Ta, and Ti anomalies but positive Zr and Hf anomalies (**Fig.7.10h**). On the contrary, high-Al samples display high Ba-Sr, ΣREE (147-223 ppm) with highly fractionated REE patterns [$(La/Yb)_N = 20.99$-45.67] together with strongly negative Nb-Ta-Ti anomalies on multi-element diagram (**see fig.7.10g, h**).

The 3230-3177 Ma diapiric trondhjemites contain quartz, sodic plagioclase (An_{10-12}), minor K-feldspar, biotite and rare primary muscovite with accessory zircon, titanite and Fe-Ti oxides. They exhibit high-Al (>15.0 wt.%) except three samples which show low-Al (<14 wt.%). Elemental characteristics like moderate to high Ba (371-724 ppm), Sr (322-735 ppm), low to moderate total REE (32-139 ppm) and moderate to highly fractionated REE [$(La/Yb)_N$ = 5.27-20.03, **Fig.7.10i**), strong negative Nb-Ti anomalies but positive and negative Sr anomalies (**Fig.7.10j**).

The other TTG-type granitoids found adjacent to the Nuggihalli, J.C.Pura, Ghattihosahalli, Banasandra, Nagamangala greenstone belts of the cratonic core show TTG affinity and contain quartz, sodic plagioclase (An_{12-28}), minor K-feldspar, biotite ± hornblende. They exhibit moderate to high SiO_2 (64.8-72.2 wt.%), high-Al (14.6-16.6 wt.%), low to moderate Ba, Sr, total REE (52-151 ppm), moderate to highly fractionated REE patterns (**Fig.7.10k**) with [$(La/Yb)_N$= 13.75-51.50)] without any significant Eu anomalies except few samples show either negative or positive anomalies (Eu/Eu* = 0.72-1.22). They display negative Ba, Nb, Ta, Ti with flat or negative Sr anomalies on multi-element diagram

(**Fig.7.10l**). These granitoids exhibit ages in the range of 3400-3200 Ma (Jayananda et al., 2018, in prep; Ranjan et al., 2020; Bidyananda et al., 2016; Ao et al., 2021).

7.4 Zircon Lu-Hf isotopes

Zircon populations for each sample show good consistency in their Lu-Hf isotope systematics (**Table 1**). Zircons from >3400 Ma samples have present-day $^{176}Lu/^{177}Hf$ that range from 0.0003 to 0.0028 and present-day $^{176}Hf/^{177}Hf$ from 0.280612 to 0.280829, which give initial ε_{Hf} between +1.1 and +3.6. Zircons from 3350-3270 Ma samples exhibit present-day $^{176}Lu/^{177}Hf$ from 0.0008 to 0.0080 and present-day $^{176}Hf/^{177}Hf$ from 0.280769 to 0.281271, which give initial ε_{Hf} between +1.6 and +5.5 and three much higher datapoints with ε_{Hf} of +9.5, +11.1 and +11.7. The youngest group (3177 Ma) represented by one sample has present-day $^{176}Lu/^{177}Hf$ that range from 0.0011 to 0.0025 and present-day $^{176}Hf/^{177}Hf$ from 0.280833 to 0.280935, which give initial $\mathcal{E}_{Hf(T)}$ between +0.9 and +2.6. Overall, Lu-Hf isotope data show weakly to strongly depleted (compared to CHUR) signatures, hence, positive ε_{Hf} at the time of crystallization (+1.9 ± 0.6 to +4.9 ± 0.6; **Fig.7.11a**). Hafnium isotope signatures show a slight increase from 3430 to 3340 and then a decrease towards 3170 Ma, therefore, indicating tapping of an overall mildly depleted source, then a more depleted one that correspond to the backward projection of arc mantle present-day compositions (Dhuime et al., 2012; Iizuka et al., 2013), and finally a mildly depleted one again. Our new data are consistent with and complement literature data for igneous and detrital zircons, although the latter are not shown on **Fig. 7.11a** because detrital zircons commonly show much more variability than igneous crystals due to inherent impossibility to smooth out analytical scatter by considering multiple crystals or domains within crystals (e.g., Lancaster et al., 2015; Ranjan et al., 2022). As a consequence, we will only discuss Hf isotope data for igneous zircons to avoid artificial blurring of the magmatic signature of WDC granitoid formation.

8. Petrogenesis of greenstone volcanic rocks

8.1 Timing of greenstone formation

In the southwestern block, the contacts between greenstone ultramafic rocks and granitoids (TTG-type gneisses) are tectonized. It is difficult to provide precise ages for the ultramafic volcanism as ^{147}Sm/^{144}Nd ratios of a few samples were affected by fluid flow associated with metamorphism and intrusion of ca. 3200 Ma diapiric trondhjemites. Ultramafic to mafic rocks of all of the three blocks together define an Sm-Nd whole rock isochron age of 3028 ± 53.3 Ma (MSWD = 2.3) which coincides with the cooling path of an amphibolite facies metamorphic event dated at 3091 ± 12 Ma (Jayananda et al., 2015). The ultramafic-mafic volcanic rocks of the southwestern block define a Sm-Nd whole-rock errorchron age of 3029 ± 91.5 Ma (MSWD 1.2) which coincides with the cooling path of metamorphic event (Jayananda et al., 2013a). However, the occurrence of ultramafic-mafic volcanic rocks as large disrupted fragments within the 3400-3350 Ma granitoids of the southwestern block implies that volcanic rocks erupted prior to 3350 Ma.

U-Pb zircon ages of this study together with published zircon ages (Jayananda et al., 2015; Guitreau et al., 2017; Ranjan et al., 2020) for adjacent granitoids reveal three major stages of formation. Zircon xenocrysts from trondhjemite to granite (Guitreau et al., 2017) and granodiorite from this study indicate a first stage of formation at 3600-3500 Ma. Our new U-Pb zircon data for tonalitic to granodioritic gneisses reveal a second episode at 3468-3410 Ma whilst zircon ages from several tonalitic to granodioritic samples indicate 3350-3300 Ma that correspond to a third stage of granitoid (TTG-type gneisses) formation.

The ultramafic-mafic volcanic rocks of the northcentral block give an imprecise Sm-Nd regression age of 3124 ± 249 Ma (MSWD 2.1) which probably reflects partial resetting during metamorphic cooling. However, our U-Pb zircon data from a pyroclastic felsic flow from high stratigraphic levels with the Holenarsipur stratigraphy returned an age of 3305 ± 10 Ma. The granitoids adjoining to the northcentral block yielded zircon U-Pb ages of 3429 ± 9 Ma and 3429 ±11 Ma without visible inherited cores. Stratigraphic relationships between northcentral block and adjoining granitoids remain uncertain due to tectonized contacts but the 3305 ± 10 Ma pyroclastic flow may represent a terminal stage of greenstone volcanism, hence, placing constraints on the timing of the northcentral block volcanism before 3305 Ma.

The greenstone volcanic rocks of the eastern block provide a whole-rock Sm-Nd regression age of 3345 ± 111 Ma (MSWD=1.8) which is close to the U-Pb zircon age of 3347 ± 11 Ma obtained for a plagiogranite that is interlayered with gabbroic rocks and that we interpret as a marker of a terminal stage of volcanism. Published U-Pb zircon ages for granitoids from the western margin of the Eastern block indicate younger ages of 3276 ± 5 Ma (Jayananda et al., 2015) and 3289 ± 5 Ma (Ranjan et al., 2020), consistent with a recent zircon age of 3242 ± 17 Ma (Panicker et al., 2021) as well as with a whole-rock Sm-Nd regression age of 3285 ± 170 Ma for an anorthosite body that intrudes the Eastern block (Bhaskar-Rao et al., 2000).

Sm-Nd whole rock isotope data for ultramafic-mafic volcanic rocks from stratigraphically equivalent greenstone belts(i.e. Nuggihalli-Kalyadi, Banasandra and J.C. Pura) together with Holenarsipur volcanic rocks provide a whole-rock Sm-Nd regression age of 3356 ± 68 Ma which is assumed to represent an average age for widespread ultramafic volcanism (Jayananda et al., 2008), which is consistent with the timing of formation of volcanic rocks in the three blocks of the Holenarsipur greenstone belt.

8.2 Effects of alteration

Elemental and isotopic data on komatiite and komatiitic-basalts from Archean cratons reveal mobility of some of the incompatible elements by fluid flow associated with metamorphism

(Gruau et al., 1992; Lahaye et al., 1995; Polat et al., 2002; Polat and Hofmann, 2003; Chavagnac, 2004; Ordóñez-Calderón et al., 2008; Jayananda et al., 2008, 2016). The effect of low-grade metamorphism and hydrothermal alteration in element mobility in the Paleoarchean komatiites of the Western Dharwar craton have been discussed in detail elsewhere (e.g. Jayananda et al., 2008, 2016; Tushipokla and Jayananda, 2013). The studied komatiites and komatiitic-basalts of the Holenarsipur greenstone belt were affected by fluid flow associated with the intrusion of the 3200 Ma diapiric trondhjemite plutons as reflected in numerous quartzite veins with large tourmaline crystals traversing the volcanic rocks spatially associated with the plutons.

Major elements (TiO_2, Al_2O_3, CaO, Fe_2O_3) together with trace elements Ni, Cr, V and Y define moderate to strong linear trends against MgO on the Harker binary diagrams which preclude extensive alteration of the studied greenstone volcanic rocks. However, large scattering of LIL elements (K, Rb, Ba, Sr) on the Harker binary plots (**see fig.7.1d,e**) nevertheless indicate their mobility during secondary processes, which is common in many komatiites (Arndt et al., 2008). The heat and fluids associated with the trondhjemite intrusions and following 3100 Ma metamorphic event (e.g., Rogers et al., 1986; Jayananda et al., 2013a, 2015; Dasgupta et al., 2019) probably caused the mobility of large ion lithophile elements (K, Rb, Ba, Sr), Ce and Eu. On the other hand, the majority of samples show relatively uniform Al_2O_3/TiO_2 and $(Gd/Yb)_N$ with smooth REE and primitive mantle normalized multi-element diagrams (**see figs.7.6a**).

Incompatible element ratios such as Nb/U and Nb/Th are commonly used to evaluate the composition of source reservoirs of komatiites since these ratios are not significantly modified by magmatic processes (Campbell, 2002). Most of our data distribute continuously between MORB, primitive mantle (PM), and continental crust (CC) values (Sun and McDonough, 1989; Workman and Hart, 2005; **Fig.8a**) whilst some samples show excess scatter and even decoupling between Nb/U and Nb/Th. This is hard to reconcile with mantle processes and more likely reflect secondary alteration by fluids containing variable proportions of U and Th, these two elements being readily mobile in crustal fluids.

Most $^{147}Sm/^{144}Nd$ and $^{143}Nd/^{144}Nd$ data for the studied volcanic rocks from three greenstone units define a linear array though with some scatter probably due to re-opening of Sm-Nd system coincide with LILE scattering. These elemental disturbances are probably a response to ca.3200 Ma trondhjemite intrusions and/or subsequent two metamorphic events at 3100 Ma and 2500 Ma. To minimize the effects of hydrothermal alteration in the following discussion, we have used relatively immobile elements for which a magmatically-coherent behaviour was observed, as well as samples for which Sm-Nd isotope data appeared consistent with the main regression.

8.3 Crustal contamination

Several attempts have been made to quantify the effect of crustal contamination in Archean komatiites and basalts (e.g. Puchtel et al., 1997, 1998; Polat et al., 1999, 2006). Incompatible elements used to constrain source reservoirs of Archean komatiites are also sensitive to crustal contamination processes and to some extent affected by the degree of mantle melting (c.f Puchtel et al., 1997, 1998; Polat et al., 1999, 2006). Therefore, it is important to characterize the role of crustal contamination while using incompatible elemental data in order to constrain mantle sources most rigorously. Incompatible element ratios are suitable indicators of crustal contamination as these elements are enriched in the continental crust. In particular, Zr/Th ratios are used to characterize crustal contamination of komatiites and basalts as continental crust is enriched in Th (Zr/Th = ~20) compared to the primitive mantle (Zr/Th =116; Fan and Kerrich, 1997). Field relationships in the Holenarsipur greenstone belt reveal that komatiites and komatiitic basalts erupted in marine environments as argued by visible pillow or flow-top pillow breccia structures. Most of the studied samples are not enriched in LIL elements and LREE but show flat REE patterns (**see figs 7.2a-l**). This together with high Zr/Th values (>80) preclude large-scale crustal contamination for the majority of studied komatiites and komatiitic basalts. A few samples from southwestern and northcentral blocks, nevertheless, show low Zr/Th values (60-70) which suggest minor ancient crustal contamination, or secondary enrichment of Th. Further, Kerrich et al. (1999) have used $(La/Sm)_N$ values to evaluate crustal contamination of Archean basalts from the Superior Province and showed that crustally contaminated basalts have high $(La/Ce)_N$ values (>1.5). In the studied greenstone volcanic rocks, a few samples (~10%) from the Holenarsipur, Nuggihalli, Kalyadi, J.C. Pura, and Nagamangala greenstone belts show $(La/Ce)_N$ values >1.5 which indicate possible traces of crustal contamination. This is consistent with the observed Nb/Th values that also preclude extensive contamination by pre-existing crust (Polat et al., 2002; Polat and Hoffmann, 2003). Nd isotope data and Nb/Th ratios are not correlated (**Fig. 8b**) which would be the case if Nd isotope signatures of the studied komatiites were controlled by crustal contamination with the least radiogenic being associated with the lowest Nb/Th ratios. This indicates that Nd isotope signature variability is either an artefact of secondary alteration or reflects source heterogeneity, or both. Most data presented in this contribution, either new or from the literature, can be used to discuss magmatic differentiation processes and composition of mantle source reservoirs.

8.4 Magmatic differentiation

The majority of greenstone volcanic rocks from the cratonic core are komatiite to komatiitic basalt in composition. Despite large variations in texture, mineralogy, major and trace element compositions, individual greenstones as well as greenstones altogether define moderate to strong linear trends on the Harker's binary diagrams (**see fig.7.1d, e**) which indicate that they share a common petrogenetic processes. Komatiites with more than 35 wt.% MgO possibly represent cumulate layers, whereas rocks with lower MgO content most likely represent liquid compositions. Among the greenstone volcanic rocks, Holenarsipur komatiites and komatiitic basalts from the three blocks plot co-linearly on binary plots of Al_2O_3, TiO_2, Fe_2O_3, CaO versus MgO suggesting their magmatic evolution by similar differentiation processes which essentially controlled by olivine fractionation (**see fig.7.1d**). Komatiites and komatiitic basalts from other greenstone belts in the cratonic core follow the same trends except few J.C. Pura komatiitic basalt samples which seem to have additional minerals (i.e., olivine, pyroxene, feldspar, ilmenite) controlling their compositions as illustrated in MgO versus SiO_2 or MgO versus TiO_2 plots (**see fig.7.1d**). Among trace elements, Ni and Cr exhibit positive correlations with MgO which suggest olivine and possible chromite fractionation, also consistent with the negative correlations between Zr, Y, V and MgO which likely reflect enrichment by fractional crystallization or increasing depletion concomitant with higher degrees of partial melting. Commonly flat REE and trace element patterns indicate large degrees of partial melting (>40%). Negative Ti anomalies on the primitive mantle normalized multi-element patterns coupled with negative correlation of TiO_2 with MgO on the Harker binary plots very likely reflect a control by accessory phase rutile.

8.5 Source characteristics and petrogenetic processes

Komatiites and komatiitic basalts from the Archean greenstone belts are key to our understanding of thermal and chemical evolution of the mantle, continental growth and geodynamics of the early earth (Polat et al., 1999, 2006;Arndt et al., 2008; Herzberg et al., 2010; Mole et al., 2015; McKenzie, 2020). Despite numerous studies on the Archean komatiites involving petrologic, elemental, isotopic, experimental and simulation models, the origin of komatiite magma is still subject of much discussion on whether the magma originated by anhydrous melting of deep mantle (for reviews see Arndt et al., 2008; Herzberg, 1995;

Herzberg et al., 2010; Mc Kenzie, 2020) or wet melting of the shallow mantle (Parman et al., 1997), or deep hydrous mantle reservoirs (Sobolev et al., 2019). Archean komatiite flows are characterized by high MgO content (18-35 wt.%) excluding cumulate layers which contain >35.0 wt.%, but conversely low Al_2O_3 concentrations and very low incompatible element contents. These characteristics are attributed to high-degree (40-50%) partial melting of deep mantle reservoirs (Arndt, 2003; Sossi et al., 2016). Archean komatiites are commonly divided into two principal types including the Al-depleted and Al-undepleted (Arndt and Nisbet, 1982). Subsequently, Arndt (2003) proposed Al-depleted komatiites to ca.3500 Ma Barberton-type with sub-chondritic Al_2O_3/TiO_2 (<16), CaO/Al_2O_3 (>1.0), fractionated REE patterns with high $(Gd/Yb)_N$ (>1.0), whilst Al-undepleted komatiites to 2700 Ma Munro-type (Abitibi-type) characterized by near chondritic Al_2O_3/TiO_2 (≤20), CaO/Al_2O_3 (<1.0) and poorly fractionated with $(Gd/Yb)_N$ (<1.0). Incompatible trace element ratios like Zr/Nb, Nb/Th, Nb/Yb, Th/Yb, Zr/Y, Nb/Y, $(Gd/Yb)_N$, La/Yb and Hf/Sm are extensively used to evaluate their mantle source reservoirs, mineralogy of melt residue, depths and tectonic contexts of melt generation (e.g. Fitton et al., 1997; Baksi, 2001; Condie, 2003; Chavagnac, 2004; Sossi et al., 2016; Jayananda et al., 2016; Wyman, 2020). Low Zr/Nb and Hf/Sm together with high Nb/Y and La/Yb in the Al-depleted Archean komatiites are usually attributed to the existence of depleted reservoirs and recycled materials along with enriched components in the deep mantle by 3500 Ma (Kellogg et al., 1999; Kerrich and Xie, 2002; Polat and Kerrich, 2000). Further, low Zr/Nb and Hf/Sm ratios coupled with high La/Yb and Nb/Y values in the Al-depleted komatiites may be linked to majorite fractionation, whilst high Zr/Nb and Nb/Y ratios in Al-undepleted komatiites could be related to melting of shallow mantle source with garnet entering into melt. Sossi et al (2016) while addressing the petrogenesis of komatiites from the five Archean cratons argued that Al-depleted Barberton type komatiites were generated by high-degree batch melting (~ 40%,) at high pressure (9.0 GPa) and high temperature (Tp = 1950°C), hence, in the deep mantle where majorite can be stable in the melting residue. In contrast, Al-undepleted Munro-type komatiites originated in a shallower mantle by moderate pressure fractional melting (~ 25%, 5.0 GPa, Tp = 1750°C) as density contrast between the liquid and solid increase at such depths. More recent thermodynamic model has shown that komatiite melts originate at great depth (~600 km) in a rising plume where Ca-perovskite is stable as a residual phase, therefore, accommodating a fair amount of trace elements which, in turn, accounts for low contents of incompatible elements in generated komatiitic magmas (McKenzie, 2020).

The 3400-3200 Ma old komatiite and komatiitic basalts from the cratonic core in the WDC show significant variation in elemental compositions and Nd isotope signatures suggesting distinct mantle source reservoirs, depth and degree of melting and tectonic context of melt generation.

8.5.1 The Holenarsipur greenstone volcanic rocks – the three blocks

The petrogenetic interpretations were made on the samples devoid of evident alteration and weathering. However, exact petrological type of ultramafic-mafic rocks from three blocks may not be good indicators of their origin, but geochemical signatures can help constrain source reservoirs and unravel the geodynamic context of formation of such rocks (e.g., Xie and Kerrich, 1994, 1995; Puchtel et al., 1997, 1998; Polat et al., 1999, 2006; Pearce, 2008; Sobolev et al., 2016). Major elements of three greenstone units plotted on triangular diagrams (Al_2O_3-Fe_2O_3+TiO_2- MgO; Jensen, 1976) and (CaO-MgO-Al_2O_3; Viljoen et al., 1982) reveal dominant komatiite to komatiitic basalt composition although with some distinctions in trace element signatures indicating independent histories.

The southwestern block has an affinity with an oceanic plateau with remnants of microcontinent. Incompatible element contents (REE, Nb, Y, Th, Zr; **Figs. 7.2a-d**) reveal two groups. The low REE group (ΣREE = 4.4-18.8 ppm with lower SiO_2 44.1-46.0 wt.%) exhibit flat to slightly fractionated REE patterns (**Fig. 7.2a**) with $(Gd/Yb)_N$ = 0.53-1.86 which suggest their derivation by high-degree partial melting of a shallow depleted mantle, hence, without residual garnet. This is consistent with the absence of Nb anomalies together with positive Zr and Y anomalies on primitive mantle normalized multi-element diagram (**Fig. 7.2b**). The high-REE group (ΣREE = 20.6-66.7 ppm) with fractionated REE [$(Gd/Yb)_N$ 1.22-2.29 (**Fig. 7.2c**) combined with positive Nb, coupled negative Zr and Hf anomalies on multi-element diagrams (**Fig. 7.2d**) suggest origin of melts from deeper primitive mantle reservoirs with possible residual garnet (majorite). Sm-Nd isotope data of the komatiites were used to calculate $\varepsilon_{Nd(T)}$ at 3350 Ma to constrain mantle sources and possible crustal contamination. Nine samples with large range of values ($\varepsilon_{Nd(T)}$ = -0.1 to +4.6) suggest chondritic to depleted (MORB-like) mantle reservoirs whilst two samples with negative ($\varepsilon_{Nd(T)}$ = -0.8 to -1.6) values are likely related to possible contamination of pre-existing crust or artefact of secondary modification of the Sm-Nd system (Meen et al., 1992). Plots of incompatible element ratios like Th/Yb versus Nb/Yb (**Fig. 8c;** Van Kranendonk et al., 2015) and Nb/Y versus Zr/Y (**Fig.8d;** Condie, 2003) suggest primitive to depleted mantle sources whilst Zr/Nb versus Nb/Th plot (**Fig.8e;** Condie, 2003) attribute their eruption as oceanic plateaus. The above lines of arguments for oceanic plateau origin of southwestern block komatiites are consistent with studies on komatiites from other cratons (e.g., Desrochers et al., 1993; Storey et al., 1991; Kusky and Kidd, 1992).

The northern block is likely an oceanic arc with coeval mini volcanic plateau fragments. Major element data (SiO_2 = 45.1 to 68.6 wt.%; MgO = 23.9 to 9.7 wt.%) reveal komatiite, komatiitic basalt, basalt to dacite compositions. Komatiites contain low to moderate ΣREE (14.6-59.1 ppm), display flat to fractionated REE patterns with $(Gd/Yb)_N$ ratios of 0.99-1.68 (**Fig.7.2e**) whilst komatiitic basalts show moderate to high ΣREE (27.3-138.0 ppm) and display fractionated REE patterns [$(Gd/Yb)_N$ = 0.94-1.93)] (**Fig.7.2g**), hence, implying heterogeneous mantle reservoirs whilst negative Nb anomalies coupled with either positive or no significant

Zr, Hf and Y anomalies on the multi-element diagrams (**Fig.7.2f and h**) suggest an origin from shallower depths. These elemental characteristics, lithological association of komatiite-komatiitic basalt- basalt- dacite points to a possible oceanic arc environment. Incompatible element ratios like Th/Yb versus Nb/Yb and Nb/Y versus Zr/Y (**see fig.8c, d**) indicate heterogenous sources involving primitive to enriched MORB mantle, with few samples showing modern N-MORB signatures, whilst on Zr/Nb versus Nb/Th studied samples essentially fall within the field of arc magmas. These geochemical characteristics point to a possible oceanic arc origin, nevertheless with local mantle heterogeneities (**see fig. 8e**). Initial Nd isotope ratios for the ten samples gave with ($\varepsilon\mathrm{Nd}_{(T)}$=3350 Ma) values ranging from -0.4 to +4.5, except one sample having -2.6, which suggest chondritic to depleted mantle sources with possible traces of ancient crustal contamination and/or secondary alteration for the negative $\varepsilon\mathrm{Nd}_{(T)}$ value.

The eastern block resembles an oceanic crustal section close to a spreading centre. The komatiitic to basaltic volcanic rocks with SiO_2 ranging from 42.7 to 50.0 wt.% form two groups: low ΣREE and high ΣREE. The low ΣREE (5.80-22.20 ppm) group displays flat patterns with depletion in LREE and poorly fractionated [$(Gd/Yb)_N$ = 0.61-1.38] suggest a depleted mantle reservoir similar to N-MORB source (e.g., Xie and Kerrich, 1994, 1995; Puchtel et al., 1997, 1998; Polat et al., 1999, 2006). The absence of Nb anomalies, coupled with positive Zr, Y anomalies on the multi-element diagram (**Fig. 7.2i, j**) point to melt origin from a shallow depleted mantle which is consistent with $\varepsilon\mathrm{Nd}_{(T)}$ of +2.46 to +5.5 at 3350 Ma. On the contrary, the high ΣREE (48.39-294.79 ppm) group shows fractionated REE patterns [$(Gd/Yb)_N$ = 1.16-1.96] coupled with positive Nb anomalies and negative Hf-Y anomalies on the multi-element diagrams (**Fig. 7.2k, l**) which coupled with $\varepsilon\mathrm{Nd}_{(T)}$ of -0.8 to +0.1 at 3350 Ma suggest a primitive mantle source. Elemental ratios like Th/Yb versus Nb/Yb, and Nb/Y versus Zr/Y, indicate their origin from essentially N-MORB to E-MORB sources (**Fig.8c, d**).

Moreover, on Zr/Nb versus Nb/Th plot suggest that volcanic rocks of the eastern block originated from different depths in the mantle with affinities to modern N-MORB to E-MORB, hence, pointing to a likely preserved oceanic crust (Xie and Kerrich, 1995) close to a spreading centre (**Fig. 8e**).

8.5.2 Stratigraphically equivalent greenstone belts in the cratonic core

The Nuggihalli-Kalyadi volcanic assemblages are mainly komatiitic sharing similar compositional characteristics (low SiO_2 = 38.9-46.9 wt.%; high MgO = 30.9-34.9 wt.%; CaO/Al_2O_3 = 0.63-1.32; Al_2O_3 /TiO_2 = 9.78-23.48), high compatible element contents (Ni = 1388-1960 ppm; Cr = 2209-3859 ppm) and variable depletion in incompatible trace elements (ΣREE = 4.2-30.9 ppm). Their trace element ratios (e.g., $(Gd/Yb)_N$ = 0.43-1.24) coupled with sub-chondritic to moderate total REE contents, suggest their origin from heterogeneous mantle (highly depleted to primitive mantle) reservoirs at different depths. The flat REE patterns coupled with positive Zr, Ti and Y anomalies (two samples with negative anomalies) on PM normalized multi-element diagrams are consistent with their origin by high-degree melting (40-50%) of mantle at different depths, hence, with possible influence of residual garnet. Incompatible element ratios like Th/Yb versus Nb/Yb (**see fig.8c**) coupled with Sm/Nd versus Nb/Th reveal highly depleted to primitive mantle sources which is consistent with $\varepsilon_{Nd(T)}$ of +0.5 to +5.4. These observations altogether suggest dominant depleted mantle reservoirs for the source of the Nuggihalli-Kalyadi volcanic rocks.

The J.C. Pura greenstone volcanic assemblages are dominantly komatiite to komatiitic basalt flows with massive cumulate layers. These thick lava flows along with cumulates were interpreted as differentiation sections of a volcanic plateau (Jayananda et al., 2016). The komatiite flows contain high MgO contents (22.3-31.9 wt.%), low SiO_2 (45.1-47.2 wt.%), variable CaO/Al_2O_3 (0.70-1.66) and Al_2O_3/TiO_2 (5.38-22.47), low to moderate total REE (14.06-45.92 ppm), whilst komatiitic basalts show lower MgO (12.9-15.3 wt.%), higher SiO_2 (49.0-50.5 wt.%), variable CaO/Al_2O_3 (0.77-1.30), and slightly higher Al_2O_3/TiO_2 (15.5-20.8). In contrast, the cumulate layers are characterized by higher MgO contents (35.1-42.2 wt.%) and low SiO_2 (41.1-45.4 wt.%), CaO/Al_2O_3 (0.70-1.66), and Al_2O_3/TiO_2 (5.38-22.47). The moderate to strong linear trends between TiO_2, Al_2O_3, Fe_2O_3 and CaO in Harker's binary diagrams indicate fractionation of olivine, ± pyroxene, ± ilmenite (**see fig.7.1d**). Plots of CaO/Al_2O_3 versus $(Gd/Yb)_N$ (**see fig.7.6a**) and Al_2O_3/TiO_2 versus $(Gd/Yb)_N$ (**see fig.7.6b**) suggest that komatiitic magmas originated from various mantle reservoirs at different depths similar to the Barberton and Abitibi-type komatiites, with most data belonging to the former type. It is, however, hard to reliably discriminate source characteristics from effects of secondary alteration and/or fractional crystallization on these elemental ratios. The sub-chondritic to moderate total REE (3.6-57.4 ppm) coupled with $\varepsilon_{Nd(T)}$ values between +0.50 and +5.4 at 3350 Ma reveal their origin from primitive to depleted (N-MORB like) mantle reservoirs. This is also reflected on incompatible trace element ratios projected on the Th/Yb versus Nb/Yb (**see fig.8c**) and the Nb/Y versus Zr/Y plots (**see fig.8d**). The lithological associations (voluminous and thick komatiite and komatiitic basalt flows forming pillows with flow top breccias coupled with cumulates) suggest their eruption in an oceanic plateau environment. This conclusion is consistent relationships within Zr/Nb versus Nb/Th plot (Condie, 2003) suggesting eruption in oceanic plateau setting (**see fig.8e**).

Among Ghattihosahalli volcanic rocks, voluminous komatiite flows with cumulate layers (Jayananda et al., 2008) together with associated fuchsite quartzite, barite beds imply an oceanic setting. Abundant serpentine, highest MgO (39.3-41.3 wt.%) and Ni (3145-3177 ppm) coupled with low total REE (9.76-9.81 ppm) suggest a cumulative nature. Their low incompatible element contents along with their incompatible trace element ratio plots (Th/Yb vs Nb/Yb and Nb/Y vs Zr/Y), $\varepsilon_{Nd(T)}$ = +2.8 to +5.3 (**see fig.8c, d**) reveal significantly depleted mantle sources. Their high MgO contents, fractionated REE patterns [$(Gd/Yb)_N$ =2.26-2.52] together with their high CaO/Al_2O_3 (1.32-1.34) and low Al_2O_3/TiO_2 (average of 5) argue for an origin of komatiite magmas by high-degree melting (>40%) in the deep mantle (>400 km) with garnet stable in the melting residue. Elemental ratios like Zr/Nb and Nb/Th (**see fig.8e**) together with lithological associations (komatiite-fuchsite quartzite-barite) point to an eruption of deep-seated melts in an oceanic plateau setting.

Among the Banasandra volcanic rocks, voluminous komatiites displaying cumulate, spinifex, pillow to pillow breccias with hyaloclastite structures suggest their eruption in shallow marine environment to slightly above sea level. Their elemental characteristics such as high MgO (30.3-42.4 wt.%), sub-chondritic to low total REE (3.5-12.2 ppm), Nd isotopes ($\varepsilon_{Nd(T)}$ = +0.1 to +5.1 excluding two anomalous values), coupled with flat REE patterns suggest high-degree partial melting of a heterogeneous mantle (primitive to highly depleted) reservoirs which is also reflected in plots of incompatible element ratios like Th/Yb versus Nb/Yb (**see fig.8c**) and Nb/Y versus Zr/Y plots (**see fig.8d**). The observed CaO/Al_2O_3 (0.6-1.2), Al_2O_3/TiO_2 (8.2-18.5) and $(Ga/Yb)_N$ = 0.99-1.90 are compatible with an origin of komatiitic magmas from a deep mantle reservoirs retaining variable garnet (majorite?)in the melt residue. Field evidences of thick peridotitic komatiite flows forming pillow and flow-top breccias, spinifex with cumulate layers combined with incompatible element ratios such as Zr/Nb versus Nb/Th (**see fig.8e**) suggest an oceanic plateau setting.

The Nagamangala komatiites exhibit crude pillow and spinifex structures as well as low SiO_2 contents (40.5-43.9 wt.%), conversely high MgO (28.8-35.8 wt.%), Ni (1220-1589 ppm), Cr (1294-3565 ppm) but lower incompatible elements (ΣREE = 9.2-20.9 ppm; Th = 0.14-0.54 ppm; Nb = 1.1-1.25 ppm; Zr = 6.9-20.09 ppm; Hf = 0.04-0.05 ppm; Tushipokla and Jayananda, 2013). The majority of studied samples belong to Al-depleted Barberton type komatiites (CaO/Al_2O_3 = 1.02 -1.18; Al_2O_3/TiO_2 = 11.69- 16.86; $(Gd/Yb)_N$ = 0.59-1.46) whilst other samples have Al-undepleted Munro-type affinity (CaO/Al_2O_3 = 0.67- 0.98 and Al_2O_3/TiO_2 = 11.37- 19.70; $(Gd/Yb)_N$ <0.9). The Al-undepleted character ($CaO/ Al_2O_3 < 0.8$), despite high MgO, low Al_2O_3/TiO_2 (<15) and high $(Gd/Yb)_N$ >1.0, attributed to a possible loss of CaO in komatiites by post-magmatic fluid driven hydrothermal processes (Chikhaoui., 1981; Tushipokla and Jayananda, 2013). The low to moderate incompatible element contents (ΣREE = 9.24-50.98) in both Al-depleted and Al-undepleted komatiites together with their flat REE patterns and high MgO can be attributed to high-degree (40-50%) melting of deep mantle sources. The slight positive or negative Nb anomalies on multi-element diagrams are attributed plume source with possibility of recycled slab component involvement (Tushipokla and Jayananda, 2013). Incompatible element plots of Th/Yb vs Nb/Yb, Nb/Y vs Zr/Y and Nb/Th versus Nb/U also suggest depleted to primitive mantle sources, with a possible volcanic plateau environment (**see figs.8a-d**).

To summarize typical geochemical fingerprints of subduction zone such as enrichment of LIL elements, depletion of HFSE (Nb, Ta, Zr, Hf, Ti, Y and Th) compared to REE are not observed in most of komatiites and komatiitic basalts except in komatiitic basalts of the Northcentral block of the Holenarsipur schist belt. This precludes the involvement of shallow arc mantle and argue for deep mantle sources for most komatiites of the cratonic core.

9. Origin of TTG-type granitoid and diapiric trondhjemites

9.1 *Around the southwestern block (3430-3270 Ma granitoids with 3500-3600 Ma remnants)*

Major element compositions of the granitoids when projected on normative Ab-An-Or triangular plot (O'Connor, 1965) reveals dominant trondhjemite to tonalite composition with few samples extending granodiorite and granite field, (**see fig.7.9a**). On Q-Ab-Or triangular diagram (Barker and Arth, 1976) these gneisses deviate from classical calc-alkaline differentiation trend and distribute around the trondhjemite differentiation trend (**Fig.7.9b**) typical of Archean TTG suites (Martin, 1994). Considering age and geochemical characteristics, these granitoids can be grouped into two major groups, as presented in the result section, a high-Al and a low-Al group. Major elements show consistent trends between the two groups which suggest possible control by hornblende, plagioclase, garnet, titanite, ilmenite and apatite (**Fig. 7.9c**). Trace element patterns further confirm the control by rutile in both groups as argued by the negative anomalies of Nb, Ta, and Ti (**Fig. 7.10**). The influence of feldspar is confirmed in the low-Al group that exhibit strongly negative, Ba, Sr, and Eu anomalies but it is less clear in the high-Al group that only show very weak Eu, Ba, and Sr anomalies that are both positive and negative (**Fig. 7.10**). This latter group also exhibits a small, but visible positive Zr-Hf anomaly that may be due to zircon fractionation. Since low-Al gneisses are also characterized by high SiO_2 concentrations, it is hard to discriminate the influence of the source from that of fractional crystallization on rock chemical compositions. Therefore, the chemistry of these gneisses is likely dominated by fractional crystallization of the above-mentioned mineral phases, superimposed on source characteristics. Geochemical data are, here, interpreted as representative of magmatic liquids, as commonly done in the literature, but it should be kept in mind that the granitoids rarely represent pure magmatic liquids and cumulative effects can also add to factors influencing rock compositions. The high-Al group exhibits a larger range of SiO_2 than the low-Al group and it is, hence, easier to discriminate between source and fractional crystallization effects. For instance, the anomalies visible for Ba, Sr, Eu, Zr, and Hf are weak and both positive and negative (**Fig. 7.10**) which most likely indicate that they were developed in some samples in response to mineral fractionation during crystallization. On the contrary, Nb, Ta, and Ti anomalies are shared by all samples regardless of their SiO_2 content which suggest a source control, more or less accentuated by fractional crystallization.

The general shape of REE $(La/Yb)_N$ and trace element patterns indicate that the high-Al group is more fractionated than the low-Al one which is most likely a primary feature of these rocks. This is because fractional crystallization of granitoid magmas corresponding to grey gneiss compositions commonly involve plagioclase and hornblende fractionation (e.g., Martin, 1986; Laurent et al., 2020; Kendrick et al., 2021), the latter of which imposes those fractionated liquids should have lower HREE contents and, hence, more fractionated REE patterns. Therefore, the higher HREE contents and less fractionated REE patterns of the low-Al group seem to be a primary feature of this group which, consequently, indicate that the high- and low-Al gneisses cannot be genetically related. Elemental ratio plots (i.e., Nb/Ta versus Gd/Yb; Nb/Ta versus Zr/Sm; Sr/Y versus $K_2O/(Na_2O+CaO)$) indicate the involvement of mineralogical phases consistent with those deduced from separate major and trace element data and allow further discussion about the sources of these granitoids (**Fig. 9a-c**). Data plotted in **figures 9a-9f** show significant scatter that can be interpreted as resulting from fractional crystallization, different depths and mineralogy of melting residues or both. It is difficult to discriminate the influence of each parameter separately but we can conservatively conclude that the source lithologies of granitoid gneisses around the southwestern block were geochemically enriched mafic rocks ranging from low-K to high-K basaltic to tonalitic in composition and that they melted at different depths from low pressures for the low-Al group to high pressures for the high-Al group, as notably, but not only, argued by La/Yb and Sr/Y ratios (**see figs. 7.10 and 9**).

Whole-rock Nd isotope signatures together with zircon Hf isotope compositions (**Fig 7.11a, b**) indicate dominant mildly to significantly depleted sources for the granitoids around the southwestern block. Hafnium isotopes exhibit less scatter than Nd isotopes likely because the Sm-Nd isotope system can be more readily disturbed at the whole-rock scale than the Lu-Hf isotope system within zircon. Consequently, most source compositions are discussed based on the Hf isotope data. Since the granitoids cannot be directly extracted from the mantle for geochemical mass balance reasons, Hf isotopes in zircon trace the isotope composition of a mafic precursor, which was identified based on elemental geochemistry (**Fig. 9**), reveals that the source was previously extracted from the mantle. Data of granitoid gneisses sampled around the southwestern block from this study and from the literature are consistent with each other and show mantle-like signatures (**Fig. 7.11a**) which indicate that the crustal residence time of these mafic precursors were short, which was also concluded by Guitreau et al., 2017 and Ranjan et al., 2020 for WDC Peninsular gneisses. A notable feature of Hf isotope data is the slightly less depleted nature of >3400 Ma granitoids compared to the 3350-3270 Ma group that, in contrast, exhibit consistently identical signature on this time range. Also note the fairly good agreement between backward projected MORB and arc mantle signatures and those of studied granitoid gneisses (**Fig. 7.11a**).

9.2 Around the northcentral block (3430-3302 Ma granitoids)

Granitoids adjoining to the northcentral block are tonalite-trondhjemite-granite in composition and contain quartz, sodic plagioclase (An_{10-19}), minor K-feldspar, biotite with occasional hornblende. Geochemically, these granitoids are very similar to the high-Al group from the southwestern block (e.g., high $(La/Yb)_N$, negative Nb-Ta-Ti anomalies, and variable Ba, Sr, and Eu anomalies) except that they have slightly more variable total REE concentrations, as well as Sr, Eu and Ta anomalies, most likely resulting from more visible effects of fractional crystallization (**Figs. 7.10 and 9**). Moreover, Hf and Nd isotopes are also similar between granitoids found around the northcentral and the southwestern block (**Fig. 7.11**). As a consequence, they can be interpreted in the same way as the high-Al group discussed in the previous section and are perhaps local equivalents.

9.3 Around the eastern block (3289-3276 Ma granitoids)

These granitoids contain quartz, sodic plagioclase (An_{15-23}), minor K-feldspar, biotite and hornblende in mineral assemblage. Published data (Jayananda et al., 2015; Ranjan et al., 2020; Ao et al., 2021) for gneisses adjoining to the eastern block reveals younger ages of 3289 -3276 Ma that correspond to a terminal event of granitoid formation around the Holenarsipur greenstone belt. They have high-Al concentrations (14.98-16.34 wt.%) with significant variation in SiO_2 (64.14-73.11 wt.%). These granitoids have geochemical characteristics identical to the high-Al group found around the southwestern block (see section 9.2) Furthermore, some granitoids around the eastern block show more pronounced positive Zr-Hf anomalies coupled with positive Y anomalies which are, altogether, most likely related to zircon accumulation in these rocks. Isotopic data also indicate similar sources for all the granitoid gneisses regardless of their geographic location, within the limits of uncertainty considered. (**Fig. 7.11a-b**).

9.4 Diapiric trondhjemites (3230-3180 Ma plutons)

Our new zircon U-Pb ages combined with published data indicate 3230-3177 Ma for intrusion their magmatic precursors (Jayananda et al., 2015; Guitreau et al., 2017; Ranjan et al., 2020). The mineral assemblages comprise quartz, sodic plagioclase (An_{10-12}), minor K-feldspar, biotite and primary muscovite with accessory zircon, titanite and Fe-Ti oxides. They exhibit high-Al contents (>15.0 wt.%) except for three samples that show low-Al (<14 wt.%). These granitoids share many characteristics similar with the high-Al group gneisses around the southwestern and northcentral blocks (e.g., Al_2O_3 and SiO_2 concentrations, high $(La/Yb)_N$, variable Ba, Eu, and Sr anomalies, and negative Ti anomalies) but differs from these latter by the absence of Nb-Ta anomalies and, on the contrary, positive U and Th anomalies (**Fig.7.10**). These rocks seem to differ from other granitoids (TTG-type gneisses) in terms of their sources as the 3*CaO-Al_2O_3/FeO_t+MgO-5*K_2O/Na_2O triangular plot (Laurent et al., 2014) indicate a dominant tonalitic source (**see fig.9d**). However, if the whole rock chemistry particularly elemental ratios (Nb/Ta, Zr/Sm, Sr/Y, La/Yb; see fig. 9a, b, c and e) is interpreted in terms of melting pressures, the trondhjemites require moderate to high pressures similar to the high-Al group. Therefore, the magmatic precursors of these granitoids could be more evolved than that of other granitoids, hence, accounting for their slight geochemical differences.

Neodymium and Hf isotopes of the trondhjemites indicate a less depleted source compared to 3350-3270 Ma granitoids but more similar to the >3400 Ma group (**Fig. 7.11a-b).** This could be due to longer crustal residence times of their magmatic precursors compared to those of the other granitoid groups or, alternatively, their magmatic precursors being more evolved, their Lu/Hf would be lower than that of the other granitoids precursors, hence, resulting in a more rapid drift from mantle signatures (**see fig 7.11a-b**). These trondhjemite plutons could actually be the reworking products of tonalites equivalent to 3350-3270 Ma granitoids, which would be realistic both in terms of elemental and isotopic geochemistry (**Figs. 7.10 and 7.11a-b**). Alternatively, their elemental and isotopic signatures could be explained by mixed sources involving mafic crustal lithologies, akin to those of the other granitoid groups, contaminated by felsic crustal lithologies (i.e., >3270 Ma gneisses). We cannot objectively exclude either of these hypotheses, but this does not affect the geodynamic model proposed in this study. Trondhjemite plutonism was spatially linked with a major phase of crustal-scale partial convective overturn that had a major imprint on crustal reworking that shaped the fundamental architecture of the oldest Archean cratonic core in the Western Dharwar Craton (Bouhallier et al., 1993, 1995).

9.5 *Late granodiorite to granite injections (3150-3100 Ma)*

Late granodiorite to granite injections post-dates previously discussed granitoids and are commonly found as veins or dykes cross cutting the main foliation patterns in virtually all granitoid outcrops. In addition, large elongated sheets of north-south direction and coherent with north-south trending shear zones affected the Eastern block (Bouhallier et al., 1993). They contain quartz, abundant plagioclase (An_{12-14}), K-feldspar, magmatic epidote, hornblende, biotite, zircon, titanite and Fe-Ti oxides. U-Pb zircon ages indicate 3145 -3103 Ma (Jayananda et al., 2015) coinciding with the metamorphism (Jayananda et al., 2013; Dasgupta et al.,2019). Their elemental characteristics such as high SiO_2 (SiO_2-76.5-77.0 wt.%), but very low to high K_2O- 0.34-3.84 wt.% coupled with Nd isotope ($\varepsilon_{Nd(T)}$ = 0 to -0.3 Jayananda et al., 2015) and magmatic epidote suggest rapid injection of magmas originating from a chondritic to depleted juvenile lower crustal source with possible minor ancient crustal contamination (Jayananda et al., 2015).. The injection of these granites mark regional metamorphism and terminal event of the cratonic core formation.

9.6 *Granitoids around other greenstone belts in the cratonic core*

Our data together with published record (Bhaskar Rao et al., 1983; Naqvi et al 1983; Callahan and Rogers, 1987; Chardon, 1997; Jayananda et al., 2019; Sebastian et al., 2021) for gneisses and other granitoid rocks adjacent to the Nuggihalli, Kalyadi, J.C. Pura, Chitradurga belt, and Nagamangala greenstone belt contain quartz, plagioclase (An_{12-27}), minor K-feldspar, biotite, hornblende with accessory zircon, apatite, titanite and opaque phases. They show the same geochemical features as high-Al granitoids (**Fig. 7.10k-l, 9a-f)** which, therefore, point to a similar petrogenetic processes and possibly genetic link with the 3400-3300 Ma granitoids around Holenarsipur greenstone belt.

10. Geodynamic implications

10.1 Crust-mantle differentiation

Incompatible elements (Th, U, Nb, Zr, Hf, REE) together with Nd-Hf isotope data of Archean komatiites and basalts reveal that mantle reservoirs from which komatiite magmas originated were already depleted (Jahn et al., 1982; Jochum et al., 1991; Blichert-Toft and Arndt, 1999; Condie, 2003; Chavagnac, 2004; Campbell, 2003; Kerrich and Xie, 2002; Polat et al., 2000; Mole et al 2015; Jayananda et al., 2008, 2016). Nd isotopic data from the present study combined with published record (**see fig. 7.11b**) on the 3400-3200 Ma komatiites and komatiitic basalts (Jayananda et al., 2008; Mukherjee et al., 2012; Maya, et al.,2017; Patra et al., 2020; Ravindran et al., 2021) reveal a widespread ultramafic volcanism which originated from deep mantle reservoirs and that contributed to large scale crustal growth during 3400-3200 Ma. Incompatible elemental ratios (Nb/U, Nb/Th, Th/Yb, Nb/Yb **see figs.8a-d**), sub-chondritic to moderate REE contents and Nd isotope data of the komatiites and komatiitic basalts reveal large-scale mantle heterogeneity (primitive to depleted mantle) which experienced long-term depletion history. The existence of such 3400-3200 Ma depleted deep mantle reservoirs in turn imply an earlier episode of extraction of ultramafic magmas or link to global differentiation of silicate Earth close to 4500 Ma (Boyet and Carlson, 2005).

Our new U-Pb zircon ages for the granitoids coupled with recent published zircon ages (Guitreau et al., 2017; Jayananda et al., 2015,2019; Ranjan et al., 2020; Ao et al., 2021) show major episodes of TTG-type granitoids formation during 3450-3400 Ma and 3350-3270 Ma time windows, hence, contributing to high rates of continental growth with earlier events of purported crustal growth at 3500 Ma and 3600 Ma (Meen et al., 1992; Guitreau et al., 2017; Ao et al., 2021). Neodymium and Hafnium isotope data are consistent with the existence of depleted shallow upper mantle reservoirs with very minor or no inputs from pre-existing crust during formation of the granitoids (TTG-gneisses). These granitoids therefore represent successive stages of juvenile continental growth of the WDC. Elemental and Nd-Hf isotopic characteristics of the granitoids (TTG-type) and greenstone volcanic assemblages indicate large scale chemical and isotopic heterogeneity with long-term depletion history of the Paleoarchean mantle reservoirs from which the preserved crust of the cratonal core was extracted. The existence of such shallow and deep depleted mantle reservoirs imply earlier episodes of mantle differentiation through extraction of granitoid precursors and ultramafic-mafic greenstone volcanic assemblages. Published U-Pb ages and Lu-Hf isotope data for magmatic and detrital zircons (Nutman et al., 1992; Bhaskar Rao et al., 2008; Hokada et al., 2013; Lancester et al., 2015; Guitreau et al., 2017; Ao et al., 2021) together with Nd isotope [($\mathcal{E}Nd_{(T)}$=3350 Ma)= -2.8 with TDM age of 3890 Ma] signatures (Jayananda et al., 2015) and radiogenic Pb in feldspars of the 3400 Ma old gneisses (Meen et al., 1992) can be attributed to earlier episodes of mantle differentiation and crustal growth that possibly occurred in the 3600-3800 Ma time window. The above arguments show that the mantle source reservoirs of the cratonic core in the WDC had a long term depletion history (3800-3200 Ma). The above lines of arguments suggest extraction of crust in successive stages contributing to major continental growth and evolution of complimentary depleted mantle reservoirs.

10.2 Geodynamic context of cratonic core formation

Despite the fact that numerous studies addressed the tectonic context of Archean continental growth, this topic remains a subject of much debate and discussion after two decades (e.g., Bouhallier et al., 1993; Choukroune et al., 1995;Chardon et al., 1996; Polat et al., 2002; Bedard, 2018; Wyman, 2018; Kusky et al., 2018; Brown et al., 2020; Hyung and Jacobson, 2020; Sotiriou and Polat, 2020; Nutman et al., 2021; Windley et al., 2021; Kusky et al., 2021 and Sotiriou et al., 2022). Tectonic regimes operating in the Archean Earth were necessarily controlled by thermal and mechanical state of the lithosphere which, in turn, was controlled by a hotter mantle (Choukroune et al., 1994; Monteux et al., 2020). Archean cratons differ from post-archean shields by the existence of unique lithological assemblages that comprise komatiites in greenstone belts and polyphase grey gneisses with TTG-affinity in granitoids, hence, suggesting that specific tectonic processes operated during the Archean (Choukroune et al., 1997). Several models have been proposed for the formation of the Western Dharwar Craton which involve both vertical motions associated with mantle plume (Choukroune et al., 1995; Jayananda et al., 2016), horizontal tectonics (Chadwick et al 2000) and combined plume -arc formation model (Jayananda et al., 2008, 2018). The different lithological associations in individual greenstone units combined with their elemental and isotope tracers reveal that each greenstone belt in the cratonic core represent a distinct tectonic unit and it is proposed that the three distinct tectonic units of the Holenarsipur belt correspond to an oceanic plateau, an oceanic arc and a preserved section of oceanic crust close to a spreading center (similar to modern ocean ridge?). Among the three tectonic units of the Holenarsipur greenstone units, the southwestern block with komatiite-komatiitic basalt and adjacent shallow water sedimentary sequences like conglomerate- quartzite -pelite (garnet-staurolite-kyanite-muscovite-biotite) points to an oceanic plateau which is consistent with their elemental and Nd isotope signatures of their origin from deep depleted to primitive mantle source. The rock assemblages of the northcentral block like abundant komatiite and komatiitic basalt-basalt-dacite sequence interlayered with chloritoid-chlorite-garnet bearing pelites imply an oceanic arc possibly adjacent to a volcanic plateau. The Nd isotope data (chondritic to depleted source) coupled with the incompatible element signatures (**see fig. 8e**) of the volcanic rocks of the northcentral block is also consistent with an oceanic arc setting. In contrast the lithological sequences such as pillowed basalts, sheeted dykes, gabbros-foliated gabbros, plagiogranite, layered gabbros and peridotite in the eastern block represents a section of preserved oceanic crust of the spreading centre with N-MORB and E-MORB signatures as revealed by elemental and Nd isotope data. Among other stratigraphically equivalent greenstone belts, the lithological association (komatiite-komatiitic basalt peridotitic to dunite with chromite layers, komatiitic basalt-gabbro-anorthosite-plagiogranite) coupled with Nd isotope and elemental signatures (N-MORB to E-MORB) of the Nuggihalli-Kalyadi belts could also correspond to a preserved section of oceanic crust. On the contrary, thick and voluminous komatiite-komatiitic basalts with minor high-Mg basalts together with elemental and Nd isotope tracers showing dominant primitive to depleted mantle signatures of the J.C. Pura, Banasandra, Ghattihosahalli and Nagamangala greenstone belts suggest a volcanic plateau setting (Jayananda et al., 2008, 2016; Tushipokla and Jayananda, 2013). To summarize, the preserved greenstone assemblages in the cratonic core of the WDC probably represent preserved oceanic volcanic plateaus, oceanic arcs and oceanic ridge formed within time window of 3400-3200 Ma.

The identification of the three distinct greenstone assemblages in the Holenarsipur greenstone belt, and equivalents in the cratonic core, with independent tectonic histories is a very important discovery because their assembly into cratonic framework requires some sort of horizontal motion during the Paleoarchean. In addition, the granitoids (TTG-type gneisses) adjoining to the Holenarsipur greenstone belt exhibit coeval ages of 3430 Ma to 3300 Ma in the SW block, whereas 3430-3339 Ma adjoining to Northcentral block, and 3285-3276 Ma to the western boundary of the eastern block. Strain fabrics data (Bouhallier et al., 1993) and U-Pb zircon ages indicate that assembly of the three tectonic units (greenstone and adjoining granitoid gneisses) coincide with the intrusion of the 3230-3177 Ma diapiric trondhjemites, therefore, suggesting that pre-3200 Ma horizontal motion terminated with the assembly of different tectonic units (oceanic plateaus, arcs, intervening continental fragments and ocean ridge crust) and intrusion of trondhjemites plutons. These field characteristics and timing are shared by granitoids and detrital zircons from the adjoining greenstone belts in the cratonic core (Meen et al., 1992; Jayananda et al., 2008, 2019; Bidyananda et al., 2016; Ao et al., 2021; Ranjan et al., 2022).

There is consensus on the fact that Archean granitoids and especially the TTGs formed by hydrous partial melting of young basaltic precursors at different depths in pressure-temperature conditions where amphibole and garnet (± plagioclase, ± ilmenite) are stable in melting residues (Moyen and Martin, 2012; Nédélec et al., 2012). These conditions are necessary to account for the mineralogy and geochemistry of the TTG-type grey gneisses to which the WDC granitoids belong. However, the geological and tectonic process that allows these conditions to be reached is still a matter of debate (e.g., Smithies et al., 2009; Johnson et al., 2017; Bédard, 2018; Moyen and Laurent, 2018; Hildebrand et al., 2018; Hastie and Fitton, 2019). The ideal candidate among known, and clearly identified geological process is the subduction because it can bring material down into the mantle depth at rates fast enough to avoid complete dehydration of the oceanic slab before reaching the hydrous solidus of wet basalt. However, some workers (e.g., Rey and Coltice, 2008) argue that rheological parameters of the Archean crust does not seem to be in favor of plate tectonics in the Paleoarchean. In contrast several other workers argue for horizontal motion of tectonic plates with eventual subduction as early as Eoarchean (Kusky et al., 2013; Hynes, 2014; Hastie and Fitton, 2019; Korenaga, 2021; Windley et al., 2021; Nutman et al., 2021). Alternative models for plate tectonics does exist which invoke horizontal motion that would result in either intermittent subduction (Van Hunen and Moyen, 2012), formation of slices that pile downward (de Wit, 1998), or formation of duplex structures (Komiya et al., 2015). Recent numerical modeling also propose that some localized horizontal motions can develop at the margin of massive mantle plumes (e.g., Gerya, 2014; Baes et al., 2016) which could reconcile many of contradictory observations and fit in a fair amount of the Archean tectonic models involving both vertical and horizontal motions during the same time frame (e.g., Choukroune et al., 1997; Jayananda et al., 2008; Guitreau et al., 2012; Nagel et al., 2012; Martin et al., 2014; Bédard, 2018). Recent phase-equilibrium and mechanical modelling study (Miocevich et al., 2022) on the Lewisian gneiss complex concluded that sagduction is not a process viable in the Archean Earth. However, the small volume of mafic layers present in the high-grade Lewisian gneiss complex together with the fact that this terrane is small compared to other well-studied lower-grade Archean cratons (e.g., Pilbara-Western Australia, Barberton-South Africa, Superior Province-Canada) is probably not sufficient to firmly conclude on to the viability of sagduction.for the entire Archean crust. Yet, their model may be region specific. Therefore, we favour a model in which large volumes of high-density ultramafic-mafic volcanics associated with TTG type granitoids in the cratonic core of the western Dharwar craton possibly caused inverse density stratification during reheating of crust spatially linked to the emplacement of hot trondhjemite magmas close to ca.3200 Ma, in a way perhaps akin to the environments described in Choukroune et al. (1995, 1997). Furthermore, detailed strain fabrics mapping and kinematic analysis across Paleoarchean cratons (e.g., Kaapvaal and Pilbara) also reveal partial convective overturns which likely drove sagduction processes duringthe Paleoarchean (Collins et al., 1998; Gardiner et al., 2017; Peterson et al., 2019; Wiemer et al., 2018).

Sagduction is a vertical tectonic process clearly identified in the Archean (e.g., Gorman et al., 1978; Bouhallier et al., 1995; Chardon et al., 1996) that could possibly replace the need for horizontal tectonics (e.g., Van Kranendonk et al., 2014). In addition, proposed sources for the formation of TTG-type granitoids match well with tholeiitic basalts present in greenstone belts (e.g., Rapp and Watson, 1995; Nédélec et al., 2012; Guitreau et al., 2012; Martin et al., 2014). As mentioned earlier, the western Dharwar craton presents a continuous tilted crustal panel from upper to lower crust which, hence, allows the sinking of the high-density greenstone volcanics of the Dharwar craton to be followed. Yet, sinking greenstone volcanics exhibit a continuous increase in metamorphic grade until granulite facies (e.g., Raase et al., 1986; Jayananda et al., 2013a) without any evidence for *in-situ* partial melting and melt migration upwards. However, numerical modeling suggests that this process can produce anatectic melts (Nicoli, 2020) but it would have to be investigated further if geochemical signatures of 3600-3300 Ma granitoids in the cratonic core of the WDC could be reproduced by such a process since this author used 3000 Ma granitoids composition to compare to his model whereas field evidence suggest that the WDC acquired its architecture by 3200 Ma ago (e.g. Jayananda et al., 2018).

Regardless of the capacity of sagduction to induce granitoid formation, sagduction alone cannot account for the assembly of the three independent tectonic blocks around Holenarsipur greenstone belt and other tectonic units formed in the same time window in the cratonic core. Therefore, our preferred model for the formation of the cratonic core in the western Dharwar craton is as follows. Vertical motions of mantle plumes in upwelling zones produced oceanic plateaus during 3400-3300 Ma, which possibly initiated horizontal motions due to boundary forces. Horizontal density contrasts could have facilitated the triggering of protosubduction (e.g., duplex, downward piling of slices) and, hence, the development of oceanic arcs, ridges (e.g., Nair and Chacko, 2008), which lead to generation of the protoliths for the 3400-3300 Ma granitoids (TTG-type gneisses) thus contributing to major juvenile continental growth. The location of these horizontal movements could have also been facilitated by rheological weakness (Rey and Coltice, 2008; Rey et al., 2014) that could be due to the presence of pre-existing granitoids such as those older than 3430 Ma and up to 3600 Ma in adjacent to some of the oceanic plateaus (e.g., Guitreau et al., 2017). The assembly of different tectonic units ended with the culmination of some sort of subduction of intervening oceanic crust between oceanic plateaus/ridges and eventual slab breakoff causing mantle upwelling which resulted in melting of the newly formed juvenile crust and pre-existing granitoid crust (3600-3300 Ma) at different levels (14-18 kbar), in turn, forming trondhjemite magmas during 3200 Ma and their intrusion mark the terminal magmatic event of juvenile crustal growth in the cratonic core. The hot trondhjemite magma intrusions associated with the mantle upwelling caused the partial convective overturn of the crust which drove the gravitational collapse of high-density greenstone material and rise of low-density domes that resulted in dome-keel patterns as revealed by the strain fabrics mapping and kinematic analysis on the scale of cratonal core (Bouhallier et al., 1993,1995; Choukroune et al., 1995;Chardon et al., 1996). This dome-keel formation is spatially associated with medium to high grade metamorphism, crustal reworking and granite emplacement (granite sheets injected into the gneisses of southwestern block and Chikmagalur granite; Jayananda et al., 2015) and cratonization of Paleoarchean crust close to 3100 Ma (Jayananda et al., 2013, 2015; Dasgupta et al., 2019). The cratonized mature crustal segment form provenance for the detritus (e.g., quartzites and conglomerates) in the <3100 Ma sedimentary basins formed (Hokada et al., 2013;Chatterjee and Das, 2004; Jayananda et al., 2018; Ranjan et al., 2022). Finally, crustal adjustments through metamorphic cooling, crustal reworking, and 3000 Ma hybrid potassic granite formation (e.g., Bellur-Nagamangala potassic granites) marked the final cratonization of the cratonal core in the WDC (e.g., Jayananda et al., 2019, 2020; Ao et al., 2021).

This model may apply to other parts of the WDC and spatially associated blocks that recorded similar histories either within the sedimentary record or the meta-igneous record. This is the case for the Bababudan basin (Jayananda et al., 2015; Lancaster et al., 2015; Bidyananda et al., 2016), western margin of the Chitradurga greenstone belt (Chardon et al., 1997; Lancaster et al., 2015; Wang and Santosh, 2019; Ravindran et al., 2021), Coorg massifs (Santosh et al., 2015; Roberts and Santosh, 2018), Sakaleshpur and Western Ghats (Jayananda et al in prep.). For instance, zircon U-Pb ages of magmatic and detrital zircons from Coorg massifs were attributed to three major crust forming events at 3500 Ma, 3370-3270 Ma, and

3190-3140 Ma (Santosh et al., 2015; Amal Dev et al., 2016; Roberts and Santosh, 2018) with remnants as old as 3750 to 4030 Ma (Santosh et al., 2015). The Coorg massif is considered as an exotic Mesoarchean supercontinent (Santosh et al., 2015) assembled with the Dharwar craton during Mesoproterozoic but our zircon age data (3500-3200 Ma) between the Holenarsipur greenstone belt and Coorg massifs (Jayananda et al unpublished data) together with a recent study (Roberts and Santosh, 2018), in contrast, suggest a common crustal building history of 3500-3200 Ma followed by granite intrusion and metamorphism at 3150-3100 Ma in the context of collision leading to the stabilization of the craton close to 3100 Ma.

10.3 Comparison with coeval cratons and global implications

Archean crustal nuclei originated as micro-blocks in diverse tectonic environments assembled through lateral motions which resulted in large cratonic cores with thick crustal roots. Our study in the western Dharwar craton reveals that different tectonic units were juxtaposed through horizontal motion culminating into subduction (3350-3230 Ma) with eventual slab break off drive mantle upwelling causing melting of thickened crust resulting in generation of the trondhjemite magmas. The intrusion of these trondhjemite magmas, in turn, caused partial convective overturn which led to the development of dome-keel structures at 3200 Ma, followed by HT/HP metamorphism, late-kinematic minor granite intrusions during 3145-3100 Ma marking the final stabilization of cratonal core with the development of crustal roots which supplemented by seismic tomographic data (Gupta et al., 2003) indicating thick crust (45-55 km).

The 3600-3100 Ma crustal history of the western Dharwar craton correlates with the crustal growth history and thermal record of the Singhbhum craton, Eastern India (Upadhyay et al., 2014), the Kaapvaal craton, South Africa (Kroner et al., 2014), Pilbara craton, western Australia (Van Kronendonk et al.2015), Sao Francisco craton (Teixeira et al., 2017), the Slave province (Bleeker 2002). The TTG-greenstone assemblages in the Singhbhum craton preserve a record of two major stages of magmatism including 3450-3440 Ma tonalitic to trondhjemite and 3350-3320 Ma granodiorite to granite phase (Upadhyay et al., 2014) with vestiges of TTG-greenstone assemblages as old as 3610-3507 Ma (Mukhopadhyay et al., 2008; Nelson et al., 2014). These Paleoarchean crust building events were followed by a partial convective overturn, thermal event, and craton formation at 3200-3100 Ma, hence, comparable to the crustal history of the cratonic core in the western Dharwar craton.

The Kaapvaal craton contains microblocks which comprise greenstone belts and TTGs formed during 3600-3300 Ma and assembled through lateral motion in the context of subduction, thereby causing thickening, metamorphism, reworking, deformation, and generation of granites ca 3230-3100 Ma (Kamo and Davis, 1994; Schoene et al., 2008). Both the Holenarsipur and the Barberton greenstone belts with their adjacent granitoids of TTG-affinity and intrusive plutons share comparable protracted crustal histories in term of lithological assemblages, magmatism, dome-keel patterns, and metamorphic record (Compston and Kroner, 1988; Van Kranendonk et al., 2010; Jayananda et al., 2018; Wang et al., 2019). The Barberton greenstone belt is an assembly of allochthonous sequences with independent protracted crustal and tectonic histories which were interpreted as juxtaposed through active convergence (Schoene et al., 2008). The volcanic sequences from different stratigraphic units of the Barberton greenstone belt yield ages of 3644 to 3300 Ma (Armstrong et al., 1990; Kroner et al., 1996; Byerly et al. 1996; Chavagnac, 2004) whereas the surrounding granitoids (TTG-type gneisses) extending into Swaziland formed in major events between 3660 and 3300 Ma, and granite plutons emplaced at 3230-3100 Ma (Compston and Kröner, 1988; Kroner et al., 2014; Zeh et al., 2011; Armstrong et al., 1990; Kamo and Davis, 1994). The intrusion of hot trondhjemite magmas into the greenstone sequence and adjoining granitoids (TTGs) at 3226-3180 Ma initiated gravity driven partial convective overturn wherein colder high-density greenstones collapse into low density softer granitoids (TTG-type gneisses) resulting in dome-keel structures (Van Kranendonk et al., 2010). The 3200 Ma old garnet-bearing high-pressure metamorphic assemblages in the Barberton region interpreted to be resulted by partial convective overturn during formation of plutons (Wang et al., 2019). On the contrary, the Assegaai De Kraalan and Witrivier greenstone belts from the southeast of the Kaapvaal craton contain dominant ultramafic-mafic volcanic rocks with intercalated chert and BIFs. These greenstone sequences are dated at 3222 ± 8 Ma and 3193 ± 5 Ma intrusions and show an initial low T/P followed by high T/P metamorphic assemblages which is overall interpreted as a response to crustal thickening through convergence during Paleoarchean (Saha et al., 2010).

The east Pilbara craton in Western Australia preserves an Archean crustal record with granite-greenstone assemblages display classical dome and basin patterns which share similarities with the oldest cratonic core (3600-3200 Ma) of the western Dharwar craton. The Archean continental nuclei in the east Pilbara craton built in successive stages through granitoid formation and greenstone volcanism during 3660-3220 Ma (Nelson et al., 1999; van Kranedonk et al., 2015; Gardiner et al., 2017; Peterson et al., 2019; Wiemer et al., 2018; Kusky et al., 2021). The oldest crustal remnants identified are dated from 3660 to 3580 Ma using zircon in tonalitic gneiss enclaves and metagabbro whereas detrital U-Pb zircon ages reveal 3710 Ma (Thorpe et al., 1992), thus, indicating the existence of an even older crust. U-Pb dating of zircons from leucogabbro and gabbro indicate 3588±5 Ma and 3578±5Ma, respectively (Peterson et al., 2019) which are correlated with similar U-Pb zircon ages for TTGs from Muccan dome. Furthermore, 3467 Ma U-Pb zircon age of TTG suite from Warrawigine dome (Kemp et al., 2017), and U-Pb zircon ages of 3484-3462 Ma from Callina Supersuite, 3451-3416 Ma Tambina Supersuite and 3324-3277 Ma from Emu Pool Supersuite and 3274-3223 Ma Cleland Supersuite (Van Kranendonk et al., 2007; Gardiner et al., 2017; Peterson et al., 2019) are also consistent. The TTGs suite formation terminated with younger 3250-3220 Ma magmatic event of monzogranite and syenogranite formation which belong to Cleland Supersuite (Gardiner et al., 2017; Peterson et al., 2019). To summarize, widespread granitoid magmas with TTG affinity emplaced during 3600-3300 Ma and contemporaneous greenstone volcanism contributed to the continental growth (Nelson et al., 1999; Van Kranendonk et al., 2007; Gardiner et al., 2017; Peterson et al., 2019) followed by partial convective overturn of crust which resulted in dome and keel patterns supposedly developed at 3325-3300 Ma (Collins et al., 1998) and followed by late magmatic intrusions ca.3250-3200 Ma (Gardiner et al., 2017; Peterson et al., 2019; Wiemer et al., 2018). On the contrary a more recent study (Kusky et al., 2021) argues that development of large domal structures is linked to late orogenic shortening which was synchronous with or soon-after intrusion of 3274-3223 Ma plutons.

The Archean crustal record (3650-3180 Ma) of the northern Sao Francisco craton (Teixeira et al., 2017) in Brazil correlates with the formation history of the cratonic core in the WDC. The preserved Archean crust (TTG-greenstone assemblages and intrusive granites) formed through a multi-stage history. U-Pb zircon ages reveal that the oldest TTGs in Roacho de Santana formed at 3648 ± 69 Ma whereas remnants of the Hadean record were found as detrital zircon (4100 Ma; Paquette et al., 2015). Widespread TTG formation at 3403-3325 Ma (Nutman and Cordani, 1993; Martin et al., 1997; Dantas, et al., 2013; Santos-Pintos et al., 2012) and 3305 ± 9 Ma greenstone volcanism (Peucat et al., 1995) contributed to large scale continental growth. Late-stage granodioritic to granite intrusions dated at 3250 Ma (Bastos Leal et al., 2003), 3184 ± 6 Ma (Nutman and Cordani, 1993), 3158 ± 2 Ma (Martin et al., 1997) and 3040 Ma (Peucat et al., 2002) represent terminal juvenile additions followed by reworking of ancient crust (Barbosa et al., 2013) and stabilization of the Sao Francisco craton.

Globally, the 3600-3100 Ma time window appears to represent a major period of crust-mantle differentiation, continental growth, reworking of pre-existing crust, LP-HT metamorphism, and eventual formation of stable Archean cratonic cores. The continental growth and craton formation involved episodic formation of granitoids and coeval, though unrelated, greenstone volcanic rocks early in mantle upwelling zones followed by arc setting resulting in the formation of diachronous blocks representing cycles of magmatism and sedimentation. Assembly of these crustal blocks was likely driven through horizontal motions with eventual convergence in arc settings and slab breakoff leading to high pressure melting of mafic crust and generation hot-felsic magmas and hybrid granitoids. Formation of these hot magmas induced partial convective overturn of rheologically weaker low-density felsic crust. This led to a gravitational collapse of high-density greenstones into low density infracrustal gneisses and the development of regional dome-keel patterns, HT/HP metamorphism and cratonization at 3200-3100 Ma. Small differences observed between Archean cratons can certainly arise from distinct abundances of involved lithological units, as well as local age differences and pre-histories. Furthermore, Windley et al., (2021) suggested that the onset of horizontal motion of tectonic plates began by the Eoarchean and contributed to the Archean continental growth through collision of arcs and continents whilst the development of domal patterns in Archean cratons are attributed to orogenic shortening and related deformation caused by late magmatic intrusions originated during massive slab breakoffs in subduction zones (Kusky et al., 2021). Long-term accumulation of evidence suggests that the Earth's global geodynamics evolved throughout the Archean to progressively initiate modern-plate tectonics (e.g. Korenaga, 2013; Moyen and Laurent, 2018) which did not likely occurred everywhere at the same time but most likely gradually evolved from local and punctual tectonic events to a more globally-connected system of plates (e.g. Laurent et al., 2014). However, it is important to note that the horizontal motions we have evidenced in the Western Dharwar craton, and which we compare to other cratons, are valid regardless of their actual origin (e.g., plate tectonics, lower crustal flow, plume-related lithospheric adjustment).

11. Conclusions

This synthesis integrates our new data with published record of field, petrographic, geochronologic, elemental and isotope (Nd-Hf-Sr-Pb) data of greenstone volcanic rocks, granitoids (TTG-type) and diapiric trondhjemites from the cratonic core of the western Dharwar craton and address processes involved in the origin of the oldest continental nuclei, evolving tectonics of the Archean earth and formation of the cratonic cores worldwide. The salient conclusions of this synthesis can be summarized as follows:

1. The oldest preserved crustal nuclei in the western Dharwar craton comprises komatiite-dominated greenstone assemblages, TTG-type grey gneisses and diapiric trondhjemites forming a wide time (3600-3200 Ma) and tectonic window for the early earth dynamics, crust-mantle evolution and formation of cratonic cores.
2. The preserved crust in the cratonic core accreted in three major episodes during 3430-3400 Ma, 3350-3270 Ma and 3230-3170 Ma with remnants of crust formed between 3500 and 3600 Ma.
3. Field evidence together with elemental and Nd isotope signatures of greenstone volcanic assemblages in the cratonic core suggest their independent histories which point to an origin in primitive to depleted mantle reservoirs probably formed as oceanic plateaus, oceanic arc and oceanic crust section of the spreading center.
4. The magmatic precursors of the TTG-type granitoids originated by partial melting of short-lived mafic crust at different depths (10-15 kbar) without or with variable garnet in source residue whilst diapiric trondhjemite magmas formed by melting of base of the (thickened) mafic- tonalitic crust with probable garnet in residue.
5. Horizontal motion of the oceanic crust intervening to pre-existing continental nuclei, oceanic plateaus, arcs and ridges during 3200 Ma led to the assembly of different tectonic elements into the cratonic core. Continued subduction with slab breakoff

caused asthenosphere upwelling that caused melting of thickened crust generating trondhjemite magmas which upon upward movement caused partial convective overturn and gravitational collapse of high-density greenstones into low-density granitoids of TTG-affinity causing dome-keel structures and HT-LP metamorphism.

6. The crust building processes, continental growth and craton forming mechanisms documented in the cratonic core of the WDC also documented in other Archean cratonic cores in Peninsular India, Southern Africa, Western Australia and South America. Therefore it appears that globally 3600-3200 Ma time window corresponds to major period of mantle differentiation, high rates of juvenile crustal growth, transient tectonics and craton formation worldwide.

Acknowledgements

This work was funded by DST projects (ESS/16/334/2007; DST-FIST [SR/FST/ESI-146/2016(C)]), program and continued by French Agence National de la Recherche through the funded project "Zircontinents" (ANR-17-CE31-0021) and LabEx ClerVolc (ANR-10-LABX-0006). This is ClerVolc contribution number 574. M.J gratefully acknowledge Jean-Jacques Peucat, Dominique Chardon, Jean-Francois Moyen and Herve Martin for thought provoking discussions over years on the Dharwar craton, Archean tectonics and origin of protocontinents. K. R. Aadhiseshan acknowledges financial support of Dr. D.S. Kothari Post-doctoral Fellowship [DSKPDF-F.4-2/2006 (BSR)/ES/19-20/0020)]. R. V. Gireesh, Tushipokla, S.V. Balaji Manasa Rao., B. Tarun Kumar and Tarun Thomas are thanked for their assistance at various stages. We thank two anonymous reviewers for insightful reviews and recommendations which greatly contributed to improve quality and visibility of the contribution. Prof. Tim Kusky thanked for efficient editorial handling, helpful comments and suggestions.

Author contributions

M.J designed the project, carried out field work, generated and compiled the data base and wrote the original manuscript; M.G participated in field work, generated data related to zircon (i.e., images, U-Pb, and Lu-Hf) , co-drafted some figures, provided intellectual inputs in data interpretation, and participated in the writing of the present manuscript. KRA participated in field work, compiling the data, drafted figures and provided intellectual inputs; T.M and SLC have analyzed greenstone volcanic rocks for elemental and Nd isotopes and provided intellectual inputs.

Competing financial interests: The authors declare no competing financial interests.

References

Achterberg, E., Ryan, Chris Jackson, Simon Griffin, W., 2001. LA-ICP-MS in the Earth Sciences - Appendix 3, data reduction software for LA-ICP-MS. Short Course. 29. 239-243.

Adams, J., Rushmer, T., O'Neil, J., Francis, D., 2012. Hadean greenstones from Nuvvuagittuq fold belt and origin of the early continental crust. Geology, 40, 363-366.

Amaldev, T., Santosh, M., Tang, L., Baiju, K.R., Tsunogae, T., and Satyanarayanan, M., 2016. Mesoarchean convergent margin processes and crustal evolution: Petrologic, geochemical and zircon U-Pb and Lu-Hf data from the Mercara Suture Zone, southern India. Gondwana Research 37, 182-204.

Anhaeusser, C.R., 2014. Archean greenstones and associated granitic rocks - a review. Journal of African Earth Sciences 100, 684-732.

Ao, W., Zhai, M., Zhao, Y., Zhang, C., Sun, Y., George, P.M., Sajeev, K., Gou, L., Lu, J., Hu., Y., 2021. Paleo-Mesoarchean crustal growth and reworking in the western Dharwar Craton, southwestern India: Evidence from trondhjemitic gneiss and granitic gneiss. Precambrian Research, 367, 106428, https://doi.org/10.1016/j.precamres.2021.106428.

Arndt, N.,2003, Komatiites, kimberlites and boninites: Journal of Geophysical Research, 108, 2293–2304. doi:10.1029/ 2002JB002157.

Arndt, N.T., Lesher, C.M., and Barnes, S.J.,2008, Komatiites: New York, Cambridge University Press, 467 p.

Arndt, N.T., and Nisbet, E.G.,1982, Komatiites: UK, George Allen and Unwin Publications, 526 p.

Armstrong, R.A., Compston, W., de Wit, M.J., Williams, I.S., 1990. The stratigraphy of the 3.5-3.2 Ga Barberton greenstone belt revisited: a single zircon ion microprobe study. Earth and Planetary Science Letters, 101, 90–106.

Baes, M., Gerya, T., Sobolev, S.V., 2016. 3-D thermo-mechanical modelling of plume induced subduction initiation. Earth Planetary Science Letters 453, 193–203.

Balaram, V., and Gnaneswar Rao, T., 2003. Rapid determination of REE and other trace elements in geological samples by microwave acid digestion and ICP-MS: Atomic Spectroscopy, 24, 206–212.

Barbosa, N, Teixeira, W., Leal L.R.B., Leal A.B.M., 2013. Evolução crustal do sector occidental do Bloco Arqueano Gavião, Cráton do São Francisco, com base em evidências U–Pb, Sm–Nd e Rb–Sr. Geologia USP. Série Cient. 13: 63–88.

Barker, F., 1979. Trondhjemite: definition, environment and hypotheses of origin. In: Barker, F. (Ed.), Trondhjemites, Dacites and Related Rocks. Elsevier, Amsterdam, pp. 1–12.

Barker, F., Arth, J.G., 1976. Generation of trondhjemite-tonalite liquids and Archean bimodal trondhjemite-basalt suites. Geology 4, 596–600.

Baksi, A.K., 2001, Search for a deep mantle component in mafic lava using a Nb-Y-Zr plot: Canadian Journal of Earth Sciences, 38, 813–824.

Bastos Leal L.R, Cunha J.C, Cordani U.G, Teixeira W, Nutman, A, Menezes, Leal A, B., Macambira M.J.B., 2003. SHRIMP U–Pb, ^{207}Pb/^{206}Pb zircon dating and Nd isotopic signature of the Umburanas greenstone belt, Northern São Francisco Craton, Brazil. Journal of South American Earth Sciences, 15: 775–785.

Bédard, J.H., 2006. A catalytic delamination-driven model for coupled genesis of Archaean crust and sub-continental lithospheric mantle. Geochimica et Cosmochimica Acta 70, 1188-1214.

Bédard, J.H., 2018. Stagnant lids and mantle overturns: implications for Archaean tectonics, magma genesis, crustal growth, mantle evolution, and the start of plate tectonics. Geoscience Frontiers, 9, 19–49.

Begemann, F., Ludwig, K.R., Lugmair, G.W., Min, K., Nyquist, L.E., Patchett, P.J., Renne, P.R., Shih, C.Y., Villa, I.M., and Walker, R.J., 2001. Call for an improved set of decay constants for geochronological use: Geochimica et Cosmochimica Acta, 65, 111–121

Bhaskar Rao, Y. J, Kumar. A, Vrevsky, A. B., Srinivasan, R., and Anantha Iyer, G. V., 2000. Sm-Nd ages of two meta-anorthosite complexes around Holenarsipur: Constraints on the antiquity of Archean supracrustal rocks of the Dharwar craton. Proc. Indian Acad. Sci. (Earth Planet. Sci.), 109, 57-65.

Bhaskar Rao, Y.J., Griffin, W.L., Ketchum, J., Pearson, N.J., Beyer, E., and O'Reilly, S.Y., 2008. An outline of juvenile crust formation and recycling history in the Archaean Western Dharwar craton, from zircon in situ U-Pb dating and Hf isotopic compositions. abstract, Goldschmidt conference 2008: Geochimica et Cosmochimica Acta, 72, p. A81.

Bhaskar Rao, Y.J., Sivaraman, T.V., Pantulu, C.V.C., Gopalan, K., and Naqvi, S.M., 1992. Ages of late Archaean metavolcanics and granites, Dharwar craton: Evidence for early Proterozoic thermo-tectonic events: Precambrian Research, 38, 246–270.

Bhaskar Rao, Y.J., Beck, W., Rama Murthy, V., Charan, S.N. and Naqvi, S.M., 1983. Geology, Geochemistry and age of metamorphism of Archaean Grey Gneisses around Channarayapatna, Hassan District, Karnataka, South India, Memoir Geological Society of India, v. 4, pp. 309-328.

Bidyananda, M., Goswami, J.N., and Srinivasan, R., 2011, Pb–Pb zircon ages of Archean meta-sediments and gneisses from the Dharwar Craton, southern India: Implications for the antiquity of the eastern Dharwar craton: Journal of Earth System Science,120, 643–661. doi:10.1007/s12040-011-0094-1.

Bidyananda, M., Gerdes, A., Goswami, J.N., 2016. U-Pb and Hf isotope records in detrital and magmatic zircon from Eastern and western Dharwar Craton, southern India: evidence for coeval Archean crustal evolution. Precambrian Research, 275, 496–512.

Bleeker, W., 2002. Archean Tectonics: A review with illustrations from the Archean Slave craton. Geological Society, London, Special Publications, 199, 151-181.

Blichert-Toft, J., 2008. The Hf isotopic composition of zircon reference material 91500. Chemical Geology, 253, 252-257.

Blichert-Toft, J., Arndt, N.T., 1999. Hf isotope compositions of komatiites. Earth and Planetary Science Letters, 171, 439– 451.

Bosak, T., Moore, K.R., Gong, Jian., Grotzinger., J.P.,2021. Searching for biosignatures in sedimentary rocks from early Earth and Mars. Nature Reviews, https://doi.org/10.1038/s43017-021-00169-5.

Bouhallier, H., 1995. Evolution structurale et métamorphique de la croûte continentale archéenne (craton de Dharwar, Inde du sud). Mém. Doc., Géosciences-Rennes 60, 277p.

Bouhallier, H., Chardon, D. and Choukroune, P., 1995. Strain patterns in Archaean dome-and-basin structures: the Dharwar craton (Karnataka, South India). Earth and Planetary Science Letters, 135, 57-75.

Bouhallier, H., Choukroune, P. and Ballèvre, M., 1993. Diapirism, bulk homogeneous shortening and transcurrent shearing in the Archaean Dharwar craton: the Holenarsipur area, southern India. Precambrian Research, 63, 43-58.

Bouhallier, H., Guiraud, M., 1994. Sagduction et circulations de fluides dans la ceinture de roches vertes d'Holenarsipur (Karnataka, Inde du Sud): caractérisation par I'Ctude P-T-X(H,O) des metapelites, 1Seme R & M. Sci. Terre, 9.

Bouvier A., Vervoort, J. D., Patchett, J., 2008. The Lu-Hf and Sm-Nd isotopic composition of CHUR: constraints from unequilibrated chondrites and implications for the bulk composition of the terrestrial planets. Earth and Planetary Sciences Letters, 280, 285-295.

Boyet, M., Carlson, R.W., 2005. 142Nd evidence for early (>4.53 Ga) global differentiation of silicate Earth. Science 309, 577–581.

Brown, M., Johnson, T., Gardiner, N.J., 2020. Plate Tectonics and the Archean Earth. Annual Review of Earth and Planetary Sciences, 48, 291-320. https://doi.org/10.1146/annurev-earth-081619-052705

Byerly, G.R., Kroner, A., Lowe, D.R., Todt, W., Walsh, M.M., 1996. Prolonged magmatism and time constraints for sediment deposition in the Early Archean Barberton greenstone belt: evidence from the Upper Onverwacht and Fig Tree groups. Precambrian. Research, 78, 125 – 138.

Callahan E.J., Rogers, J.J.W., 1987. Thorium and uranium contents of gneisses and trondhjemites in the Western Dharwar craton. India. Canadian Journal of Earth Sciences, 24, 934-940.

Campbell, I.H., 2002, Implications of Nb/U, Th/U and Sm/Nd in plume magmas for the relationship between continental and oceanic crust formation and the development of the depleted mantle: Geochimica et Cosmochimica Acta, 66, 1651–1661. doi:10.1016/S0016-7037(01)00856-0.

Campbell, I.H., 2003. Constraints on continental growth models from Nb/U ratios in the 3.5 Ga Barberton and other Archaean basalt-komatiite suites. Am. J. Sci. 303, 319–351.

Catling, D.C., Zahnle, K.J.., 2020. The Archean atmosphere. Science Advances, 2020;6: eaax1420.Cawood, P.A., Hawksworth, C.J., Pisarevsky, S.A., Dhuime, B., Capitanio, F.A., Nebel, O. 2018. Geological archive of the onset of plate tectonics. Philosophical Transactions of the Royal Society A: Mathematical, Physical and Engineering Sciences, 376, 20170405.

Chadwick, B., M. Ramakrishnan, M. N. Viswanatha and Srinivasa Murthy, 1978: Structural studies in the Archean Sargur and Dharwar supracrustal rocks of Karnataka craton. Journal of the Geological Society of India, 22, 557-567.

Chadwick, B., Ramakrishnan M., Viswanatha, M.N., 1981. Structural and metamorphic relations between Sargur and Dharwar supracrustal rocks and Peninsular gneiss in Central Karnataka. Journal of the Geological Society of India, 22, 557-569.

Chadwick, B., Vasudev, V.N., and Hedge, G.V., 2000, The Dharwar craton, southern India, interpreted as the result of late Archaean oblique convergence: Precambrian Research, v. 99, p. 91–101. doi:10.1016/S0301-9268(99) 00055-8.

Chardon, D., Choukroune, P., Jayananda, M., 1996. Strain patterns, de´collement and incipient sagducted greenstone terrains in the Archaean Dharwar craton (south India). Journal of Structural Geology, 18, 991–1004.

Chardon, D., Choukroune, P., Jayananda, M., 1998. Sinking of the Dharwar basin (South India): implications for Archaean tectonics. Precambrian Research, 91, 15–39

Chardon, D., 1997. Les Déformations Continentales Archeennes : Exemples Naturels Et Modélisation Thermomécaniques. Mémoire Géosciences-Rennes, vol. 76. Université de Rennes 1, France, pp. 1–300 (PhD. Thésis).

Chardon, D., Jayananda, M., Chetty, T.R.K., Peucat, J-J., 2008. Precambrian continental strain and shear zone patterns: the South Indian case. Journal of Geophysical Research – Solid Earth 113, B08402. http://dx.doi.org/10.1029/2007JB005299.

Chardon, D., Jayananda, M., Peucat, J-J., 2011. Lateral constrictional flow of hot orogenic crust: Insights from the Neoarchean of south India, geological and geophysical implications for orogenic plateaux. Geochemistry, Geophysics, Geosystems 12, Q02005. http://dx.doi.org/10.1029/2010GC003398.

Chatterjee, R.S., and Das, S., 2004. Tattekere conglomerate–quartzite association: origin and stratigraphic position of a disputed Archean Formation in the supracrustals of Karnataka, India. Journal of Asian Earth Sciences, 23, 247-261. DOI:10.1016/S1367-9120(03)00126-3

Chavagnac, V., 2004. A geochemical and Nd isotopic study of Barberton komatiites (South Africa): Implication for the Archean mantle: Lithos, v. 75, p. 253–281. doi:10.1016/j. lithos.2004.03.001.

Chikhaoui, M., 1981. Les roches volcaniques du proterozoique superieur de la chaine pan-Africaine dans le NW de l' Afrique (Hoggar, Anti-Atlas, Adrar des Iforas): caracterisation geochimique et mineralogique, implications geodynamiques. These d' Etat, Montpellier,183p.

Choukroune, P., Bouhallier, H., Arndt, N.T., 1995. Soft lithosphere during periods of Archaean crustal growth or crustal reworking. In: Coward, M.P., Riess, A.C. (Eds.), Early Precambrian Processes. Geological Society of London, Special Publication, vol. 95. pp. 67–86

Choukroune, P., Ludden, J.N., Chardon, D., Calvert, A.J., Bouhallier, H., 1997. Archaean crustal growth and processes: a comparison of the Superior province and the Dharwar craton India. In: Burg, J.P., Ford, M. (Eds.), Orogeny Through Time, Geological Society Special Publication 121, 63–98.

Chu, N., Taylor, R.N., Chavagnac, V., Nesbitt, R.W., Boella, R.M., Milton, J.A., German, C.R., Bayon, G., Burton, K., 2002. Hf isotope ratio analysis using multi-collector inductively coupled plasma mass spectrometry: an evaluation of isobaric interference corrections. Journal of Analytical Atomic Spectrometry, 17, 1567–1574.

Collins W. J., Van Kranendonk, M.J., Teyssier, C. 1998. Partial convective overturn of Archean crust in the east Pilbara Craton, Western Australia: driving mechanisms and tectonic implications. Journal of Structural Geology, 20 (9-10), 1405-1424.

Compston, W. Kroner, A., 1988. Multiple zircon growth within early Archaean tonalitic gneiss from the Ancient Gneiss Complex, Swaziland. Earth and Planetary Science Letters, 87, 13-28.

Condie, K.C., 2003. Incompatible element ratios in oceanic basalts and komatiites: Tracking deep mantle sources and continental growth rates with time. Geochemistry Geophysics. Geosystems. 4 (1), 1005, doi: 10.1029/2002GC000333.

Corfu, F., Hanchar, J. M., Hoskin, P. W. O., Kinny, P., 2003. Atlas of zircon textures. Reviews in Mineralogy and Geochemistry, 53, 469–500.

Dantas E.L, Brito Neves B.B, Fuck R.A., 2013. Looking for the Early Archean rocks in South America: U–Pb dating and Hf isotopes in zircons from the north São Francisco Craton, Brazil. Geological Society of America Annual Meeting 2013, Paper 269-5.

Dasgupta, A., Bhowmik, S.K., Dasgupta, S., Avila, J., Ireland, T.R., 2019. Mesoarchean clockwise metamorphic P-T path from the Western Dharwar Craton. Lithos, 342-343, 370-390.

Defant, M.J., Drummond, M.S., 1990. Derivation of some modern arc magmas by melting of young subducted lithosphere. Nature 347, 662–665.

De Paolo, D.J., 1981. Neodymium isotopes in Colorado Front Range and crust–mantle evolution in Proterozoic. Nature, 291, 193–196.

Desrochers, J.P., Hubert, C., Ludden, J.N., Pilote, P., 1993. Accretion of Archean oceanic plateau fragments in the Abitibi, greenstone belt, Canada. Geology 21, 451-454.

Devapriyan, G.V., Anantharamu, T.R., Vidyadharan, K.T., Raghu Nandan, K.R., 1994. Spinifex textured peridotitic komatiite from Honnabetta area, Nagamangala schist belt, Karnataka. Journal of the Geological Society of India, 44, 483–493.

de Wit, M.J., 1998. On Archean granites, greenstones, cratons and tectonics: does the evidence demand a verdict? Precambrian Research, 91, 181-226.

Dhuime, B., Hawksworth, C.J., Cawood, P.A., Storey, C.D., 2012. A change in the geodynamics of continental growth 3 billion years ago. Science 335, 1334–1336.

Drummond, M.S., Defant, M.J., 1990. A model for trondhjemite-tonalite-dacite genesis and crustal growth via slab melting: Archean to modern comparisons. J. Geophys. Res. 95, 503–521.

Drury, S.A., Van Calstren, P.C., Reeves-Smith, G.J., 1987. Sm–Nd isotopic data from Archaean metavolcanic rocks at Holenarasipur, South India. J. Geology, 95, 837–843.

Drury, S.A., and Holt, R.W., 1980. The tectonic framework of the South Indian craton: A reconnaissance involving LANDSAT imagery. Tectonophysics, 65 (3-4), 1-15.

Fan, J., and Kerrich, R., 1997, Geochemical characteristics of Al-depleted and undepleted komatiites and HREE-enriched tholeiites, western Abitibi greenstone belt: Variable HFSE/REE systematics in a heterogeneous mantle plume: Geochimica et Cosmochimica Acta, 61, 4723–4744. doi:10.1016/S0016-7037(97)00269-X

Fisher, C.M., Vervoort, J.D., Hanchar, J.M., 2014. Guidelines for reporting zircon Hf isotopic data by LA-MC-ICP-MS and potential pitfalls in the interpretation of these data. Chemical Geology, 363, 125–133.

Fisher, C.M. Hanchar J. M., Samson S. D., Dhuime B., Blichert-Toft J., Vervoort J. D. and Lam R., 2011. Synthetic zircon doped with hafnium and rare earth elements: A reference material for in situ hafnium isotope analysis. Chemical Geology 286, 32-47.

Fitton, J.G., Saunders, A.D., Norry, M.J., Hardarson, B.S., Taylor, R.N., 1997, Thermal and chemical structure of the Iceland plume: Earth and Planetary Science Letters, 153, 197–208. doi:10.1016/S0012-821X (97)00170-2.

Garde, A.A., Windley, B.F., Kokfelt, T.F., Keulen, N., 2020. Archaean plate tectonics in the North Atlantic Craton of West Greenland revealed by well-exposed horizontal crustal tectonics, island arcs and tonalite-trondhjemite-granodiorite complexes. Frontiers in Earth Science 8: 540997.

Gardiner, N.J., Hickman, A.H., Kirkland, C.L., Lu, Y., Johnson, T.E., Zhao, J.-X., 2017. Processes of crust formation in the early earth imaged through Hf isotopes from the East Pilbara Terrane. Precambrian Research 297, 56-76.

Gerya, T., 2014. Precambrian geodynamics: concepts and models. Gondwana Research, 25, 442–463.

Gorman, B.E., Pearce, T.H., and Birkett, T.C., 1978. On the structure of Archaean greenstone belts, Precambrian Research, 6. 23-41.

Grocolas, T., Bouilhol, P., Caro1, G., Stephen J. Mojzsis, S.J., 2022. Eoarchean subduction like magmatism recorded in 3750 Ma mafic-ultramafic rocks of the Ukaliq supracrustal belt (Québec). Contributions to Mineralogy and Petrology 177: 39.

Gruau, G., Tourpin, S., Fourcade, S., Blais, S., 1992. Loss of (Nd, O) and chemical (REE) memory during metamorphism of komatiites: new evidence from Eastern Finland. Contributions to Mineralogy and Petrology, 112, 66–82.

Guitreau, M., Blichert-Toft, J., Martin, M., Mojzsis, S.J., Albarède, F., 2012. Hafnium isotope evidence from Archean granitic rocks for deep-mantle origin of continental crust. Earth and Planetary Science Letters, 337-338, 211-223.

Guitreau, M., Mukusa, S.B., Loudin, L., Krishnan, S., 2017. New constraints on early formation of western Dharwar craton (India) from igneous zircon U-Pb and Lu-Hf isotopes. Precambrian Research, 302: 33-49.

Guitreau, M., Boyet, M., Paquette, J. L., Gannoun, A., Konc, Z., Benbakkar, M., Suchorski, K., Hénot J. M., 2019. Hadean protocrust reworking at the origin of the Archean Napier Complex (Antarctica). Geochemical Perspectives Letters 12, 7-11.

Gupta, S., Rai, S.S., Prakasam, K.S., Srinagesh, D., Chadha, R.K., Priestley, P., Gaur, V.K., 2003. First evidence for anomalous thick crust beneath mid-Archean western Dharwar craton. Current Science, 84, 1219–1225.

Hamilton., 1998. Archean magmatism and deformation were not products of plate tectonics. Precambrian Res. 91, 143–179.

Hashizume K, Pinti D, Orberger B, Cloquet C, Jayananda M, Soyama H 2016. A biological switch at the ocean surface as a cause of laminations in a Precambrian iron formation. Earth Planet Sci Lett 446:27–36. https://doi.org/10.1016/j.epsl.2016.04.023Hastie, A.R., Fitton, J.G., 2019. Eoarchaean tectonics: New constraints from high pressure-temperature experiments and mass balance modelling. Precambrian Research 325, 20-38.

Herzberg, C., 1995. Generation of plume magmas through time - an experimental perspective: Chemical Geology, v.126, p. 1–16. doi:10.1016/0009-2541(95)00099-4

Herzberg C, Condie K, Korenaga J., 2010. Thermal history of the Earth and its petrological expression. Earth Planet Sci Lett 292 (1-2): 79–88

Hiess, J., Condon, D. J., McLean, N., Noble, S.R., 2012. U238/U235 Systematics in Terrestrial Uranium-Bearing Minerals. Science 335(6076):1610-4. DOI:10.1126/science.1215507

Hildebrand, R.S., Whalen, J.B., Bowring, S.A., 2018. Resolving the crustal composition paradox by 3.8 billion years of slab failure magmatism and collisional recycling of continental crust. Tectonophysics 734-735, 69-88.

Hoffmann, J. E., Münker, C, Polat, Ali & Rosing, Minik Schulz, Toni, 2011. The origin of decoupled Hf–Nd isotope composition in Eoarchean rocks from southern West Greenland. Geochimica et Cosmochimica Acta. 75. 6610-6628. Doi:10.1016 /j.g2011.08.018.

Hoffmann, J.E., Chao Z., Moyen, J-F., Nagel, T.J., 2019. The Formation of Tonalites-Trondhjemite-Granodiorites in Early Continental Crust. Chapter 7, 133-168, in Earth's Oldest Rocks. https://doi.org/10.1016/B978-0-444-63901-1.00007-1.

Hokada, T., Horie, K., Satish-Kumar, M., Ueno, Y., Nasheeth, A., Mishima, K., Shiraishi, K., 2013. An appraisal of Archaean supracrustal sequences in Chitradurga Schist Belt, western Dharwar Craton, southern India. Precambrian Res. 227, 99–119. http://dx.doi.org/10.1016/j.precamres.2012.04.006

Hussain S. M. and Naqvi S. M., 1983. Geological, geophysical and geochemical studies over the Holenarasipur schist belt, Dharwar craton, India. In Precambrian of South India. Memoir No. 4 (Editors Naqvi S. M. and Rogers J. J. W.) 73-95. Geological Society of India, Bangalore.

Hynes, A., 2014. How feasible was subduction in the Archean? Canadian Journal of Earth Sciences 51, 286-296.

Hyung, E., Jacobsen, S.B., 2020. The 142Nd/144Nd variations in mantle-derived rocks provide constraints on the stirring rate of the mantle from the Hadean to the present. Proceedings of the National Academy of Sciences of the United States of America 117, 14738-14744. https://doi.org/10.1073/pnas.2006950117.

Ickert, R. 2013. Algorithms for estimating uncertainties in initial radiogenic isotope ratios and model ages. Chemical Geology 340, 131–188.

Iizuka, T., Komiya, T., Johnson, S.P., Kon, Y., Maruyama, S., Hirata, T., 2009. Reworking of Hadean crust in the Acasta gneisses, North-western Canada: Evidence from in-situ Lu–Hf isotope analysis of zircon. Chemical Geology 259, 230-239.

Iizuka, T., Campbell, I., Allen, C.M., Gill, J., Maruyama, S., Makoka, F., 2013. Evolution of the African continental crust as recorded by U–Pb, Lu–Hf and O isotopes in detrital zircons from modern rivers. Geochimica et Cosmochimica Acta. 107. 96–120.

Iizuka T, Yamaguchi, A., Haba, M.K., Amelin, Y., Holden, P., Zink, S., Huyskens, M.H., Ireland, T.R., 2015. Timing of global crustal metamorphism on Vesta as revealed by high-precision U−Pb dating and trace element chemistry of eucrite zircon. Earth Planetary Science Letters, 409: 182–192

Jaffey, A.H., Flynn, K. F., Glendenin, L. E., Bentley, W. C., Essling, A. M., 1971. Precision measurement of half-lives and specific activities of 235U and 238U. Physics Reviews. C4, 1889.

Jafri, S.H., Khan, N., Ahmad, S.M., Saxena, R., 1983. Geology and geochemistry of Nuggihalli schist belt, Dharwar craton, Karnataka, India. Memoir 4, Geological Society of India, 111-120.

Jahn, B.-M., Gruau, G., Glikson, A.Y., 1982. Komatiites of the Onverwacht Group, S. Africa: REE geochemistry, Sm/Nd age and mantle evolution. Contrib. Mineral. Petrol. 80, 25–40.

Jahn, B., Glikson, A.Y., Peucat, J.-J., Hickman, A.H., 1981. REE geochemistry and isotopic data of Archean silicic volcanics and granitoids from the Pilbara block, Western Australia: implications for early crustal evolution. Geochimica et Cosmochimica Acta 45, 1633-1652.

Jahn, B. M., Litvinovsky, B. A., Zanvilevich, A. N., and Reichow, M., 2009, Peralkaline granitoid magmatism in the Mongolian-Transbaikalian Belt: Evolution, petrogenesis and tectonic significance: Lithos, v. 113, n. 3–4, p. 521–539, http://dx.doi.org/ 10.1016/ j.lithos. 2009.06.015.

Jayananda, M., Kano, T., Peucat, J.-J., Channabasappa, S., 2008. 3.35 Ga komatiite volcanism in the western Dharwar craton: constraints from Nd isotopes and whole rock geochemistry. Precambrian Research, 162,160–179. http://dx.doi.org/10.1016/j. precamres. 2007.07.010 Elsevier.

Jayananda, M., Tsutsumi, Y., Miyazaki, T., Gireesh, R.V., Kapfo, Kowe-u, Tushipokla, Hidaka, H., Kano, 2013a. Geochronological constraints on Meso-Neoarchean regional metamorphism and magmatism in the Dharwar craton, southern India. J. Asian Earth Sci. 78, 18–38. http://dx.doi.org/10.1016/j.jseaes. 2013.04.033.

Jayananda, M., Peucat, J.-J., Chardon, D., Krishna Rao, B., Corfu, F., 2013b. Neoarchean greenstone volcanism, Dharwar craton, Southern India: constraints from SIMS zircon geochronology and Nd isotopes. Precambrian Research, 227, 55-76. https:// doi.org/10.1016/ j.precamres.2012.05.002.

Jayananda, M., Chardon, D., Peucat, -J.-J., Fanning, C.M., 2015. Paleo- to Mesoarchean TTG formation and continental growth, western Dharwar craton, southern India: SHRIMP U-Pb zircon geochronology, whole-rock geochemistry, and Nd-Sr isotopes. Precambrian Research, 268, 295–322. http://dx.doi.org/10.1016/j.precamres.2015.07.015.

Jayananda, M., Duraiswami, R.A., Aadhiseshan, K.R., Gireesh, R.V., Prabhakar, B.C., Kafo, Kowe-u, Tushipokla, Namratha, R., 2016. Physical volcanology and geochemistry of Paleoarchean komatiite lava flows from the western Dharwar craton, southern India: implications for Archaean mantle evolution and crustal growth. International Geology Review, 58-13, 1569–1595.

Jayananda, M., Santosh M., Aadhiseshan, K. R., 2018. Formation of Archean continental crust in the Dharwar craton, Southern India. Earth Science Reviews, 181, 12-42.

Jayananda, M, Martin G, Tarun Thomas T, Martin H, Aadhiseshan KR, Gireesh RV, Peucat J-J, Satyanarayanan M., 2019a. Geochronology and geochemistry of Meso- to Neoarchean magmatic epidote-bearing potassic granites, Western Dharwar Craton (Bellur–Nagamangala–Pandavpura corridor), Southern India: implications for the successive stages of crustal reworking and cratonization. In: Dey S, Moyen J-F (eds) Archean granitoids of India: windows into early Earth tectonics. Geological Society, London, Special Publications, vol 489. Geological Society of London, London. https://doi.org/10.1144/SP489-2018-125.

Jayananda, M., Aadhiseshan, K.R., Monika, A.K., Wilde., S.A., Kowete-U, S., Guitreau, M., Santosh, M., Gireesh, R.V., 2020. Multi-stage crustal growth and Neoarchean geodynamics in the Eastern Dharwar Craton, southern India. Gondwana Research, 78, 228-260.

Jayananda, M., Chardon, D., Peucat, J.-J., Capdevila, R., 2006. 2.61 Ga potassic granites and crustal reworking in the western Dharwar craton, southern India: tectonic, geochronologic and geochemical constraints. Precambrian Research, 150, 1–26.

Jensen L.S., 1976. A new method of classifying alkali volcanic rocks: Ontario Division Mineral, Miscellaneous Paper, 66:22.

Jochum, K.P., Arndt, N.T., and Hofmann, A.W., 1991, Nb-Th-La in komatiites and basalts: Constraints on komatiite Petrogenesis and mantle evolution: Earth Planetary Science Letters, v. 107, p. 272–289. doi:10.1016/0012-821X (91)90076-T.

Johnson T.E., Brown M., Gardiner N.J., Kirkland C.L., Smithies, R.H., 2017. Earth's first stable continents did not form by subduction. Nature 2017 Mar 9; 543(7644): 239-242. doi: 10.1038/nature21383. E.pub 2017 Feb 27.

Johnson, T.E., Gardiner, N.J., Miljkovi´ C. K., Spencer, C.J., Kirkland, C.L., Bland, P.A., Smithies, H., 2018. An impact melt origin for Earth’s oldest known evolved rocks. Nature Geoscience, 11, 795–799.

Kaczmarek, M.A., Reddy, S.M., Nutman, A.P., Friend, C.R.L., Bennett, V.C., 2016. Earth’s oldest mantle fabrics indicate Eoarchean subduction. Nature communications 7: (10665). DOI: 10.1038/ncomms10665.

Kamo, S., and D. W. Davis, 1994. Reassessment of Archean crustal development in the Barberton Mountain Land, South Africa, based on U-Pb dating. Tectonics, 13, 167 – 192, doi:10.1029/93TC02254.

Kellogg, L. H., B. H. Hager, and R. D. van der Hilst, 1999. Compositional stratification in the deep mantle, Science, 283, 1881– 1884.

Kemp, A., Vervoot, J.D., Bjorkman, K., Iaccheri, L., 2017. Hafnium isotope characteristics of Paleoarchean zircon OG1/OGC from the Owens Gulley Diorite, Pilbara Craton, Western Australia. Geostandards Analyt. Res. 41, 659–673. https://doi.org/10.1111/ggr.12182.

Kendrick, J., Duguet, M., and Yakymchuk, C., 2021. Diversification of Archean tonalite-trondhjemite-granodiorite suites in a mushy middle crust: Geology 50 (1), 76-80. https://doi.org/10.1130/G49287.1.

Kerrich, R., and Xie, Q.,2002, Compositional recycling structure of an Archaean super-plume: Nb–Th–U–LREE systematics of Archaean Komatiites and basalts revisited: Contributions to Mineralogy and Petrology, v. 142, p. 476–484. doi:10.1007/s004100100301.

Kerrich R, Polat A, Wyman D and Hollings P 1999 Trace element systematics of Mg- to Fe-tholeiitic basalt. Suites of the Superior Province: Implications for Archean mantle reservoirs and greenstone belt genesis; Lithos 46, 163–187.

Komiya, T., Yamamoto, S., Aoki, S., Sawaki, Y., Ishikawa, A., Tashiro, T., Koshida, K., Shimojo, M., Aoki, K., Collerson, K.D., 2015. Geology of the Eoarchean, >3.95 Ga, Nulliak supracrustal rocks in the Saglek Block, northern Labrador, Canada: The oldest geological evidence for plate tectonics, Tectonophysics, 662, 40-62.

Korenaga J., 2013. Initiation and evolution of plate tectonics on Earth: theories and observations. Annual Review of Earth and Planetary Sciences, 41:117–151.

Korenaga, J., 2021. Hadean geodynamics and the nature of early continental crust. Precambrian Research 359, 106178. https://doi.org/10.1016/j.precamres.2021.106178.

Kröner, A., Hegner, E., Wendt, J.I., Byerly, G.R., 1996. The oldest part of the Barberton granitoid-greenstone terrain, South Africa: evidence for crust formation between 3.5 to 3.7 Ga. Precambrian Research, 78, 125-138.

Kröner, A., Hoffmann, J.E., Xie, H., Münker, C., Hegner, E., Hofmann, A., Wang, Y., 2014. Generation of early Archean grey gneisses through crustal recycling in the Eastern Kaapvaal craton, southern Africa. Precambrian Research, 255, 833-846.

Kunugiza, K., Kato, Y., Kano, T., Takaba, Y., Kuruma, I., Sohma, T., 1996. An Archean tectonic model of the Dharwar craton, southern India: the origin of the Holenarasipur greenstone belt (Hassan district, Karnataka) and reinterpretation of the Sargur-Dharwar relationship. Journal of Southeast Asian Earth Sciences 14 (3-4), 149-160.

Kusky, T.M., Kidd, W.F., 1992. Remnants of an Archean oceanic plateau, Belingwe greenstone belt, Zimbabwe. Geology 20, 43-46.

Kusky, T., Polat, A., 1999. Growth of Granite-Greenstone terranes at convergent margins, and stabilization of Archean cratons. Tectonophysics 305, 43-73.

Kusky, T. M., Windley, B. F., Polat, A., 2018. Geological evidence for the operation of plate tectonics throughout the Archean: Records from Archean paleo-plate boundaries. Journal of Earth Science 29, 1291-1303.

Kusky, T., Windley, B.F., Polat, A., Wang, L., Ning, W., Zhong, Y., 2021. Archean dome- and basin style structures form during growth and death of intraoceanic and continental margin arcs in accretionary orogens. Earth-Science Reviews 220, 103725.

Kusky, T.M., Windley, B.F., Safonova, I., Wakita, K., Wakabayashi, J., Polat, A., Santosh, M., 2013. Recognition of plate stratigraphy in accretionary orogens through Earth history: A record of 3.8 billion years of sea floor spreading, subduction, and accretion. Gondwana Research 24, 501-547.

Lahaye, X., Arndt, N.T., Byerly, G., Chauvel, C., Fourcade, S., Gruau, G., 1995. The influence of alteration on the trace-element and Nd isotopic compositions of Komatiites. Chem. Geol. 126, 43–64

Lancaster P.J, Dey S, Storey CD, Mitra AM, Bhunia R.K 2015. Contrasting crustal evolution processes in the Dharwar Craton: insights from detrital zircon U–Pb and Hf isotopes. Gondwana Research, 28: 1361–1372. https://doi.org/10.1016/j.gr.2014.10.010.

Laurent, O., Martin, H., Moyen, J.-F., Doucelance, R., 2014. The diversity and evolution of late-Archean granitoids: evidence for the onset of "modern-style" plate tectonics between 3.0 and 2.5 Ga. Lithos, 205, 208–235.

Laurent, O., Björnsen, J., Wotzlaw, J-F., Bretscher, S., Silva, M. P., Moyen, J-F., Ulmer, P., Bachmann, O., 2020. Earth's earliest granitoids are crystal-rich magma reservoirs tapped by silicic eruptions. Nature geoscience, 13, 163-169.

Lee, J., Hacker, B.R., Dinklage, W.S., Wang, Y., Gans, P., Calvert, A., Wan, J.L., Chen, W., Blythe, A.E., McClelland, W., 2000. Evolution of the Kangmar Dome, southern Tibet: Structural, petrologic, and thermochronologic constraints. Tectonics 19, 872-895.

LeRoux, L. J. and Glendenin, L. E., 1963. Half-life of thorium-232. Proc. National Conference on Nuclear Energy, 83-94.

Ludwig, K. R., 2008. User's manual for Isoplot 3.6: A geochronological toolkit for Microsoft Excel (Spec. Pub. 4). Berkeley, CA: Berkeley Geochronology Centre.

Martin H, Peucat J-J, Sabaté P, Cunha J.C., 1997. Crustal evolution in the early Archaean of South America: example of the Sete Voltas Massif, Bahia State, Brazil. Precambrian Research, 82, 35–62.

Martin, H., Moyen, J.-F., Guitreau, M., Blichert-Toft, J., Le Pennec, J.-L., 2014. Why Archean TTG cannot be generated by MORB melting in subduction zone. Lithos 198-199, 1-13.

Martin, H., 1986. Effect of steeper Archean geothermal gradient on geochemistry of subduction zone magmas. Geology, 14, 753–756.

Martin, H., 1994. The Archaean grey gneisses and genesis of continental crust. In: Condie, K.C. (Ed.), Archaean Crustal Evolution, Developments in Precambrian Geology. vol. 11. Elsevier, pp. 205–259.

Martin, H., Smithies, R.H., Rapp, R., Moyen, J.F., Champion, D., 2005. An overview of adakite, tonalite-trondhjemite-granodiorite (TTG), and sanukitoid: relationships and some implications for crustal evolution. Lithos 79, 1–24.

Maya, J.M., Bhutani, R., Balakrishnan, S., Rajee Sandhya, S., 2017. Petrogenesis of 3.15 Ga old Banasandra komatiites from the Dharwar craton, India: implications for early mantle heterogeneity. Geoscience Frontiers, 8, 467-481

Mc Kenzie, D. 2020. Speculations on the generation and movement of komatiites. Journal of Petrology, 61, doi:10.1093/petrology/egaa061.

Meen J.K, Rogers J.J, Fullagar P.D., 1992. Lead isotopic composition of the Western Dharwar Craton, Southern India: evidence for distinct middle Archaean terrenes in a late Archaean Craton. Geochimica et Cosmochimica Acta, 56:2455–2470.

Miocevich, S.R., Copley, A., Weller, OM., 2022. Testing the importance of Sagduction: Insights from Lewisian Gneiss Complex of northwest Scotland. Precambrian Research, 379, 106708. https://doi.org/10.1016/j.precamres.2022.106708.

Miyazaki, T., Hanyu, T., Kimura, J. I., Senda, R., Vaglarov, B. S., Chang, Q., Hirahara, Y., Takahashi, T., & Kawabata, H. 2018. Clinopyroxene and bulk rock Sr‑Nd‑Hf‑Pb isotope compositions of Raivavae Ocean Island basalts: Does clinopyroxene record early-stage magma chamber processes? Chemical Geology, 482, 18‑ 31.

Mole, D.R., Fiorentini, M.L., Thebaud, N., Cassidy, K.F., McCuig, T., Kirkland, C.L., Romono, S.S., Doublier, M.P., Belusova, E.L., Barnes, S.J., and Miller, J.,2015, Archean komatiite volcanism controlled by evolution of early continents: Proceedings of the National Academy of Sciences, doi:10.1073/pnas.1400273111.

Monrad, J.R., 1983. Evolution of sialic terranes in the vicinity of the Holenarasipur belt Hassan District, Karnataka, India. In: Naqvi, S.M., Rogers, J.J.W. (Eds.), Precambrian of South India. Geological Society of India Memoir No. 4, pp. 343–364.

Monteux, J., Andrault, D., Guitreau, M., Samuel, H., Demouchy, S., 2020. A mushy Earth's mantle for more than 500 Myr after the magma ocean solidification. Geophysical Journal International, 221, 1165–1181.

Moyen J-F, Laurent O., 2018. Archaean tectonic systems: a view from igneous rocks. Lithos, 302-303:99–125.

Moyen, J.-F., Martin, H., 2012. Forty years of TTG research. Lithos, 148, 312-336.

Moyen, J.-F., 2009. High Sr/Y and La/Yb ratios: the meaning of the "adakitic signature". Lithos, 112, 556–574

Moyen, J.-F., 2011. The composite Archean grey gneisses: petrological significance, and evidence for a non-unique tectonic setting for Archean crustal growth. Lithos, 124, 21-36.

Mukherjee R., Mondal S K., Frei R, Rosing M T., Waight T. E., Zhong H and Kumar G R., 2012 The 3.1 Ga Nuggihalli chromite deposits, Western Dharwar craton (India): Geochemical and isotopic constraints on mantle sources, crustal evolution and implications for supercontinent formation and ore mineralization; Lithos, 155392–409.

Mukhopadhyay J, Beukes N.J, Armstrong R.A, Zimmermann, U, Ghosh G, Medda R.A 2008. Dating the oldest greenstone in India: a 3.51-Ga precise U-Pb SHRIMP zircon age for dacitic lava of the Southern iron ore group, Singhbhum Craton. Journal of Geology, 116, 449–461.

Nagel, T.J., Hoffmann, J.E., Münker, C., 2012. Melting of Eoarchean tonalite-trondhjemite-granodiorite suite from thickened mafic arc crust. Geology, 40, 375-378.

Nair, R., Chacko, T., 2008. Role of oceanic plateaus in the initiation of subduction and origin of continental crust. Geology, 36 (7), 583-586.

Naqvi, S.M., 1981. The oldest supracrustals of the Dharwar Craton, India. Journal of the Geological Society of India, 22 (10), 458–469.

Naqvi, S.M., 1985. Chitradurga schist belt; an Archaean suture (?). Journal of the Geological Society of India, 26, 511–525.

Naqvi, S. M., & Rogers, J. J. W., 1987. Precambrian geology of India. Oxford Monographs on Geology and Geophysics, 6, 223.

Naqvi, S.M., Divakara Rao, V., Hussain, S.M., Narayana, B.L., Nirmal Charan, S., Govil, P.K., Bhaskar Rao, Y.J., Jafri, S.H., Rama Rao, P., Balaram, V., Ahmad Masood., Pantulu, K.P., Gnaneswar Rao, T., and Subba Rao, D.V., 1983. Geochemistry of gneisses from Hasan district and adjoining areas, Karnataka, India, Memoir Geological Society of India,v. 4, pp. 401-413.

Naqvi, S.M., Ram Mohan, M., Rana Prathap, J.G., Srinivasa Sarma, D., 2009. Adakite–TTG connection and fate of Mesoarchean basaltic crust of Holenarsipur nucleus, Dharwar Craton, India. Journal of Asian Earth Sciences, 35, 416–434.

Nebel, O., Capitanio, F.A., Moyen, J.F., Weinberg, R.F., Clos, F., Nebel-Jacobsen, Y.J., Cawood, P.A., 2018. When crust comes of age: on the chemical evolution of Archaean, felsic continental crust by crustal drip tectonics. Philosophical Transactions of the Royal Society A: Mathematical, Physical and Engineering Sciences, 376, 20180103.

Nédélec, A., Chevrel, M.O., Moyen, J.F., Ganne, J., Fabre, S., 2012. TTGs in the making: Natural evidence from Inyoni shear zone (Barberton, South Africa), Lithos, doi:10.1016/ j.lithos.2012.05.029.

Nelson, D.R., Trendall, A.F., Altermann, W., 1999. Chronological correlations between the Pilbara and Kaapvaal cratons. Precambrian Research, 97, 165-189.

Nelson, D.R., Bhattacharya, H.N., Thern, E.R., Altermann, W., 2014. Geochemical and Ion microprobe U–Pb zircon constraints on the Archaean evolution of Singhbhum Craton, Eastern India. Precambrian Research, http://dx.doi.org/10.1016/j. precamres.2014.09.024.

Nicoli, G., 2020. Water budget and partial melting in an Archean crustal column: example from the Dharwar Craton, India. Geological Society, London, Special Publications, 489, 115-133.

Nutman AP, Cordani U.G., 1993. SHRIMP U–Pb zircon geochronology of Archaean granitoids from the Contendas-Mirante area of the São Francisco craton, Bahia, Brazil. Precambrian Research, 63: 179–188.

Nutman, A.P., Chadwick, B., Ramakrishnan, M., Viswanatha, M., 1992. SHRIMP U–Pb ages of detrital zircon in Sargur supracrustal rocks in western Karnataka, southern India. Journal of the Geological Society of India, 39, 367–374.

Nutman A.P, Chadwick B, Krishna Rao B, Vasudev VN 1996. SHRIMP U/Pb zircon ages of acid volcanic rocks in the Chitradurga and Sandur Groups, and granites adjacentto the Sandur Schist belt, Karnataka. Journal of the Geological Society of India, 47:153–164.

Nutman, A.P., McGregor, V.R., Friend, C.R.L., Bennett, V.C., Kinny, P.D., 1996. The Itsaq Gneiss Complex of southern West Greenland; the world's most extensive record of early crustal evolution (3,900–3,600 Ma). Precambrian Research, 78, 1–39

Nutman, A.P., Bennett, V.C., Friend, C.R.L., Yi, K., 2020. Eoarchean contrasting ultra-high pressure to low-pressure metamorphisms (< 250 to > 1000^{o}C/GPa) explained by tectonic plate convergence in deep time. Precambrian Research, 344, 105770.

Nutman, A.P., Bennett, V.C., Friend, C.R.L., Polat, A., Hoffmann, E., Van Kranendonk, M., 2021. Fifty years of the Eoarchean and the case for evolving uniformitarianism. Precambrian

Research 367, 106442. https://doi.org/10.1016/j.precamres.2021.106442.
O'Connor, J.T., 1965. A classification for quartz-rich igneous rocks based on feldsparratios. In: U.S. Geological Survey Professional Paper 525 (B). pp. 79–84.

Ordóñez-Calderón, J.C., Polat, A., Fryer, B., J.E. Gagnon, J.E., Raith, J.G., Appel, P.W.U., 2008. Evidence for HFSE and REE mobility during calc-silicate metasomatism, Mesoarchean (~3075 Ma) Ivisaartoq greenstone belt, southern West Greenland. Precambrian Research 161, 317-340.

Paces, J. B., Miller, J. D. Jr. 1993. Precise U-Pb ages of Duluth complex and related mafic intrusions, North-eastern Minnesota: Geochronological insights to physical, petrogenetic, paleomagnetic, and tectonomagmatic processes associated with the 1.1 Ga midcontinent rift system. Journal of Geophysical Research, 98(B8), 13997–14013. https://doi.org/ 10.1029/ 93JB01159.

Panicker, A.G., Mohan, M.R., Upadhyay, D., Raju, B.V., Chauhan, H., Chalapathi Rao, N.V., 2021. U-Pb zircon age, geochemistry and petrogenesis of Mesoarchean anorthositic rocks from the Holenarsipur Greenstone Belt, Western Dharwar Craton: Implications for accretionary tectonics in southern India. Lithos, 398-399. https://doi.org/10.1016/j.lithos.2021.106268

Paquette, J.L, Barbosa J.S. F., Rohais, S., Cruz S.C.P., Goncalves, P., Peucat J-J, Leal A.B., M, Santos-Pinto, M., Martin, H., 2015. The geological roots of South America: 4.1 Ga and 3.7 Ga zircon crystals discovered in N.E. Brazil and N.W. Argentina. Precambrian Research, 271: 49–55.

Parman, S.W., Dann, J.C., Grove, T.L., and De Wit, M.J., 1997. Emplacement conditions of komatiite magmas from the 3.49 Ga Komati formation, Barberton Greenstone Belt,South Africa: Earth and Planetary Science Letters, v. 150, p. 303–323. doi:10.1016/S0012-821X(97)00104-0

Patra, K., Anand, R., Balakrishnan, S., Dash, J.K., 2020. Geochemistry of ultramafic–mafic rocks of Mesoarchean Sargur Group, western Dharwar craton, India: Implications for their petrogenesis and tectonic setting. Journal of Earth System Science, 129:26. https://doi.org/10.1007/s12040-019-1269-4

Pearce, J.A., 2008. Geochemical fingerprinting of oceanic basalts with applications to ophiolite classification and the search for Archean oceanic crust. Lithos, 100, 14–48.

Peterson, A., Kemp, A.I.S., Hickman, A.H., Whitehouse, M.J., Martin, L., Gray, C.M., 2019. A new 3.59 Ga magmatic suite and a chondritic source to the east Pilbara Craton. Chemical Geology, 511, 51-70.

Peucat, J.-J., Mahabaleswar, M., Jayananda, M., 1993. Age of younger tonalitic magmatism and granulite metamorphism in the amphibolite–granulite transition zone of southern India (Krishnagiri area): comparison with older peninsular gneisses of Gorur- Hassan area. Journal of Metamorphic Geology, 11, 879–888.

Peucat, J.-J., Bouhallier, H., Fanning, C.M., Jayananda, M., 1995. Age of Holenarsipur schist belt, relationships with the surrounding gneisses (Karnataka, south India). Journal of Geology, 103, 701–710.

Peucat, J-J., Mascarenhas, J.F., Barbosa, J.S.F., de Souza, S.L., Marinho, M.M., Fanning, C.M., Leite, C.M.M., 2002. 3.3Ga SHRIMP U-Pb zircon age of a felsic metavolcanic rock from the Mundo Novo greenstone belt in the Sao Francisco craton, Bahia (NE Brazil). Journal of South American Earth Sciences 15, 363–373.

Peucat, -J.-J., Jayananda, M., Chardon, D., Capdevila, R., Mark Fanning, C., and Paquette, J.-L., 2013. The lower crust of the Dharwar Craton, Southern India: Patchwork of Archean granulitic domains: Precambrian Research, 227, 4–28. doi:10.1016/j.precamres.2012.06.009.

Polat, A., Kerrich, R., 2000. Archaean greenstone belt magmatism and the continental growth-mantle evolution connection: constraints from Th–U–Nb–LREE systematics of the 2.7 Ga Wawa subprovince, Superior province, Canada. Earth Planet. Sci. Lett. 175, 41–54.

Polat, A., Regelous, M., Hofmann, A.W., Appel, P.W.U., 2000. Contrasting geochemistry in the 3.7 – 3.8 Ga pillow basalt rims and cores, Isua greenstone belt, Greenland: implications for early Archean sea-floor alteration processes. AGU, EOS Trans. 81, F1256.

Polat, A., Frei, R., Appel, P.W.U., Dilek, Y., Fryer, B., Ordóñez-Calderón, J.C., Yang, Z., 2008. The origin and compositions of Mesoarchean oceanic crust: Evidence from the 3075 Ma Ivisaartoq greenstone belt, SW Greenland. Lithos 100, 293-321.

Polat, A., Hofmann, A.W., 2003. Alteration and geochemical patterns in the 3.7-3.8 Ga Isua greenstone belt, West Greenland. Precambrian Research 126, 197-218.

Polat, A., Hofmann, A.W., Rosing, M., 2002. Boninite-like volcanic rocks in the 3.7 - 3.8 Ga Isua greenstone belt, West Greenland: Geochemical evidence for intra-oceanic subduction zone processes in the early Earth. Chemical Geology 184, 231-254.

Polat, A., Kerrich, R., Wyman, D.A., 1998. The late Archean Schreiber-Hemlo and White River-Dayohessarah greenstone belts, Superior Province: Collages of oceanic plateaus, Oceanic island arcs, and subduction-accretion complexes. Tectonophysics 289, 295-326.

Polat, A., Kerrich, R., Wyman, D.A., 1999. Geochemical diversity in oceanic komatiites and basalts from the late Archean Wawa greenstone belts, Superior Province, Canada: trace element and Nd Isotope evidence for a heterogeneous mantle. Precambrian Research 94, 139-173.

Polat, A., Li, J., Fryer, B., Kusky, T., Gagnon, J., Zhang, S., 2006. Geochemical characteristics of the Neoarchean (2800-2700 Ma) Taishan Greenstone Belt, North China Craton: Evidence for plume-craton interaction. Chemical Geology 230, 60-87.

Polat, A., Hofmann, A.W., and Rosing, M. 2002. Boninite-like volcanic rocks in the 3.7–3.8 Ga Isua greenstone belt, West Greenland: Geochemical evidence for intra-oceanic subduction zone processes in the early Earth. Chemical Geology,184: 231–254. doi:10.1016/S0009-2541(01)00363-1.

Polat, A., Wang, L., and Appel, P.W.U. 2015. A review of structural patterns and melting processes in the Archean craton of West Greenland: Evidence for crustal growth at convergent plate margins as opposed to nonuniformitarian models. Tectonophysics, 662: 67–94. doi:10.1016/j.tecto.2015.04.006.

Puchtel, I.S., Haase, K.M., Hofmann, A.W., Chauvel, C., Kulikov, V.S., Garbe- Schönberg, C.D., Nemhin, A.A., 1997. Petrology and geochemistry of crustally contaminated komatiitic basalts from the Vetreny Belt, southeastern Baltic Shield: Evidence for an early Proterozoic mantle plume beneath rifted Archean continental lithosphere. Geochimica et Cosmochimica Acta 61, 1205 1222.

Puchtel I.S, Hofmann AW, Mezger K, Jochum KP, Shchipansky AA, Samsonov AV.,1998. Oceanic plateau model for continental crustal growth in the Archaean: a case study from the Kostomuksha greenstone belt, NW Baltic Shield. Earth and Planetary Science Letters, 155:57–74

Raase, P., Raith, M., Ackermand, D., Lal, R.K., 1986. Progressive metamorphism of mafic rocks from greenschist to granulite facies in the Dharwar craton of South India. Journal of Geology, 94, 261–282.

Radhakrishna, B.P., 1983. Archean granite-greenstone terrain of the South Indian shield. In Geological Society of India Memoir No. 4 (Eds. S.M. Naqvi and J.J.W Rogers), 1-47.

Radhakrishna, B.P., Naqvi, S.M., 1986. Precambrian continental crust of India and its evolution. Journal of Geology, 94, 145–166.

Radhakrishna, B.P., Sreenivasaiah, G., 1974. Bedded baryte from the Precambrian of Karnataka. Journal of the Geological Society of India, 15, 314–315.

Ramakrishnan, M., Viswanatha, M.N., 1981. Holenarsipur Belt. In: Swami Nath, J., Ramakrishnan, M. (Eds.), Early Precambrian supracrustals of southern Karnataka. Geological Survey of India Memoir, 112, 115–142.

Ramakrishnan, M., Venkata Dasu, S.P., Kroner, A., 1994. Middle Archaean age of Sargur Group by single grain zircon dating and geochemical evidence for the clastic origin of metaquartzite from J.C. Pura Greenstone belt, Karnataka. Journal of the Geological Society of India, 44, 605–616.

Ranjan, S., Upadhyay, D., Abhinay, K., Srikantappa, C., 2020. Paleoarchean and Neoarchean Tonalite-Trondhjemite-Granodiorite (TTG) and granite magmatism in the Western Dharwar Craton, southern India: implications for Archean continental growth and geodynamics. Precambrian Research, 105630. https://doi.org/10.1016/j.precamres.2020.105630 .

Ranjan, S., Upadhyay, D., and Srikantappa, C., 2022. Eoarchean to Neoarchean crustal evolution of the Western Dharwar Craton, southern India: Clues from U-Pb-Hf isotope composition of detrital zircon. Precambrian Research 371, 106559. https://doi.org/10.1016/j.precamres.2022.106559.

Rapp, R.P., Watson, E.B., 1995. Dehydration melting of metabasalts at 8–32 kbar: implications for continental growth and crust-mantle recycling. Journal of Petrology, 36, 891–931.

Ravindran, A., Mezger, K., Balakrishnan, Berndt, J., 2021. Hf-Nd isotopes from ultramafic and mafic rocks in the western Dharwar Craton, India, record early Archean mantle heterogeneity. Lithos, 404-405, (106491). https://doi.org/10.1016/j.lithos.2021.106491

Ravindran, A., Mezger, K., Balakrishnan, S., Kooijman, E., Schmitt, M., Berndt, J., 2020. Initial $^{87}Sr/^{86}Sr$ as a sensitive tracer of Archaean crust-mantle evolution: Constraints from igneous and sedimentary rocks in the western Dharwar. Precambrian Research, 337, 105523.

Rey, P.F., Coltice, N., 2008. Neoarchean lithospheric strengthening and the coupling of Earth's geochemical reservoirs. Geology, 36, 635-638.

Rey, P.F., Philippot, P., Thébaud, N., 2003. Contribution of mantle plumes, crustal thickening and greenstone blanketing to the 2.75–2.65 Ga global crisis. Precambrian

Res. 127, 43–60.

Rey, P.F., Coltice, N., Flament, N. (2014). Spreading continents kick-started plate tectonics. Nature 513, 405-408.

Roberts, N. M. W., Santosh, M. 2018. Capturing the Mesoarchean emergence of continental crust in the Coorg Block, southern India. Geophysical Research Letters, 45. https://doi.org/10.1029/2018GL078114.

Roberts, N.M.,Tikoff., B., 2021. Internal structure of the Paleoarchean Mt. Edgar dome, Pilbara Craton, Western Australia. Precambrian Research, 358, https://doi.org/10.1016/j.precamres.2021.106163.

Rogers, J.J.W., Callahan, E.J., Dennen, K.O., Fullagar, P.D., Stroh, P.T., Wood, L.F. 1986. Chemical evolution of Peninsular gneiss in the Western Dharwar craton, Southern India. Journal of Geology, 94, 233-246.

Rozel, A. B., Golabek, G. J., Jain, C., Tackley, P. J., Gerya, T., 2017. Continental crust formation on early Earth controlled by intrusive magmatism. Nature, 545(7654), 332–335. https://doi.org/10.1038/nature22042.

Roman, A., Arndt, N., 2020. Differentiated Archean oceanic crust: its thermal structure, mechanical stability and a test of the sagduction hypothesis. Geochimica et Cosmochimica Acta 278, 65-77.

Sebastian, S., Bhutani, R., Balakrishnan, S., Tomson, J. K., & Shukla, A. D. 2021. Geochemical and isotopic studies of potassic granite from the western Dharwar Craton, southern India: Implications for crustal reworking in the Neoarchean. Geological Journal, 56(6), 2930–2949. doi:10.1002/gj.4085.

Saha, L., Hoffmann, A., Xie, H., Hegner, E., Wilson, A., Wan, Y., Liu, D., Kroner, A., 2010. Zircon ages and metamorphic evolution of Archaean Assegaai-De Kraalen granitoid greenstone terrain, Southeast Kaapvaal Craton. American Journal of Science, 310, 1384-1320

Santosh, M., Yang, Q.-Y., Shaji, E., Tsunogae, T., Ram Mohan, M., Satyanarayanan, M., 2015. An exotic Mesoarchean microcontinent: the Coorg Block, southern India. Gondwana Research, 27, 165–195.

Santos-Pinto M, Peucat J-J, Martin H, Barbosa J.S. F, Fanning C.M, Cocherie, A., Paquette J. L. 2012.Crustal evolution between 2.0 and 3.5 Ga in the southern Gavião block (Umburanas-Brumado-Aracatu region) São Francisco Craton, Brazil. A 3.5–3.8 Ga proto-crust in the Gavião block?. Journal of South American Earth Sciences, 40: 129-142.

Saunders, A.D., Norry, M.J., Tarney, J., 1988. Origin of MORB and chemically depleted mantle reservoirs: trace element constraints. Journal of Petrology, Spec. 415–455.

Scherer, E., Münker, C., Mezger, K., 2001. Calibration of the lutetium–hafnium clock. Science, 293, 683–687.

Schoene, B., de Wit, M.J., Bowring, S. 2008. Mesoarchean assembly and stabilization of the Eastern Kaapvaal craton: A structural-thermochronological perspective. Tectonics, 27, TC5010. 1-27. doi:10.1029/2008TC002267, 2008.

Slama, J., Kosler, J., Condon, D. J., Crowley, J. L., Gerdes, A., Hanchar, J. M., 2008. Plesovice zircon: A new natural reference material for U-Pb and Hf isotopic microanalysis. Chemical Geology, 249 (1–2), 1-35.

Smithies, R.H., Champion, D.C., Van Kranendonk, M.J., 2009. Formation of Paleoarchean continental crust through infracrustal melting of enriched basalt. Earth and Planetary Science Letters, 281 (3-4), 298-306.

Smithies, R.H., Lu, Y., Johnson, T.E., Kirkland, C.H., Cassidy., K.F., Champion, D.C., Mole, D.R., Zibra, I., Gessner, K., Sapkota., J., De Paoli, M.C., Poujol., M., 2019. No evidence for high pressure melting of Earth's crust in the Archean. Nature Communications (2019)10. 5559.https://doi.org/10.1038/s41467-019-13547.x.

Sobolev, A. V., Asafov, E. V., Gurenko, A. A., Arndt, N. T., Batanova, V. G., Portnyagin, M. V., Garbe-Scho¨ nberg, D. & Krasheninnikov, S. P., 2016. Komatiites reveal a hydrous Archaean deep-mantle reservoir. Nature 531, 628-632.

Sobolev, A.V, Asafov, E.V., Gurenko, A.A., Arndt, N. A, Batanova, V.G., Portnyagin, M.V., Garbe-Schönberg, D., Wilson, A.H., Byerly, G.R., 2019. Deep hydrous mantle reservoir provides evidence for crustal recycling before 3.3 billion years ago. Nature, 571, 555-558.

Söderlund, U., Patchett, J.P., Vervoort, J.D., Isachsen, C.E., 2004. The ^{176}Lu decay constant determined by Lu–Hf and U–Pb isotope systematics of Precambrian mafic intrusions. Earth and Planetary Science Letters 219, 311–324.

Sossi P A, Eggins S M, Nesbitt R W, Nebel O, Hergt J M, Campbell I H, O'Neill H St C, Van Kranendonk M and Rhodri Davies D., 2016. Petrogenesis and geochemistry of Komatiites; Journal of Petrology, 57, 147–184.

Sotiriou, P., Polat, A., 2020. Comparisons between Tethyan Anorthosite-bearing Ophiolites and Archean Anorthosite-bearing Layered Intrusions: Implications for Archean Geodynamic Processes. Tectonics 39, e2020TC006096. https://doi.org/ 10.1029/2020TC006096.

Sotiriou, P., Polat, A., Windley, B.F., Kusky, T., 2022. Temporal variations in the incompatible trace element systematics of Archean volcanic rocks: Implications for tectonic processes in the early Earth. Precambrian Research 368, 106487. https://doi.org/10.1016/j.precamres.2021.106487.

Srikantia, S.V., Venkataramana, P., 1989. The Archaean komatiites of Nagamangala supracrustal belt, Karnataka. Journal of the Geological Society of India, 33, 210–214.

Srikantia, S.V., Bose, S. S., 1985. Archaean Komatiites from Banasandra Area of Kibbanahalli Arm of Chitradurga Supracrustal Belt in Karnataka. Journal Geological Society of India, 26, 407-417.

Storey, M., Mahoney, J.J., Kroenke, L.W., Saunders, A.D., 1991. Are oceanic plateaus sites of komatiite formation? Geology 19, 376-379.

Subba Rao, D.V., Naqvi, S.M., 1999. Archaean Komatiites from the older schist belt of Kalyadi in Western Dharwar Craton, Karnataka. Journal of Geological Society of India, 53, 347–354.

Stevenson, R.K., Patchett, P.J., 1990. Implications for the evolution of continental crust from Hf isotope systematics of Archean detrital zircons. Geochimica et Cosmochimica Acta, 54, 1683-1697.

Sun, S.-S., McDonough, W.F., 1989. Chemical and isotopic systematics of oceanic basalts: implications for mantle composition and processes. In: Saunders, A.D., Norry, M.J. (Eds.), Magmatism in the Ocean Basins. Geological Society of London, pp. 313-345. https://doi.org/10.1144/GSL.SP.1989.042.01.19. Special Publication 42.

Swami Nath, J., Ramakrishnan, M., 1981. Early Precambrian supracrustals of Southern Karnataka. Memoirs of the Geological Survey of India Memoir 112, 308p.

Swami Nath, J., Ramakrishnan, M., Viswanatha, M.N., 1976. Dharwar stratigraphic model and Karnataka craton evolution. Records of Geological Survey of India Memoir 107, 149–175.

Tanaka, T., Togashi, S., Kamioka, H., Amakawa, H., Kagami, H., Hamamoto, T., Yuhara, M., Orihashi, Y., Yoneda, S., Shimizu, H., Kunimaru, T., Takahashi, K., Yanagi, T., Nakano, T., Fujimaki, H., Shinjo, R., Asahara, Y., Tanimizu, M., Dragusanu, C., 2000. JNdi-1: a neodymium isotopic reference in consistency with LaJolla neodymium. Chemical Geology, 168, 279–281.

Taylor, P.N., Chadwick, B., Moorbath, S., Ramakrishnan, M., Viswanatha, M.N., 1984. Petrography, chemistry and isotopic ages of Peninsular Gneiss, Dharwar acid volcanic rocks and the Chitradurga granite with special reference to the late Archean evolution of the Karnataka Craton. Precambrian Research, 23:349–375.

Taylor, S.R., and McLennan, S.M., 1988. The significance of the rare earths in geochemistry and cosmochemistry. *In*: Two-hundred-year impact of rare earths on science. Gschneidner-Karl-A Jr. and Eyring-LeRoy (Eds.), Handbook Phys. Chem. Rare Earths. 11, 485-570.

Teixeira, W., Oliveira, E.P., Marques, L.S., 2017. Nature and Evolution of the Archean Crust of the São Francisco Craton. In M. Heilbron et al. (eds.), São Francisco Craton, Eastern Brazil, Regional Geology Reviews, 29-57. DOI 10.1007/978-3-319-01715-0_3. © Springer International Publishing Switzerland.

Thorpe, R.A., Hickman, A.H., Davis, D.W., Mortensen, J.K., Trendall, A.F., 1992. U–Pb zircon geochronology of Archean felsic units in the Marble Bar region, Pilbara Craton, Western Australia. Precambrian Research, 56, 169–189.

Turner, S., Wilde, S., Wörner, G., Schaefer, B., Lai, Y.J., 2020. An andesitic source for Jack Hills zircon supports onset of plate tectonics in the Hadean. Nature Communications 11:1241.

Tushipokla, Jayananda, M., 2013. Geochemical constraints on komatiite volcanism from Sargur Group Nagamangala greenstone belt, western Dharwar craton, southern India: implications for Mesoarchean mantle evolution and continental growth. Geoscience Frontiers, 4, 321–340

Upadhyay D, Chattopadhyay S, Kooijman E, Mezger K, Berndt J., 2014. Magmatic and metamorphic history of Paleoarchean tonalite-trondhjemite-granodiorite (TTG) suites from the Singhbhum Craton, Eastern India. Precambrian Research, 252:180–190.

Van de Löcht, J., Hoffmann, J.E., Rosing, M.T., Sprung, P., Münker, C., 2020. Preservation of Eoarchean mantle processes in ~3.8 Ga peridotite enclaves in the Itsaq Gneiss Complex, southern West Greenland. Geochimica et Cosmochimica Acta 280, 1-25.

Van Hunen, J., Moyen, J.-F., 2012. Archean subduction: fact or fiction? Annual Review of Earth and Planetary Sciences, 40, 195-219.

Van Kranendonk, M.J., Smithies, R.H., Griffin, W.L., Huston, D.L., Hickman, A.H., Champion, D.C., Anhaeusser, C.R., Pirajno, F., 2015. Making it thick: a volcanic plateau model for Paleoarchean continental lithosphere of the Pilbara and Kaapvaal cratons. In: Roberts, N.M.W., Van Kranendonk, M., Parman, S., Shirey, S., Clift, P.D. (Eds.), Continent Formation through Time. Geological Society of London, Special Publications 389, 83-112.

Van Kranendonk, M.J., Smithies, R.H., Hickman, A.H., Champion, D.C., 2007a. Paleoarchean development of a continental nucleus: the East Pilbara Terrane of the Pilbara Craton, Western Australia. In: Van Kranendonk, M.J., Smithies, R.H., Bennett, V.C. (Eds.), Earth's Oldest Rocks – Developments in Precambrian Geology 15. Elsevier, Amsterdam, pp. 307–335.

Van Kranendonk, M.J., Smithies, R.H., Hickman, A.H., Champion, D.C., 2007b. Secular tectonic evolution of Archaean continental crust: interplay between horizontal and vertical processes in the formation of the Pilbara Craton, Australia. Terra Nova, 19, 1–38.

Van Kranendonk, M.J., Smithies, R.H., Hickman, A.H., Wingate, M. T.D., Bodorkos, S., 2010. Evidence for Mesoarchean (~3.2 Ga) rifting of the Pilbara Craton: The missing link in an early Precambrian Wilson cycle. Precambrian Research, 177, 145-161.

Van Kranendonk, M.J., Kröner, A., Hoffmann, J.E., Nagel, T., Anhaeusser, C.R., 2014. Just another drip: re-analysis of a proposed Mesoarchean suture from the Barberton Mountain Land, South Africa, Precambrian Research, 254, 19-35.

Van Kranendonk, MJ., Smithies, R.H., Griffin, W.L., Huston, D.L., Hickman, A.H., Champion, D.C., Anhaeusser, C.R., Pirajno, F., 2015. Making it thick: A volcanic plateau origin of Paleoarchean continental lithosphere of the Pilbara and Kaapvaal cratons. In Continent Formation Through Time. Geological Society, London, Special Publications, 389, 83–111.

Venkata Dasu, S.P., Ramakrishnan, M., Mahabaleswar, B., 1991. Sargur-Dharwar relationship around the Komatiite-rich Jayachamaraja Pura greenstone belt in Karnataka. Journal of the Geological Society of India 38, 577-592

Vijaya Rao, V., Murthy, A.S.N., Sarkar, Dipankar, Bhaskar Rao, Y.J., Khare, Prakash, Prasad, A.S.S.S.R.S., Sridhar, V., Raju, S., Rao, G.S.P., Karuppannan, Prem Kumar, N., Sen, Mrinal K., 2015. Crustal velocity structure of the Neoarchean convergence zone between the eastern and western blocks of Dharwar Craton, India from seismic wide-angle studies. Precambrian Research, 266, 282-295.

Viljoen M. J, Viljoen F.P, Pearton T.N., 1982. The nature and distribution of Archaean komatiite volcanics in South Africa In: Arndt NT, Nisbet EG (eds) Komatiites. Allen and Unwin, London, 53–79.

Viswanatha M N, Ramakrishnan M and Narayana Kutty T. R., 1977. Possible spinifex texture in a serpentinite from Karnataka; Journal of the Geological Society of India, 18, 194–197.

Wang, J.Y., Santosh, M., 2019. Eoarchean to Mesoarchean crustal evolution in the Dharwar craton, India: Evidence from detrital zircon U-Pb and Hf isotopes. Gondwana Research, 72, 1-14.

Wang, H., Yang, J.H., Kröner, A., Zhu, Y. S., Li, R., 2019. Non-subduction origin for 3.2 Ga high-pressure metamorphic rocks in the Barberton granitoid-greenstone terrane, South Africa Terra Nova, 31, 373-380. DOI: 10.1111/ter.12397

Wang, J.Y., Santosh, M., Jayananda, M., Aadhiseshan, K.R., 2020. Bimodel magmatism in the Eastern Dharwar Craton, southern India: Implications for Neoarchean crustal evolution, Lithos, 354-355, (105336). https://doi.org/10.1016/j.lithos.2019.105336

Weijermars, R., Khan, M.A., 2000. Mid-crustal dynamics and island-arc accretion in the Arabian Shield: insight from the Earth's natural laboratory. Earth Sci. Rev. 49 (1-4), 77-120.

Whitney, D.L, Teyssier, C., Siddoway, C.S., 2004. Gneiss domes in orogeny: Boulder, Colorado, Geological Society of America, Special Paper 380, ISBN: 9780813723808. https://doi.org/10.1130/SPE380.

Wiedenbeck, M., Alle, P., Corfu, F., Griffin, W. L., Meier, M., Oberli, F., 1995. Three natural zircon standards for U–Th–Pb, Lu–Hf, trace 765 element and REE analyses. Geostandards Newsletter, 19(1), 1–23.

Wiemer, D., Schrank, C.E., Murphy, D.T., Wenham, L., Allen, C.M., 2018. Earth's oldest stable crust in the Pilbara Craton formed by cyclic gravitational overturns. Nature Geoscience, 11, 357–361.

Windley, B.F., Kusky, T., Polat, A., 2021. Onset of Plate Tectonics by the Eoarchean. Precambrian Research 352, 105980, doi: https://doi.org/10.1016/j.precamres.2020.105980.

Woodhead, J.D., Hergt, J.M. (2005) A preliminary appraisal of seven natural zircon reference materials for *in situ* Hf isotope determination. Geostandards and Geoanalytical Research, 29, 183-195.

Workman, R.K., Hart, S.R., 2005. Major and trace element composition of the depleted MORB mantle (DMM). Earth and Planetary Science Letters, 231, 53– 72.

Wyman, D., 2018. Do cratons preserve evidence of stagnant lid tectonics? Geoscience Frontiers, 9, 3-17.

Wyman, D., 2020. Komatiites From Mantle Transition zone Plumes. Frontiers in Earth Sciences, 8, 540744. doi. 10.3389/feart.2020.540744.

Xie, Q., Kerrich, R., 1994. Silicate-perovskite and majorite signature komatiites from the Archean Abitibi greenstone belt: Implications for early mantle differentiation and stratification. J. Geophys. Res. Lett., 99, 15799-15812.

Xie, Q., Kerrich, R., 1995. Application of isotope for precise measurements of Zr and Hf in low-abundance samples and international reference materials by inductively coupled plasma mass spectrometry: implications for Zr (Hf)/REE fractionations in komatiites. Chem. Geol., 123, 17-27.

Yogodzinski, G.M., Brown, S.T., Kelemen, P.B., Vervoort, J.D., Portnyagin, M., Sims, K.W.W., Hoernle, K., Jicha, B.R., Werner., R., 2015.The Role of Subducted Basalt in the Source of Island Arc Magmas: Evidence from Seafloor Lavas of the Western Aleutians. Journal of Petrology, 56, 441–492. https://doi.org/10.1093/petrology/egv006

Zeh, A., Gerdes, A., Millonig, L., 2011. Hafnium isotope record of the Ancient Gneiss Complex, Swaziland, southern Africa; evidence for Archean crust mantle formation and crust reworking between 3.66 and 2.73 Ga. Journal of the Geological Society of London, 168, 1-11.

Zulauf, G., Zulauf, J., Thiessen, A., Hattingen, E., 2019. Formation of dome-in-dome structures: results from experimental studies and comparison with natural examples. J. Struct. Geol. 118, 324-339.

Figure captions

Fig.1- Geological sketch map of Peninsular India showing major Archean cratons in India (modified after Geological Survey of India), square box depicting the cratonic core region.

Fig.2 - Geological sketch map of Archean Dharwar craton and study area (modified after Chardon et al., 2008, 2011; Peucat et al., 2013; Jayananda et al., 2013a). (a) Geological sketch map showing the cratonic core (b) Geological sketch map of Holenarsipur greenstone belt and adjoining TTGs showing three greenstone units and diapiric trondhjemite intrusions with age, εHf, εNd of the present study; Jayananda et al., 2015; Guitreau et al., 2017; Ranjan et al.,2020; Ao et al., 2021, foliation trajectories are from Bouhallier et al., 1993 (c) SW-NE interpretative cross section of crustal panel of Holenarsipur greenstone belt and adjoining felsic rocks with distinct lithological assemblages corresponding to three tectonic blocks (modified after Bouhallier et al., 1995) and this interpretative cross-section represents the A-A' shown in the fig. 2b.

Fig.3.1 (a) Komatiitic basalt interlayered with grey gneiss; (b) Komatiite with pillow structure (c) Tattekere conglomerate; (d) ripple marks in quartzite; (e) cross-bedding in quartzite; (f) Kyanite-staurolite-garnet bearing pelite (g) light grey granite with whitish grey trondhjemite in Hassan-Gorur road; (h) grey granodiorite with older gneissic enclave in Hassan-Gorur road; (i) late (3145 Ma) granodiorite dyke injected into TTG in Gorur-Hassan road; (j) Trondhjemite forming vertical tectonite close to Karle.

Fig. 3.2 (a) Komatiite showing pillow structure from Northcentral block about 1km east of Haradanahalli; (b) Pyroclastic felsic volcanic flow at Eastern outskirts of Haradanahalli; (c) Chlorite-chloritoid-garnet bearing pelitic rock at about 1 km east of Shigaranahalli; (d) Randomly oriented crystals of actinolite, tremolite and hornblende at about 500m NE of Haradanahalli.

Fig. 3.3 (a) Eastern block road cut section displaying section of preserved oceanic crust from pillow ultramafic through clays, BIFs, sheeted dykes, plagiogranite, gabbro/norite, layered gabbro with ultramafic and finally peridotite and this corresponds to the B-B' line shown in the fig.2b; (b) Interpretative E-W section of preserved oceanic crust. (c) Interpretative vertical section of the oceanic crust.

Fig. 4.1 (a) Photomicrograph from southwestern block (b & c) from northcentral block (d) from eastern block.

Fig. 5.1 (a) The Nuggihalli greenstone belt showing metamorphosed ultramafic rocks (peridotite, serpentinite and dunite with chromite layers, talc-tremolite schists (b) the Kalyadi greenstone belt showing komatiite volcanic rocks including serpentinites, serpentine-talc-tremolite and talc-chlorite schists (c & d) the J.C. Pura greenstone belt showing komatiite-komatiitic basaltkomatiitic basalts and minor basalt with flow top pillow breccias (e) the Banasandra greenstone belt showing spinifex texture near Kunikenahalli (f) the Nagamangala greenstone belt showing komatiite affinity with minor basalts which are interlayered with sedimentary rocks.

Fig. 5.2 (a) Photomicrograph from the Kalyadi greenstone belt (b) the Nuggihalli greenstone belt (c) the J.C. Pura greenstone belt (d) the Ghattihosahalli greenstone belt (e) the Banasandra greenstone belt (f) the Nagamangala greenstone belt.

Fig. 6.1 (a) TTG-type granitoids at the base of Bababudan (b) TTG-type granitoids west of the Nuggihalli greenstone belt (c) TTG-type granitoids west of the Chitradurga greenstone belt near Bharamanayakana durga (d) TTG-type granitoids on the Huliyar-Hosdurga road (e) TTG-type granitoids near the J.C. Pura (f) TTG-type granitoids west of the Nagamangala greenstone belt. (g) Interpretative WSW-ENE crustal scale cross- section of the cratonic core in WDC based on our field observations and published tectonic fabrics data (Bouhallier et al., 1993, 1995; Chardon, 1997; Chardon et al., 1996, 1998, 2008; the Moho depth is adopted from Gupta et al., 2003).

Fig.7.1 (a) Al_2O_3-Fe_2O_3+TiO_2- MgO (AFM) ternary plot (Jensen, 1976 modified by Viljoen et al., 1982) showing that volcanic rocks of three greenstone unit are komatiite to komatiitic basalt composition (b) CaO-MgO-Al_2O_3 ternary plot (Viljoen et al., 1982) showing dominant komatiite to komatiitic basalt except two samples of Eastern block showing tholeiite composition. (c) Feo/(Feo+MgO) versus Al_2O_3 (Arndt, 2003) binary diagram showing Barberton komatiite and komatiitic basalt field (d) Harker's binary variation diagram for major oxide against MgO showing HGB and other greenstones from cratonic core region (e) Harker's binary variation diagram for trace element against MgO showing HGB and other greenstones from cratonic core region.

Fig. 7.2 (a) Chondrite normalized low total REE group volcanic rocks of southwestern block (b) Primitive mantle normalized (Sun and McDonough, 1989) multi-element plot of low total REE group southwestern block (c) Chondrite normalized high total REE group volcanic rocks of southwestern block (d) Primitive mantle normalized (Sun and McDonough, 1989) multi-element plot of high total REE group of southwestern block (e) Chondrite normalized REE group of komatiite volcanic rocks of northcentral block (f) Primitive mantle normalized (Sun and McDonough, 1989) multi-element plot of komatiite volcanic rocks of northcentral block. (g) Chondrite normalized REE group of komatiitic-basalts of northcentral block (h) Primitive mantle normalized (Sun and McDonough, 1989) multi-element plot of komatiite-basalts of northcentral block (i) Chondrite normalized low total REE group volcanic rocks of eastern block (j) Primitive mantle normalized (Sun and McDonough, 1989) multi-element plot of low total REE group of eastern block (k) Chondrite normalized high total REE group volcanic rocks of eastern block (l) Primitive mantle normalized (Sun and McDonough, 1989) multi-element plot of high total REE group of eastern block.

Fig. 7.3 (a) Chondrite normalized REE group volcanic rocks of the Nuggihalli and Kalyadi (b) Primitive mantle normalized (Sun and McDonough, 1989) multi-element plot of the Nuggihalli and Kalyadi.

Fig. 7.4 (a) Chondrite normalized REE volcanic rocks of the J.C. Pura komatiites (b) Primitive mantle normalized (Sun and McDonough, 1989) multi-element plot of the J.C. Pura komatiites (c) Chondrite normalized REE volcanic rocks of the J.C. Pura komatiites-cumulate layers (d) Primitive mantle normalized (Sun and McDonough, 1989) multi-element plot of the J.C. Pura komatiites-cumulate layers (e) Chondrite normalized REE volcanic rocks of the J.C. Pura komatiite-basalt (f) Primitive mantle normalized (Sun and McDonough, 1989) multi-element plot of the J.C. Pura komatiite-basalt.

Fig. 7.5 (a) Chondrite normalized REE volcanic rocks of the Ghattihosahalli komatiites (b) Primitive mantle normalized (Sun and McDonough, 1989) multi-element plot of the Ghattihosahalli komatiites (c) Chondrite normalized REE volcanic rocks of the Banasandra komatiites (d) Primitive mantle normalized (Sun and McDonough, 1989) multi-element plot of the Banasandra komatiites (e) Chondrite normalized REE volcanic rocks of the Nagamangala komatiites (f) Primitive mantle normalized (Sun and McDonough, 1989) multi-element plot of the Nagamangala komatiites.

Fig. 7.6 (a) $(Gd/Yb)_N$ versus Al_2O_3/TiO_2 (after Arndt 2003) (b) $(Gd/Yb)_N$ versus CaO/Al_2O_3 (after Jahn et al. 1982) indicating role of variable residual garnet or absence of residual garnet in source mantle.

Fig.7.7 - (a) Cathodoluminescence (CL) images of the sample 18HP01A, 18HP01C, 18HP03A, 18HP03B and 18HP04A (b) cathodoluminescence (CL) images of the sample 18HP04A, 18HP04B, 18HP05, 18HP07 and 18HP10A (c) cathodoluminescence (CL) images of the sample 18HP13, 18HP15A, 18HP23, 18HP24A and 18HP39.

Fig. 7.8 (a) U-Pb Concordia diagram of sample 18HP23 southwestern block TTG (b) U-Pb Concordia diagram of sample 18HP24a southwestern block TTG (c) U-Pb Concordia diagram of sample 18HP10b southwestern block TTG (d) U-Pb Concordia diagram of sample 18HP05 southwestern block TTG (e) U-Pb Concordia diagram of sample 18HP01a southwestern block TTG (f) U-Pb Concordia diagram of sample 18HP01c southwestern block TTG (g) U-Pb Concordia diagram of sample 18HP03a southwestern block TTG (h) U-Pb Concordia diagram of sample 18HP03b southwestern block TTG (i) U-Pb Concordia diagram of sample 18HP04a southwestern block TTG (j) U-Pb Concordia diagram of sample 18HP04b southwestern block TTG (k) U-Pb Concordia diagram of sample 18HP07 northcentral block TTG (l) U-Pb Concordia diagram of sample 18HP15a northcentral block TTG (m) U-Pb Concordia diagram of sample 18HP13 felsic volcanic, northcentral block TTG (n) U-Pb Concordia diagram of sample 18HP39 plagiogranite, eastern block.

Fig.7.9 (a) Normative Ab-An-Or triangular diagram (after O' Connors, 1965) with fields from Barker (1979) showing trondhjemite, tonalite and granite extending to granodiorite field (b) normative Q–Ab–Or (Barker and Arth, 1976) showing trondhjemite and calc-alkaline trend. (c) Harker's binary diagrams for TTG-type granitoids and diapiric trondhjemite intrusions displaying moderate to weak fractionation trends.

Fig.7.10 (a) Chondrite normalized low-Al TTG REE group of southwestern block (b) Primitive mantle normalized (Sun and McDonough, 1989) multi-element plot of low-Al TTG REE group of southwestern block (c) Chondrite normalized high-Al TTG REE group of southwestern block (d) Primitive mantle normalized (Sun and McDonough, 1989) multi-element plot of high-Al TTG REE group of southwestern block (e) Chondrite normalized REE group of TTG from northcentral block (f) Primitive mantle normalized (Sun and McDonough, 1989) multi-element plot of TTG from northcentral block. (g) Chondrite normalized REE group of TTG from eastern block (h) Primitive mantle normalized (Sun and McDonough,

1989) multi-element plot of TTG from eastern block (i) Chondrite normalized REE group of Trondhjemite (j) Primitive mantle normalized (Sun and McDonough, 1989) multi-element plot of Trondhjemite (k) Chondrite normalized REE group from other western TTG (l) Primitive mantle normalized (Sun and McDonough, 1989) multi-element plot from other western TTG.

Fig.7.11 (a) $\varepsilon Hf_{(T)}$ versus time evolution diagram of TTGs from three blocks, other western TTGs and trondhjemite showing involvement of depleted mantle with traces of ancient crustal contamination. (b) $\varepsilon Nd_{(T)}$ versus time evolution diagram of greenstones, TTGs from three blocks and other greenstone belts, TTGs in the cratonic core region showing involvement of depleted mantle with traces of ancient crustal contamination.

Fig.8 (a) Nb/U versus Nb/Th plot (after Saunders et al. 1988) showing scattering indicating source composition of primitive mantle to depleted MORB source mantle for the southwestern, northcentral, eastern block and other greenstone belts in the cratonic core region (b) Nb/Th versus ƐNd plot indicating the primitive mantle and depleted MORB source for the studies samples from cratonic core region. (c) Th/Yb versus Nb/Yb binary plot (Pearce, 2008) indicating primitive to depleted mantle source for the southwestern, northcentral, eastern block and other greenstone belts in the cratonic core region (d) Nb/Y versus Zr/Y (Condie, 2003) indicating deep depleted to primitive mantle reservoir source for the samples from for the southwestern, northcentral, eastern block and other greenstone belts in the cratonic core region (e) Zr/Nb versus Nb/Th plot (Condie, 2003) showing oceanic plateau for southwestern block, J.C.Pura, Ghattihosahalli, majority of Banasandra, Nuggihalli and Kalyadi samples, arc to oceanic plateau for Northcentral block, Nagamangala samples and N-MORB to oceanic plateau for Eastern block. Arrows indicate effects of batch melting (F) and subduction (SUB); PM, primitive mantle; DM, shallow depleted mantle; ARC, arc related basalts; NMORB, normal ocean ridge basalt; OIB, oceanic island basalt; DEP, deep depleted mantle; EN, enriched component.

Fig.9 (a) Nb/Ta vs Gd/Yb (Hoffmann et al., 2011) showing the origin of TTG melt from different source composition (b) Nb/Ta vs Zr/Sm plot (Hoffmann et al., 2011) explaining the origin of TTG melt from different source composition, (c) $K_2O/(Na_2O+CaO)$ vs Sr/Y plot (Hoffmann et al., 2019) representing the different pressure level at which the studied samples generated from the source. Lines correspond to melting models derived from experimental database, as in Moyen, 2009, 2011, at different pressures and for two sources, an MORB and a more enriched mafic rock (d) $Al_2O_3/(FeO_t+MgO)-3*CaO-5*(K_2O/Na_2O)$ diagram (Laurent et al., 2014) showing the sources of studies TTGs from the cratonic core region (e) Sr/Y versus Y diagram (after Defant and Drummond, 1990; Martin et al.,2005) showing two distinct groups of TTG suites (low-Al and high-Al) and the role of residual garnet. Low-Al gneisses plot in the field defined for island arc magmas derived from mafic source without significant residual garnet. High-Al gneisses plot in the field of Archean TTG derived by melting of mafic source with variable residual garnet. Arrows indicate batch melting of mafic source with 7–30% garnet-amphibole in source residue (f) $(La/Yb)_N$ versus Yb plot (after Jahn et al., 1981; Drummond and Defant, 1990; Moyen, 2011) showing two distinct groups of TTG suites (low-Al and high-Al) derived from distinct mafic sources with or without residual garnet. The low-Al gneisses plot in the field defined for the melts derived from depleted mafic source at shallow level without any significant residual garnet. Arrows in high-Al TTG field indicate batch of melting of mafic source at deeper levels transforming into garnet bearing amphibolites residue with 7–30% garnet in residue.

Table captions

Table 1 Summary table of interpreted zircon U-Pb age and Lu-Hf characteristics for studied granitoids.

Supplementary Table captions

Supplementary Table 1. Major oxide (wt.%), trace and REE (ppm) concentrations of Holenarsipur greenstone belt and other greenstone belts in the studies cratonic core region.

Supplementary Table 2. Major oxide (wt.%), trace and REE (ppm) concentrations of TTG-type granitoids surrounding HGB and other western TTGs in the studies cratonic core region.

Supplementary Table 3. Zircon U-Pb data by LA-ICP-MS for the TTGs surrounding Holenarsipur greenstone belt along with reference material analysis.

Supplementary Table 4. *in-situ* Lu-Hf isotope data for the TTGs surrounding Holenarsipur greenstone belt along with those for reference material.

Supplementary Table 5. Sm-Nd isotopic data for rocks of the southwestern, northcentral and eastern blocks of the Holenarsipur greenstone belt.

Supplementary Table 6. Operating conditions for U-Pb and Lu-Hf isotope measurements using LA-ICP-MS and LA-MC-ICP-MS.

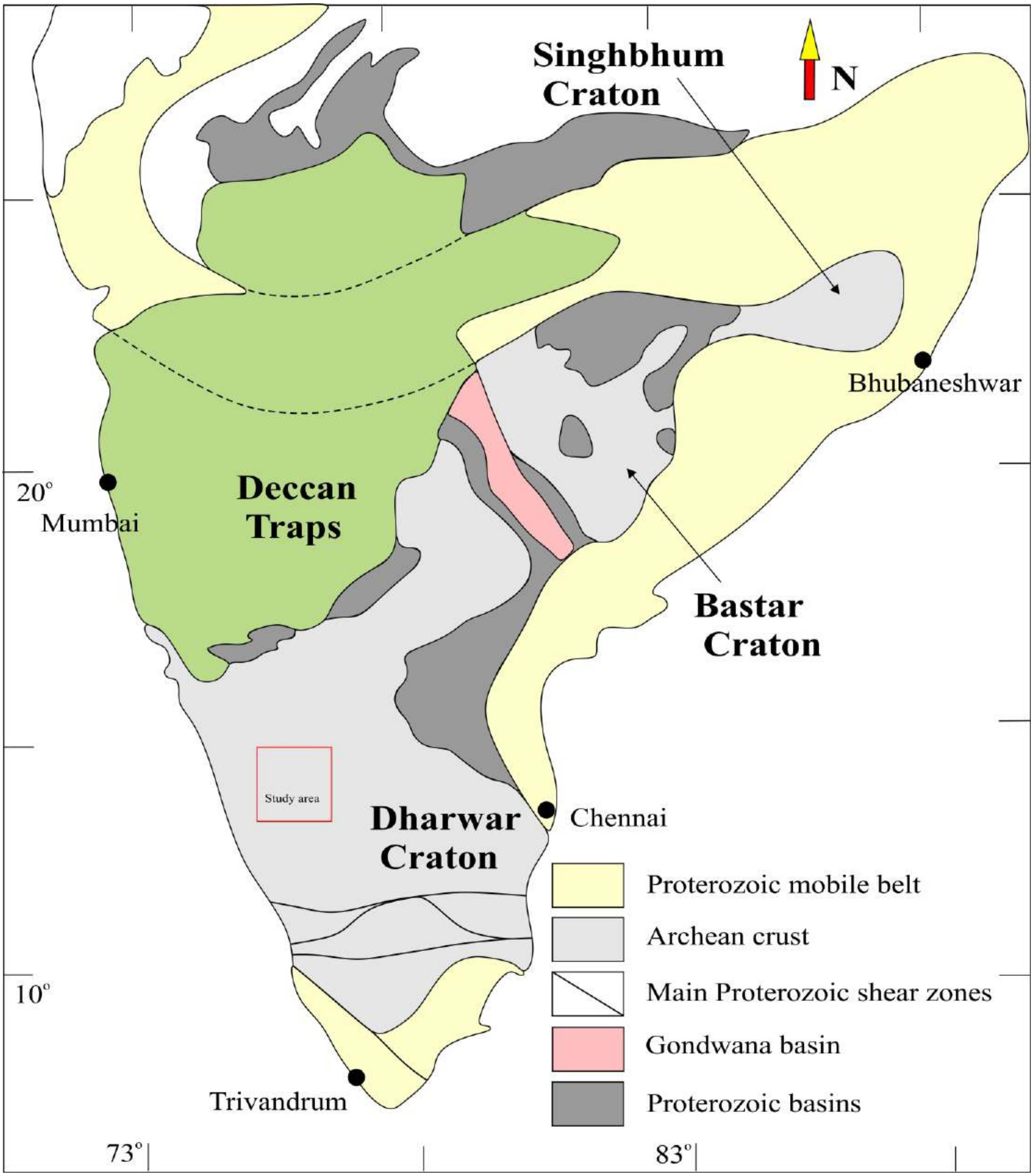
Singhbhum
Craton
N
Deccan
Traps
Bastar
Craton
Dharwar
Craton
Study area
Mumbai
Bhubaneshwar
Chennai
Trivandrum
20°
10°
73°
83°
Proterozoic mobile belt
Archean crust
Main Proterozoic shear zones
Gondwana basin
Proterozoic basins

Fig. 1

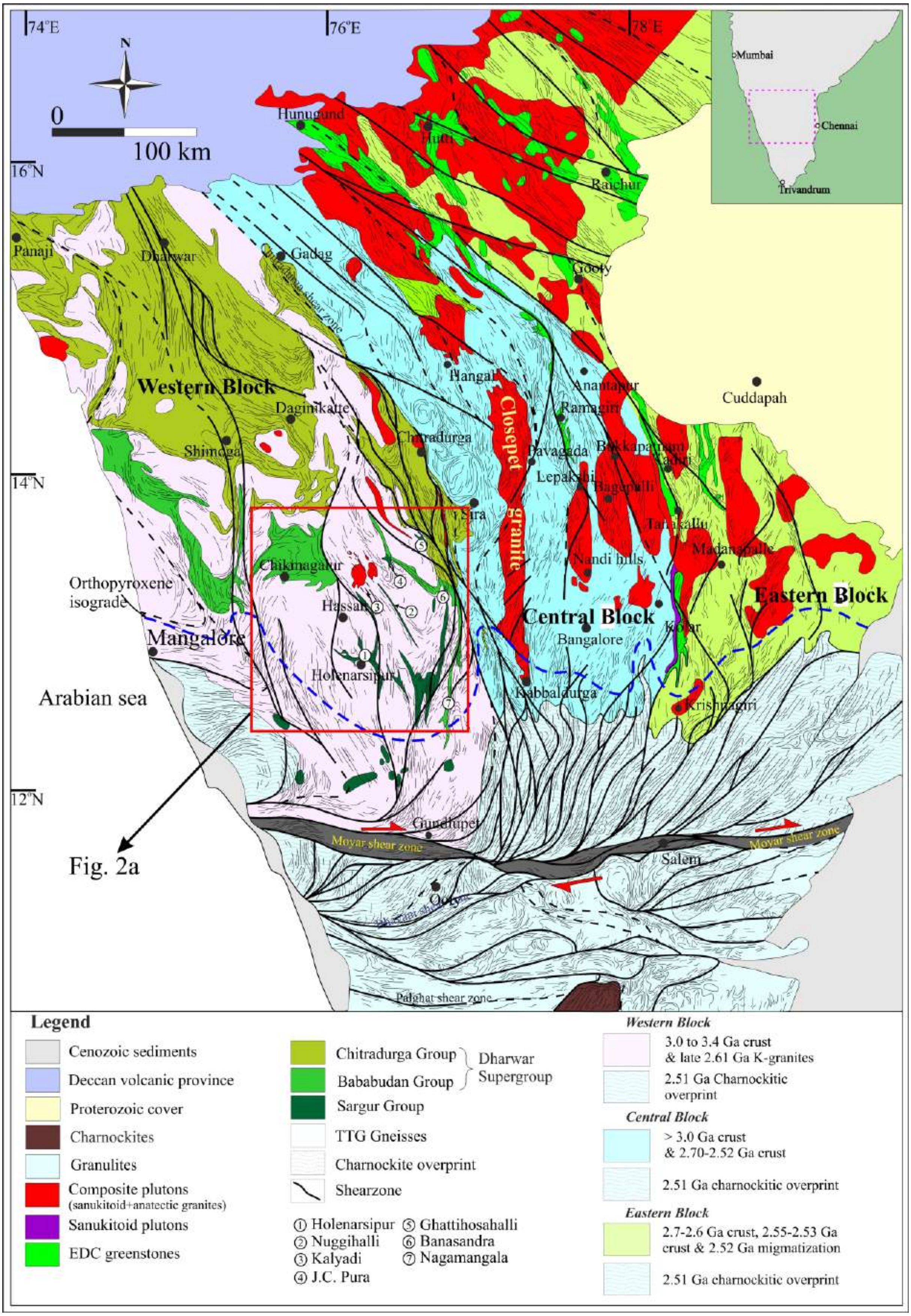
74°E
76°E
78°E
16°N
14°N
12°N
N
0
100 km
Mumbai
Chennai
Trivandrum
Hunugund
Hutti
Raichur
Panaji
Dharwar
Gadag
Chitradurga shear zone
Gooty
Western Block
Daginikatte
Hangal
Anantapur
Cuddapah
Closepet granite
Ramagiri
Shimoga
Chitradurga
Pavagada
Bukkapatnam
Kadiri
Lepakshi
Bagepalli
Sira
Tanakallu
Madanapalle
Nandi hills
Chikmagalur
Orthopyroxene isograde
Hassan
Central Block
Eastern Block
Kolar
Bangalore
Mangalore
Holenarsipur
Arabian sea
Kabbaldurga
Krishnagiri
Fig. 2a
Gundlupet
Moyar shear zone
Salem
Ooty
Bhavani shear zone
Palghat shear zone
Legend
Cenozoic sediments
Deccan volcanic province
Proterozoic cover
Charnockites
Granulites
Composite plutons (sanukitoid+anatectic granites)
Sanukitoid plutons
EDC greenstones
Chitradurga Group
Bababudan Group
Dharwar Supergroup
Sargur Group
TTG Gneisses
Charnockite overprint
Shearzone
① Holenarsipur
② Nuggihalli
③ Kalyadi
④ J.C. Pura
⑤ Ghattihosahalli
⑥ Banasandra
⑦ Nagamangala
Western Block
3.0 to 3.4 Ga crust & late 2.61 Ga K-granites
2.51 Ga Charnockitic overprint
Central Block
> 3.0 Ga crust & 2.70-2.52 Ga crust
2.51 Ga charnockitic overprint
Eastern Block
2.7-2.6 Ga crust, 2.55-2.53 Ga crust & 2.52 Ga migmatization
2.51 Ga charnockitic overprint

Fig. 2

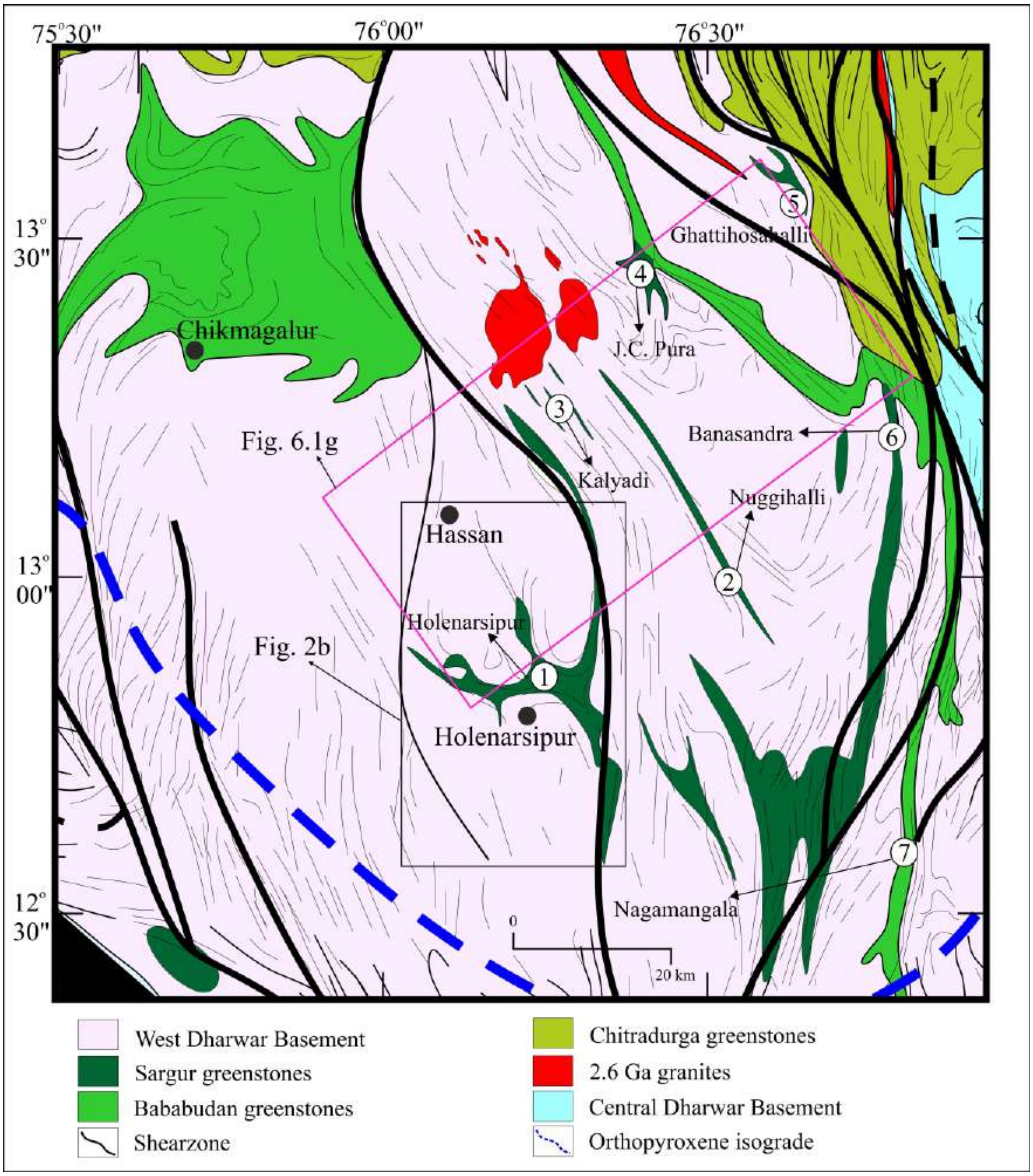
75°30"
76°00"
76°30"
13°
30"
13°
00"
12°
30"
Chikmagalur
Ghattihosahalli
J.C. Pura
Banasandra
Kalyadi
Nuggihalli
Hassan
Holenarsipur
Holenarsipur
Nagamangala
Fig. 6.1g
Fig. 2b
1
2
3
4
5
6
7
0
20 km
West Dharwar Basement
Sargur greenstones
Bababudan greenstones
Shearzone
Chitradurga greenstones
2.6 Ga granites
Central Dharwar Basement
Orthopyroxene isograde

Fig. 2a

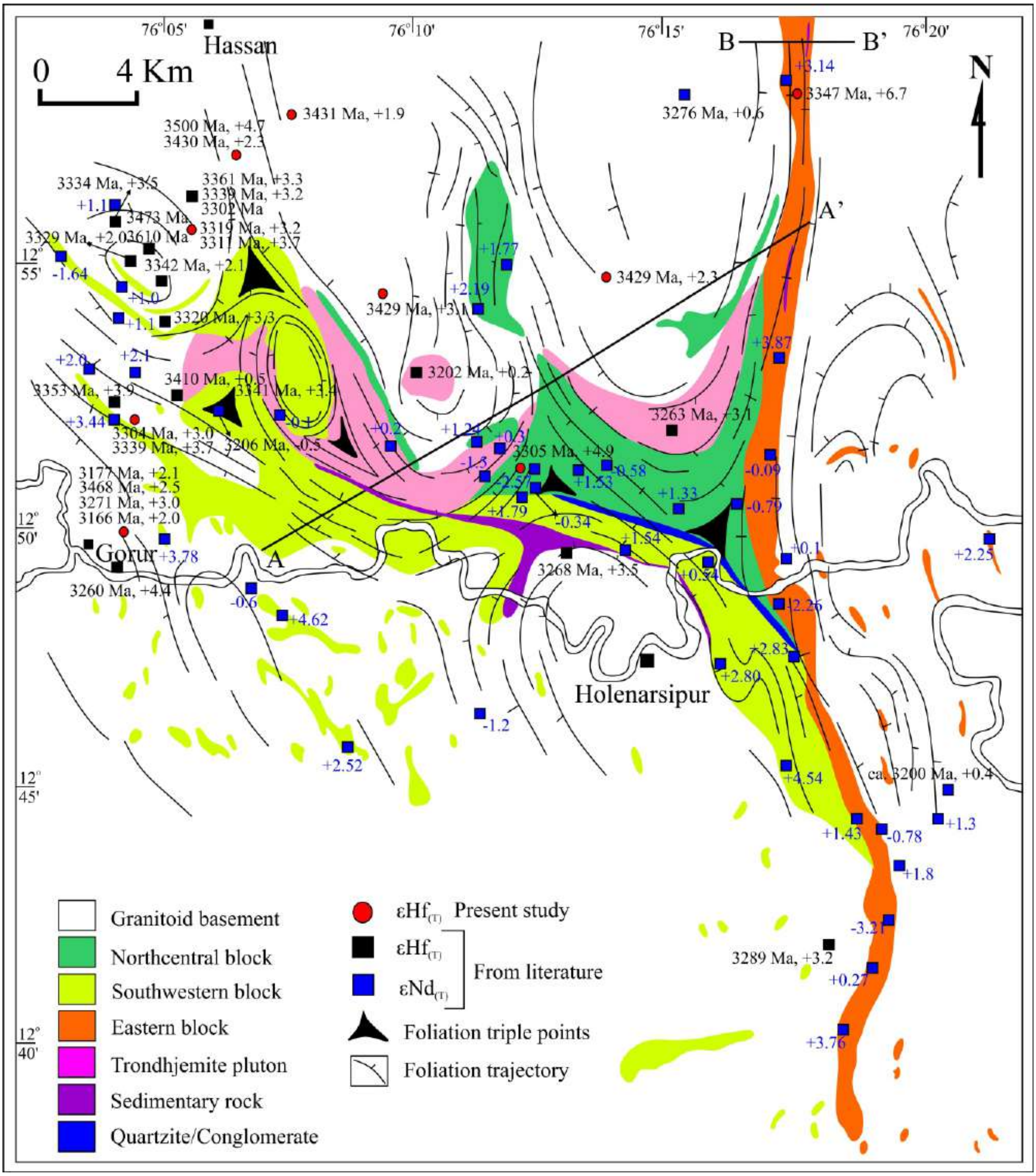
76°05'
Hassan
76°10'
76°15'
B
B'
76°20'
0 4 Km
N
+3.14
3347 Ma, +6.7
3276 Ma, +0.6
3431 Ma, +1.9
3500 Ma, +4.7
3430 Ma, +2.3
3334 Ma, +3.5
3361 Ma, +3.3
3339 Ma, +3.2
3302 Ma
+1.1
3473 Ma
3319 Ma, +3.2
3311 Ma, +3.7
3329 Ma, +2.0
3610 Ma
A'
12° 55'
-1.64
3342 Ma, +2.1
+1.77
+1.0
+2.19
3429 Ma, +2.3
3429 Ma, +3.1
+1.1
3320 Ma, +3.3
+3.87
+2.0
+2.1
3202 Ma, +0.2
3410 Ma, +0.5
3353 Ma, +3.9
3341 Ma, +3.4
3263 Ma, +3.1
+3.44
-0.1
+0.2
+1.24
+0.3
3304 Ma, +3.0
3339 Ma, +3.7
3206 Ma, -0.5
-1.3
3305 Ma, +4.9
-0.58
-0.09
3177 Ma, +2.1
3468 Ma, +2.5
-2.57
+1.53
3271 Ma, +3.0
+1.33
-0.79
3166 Ma, +2.0
+1.79
-0.34
12° 50'
+1.54
Gorur
+3.78
A
+0.1
+2.25
3268 Ma, +3.5
+0.54
3260 Ma, +4.4
-0.6
+4.62
-2.26
+2.83
+2.80
Holenarsipur
-1.2
+2.52
12° 45'
+4.54
ca. 3200 Ma, +0.4
+1.43
-0.78
+1.3
+1.8
-3.21
3289 Ma, +3.2
+0.27
12° 40'
+3.76
Granitoid basement
Northcentral block
Southwestern block
Eastern block
Trondhjemite pluton
Sedimentary rock
Quartzite/Conglomerate
εHf(T) Present study
εHf(T)
εNd(T)
From literature
Foliation triple points
Foliation trajectory

Fig. 2b

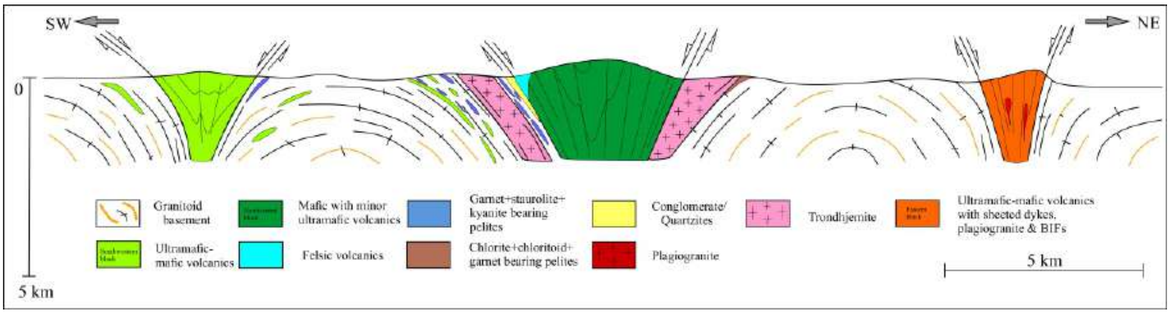

Fig. 2c

Fig. 3.1a-b

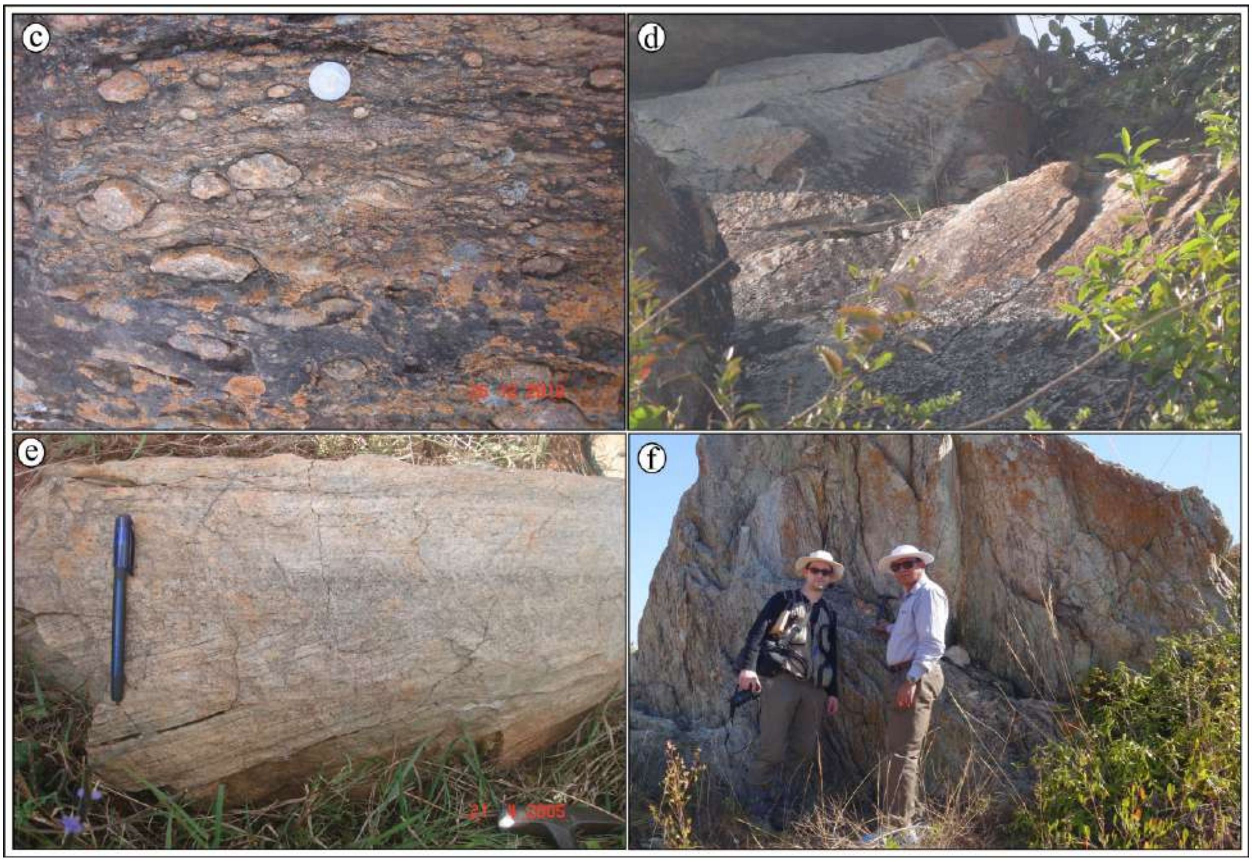

Fig. 3.1c-f

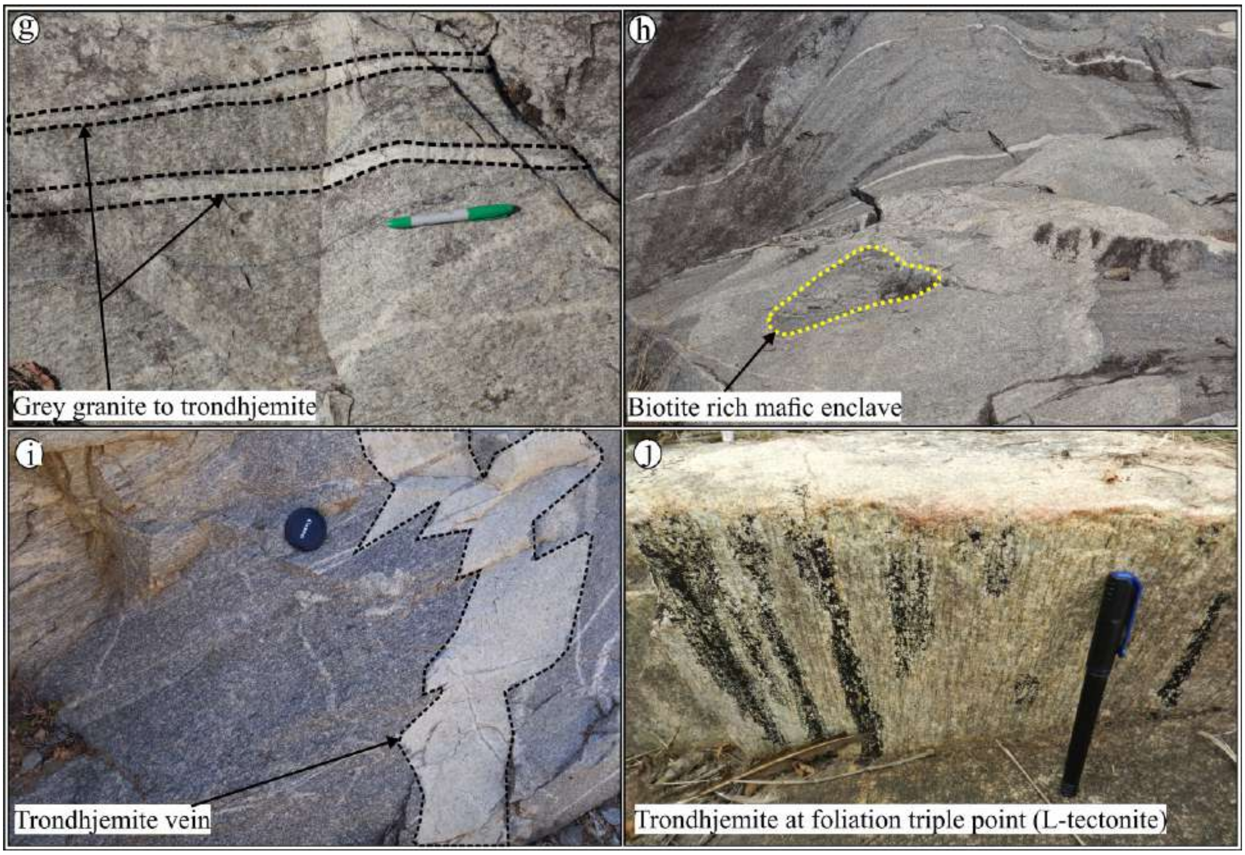

Fig. 3.1g-j

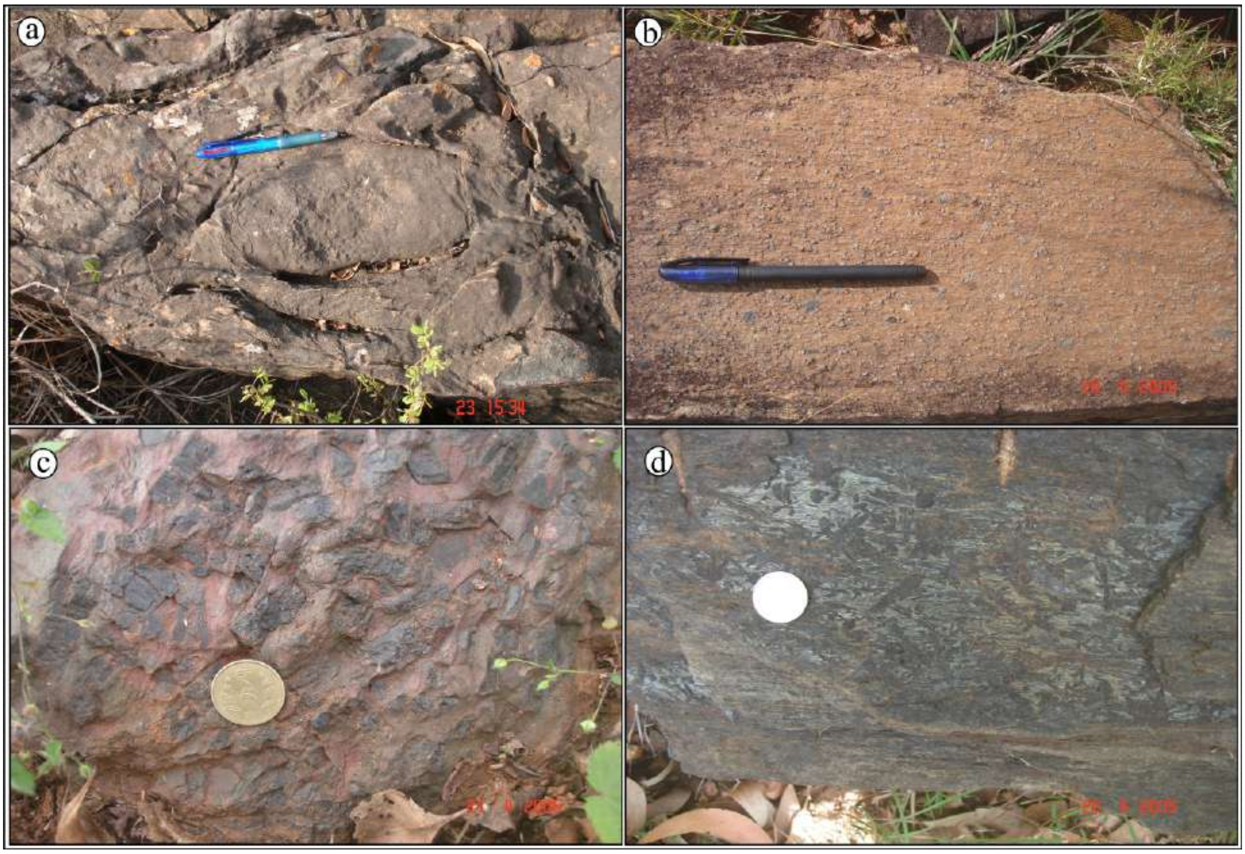

Fig. 3.2a-d

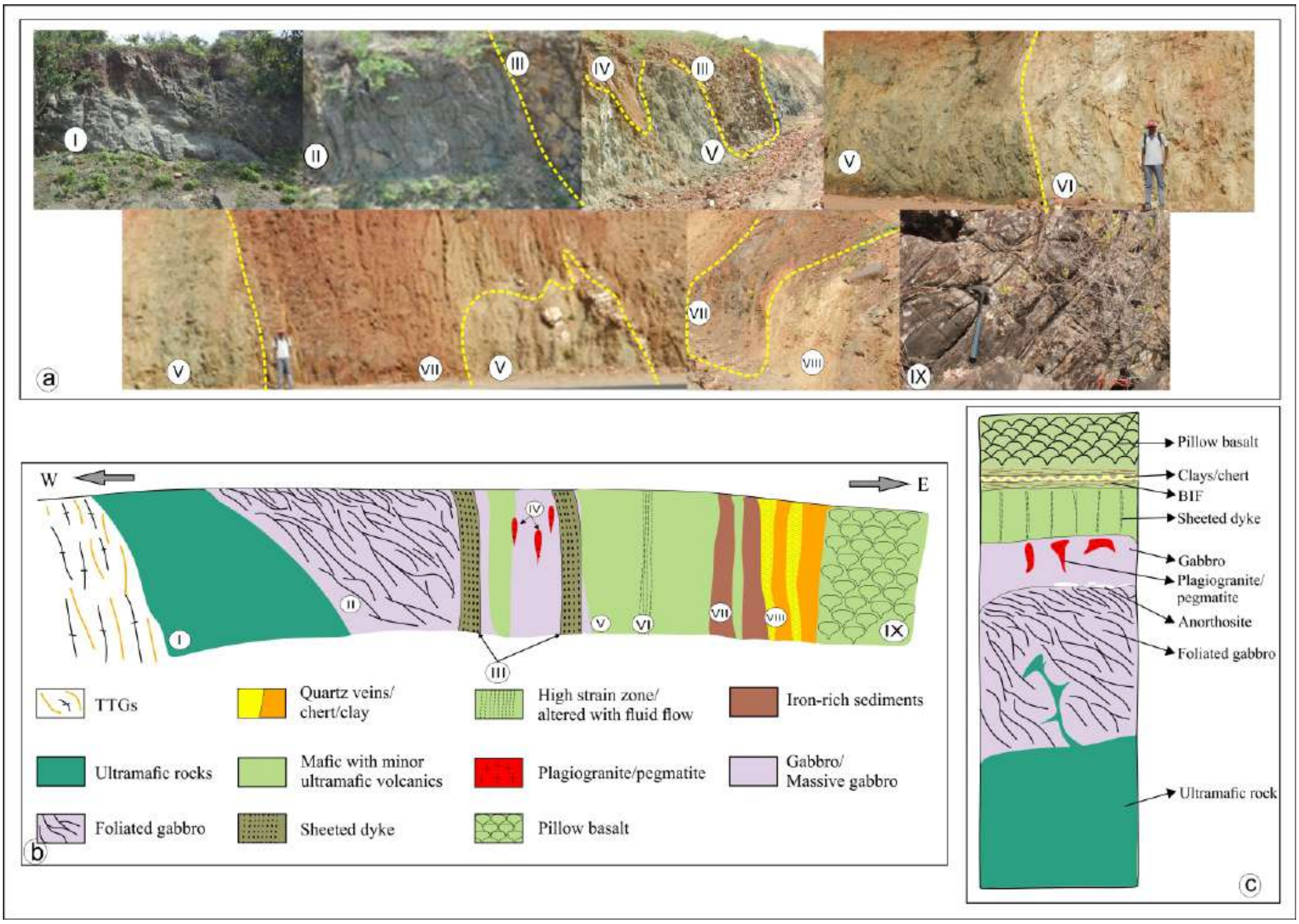
a
I
II
III
IV
III
V
V
VI
V
VII
V
VII
VIII
IX
b
W
E
I
II
IV
III
V
VI
VII
VIII
IX
TTGs
Quartz veins/ chert/clay
High strain zone/ altered with fluid flow
Iron-rich sediments
Ultramafic rocks
Mafic with minor ultramafic volcanics
Plagiogranite/pegmatite
Gabbro/ Massive gabbro
Foliated gabbro
Sheeted dyke
Pillow basalt
c
Pillow basalt
Clays/chert
BIF
Sheeted dyke
Gabbro
Plagiogranite/ pegmatite
Anorthosite
Foliated gabbro
Ultramafic rock

Fig. 3.3a-c

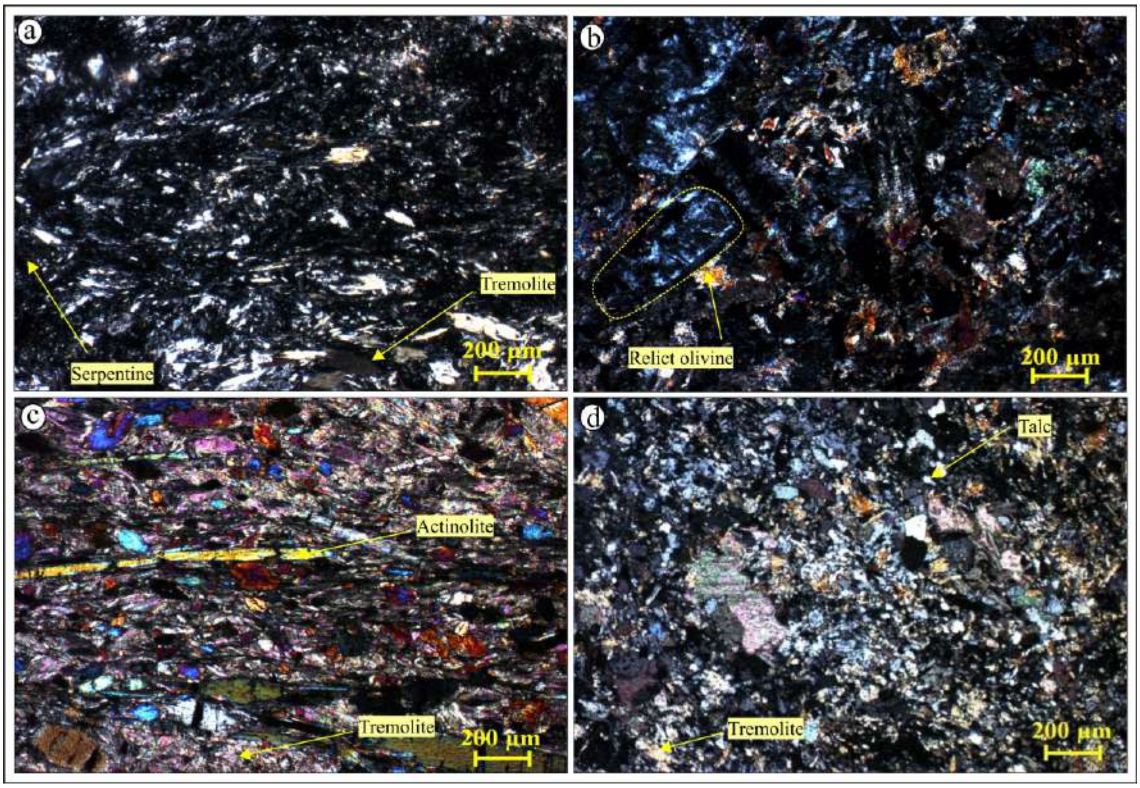
a
Serpentine
Tremolite
200 µm
b
Relict olivine
200 µm
c
Actinolite
Tremolite
200 µm
d
Talc
Tremolite
200 µm

Fig. 4.1a-f

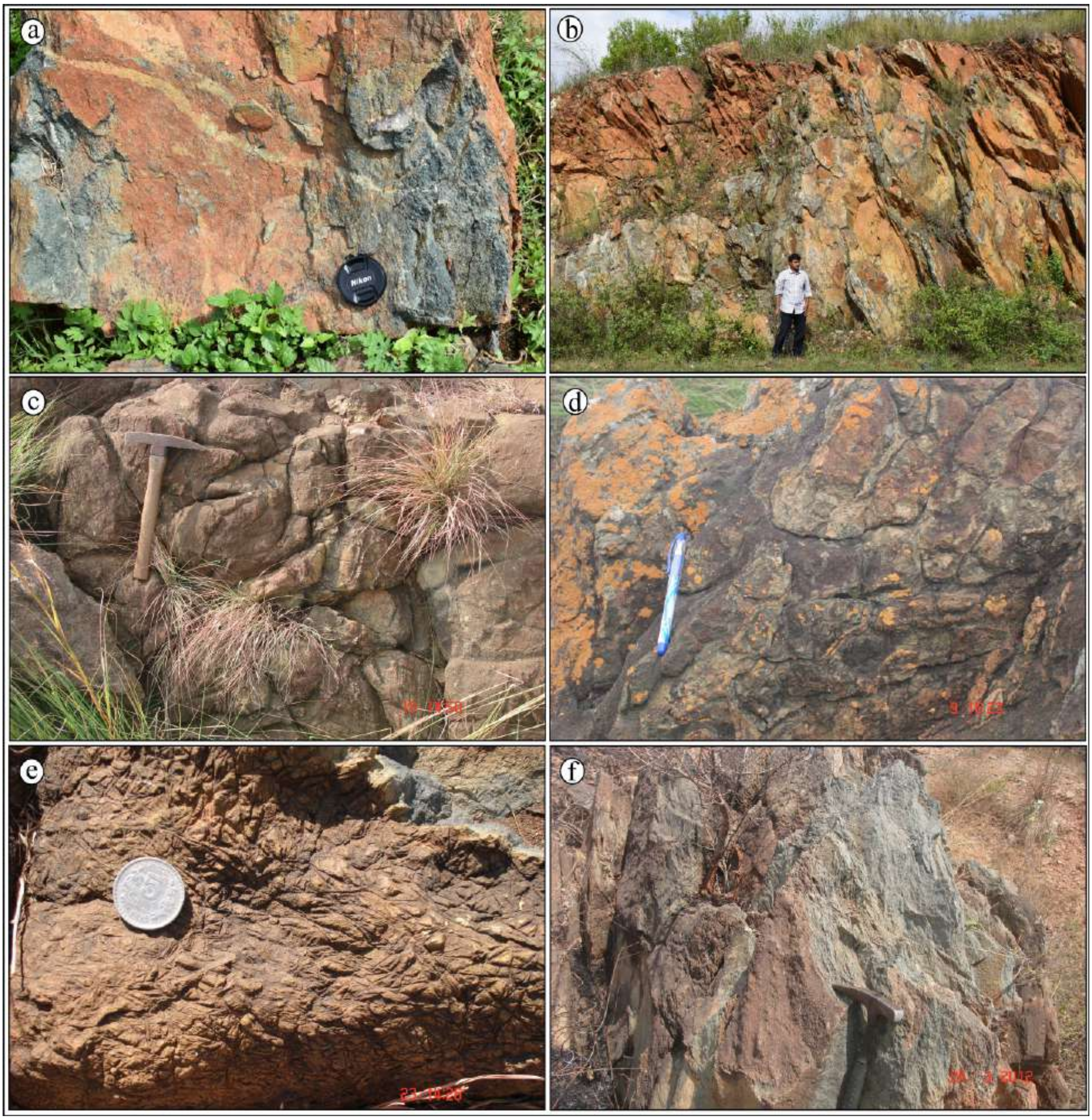

Fig. 5.1a-f

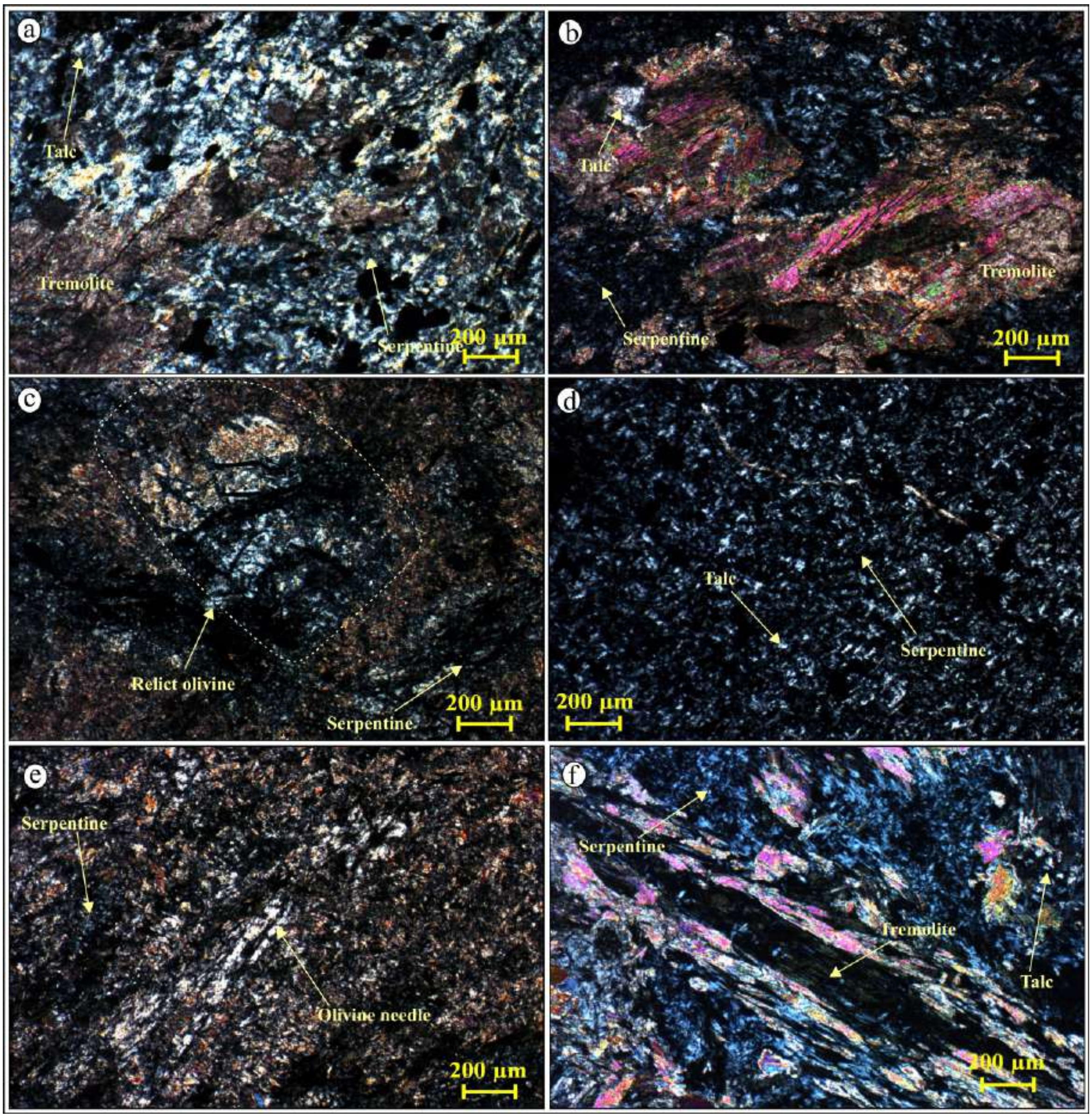
a
Talc
Tremolite
Serpentine
200 µm
b
Talc
Tremolite
Serpentine
200 µm
c
Relict olivine
Serpentine
200 µm
d
Talc
Serpentine
200 µm
e
Serpentine
Olivine needle
200 µm
f
Serpentine
Tremolite
Talc
200 µm

Fig. 5.2 a-f

Fig. 6.1 a-f

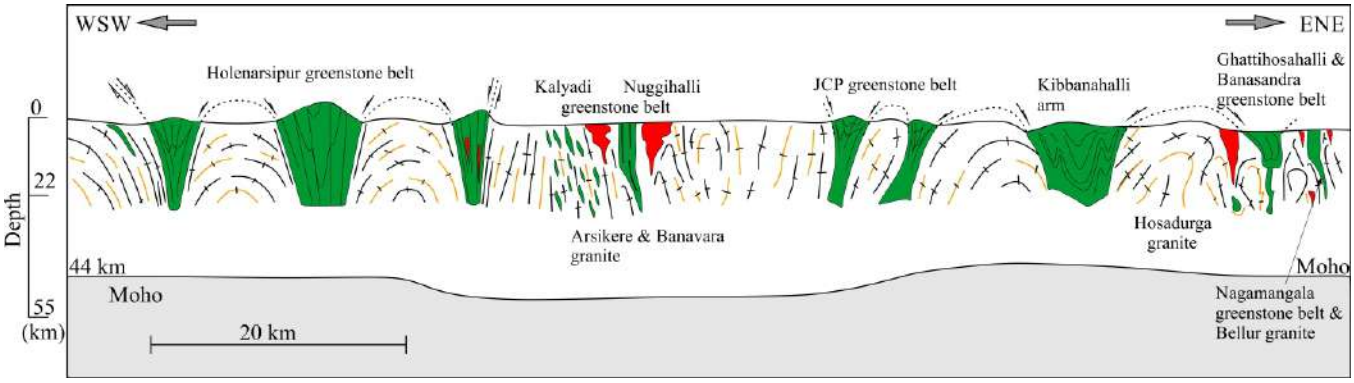

Fig. 6.1 g

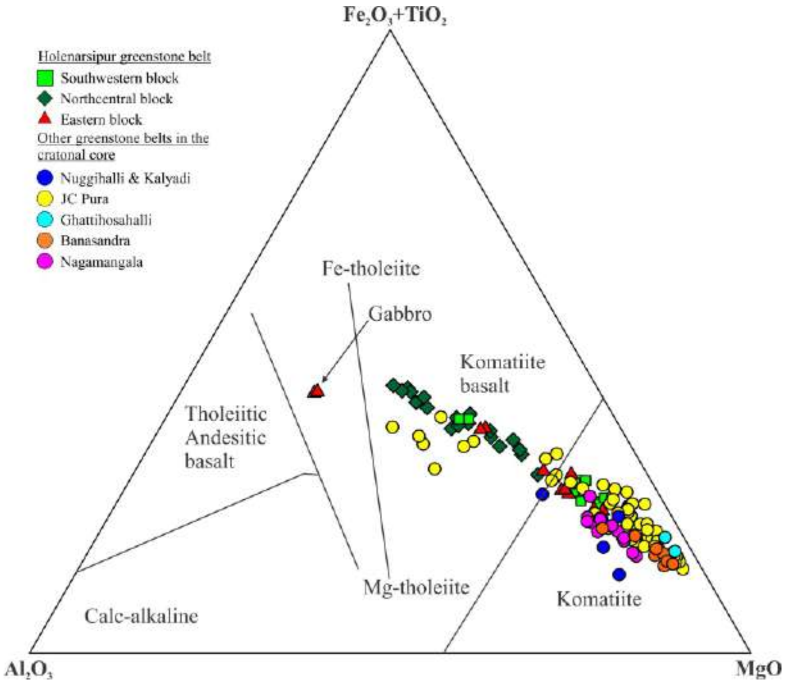

Fig. 7.1a

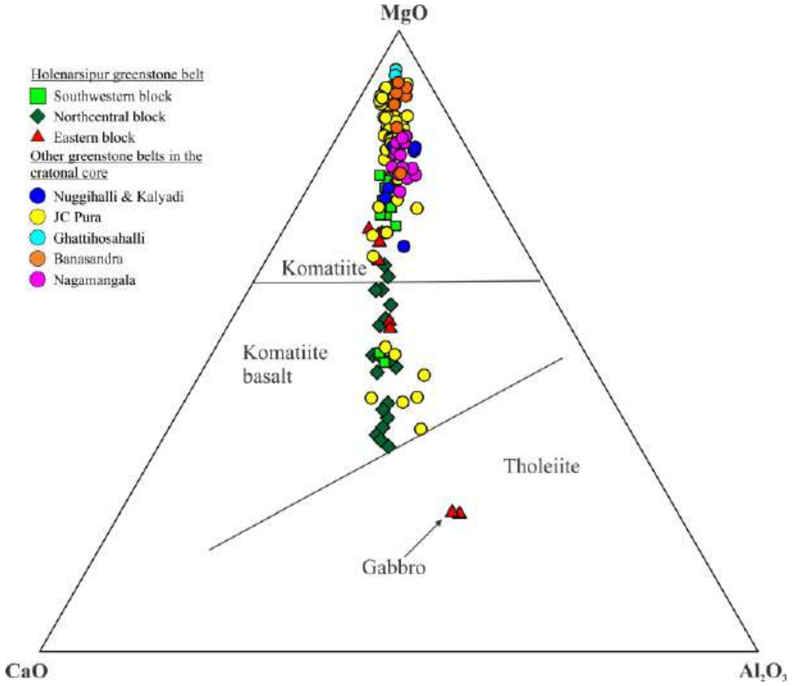

Fig. 7.1b

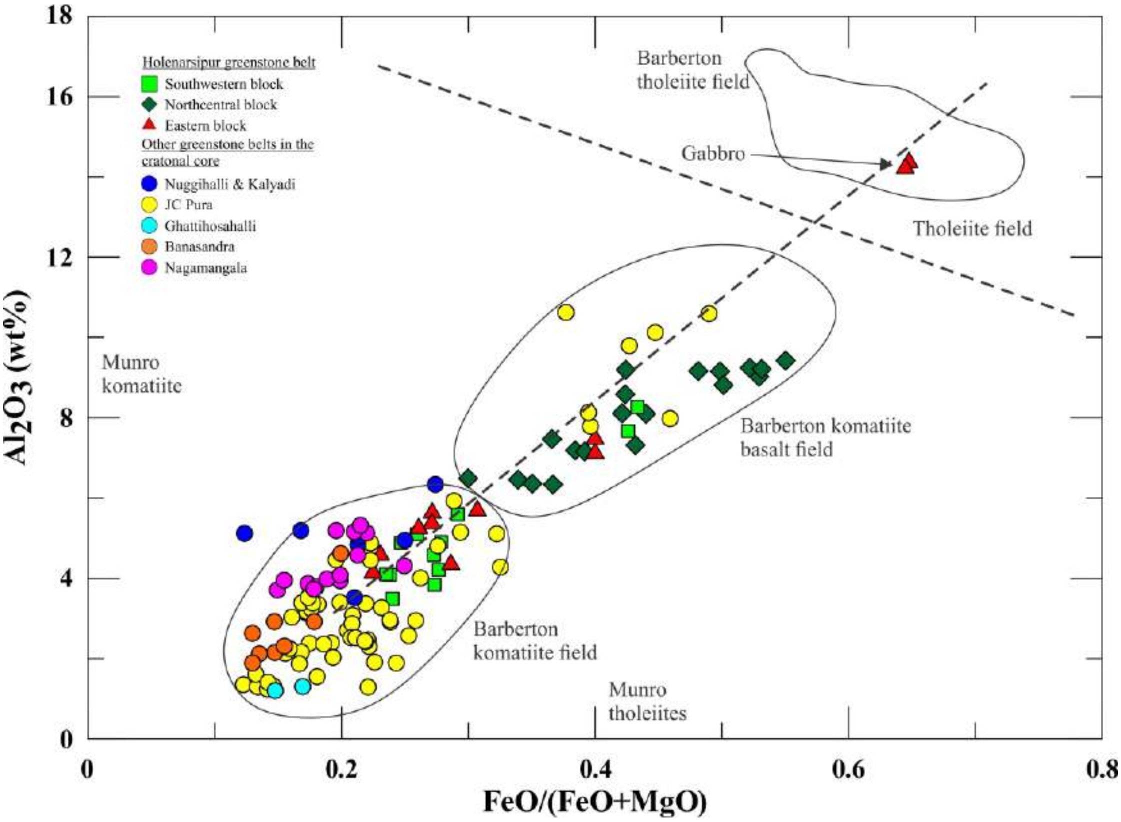
18
16
12
8
4
0
Al$_2$O$_3$ (wt%)
0
0.2
0.4
0.6
0.8
FeO/(FeO+MgO)
Holenarsipur greenstone belt
Southwestern block
Northcentral block
Eastern block
Other greenstone belts in the cratonal core
Nuggihalli & Kalyadi
JC Pura
Ghattihosahalli
Banasandra
Nagamangala
Barberton tholeiite field
Gabbro
Tholeiite field
Munro komatiite
Barberton komatiite basalt field
Barberton komatiite field
Munro tholeiites

Fig. 7.1c

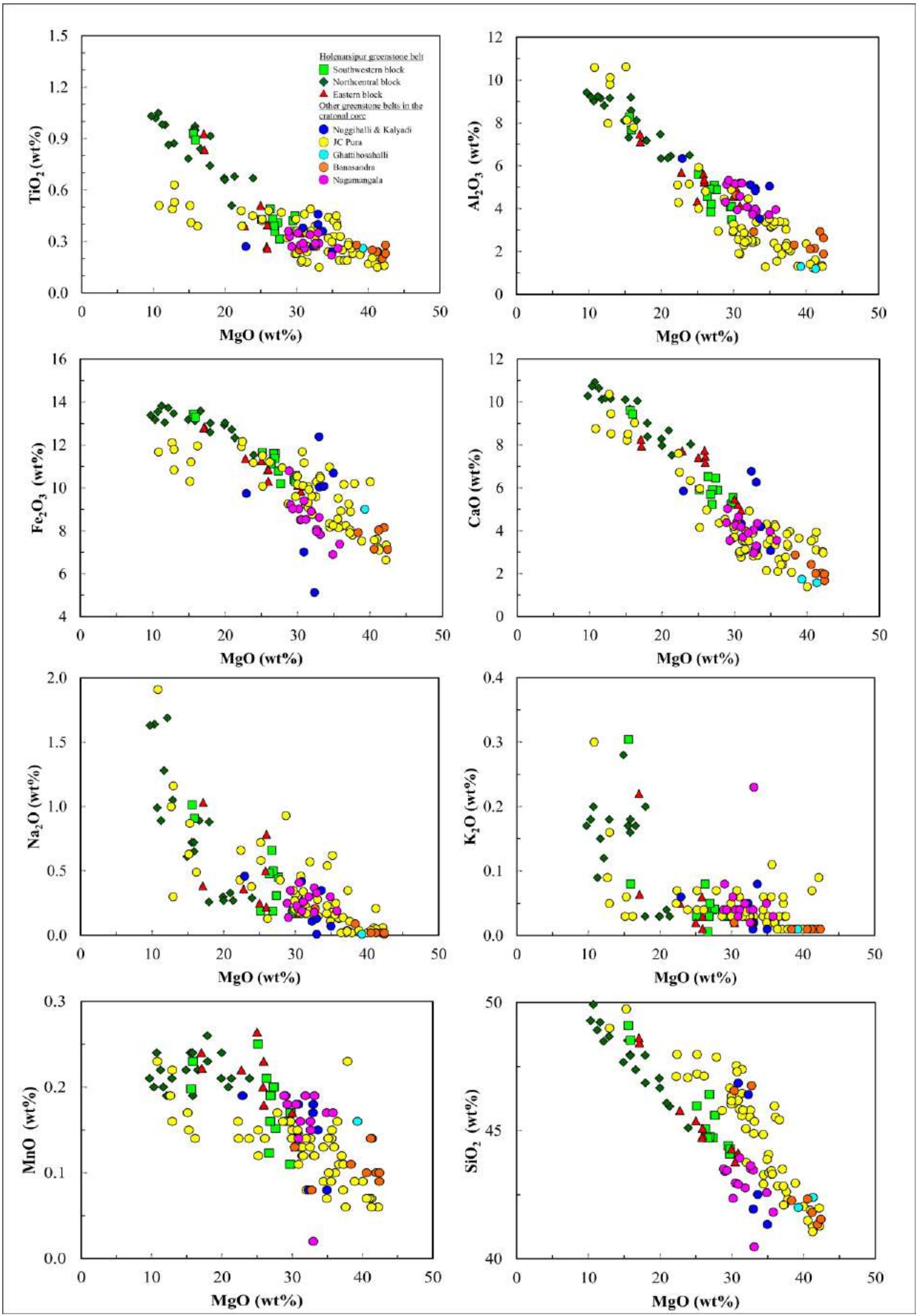
Holenarsipur greenstone belt
Southwestern block
Northcentral block
Eastern block
Other greenstone belts in the cratonal core
Nuggihalli & Kalyadi
JC Pura
Ghattihosahalli
Banasandra
Nagamangala
TiO_2 (wt%)
0.0
0.3
0.6
0.9
1.2
1.5
Al_2O_3 (wt%)
0
2
4
6
8
10
12
Fe_2O_3 (wt%)
4
6
8
10
12
14
16
CaO (wt%)
0
2
4
6
8
10
12
Na_2O (wt%)
0.0
0.5
1.0
1.5
2.0
K_2O (wt%)
0.0
0.1
0.2
0.3
0.4
MnO (wt%)
0.0
0.1
0.2
0.3
SiO_2 (wt%)
40
45
50
MgO (wt%)
0
10
20
30
40
50

Fig. 7.1d

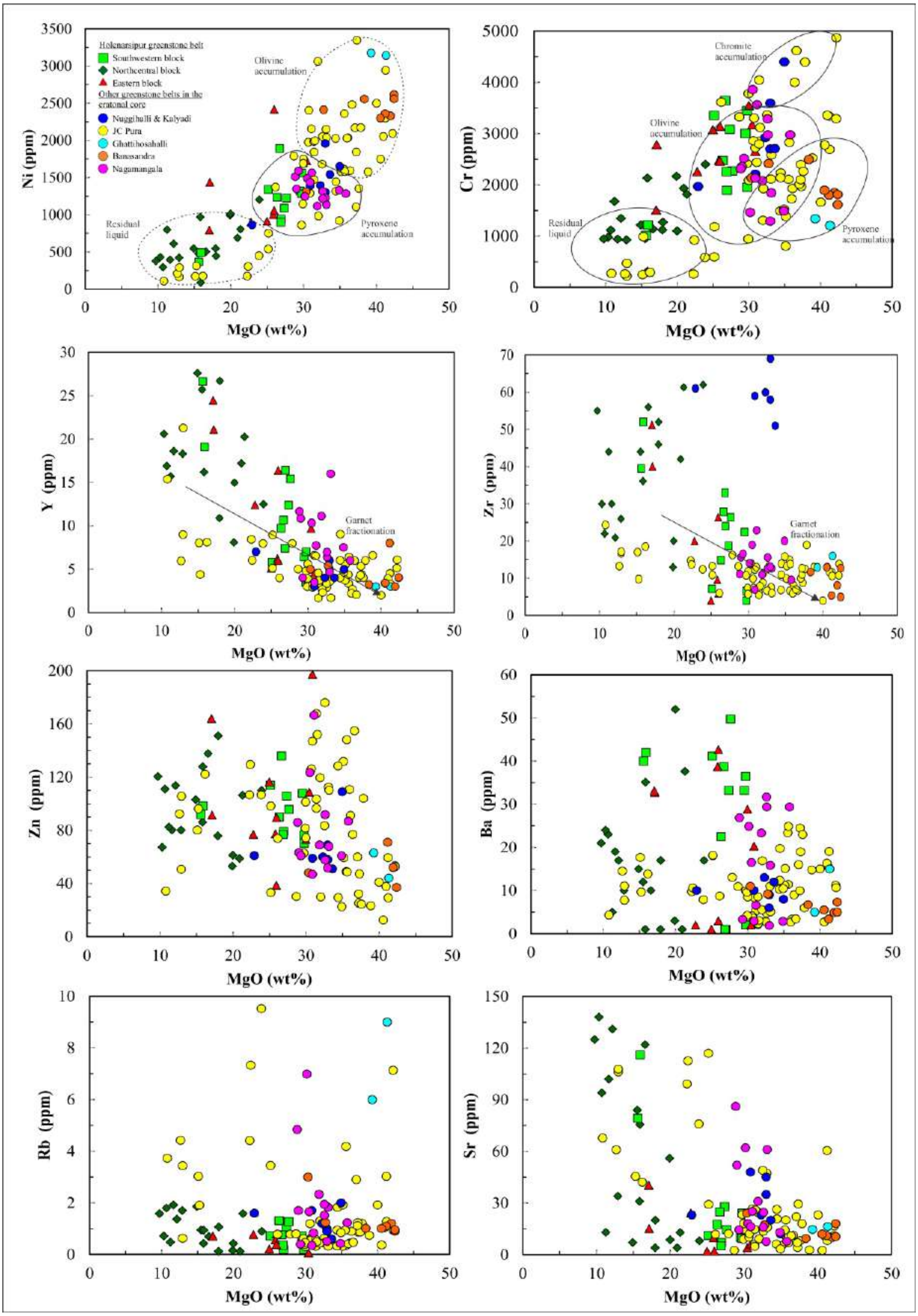
Holenarsipur greenstone belt
🟩 Southwestern block
◆ Northcentral block
▲ Eastern block
Other greenstone belts in the cratonal core
● Nuggihalli & Kalyadi
● JC Pura
● Ghattihosahalli
● Banasandra
● Nagamangala
Olivine accumulation
Residual liquid
Pyroxene accumulation
Chromite accumulation
Garnet fractionation
Ni (ppm)
Cr (ppm)
Y (ppm)
Zr (ppm)
Zn (ppm)
Ba (ppm)
Rb (ppm)
Sr (ppm)
MgO (wt%)
0
10
20
30
40
50

Fig. 7.1e

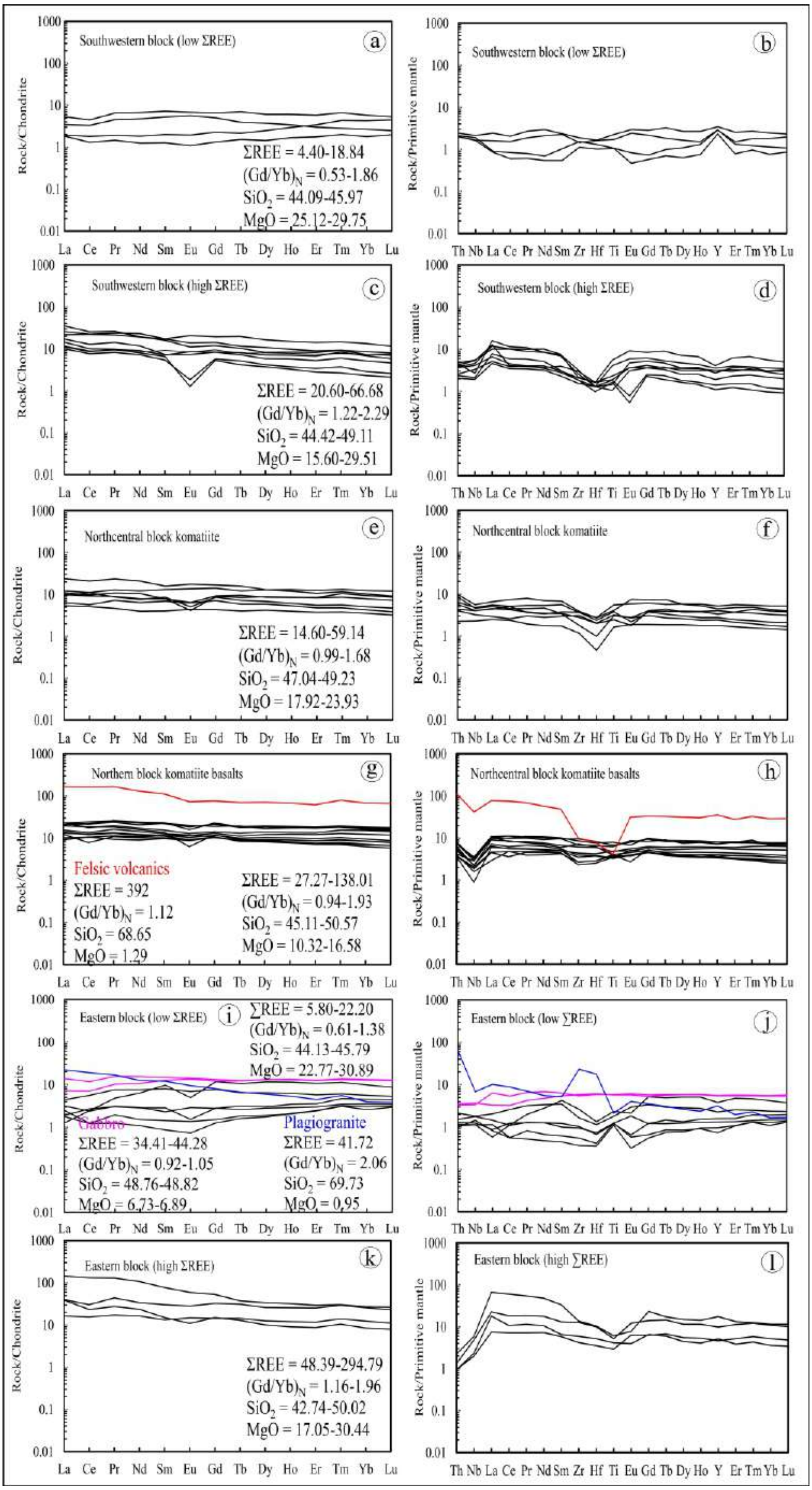
Southwestern block (low ΣREE)
a
ΣREE = 4.40-18.84
(Gd/Yb)$_N$ = 0.53-1.86
SiO$_2$ = 44.09-45.97
MgO = 25.12-29.75
Southwestern block (low ΣREE)
b
Southwestern block (high ΣREE)
c
ΣREE = 20.60-66.68
(Gd/Yb)$_N$ = 1.22-2.29
SiO$_2$ = 44.42-49.11
MgO = 15.60-29.51
Southwestern block (high ΣREE)
d
Northcentral block komatiite
e
ΣREE = 14.60-59.14
(Gd/Yb)$_N$ = 0.99-1.68
SiO$_2$ = 47.04-49.23
MgO = 17.92-23.93
Northcentral block komatiite
f
Northern block komatiite basalts
g
Felsic volcanics
ΣREE = 392
(Gd/Yb)$_N$ = 1.12
SiO$_2$ = 68.65
MgO = 1.29
ΣREE = 27.27-138.01
(Gd/Yb)$_N$ = 0.94-1.93
SiO$_2$ = 45.11-50.57
MgO = 10.32-16.58
Northcentral block komatiite basalts
h
Eastern block (low ΣREE)
i
ΣREE = 5.80-22.20
(Gd/Yb)$_N$ = 0.61-1.38
SiO$_2$ = 44.13-45.79
MgO = 22.77-30.89
Gabbro
ΣREE = 34.41-44.28
(Gd/Yb)$_N$ = 0.92-1.05
SiO$_2$ = 48.76-48.82
MgO = 6.73-6.89
Plagiogranite
ΣREE = 41.72
(Gd/Yb)$_N$ = 2.06
SiO$_2$ = 69.73
MgO = 0.95
Eastern block (low ∑REE)
j
Eastern block (high ΣREE)
k
ΣREE = 48.39-294.79
(Gd/Yb)$_N$ = 1.16-1.96
SiO$_2$ = 42.74-50.02
MgO = 17.05-30.44
Eastern block (high ∑REE)
l
Rock/Chondrite
Rock/Primitive mantle
1000
100
10
1
0.1
0.01
La Ce Pr Nd Sm Eu Gd Tb Dy Ho Er Tm Yb Lu
Th Nb La Ce Pr Nd Sm Zr Hf Ti Eu Gd Tb Dy Ho Y Er Tm Yb Lu

Fig. 7.2a-l

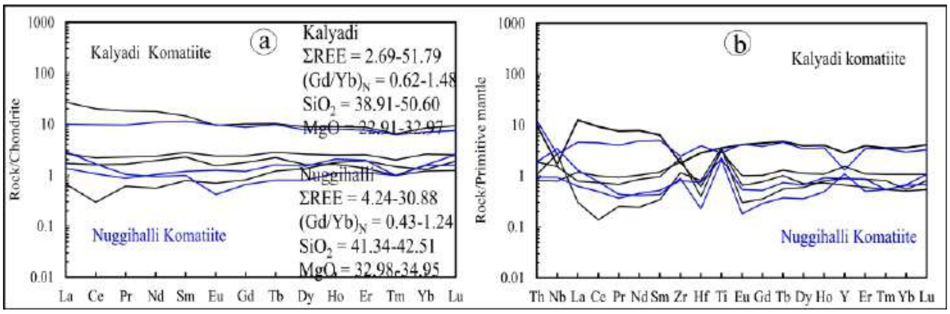

Fig. 7.3a-b

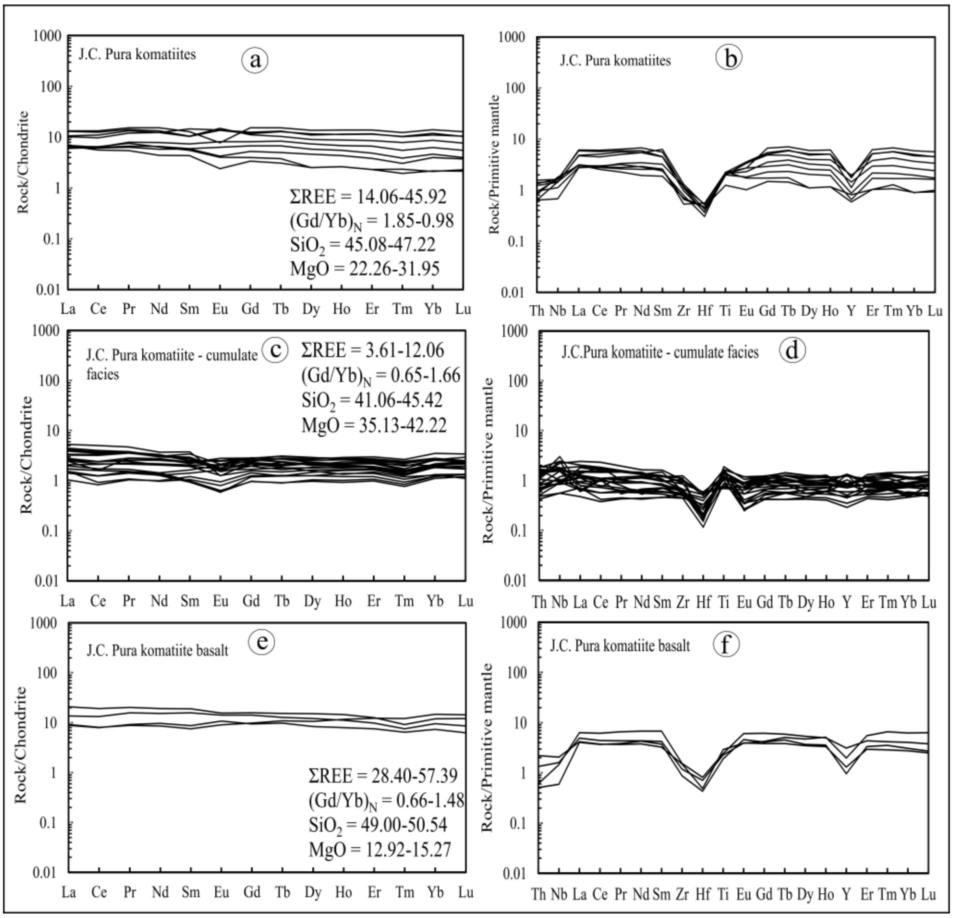

Fig. 7.4a-f

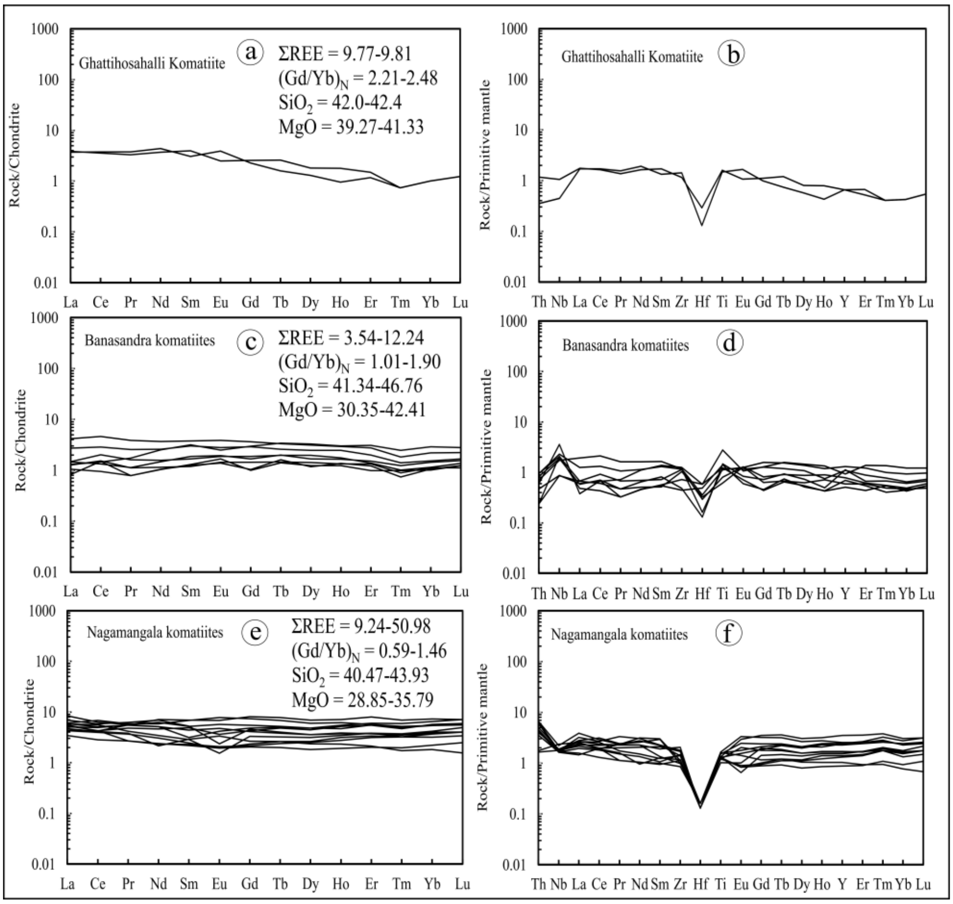
Ghattihosahalli Komatiite
a
ΣREE = 9.77-9.81
$(Gd/Yb)_N$ = 2.21-2.48
SiO_2 = 42.0-42.4
MgO = 39.27-41.33
Rock/Chondrite
1000
100
10
1
0.1
0.01
La Ce Pr Nd Sm Eu Gd Tb Dy Ho Er Tm Yb Lu
Ghattihosahalli Komatiite
b
Rock/Primitive mantle
Th Nb La Ce Pr Nd Sm Zr Hf Ti Eu Gd Tb Dy Ho Y Er Tm Yb Lu
Banasandra komatiites
c
ΣREE = 3.54-12.24
$(Gd/Yb)_N$ = 1.01-1.90
SiO_2 = 41.34-46.76
MgO = 30.35-42.41
Banasandra komatiites
d
Nagamangala komatiites
e
ΣREE = 9.24-50.98
$(Gd/Yb)_N$ = 0.59-1.46
SiO_2 = 40.47-43.93
MgO = 28.85-35.79
Nagamangala komatiites
f

Fig. 7.5a-f

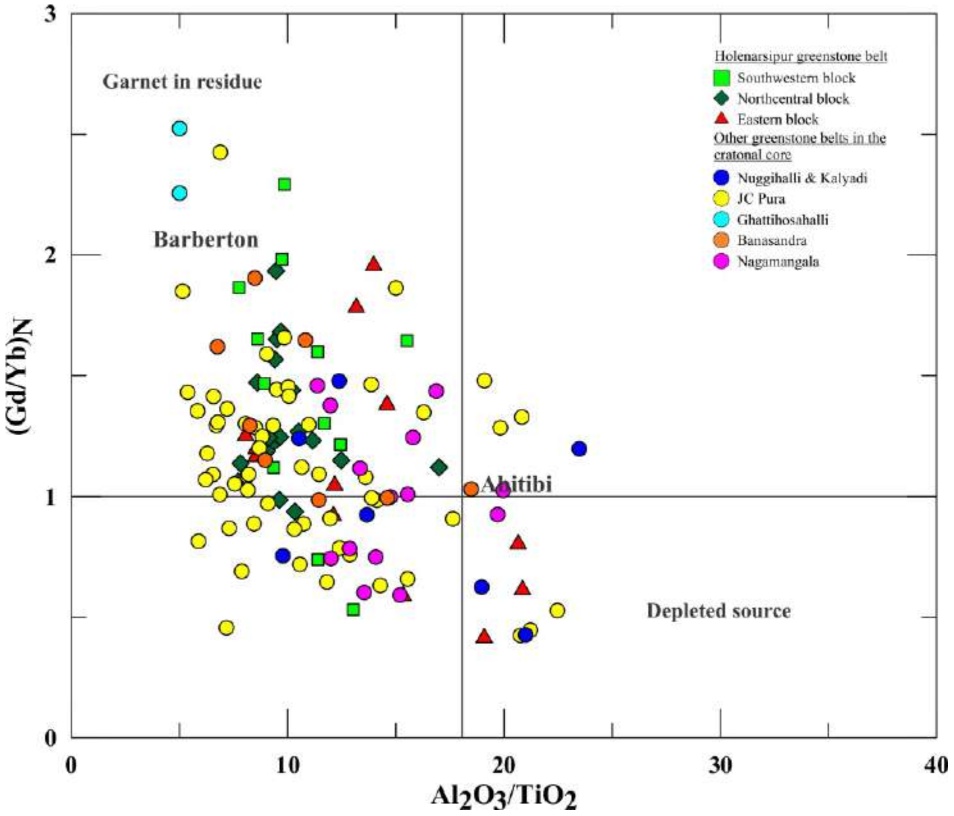

Fig. 7.6a

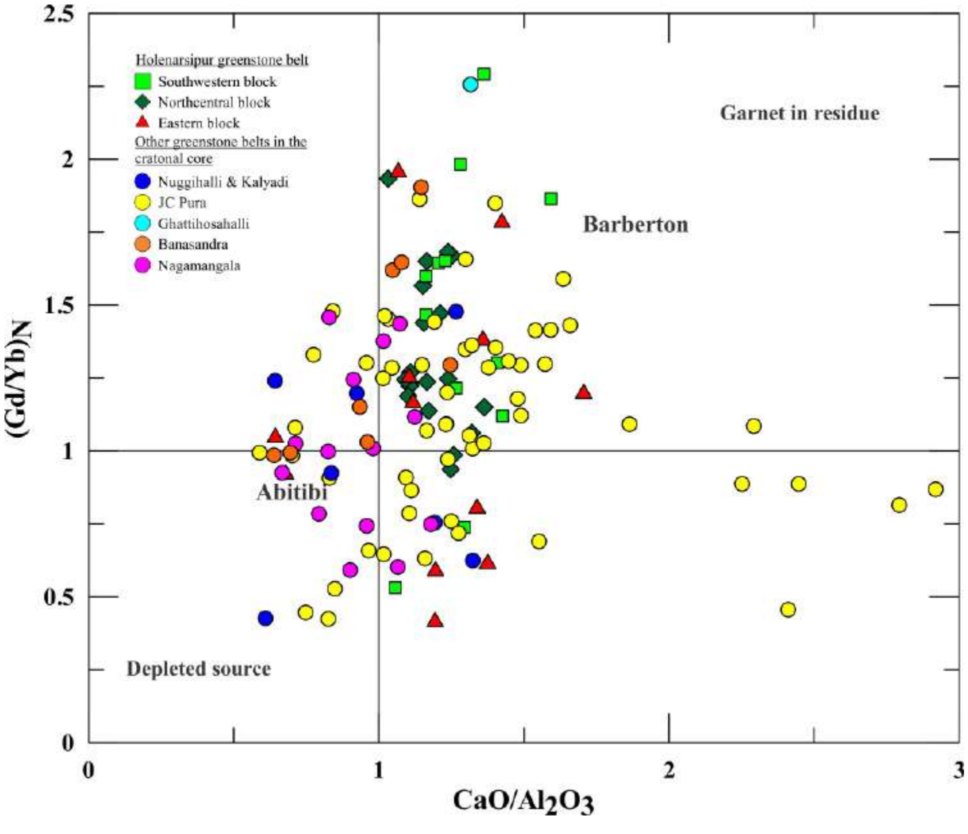

Fig. 7.6b

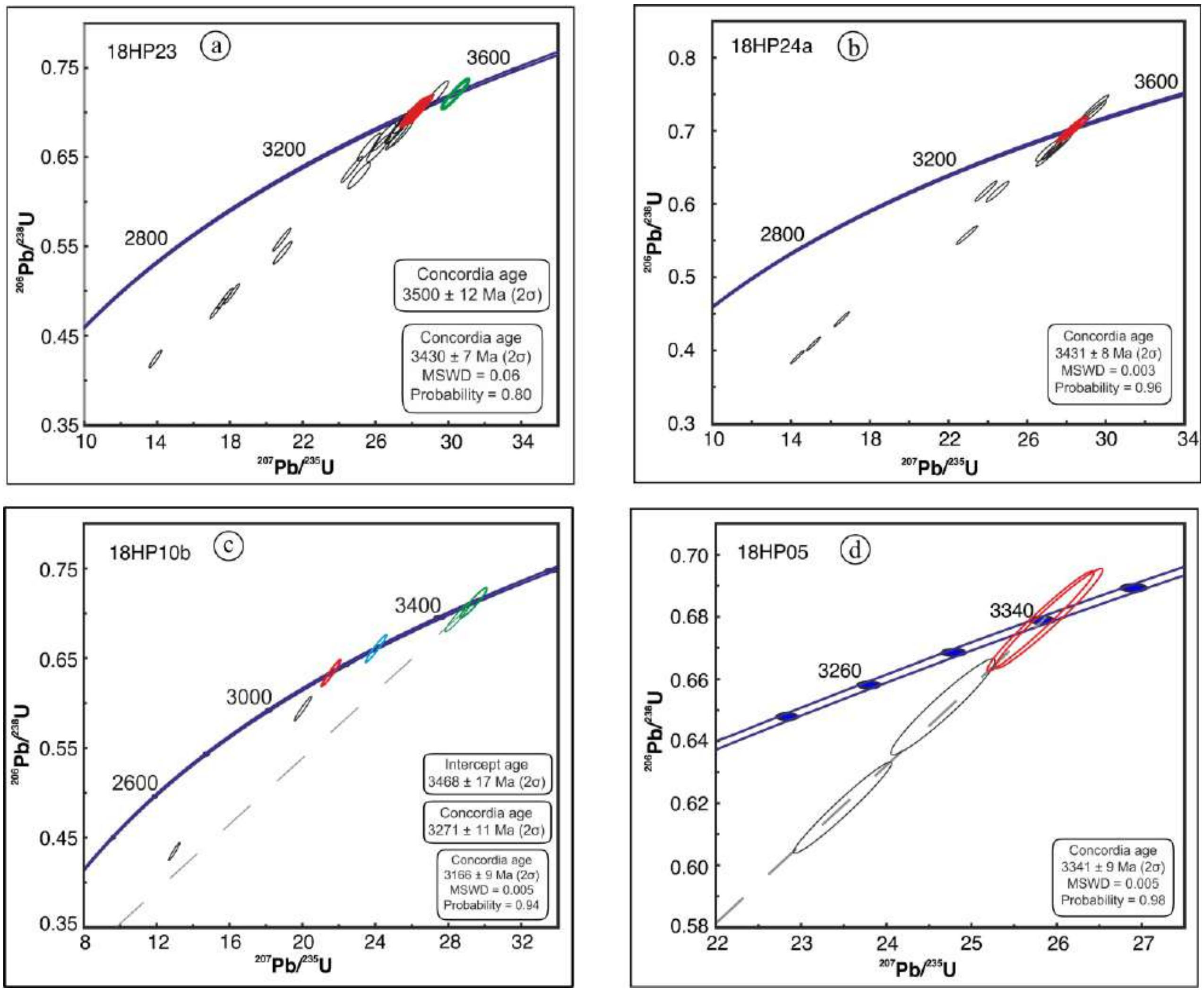
18HP23
a
3600
3200
2800
Concordia age
3500 ± 12 Ma (2σ)
Concordia age
3430 ± 7 Ma (2σ)
MSWD = 0.06
Probability = 0.80
^{206}Pb/^{238}U
^{207}Pb/^{235}U
0.75
0.65
0.55
0.45
0.35
10
14
18
22
26
30
34
18HP24a
b
3600
3200
2800
Concordia age
3431 ± 8 Ma (2σ)
MSWD = 0.003
Probability = 0.96
^{206}Pb/^{238}U
^{207}Pb/^{235}U
0.8
0.7
0.6
0.5
0.4
0.3
10
14
18
22
26
30
34
18HP10b
c
3400
3000
2600
Intercept age
3468 ± 17 Ma (2σ)
Concordia age
3271 ± 11 Ma (2σ)
Concordia age
3166 ± 9 Ma (2σ)
MSWD = 0.005
Probability = 0.94
^{206}Pb/^{238}U
^{207}Pb/^{235}U
0.75
0.65
0.55
0.45
0.35
8
12
16
20
24
28
32
18HP05
d
3340
3260
Concordia age
3341 ± 9 Ma (2σ)
MSWD = 0.005
Probability = 0.98
^{206}Pb/^{238}U
^{207}Pb/^{235}U
0.70
0.68
0.66
0.64
0.62
0.60
0.58
22
23
24
25
26
27

Fig. 7.7a-d

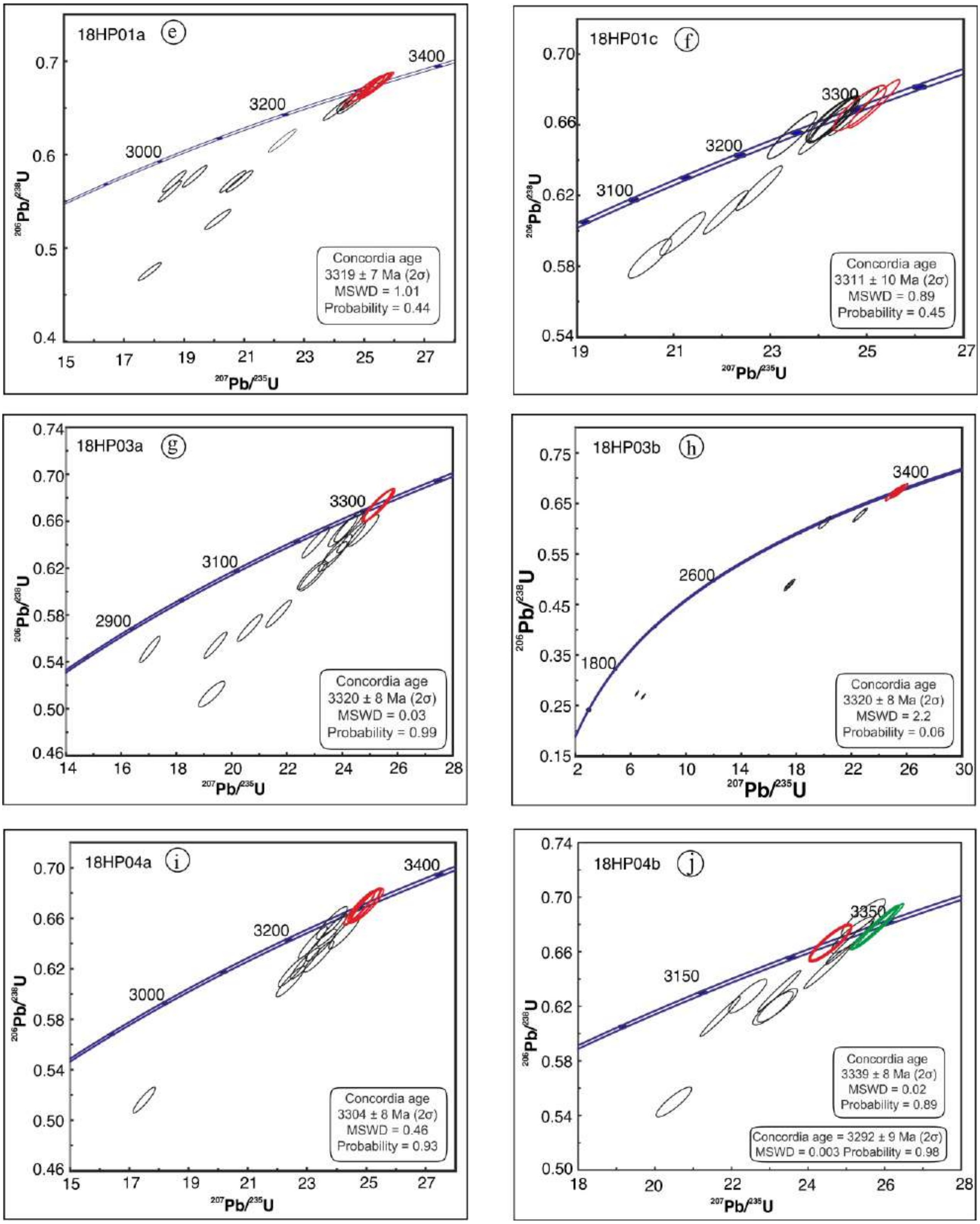
18HP01a
e
3400
3200
3000
0.7
0.6
0.5
0.4
15
17
19
21
23
25
27
$^{206}Pb/^{238}U$
$^{207}Pb/^{235}U$
Concordia age
3319 ± 7 Ma (2σ)
MSWD = 1.01
Probability = 0.44
18HP01c
f
3300
3200
3100
0.70
0.66
0.62
0.58
0.54
19
21
23
25
27
$^{206}Pb/^{238}U$
$^{207}Pb/^{235}U$
Concordia age
3311 ± 10 Ma (2σ)
MSWD = 0.89
Probability = 0.45
18HP03a
g
3300
3100
2900
0.74
0.70
0.66
0.62
0.58
0.54
0.50
0.46
14
16
18
20
22
24
26
28
$^{206}Pb/^{238}U$
$^{207}Pb/^{235}U$
Concordia age
3320 ± 8 Ma (2σ)
MSWD = 0.03
Probability = 0.99
18HP03b
h
3400
2600
1800
0.75
0.65
0.55
0.45
0.35
0.25
0.15
2
6
10
14
18
22
26
30
$^{206}Pb/^{238}U$
$^{207}Pb/^{235}U$
Concordia age
3320 ± 8 Ma (2σ)
MSWD = 2.2
Probability = 0.06
18HP04a
i
3400
3200
3000
0.70
0.66
0.62
0.58
0.54
0.50
0.46
15
17
19
21
23
25
27
$^{206}Pb/^{238}U$
$^{207}Pb/^{235}U$
Concordia age
3304 ± 8 Ma (2σ)
MSWD = 0.46
Probability = 0.93
18HP04b
j
3350
3150
0.74
0.70
0.66
0.62
0.58
0.54
0.50
18
20
22
24
26
28
$^{206}Pb/^{238}U$
$^{207}Pb/^{235}U$
Concordia age
3339 ± 8 Ma (2σ)
MSWD = 0.02
Probability = 0.89
Concordia age = 3292 ± 9 Ma (2σ)
MSWD = 0.003 Probability = 0.98

Fig. 7.7e-j

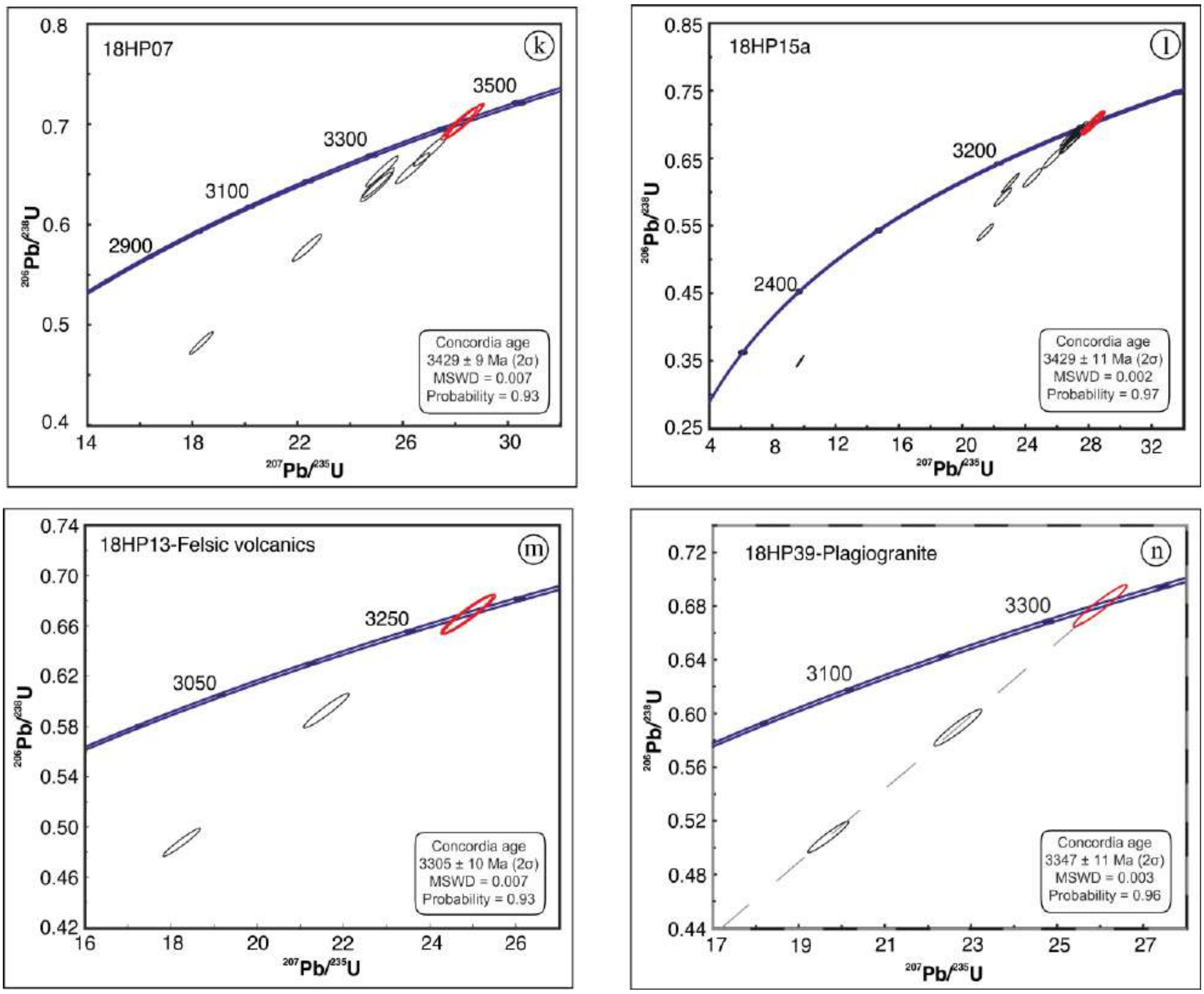
18HP07
k
3500
3300
3100
2900
Concordia age
3429 ± 9 Ma (2σ)
MSWD = 0.007
Probability = 0.93
0.8
0.7
0.6
0.5
0.4
14
18
22
26
30
^{206}Pb/^{238}U
^{207}Pb/^{235}U
18HP15a
l
3200
2400
Concordia age
3429 ± 11 Ma (2σ)
MSWD = 0.002
Probability = 0.97
0.85
0.75
0.65
0.55
0.45
0.35
0.25
4
8
12
16
20
24
28
32
^{206}Pb/^{238}U
^{207}Pb/^{235}U
18HP13-Felsic volcanics
m
3250
3050
Concordia age
3305 ± 10 Ma (2σ)
MSWD = 0.007
Probability = 0.93
0.74
0.70
0.66
0.62
0.58
0.54
0.50
0.46
0.42
16
18
20
22
24
26
^{206}Pb/^{238}U
^{207}Pb/^{235}U
18HP39-Plagiogranite
n
3300
3100
Concordia age
3347 ± 11 Ma (2σ)
MSWD = 0.003
Probability = 0.96
0.72
0.68
0.64
0.60
0.56
0.52
0.48
0.44
17
19
21
23
25
27
^{206}Pb/^{238}U
^{207}Pb/^{235}U

Fig. 7.7k-n

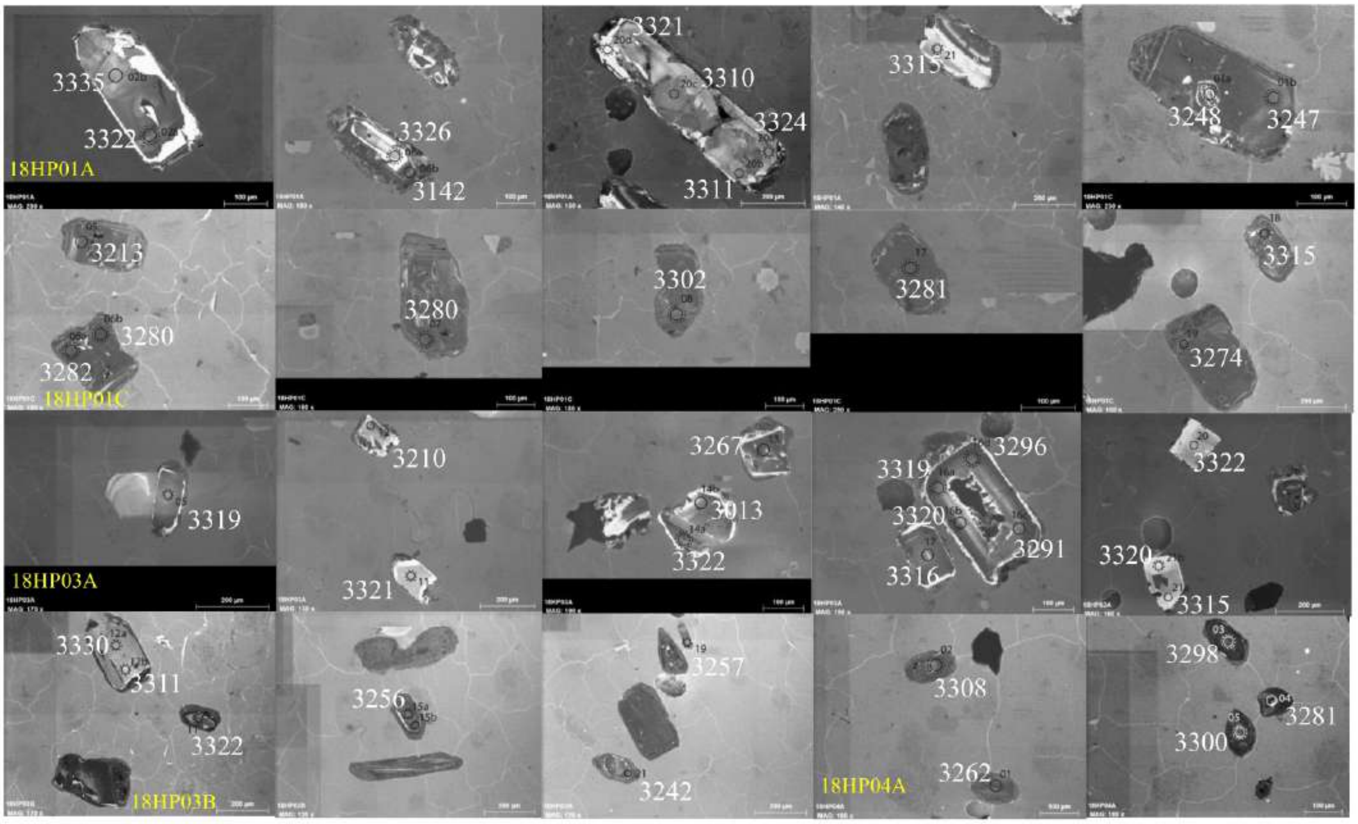

Fig. 7.8a

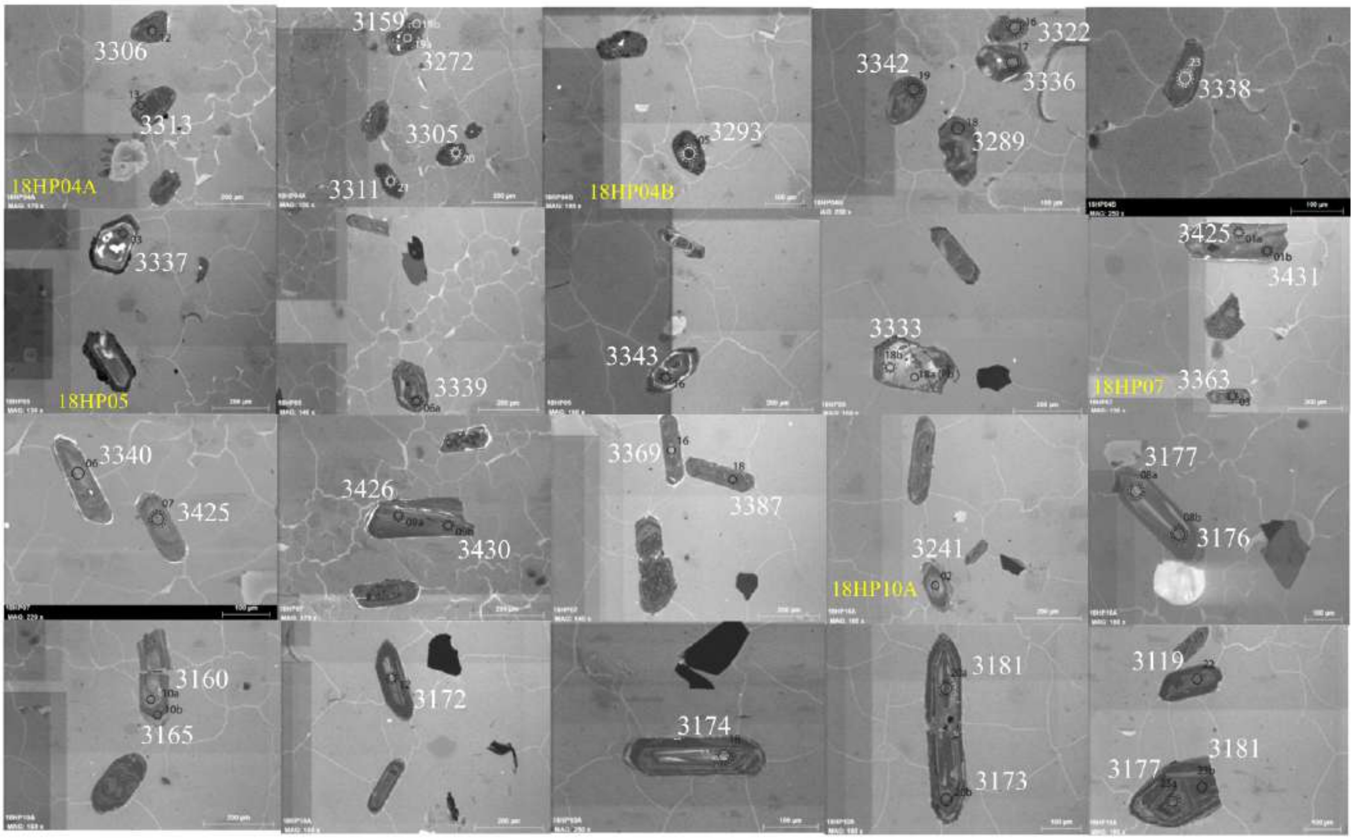

Fig. 7.8b

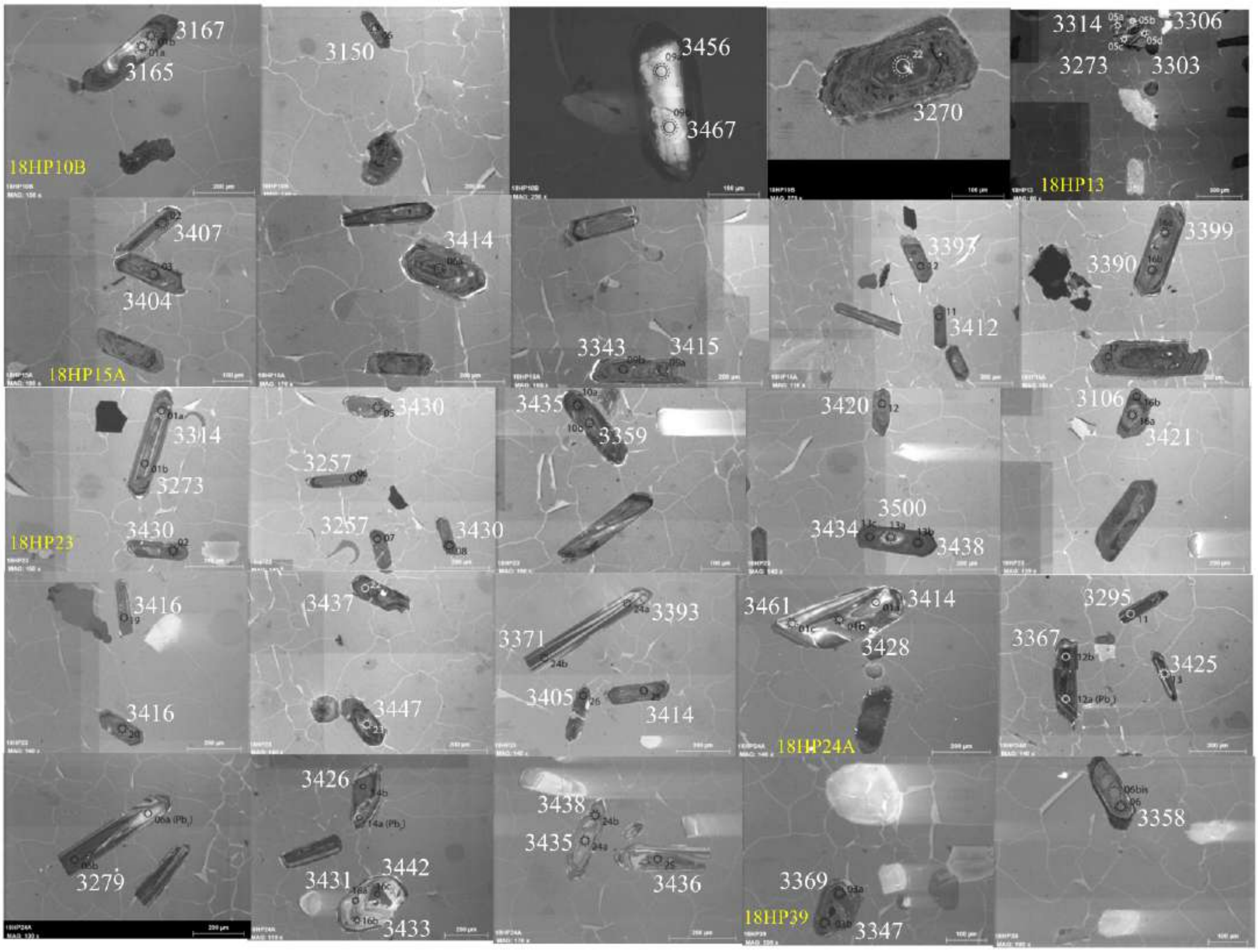
3167
01b
01a
3165
18HP10B
05
3150
3456
09a
09b
3467
22
3270
3314
05a
05b
3306
05c
05d
3273
3303
18HP13
02
3407
03
3404
18HP15A
3414
06a
3343
3415
09b
09a
3397
12
11
3412
16a
3399
3390
16b
17
01a
3314
01b
3273
18HP23
3430
02
05
3430
3257
06
3257
07
3430
08
3435
10a
10b
3359
3420
12
3500
3434
13c
13a
13b
3438
3106
16b
16a
3421
3416
19
3416
20
3437
3447
21
24a
3393
3371
24b
3405
26
3414
3461
01a
3414
01c
01b
3428
18HP24A
3295
11
3367
12b
3425
13
12a (Pb)
06a (Pb)
3279
05b
3426
14b
14a (Pb)
3431
3442
16a
16c
16b
3433
3438
24b
3435
24a
3436
25
3369
03a
18HP39
03b
3347
06bis
06
3358

Fig. 7.8c

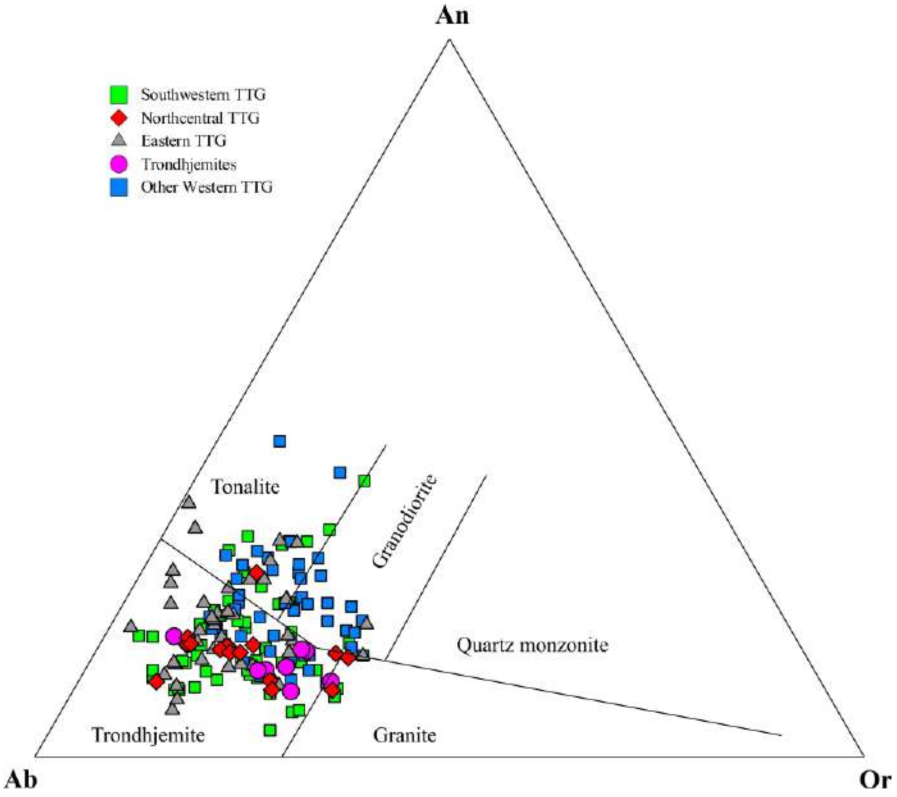

Fig. 7.9a

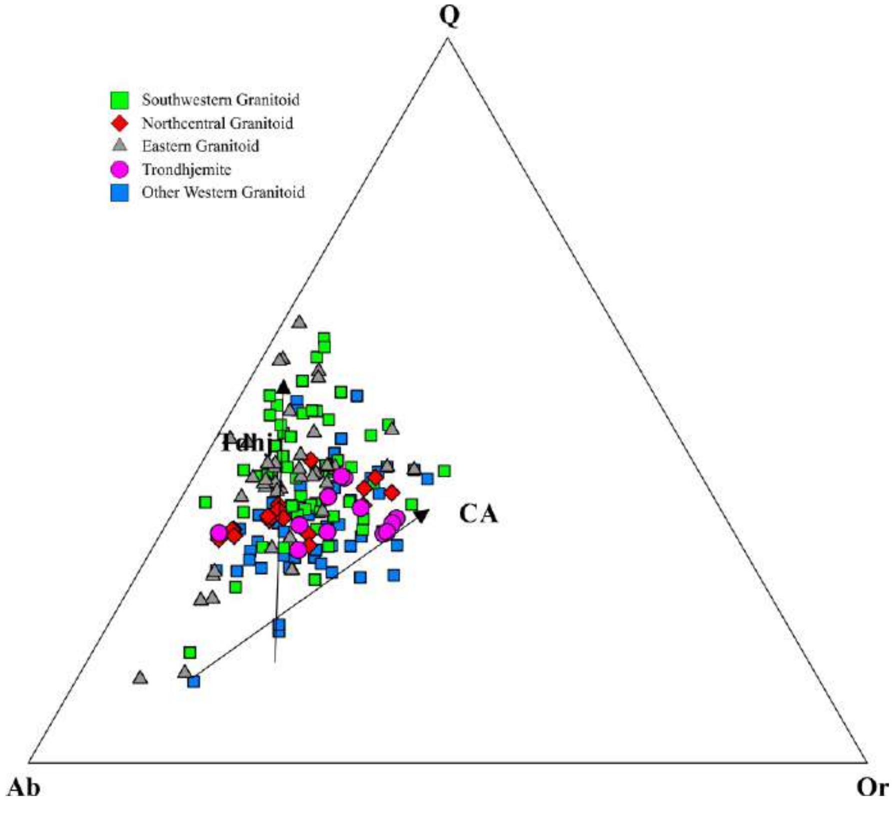

Fig. 7.9b

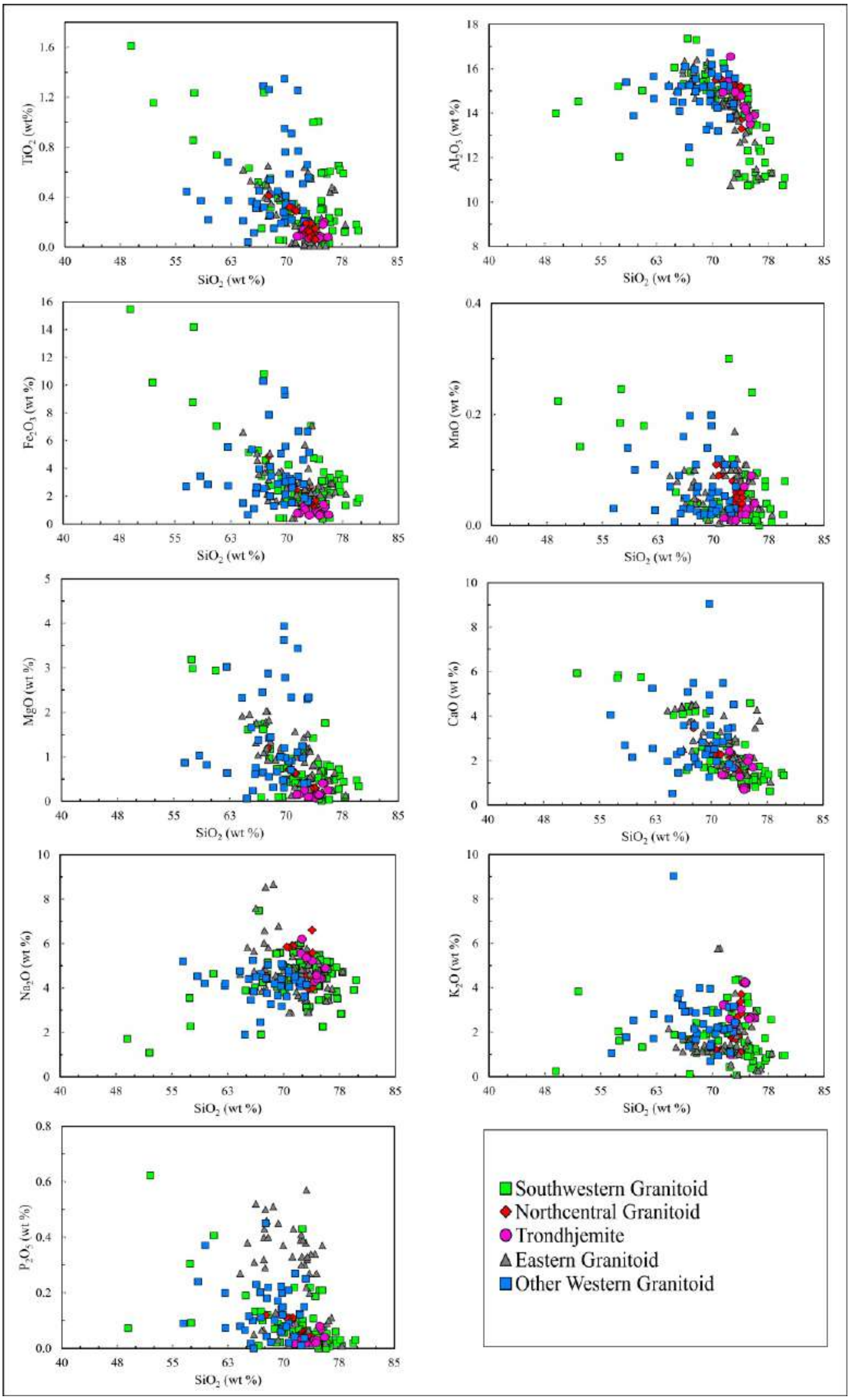

TiO$_2$ (wt%)
Al$_2$O$_3$ (wt %)
Fe$_2$O$_3$ (wt %)
MnO (wt %)
MgO (wt %)
CaO (wt %)
Na$_2$O (wt %)
K$_2$O (wt %)
P$_2$O$_5$ (wt %)
SiO$_2$ (wt %)
40
48
55
63
70
78
85
🟩 Southwestern Granitoid
◆ Northcentral Granitoid
● Trondhjemite
▲ Eastern Granitoid
🟦 Other Western Granitoid

Fig. 7.9c

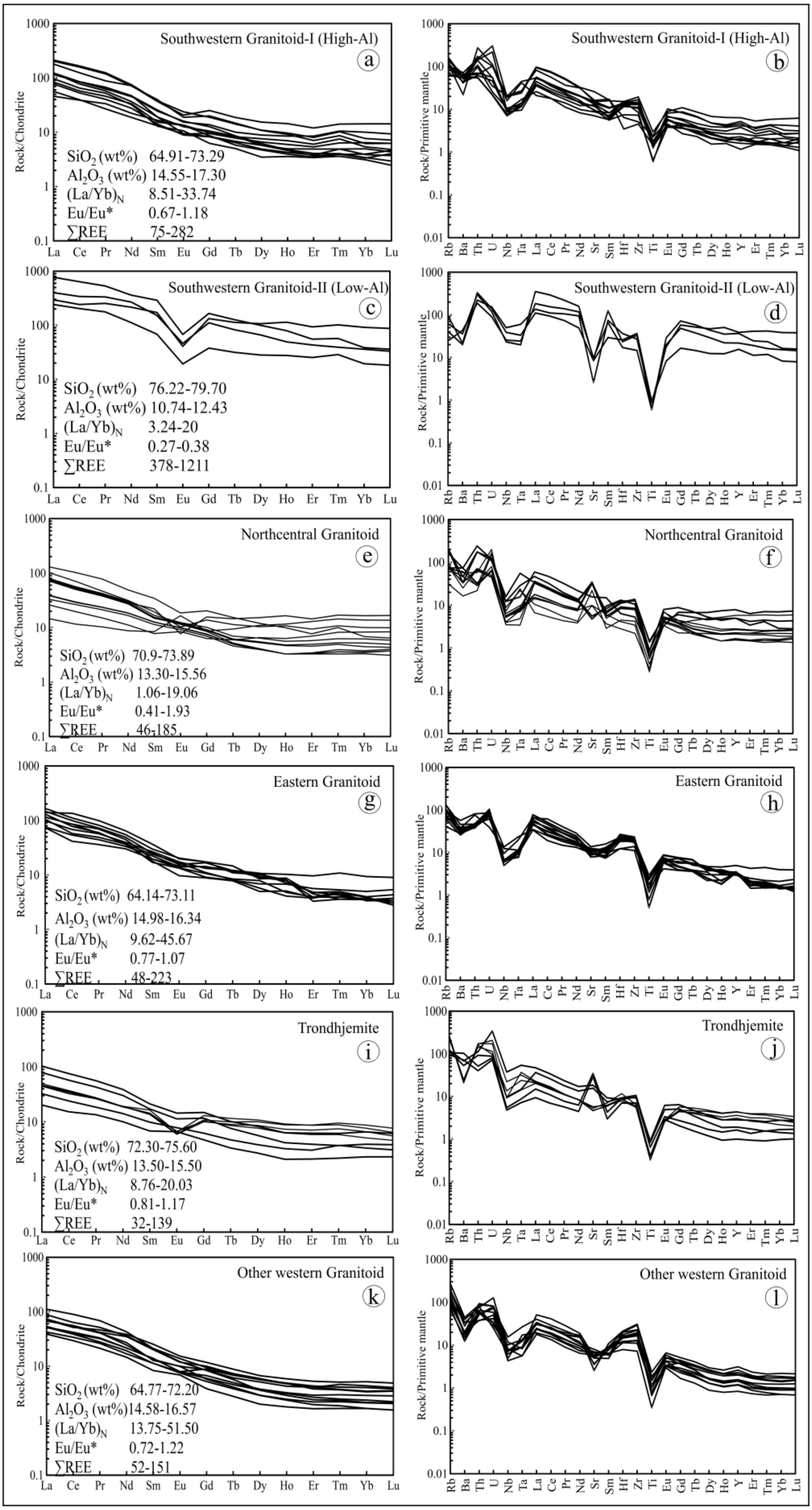
Southwestern Granitoid-I (High-Al)
a
Rock/Chondrite
SiO$_2$ (wt%) 64.91-73.29
Al$_2$O$_3$ (wt%) 14.55-17.30
(La/Yb)$_N$ 8.51-33.74
Eu/Eu* 0.67-1.18
∑REE 75-282
b
Rock/Primitive mantle
Southwestern Granitoid-II (Low-Al)
c
SiO$_2$ (wt%) 76.22-79.70
Al$_2$O$_3$ (wt%) 10.74-12.43
(La/Yb)$_N$ 3.24-20
Eu/Eu* 0.27-0.38
∑REE 378-1211
d
Northcentral Granitoid
e
SiO$_2$ (wt%) 70.9-73.89
Al$_2$O$_3$ (wt%) 13.30-15.56
(La/Yb)$_N$ 1.06-19.06
Eu/Eu* 0.41-1.93
∑REE 46-185
f
Eastern Granitoid
g
SiO$_2$ (wt%) 64.14-73.11
Al$_2$O$_3$ (wt%) 14.98-16.34
(La/Yb)$_N$ 9.62-45.67
Eu/Eu* 0.77-1.07
∑REE 48-223
h
Trondhjemite
i
SiO$_2$ (wt%) 72.30-75.60
Al$_2$O$_3$ (wt%) 13.50-15.50
(La/Yb)$_N$ 8.76-20.03
Eu/Eu* 0.81-1.17
∑REE 32-139
j
Other western Granitoid
k
SiO$_2$ (wt%) 64.77-72.20
Al$_2$O$_3$ (wt%)14.58-16.57
(La/Yb)$_N$ 13.75-51.50
Eu/Eu* 0.72-1.22
∑REE 52-151
l
1000
100
10
1
0.1
0.01
La Ce Pr Nd Sm Eu Gd Tb Dy Ho Er Tm Yb Lu
Rb Ba Th U Nb Ta La Ce Pr Nd Sr Sm Hf Zr Ti Eu Gd Tb Dy Ho Y Er Tm Yb Lu

Fig. 7.10 a-l

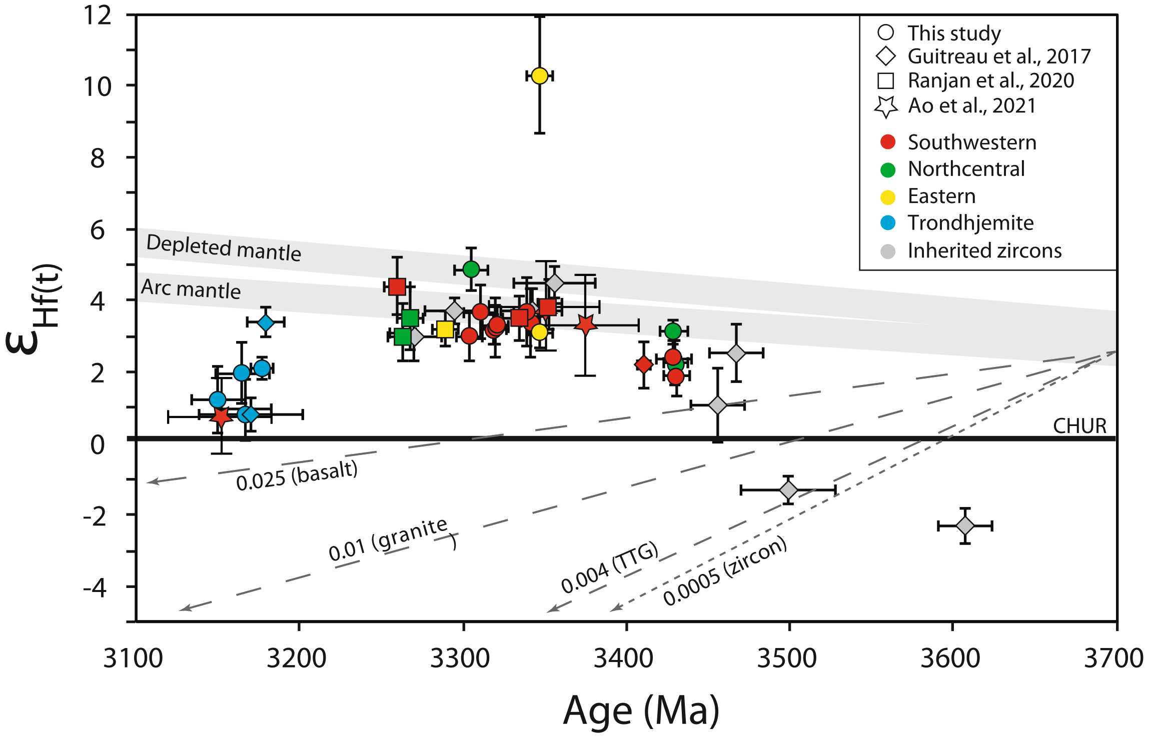

Fig. 7.11a

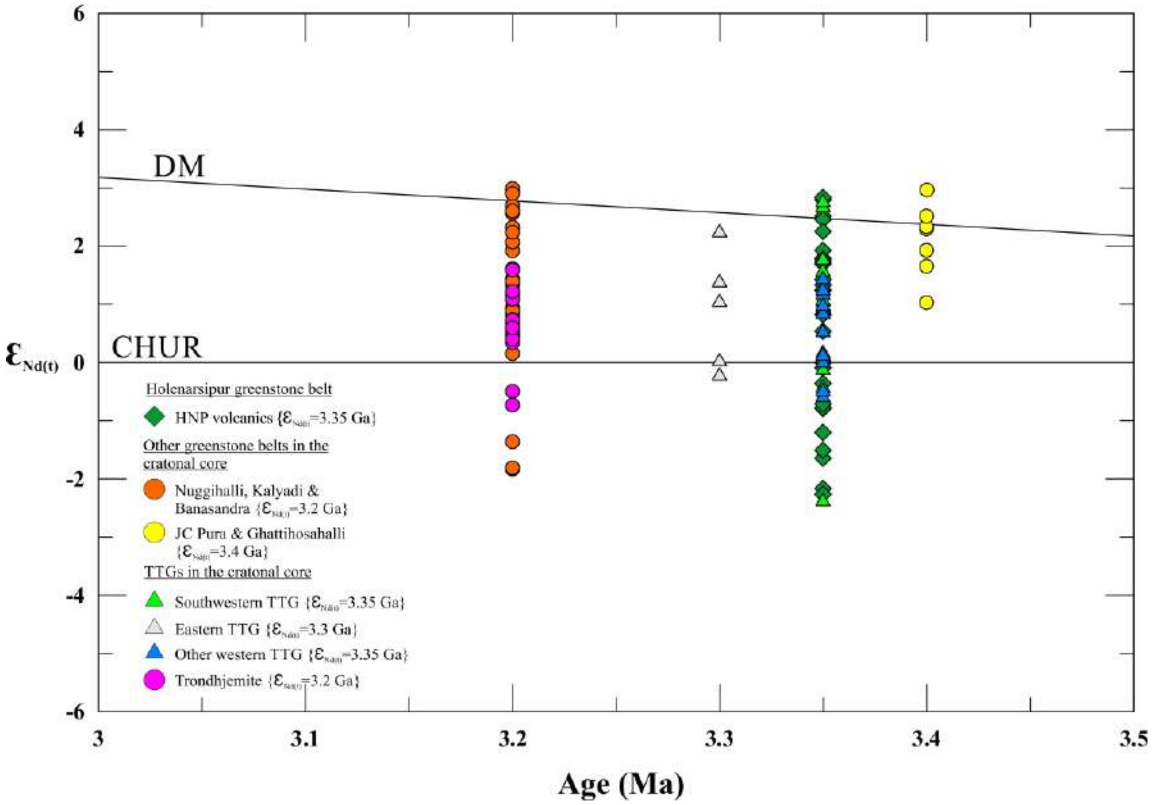

Fig. 7.11b

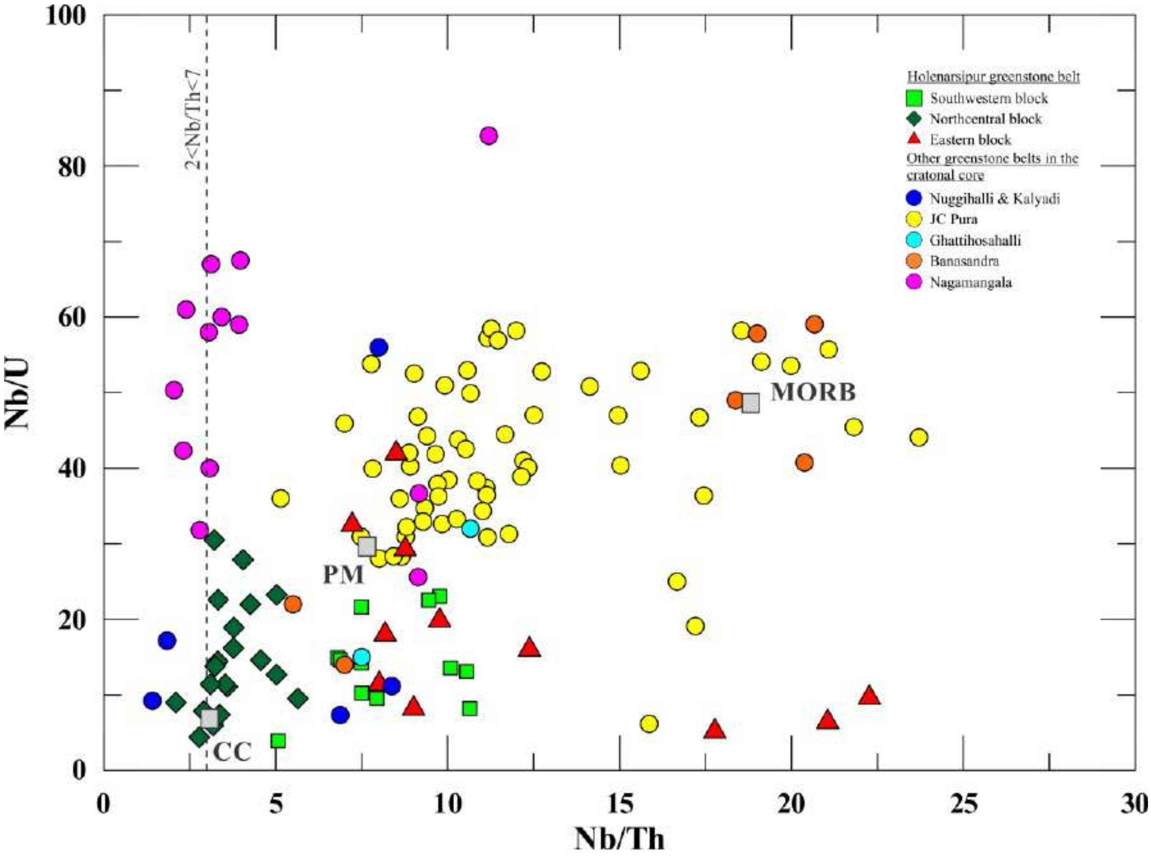
100
80
60
40
20
0
Nb/U
2<Nb/Th<7
Holenarsipur greenstone belt
🟩 Southwestern block
◆ Northcentral block
▲ Eastern block
Other greenstone belts in the cratonal core
● Nuggihalli & Kalyadi
● JC Pura
● Ghattihosahalli
● Banasandra
● Nagamangala
MORB
PM
CC
0
5
10
15
20
25
30
Nb/Th

Fig. 8a

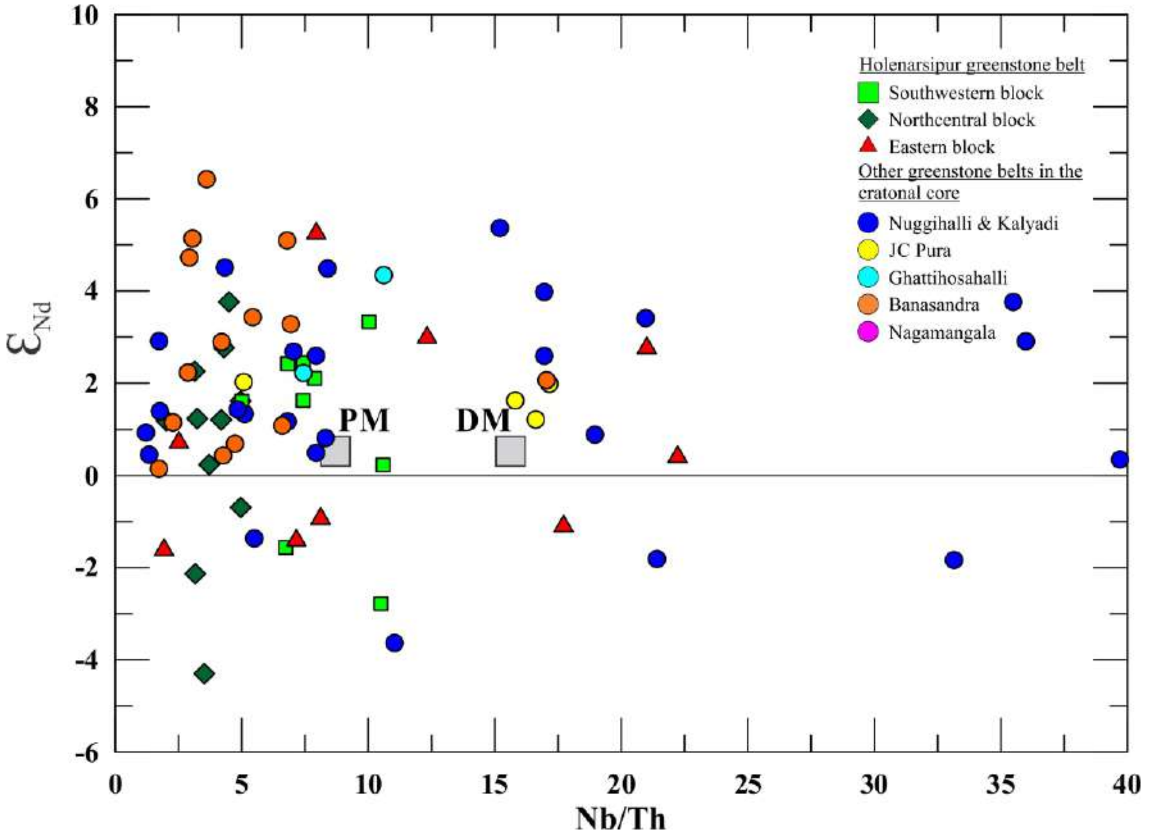
10
8
6
4
2
0
-2
-4
-6
ε_{Nd}
Holenarsipur greenstone belt
🟩 Southwestern block
◆ Northcentral block
▲ Eastern block
Other greenstone belts in the cratonal core
● Nuggihalli & Kalyadi
● JC Pura
● Ghattihosahalli
● Banasandra
● Nagamangala
PM
DM
0
5
10
15
20
25
30
35
40
Nb/Th

Fig. 8b

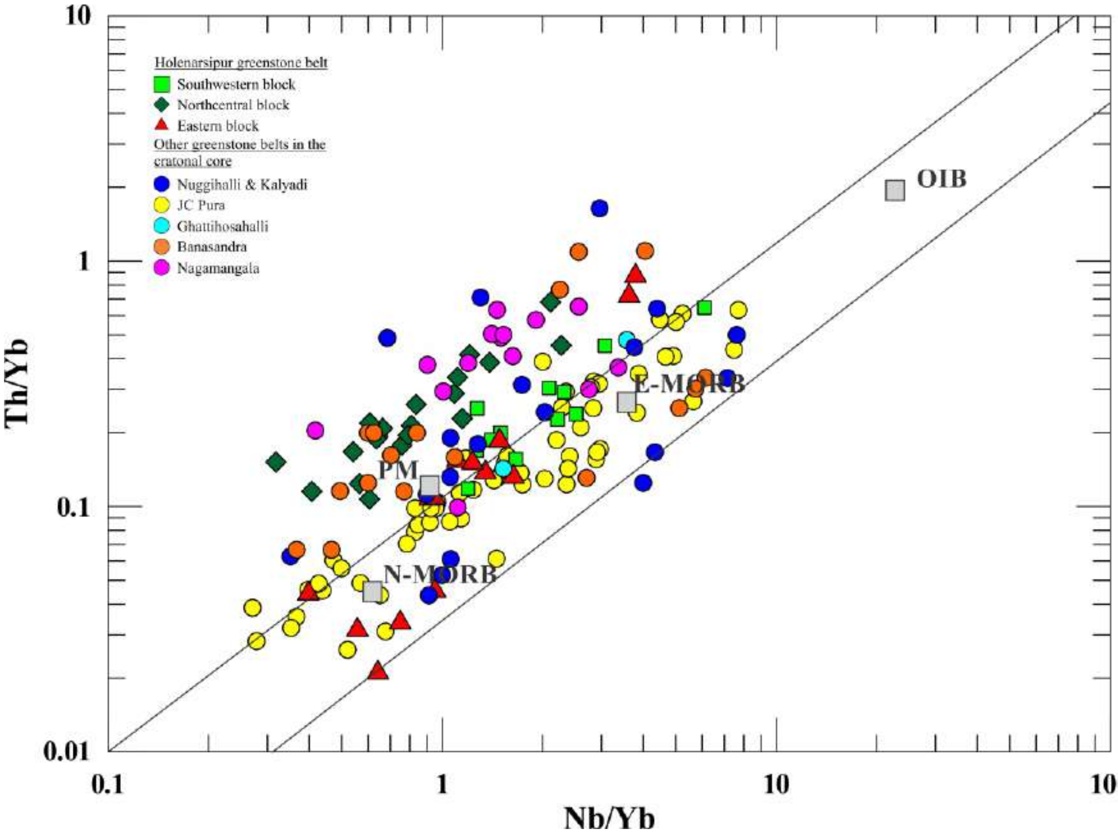
10
1
0.1
0.01
Th/Yb
0.1
1
10
100
Nb/Yb
Holenarsipur greenstone belt
Southwestern block
Northcentral block
Eastern block
Other greenstone belts in the cratonal core
Nuggihalli & Kalyadi
JC Pura
Ghattihosahalli
Banasandra
Nagamangala
OIB
E-MORB
PM
N-MORB

Fig. 8c

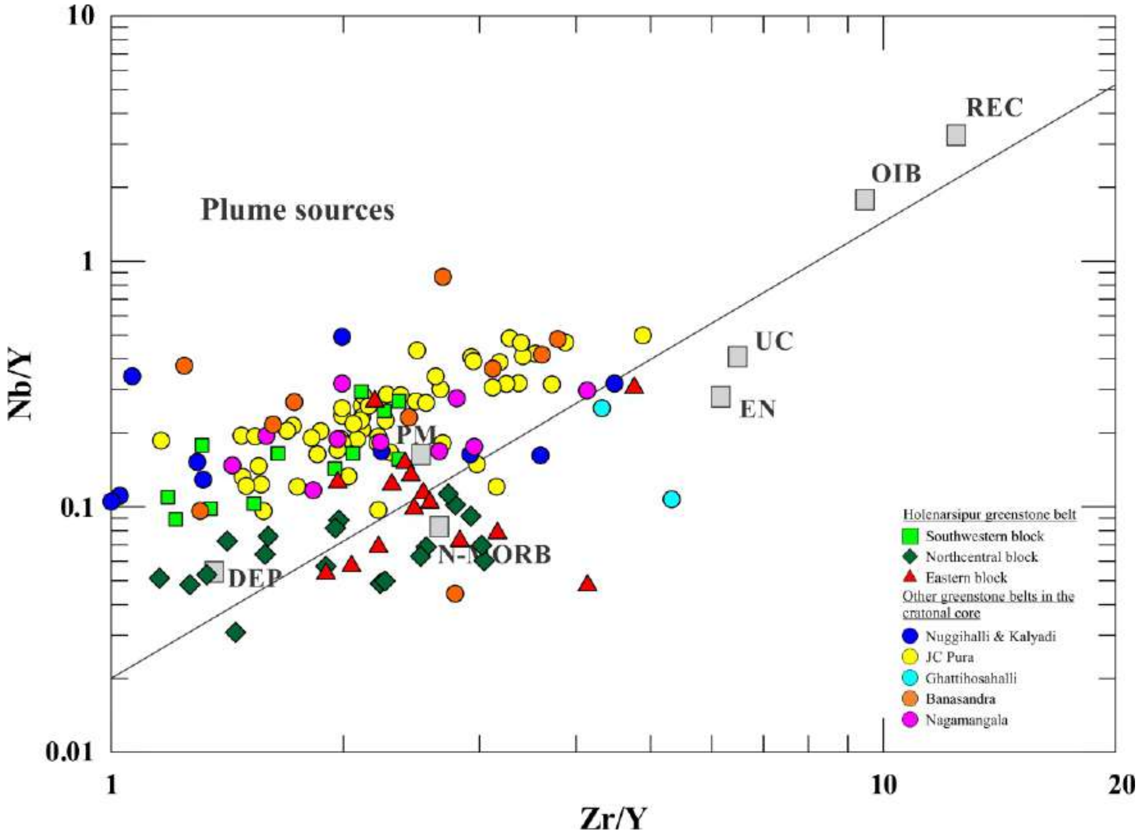
10
1
0.1
0.01
Nb/Y
1
10
20
Zr/Y
Plume sources
REC
OIB
UC
EN
PM
N-MORB
DEP
Holenarsipur greenstone belt
Southwestern block
Northcentral block
Eastern block
Other greenstone belts in the cratonal core
Nuggihalli & Kalyadi
JC Pura
Ghattihosahalli
Banasandra
Nagamangala

Fig. 8d

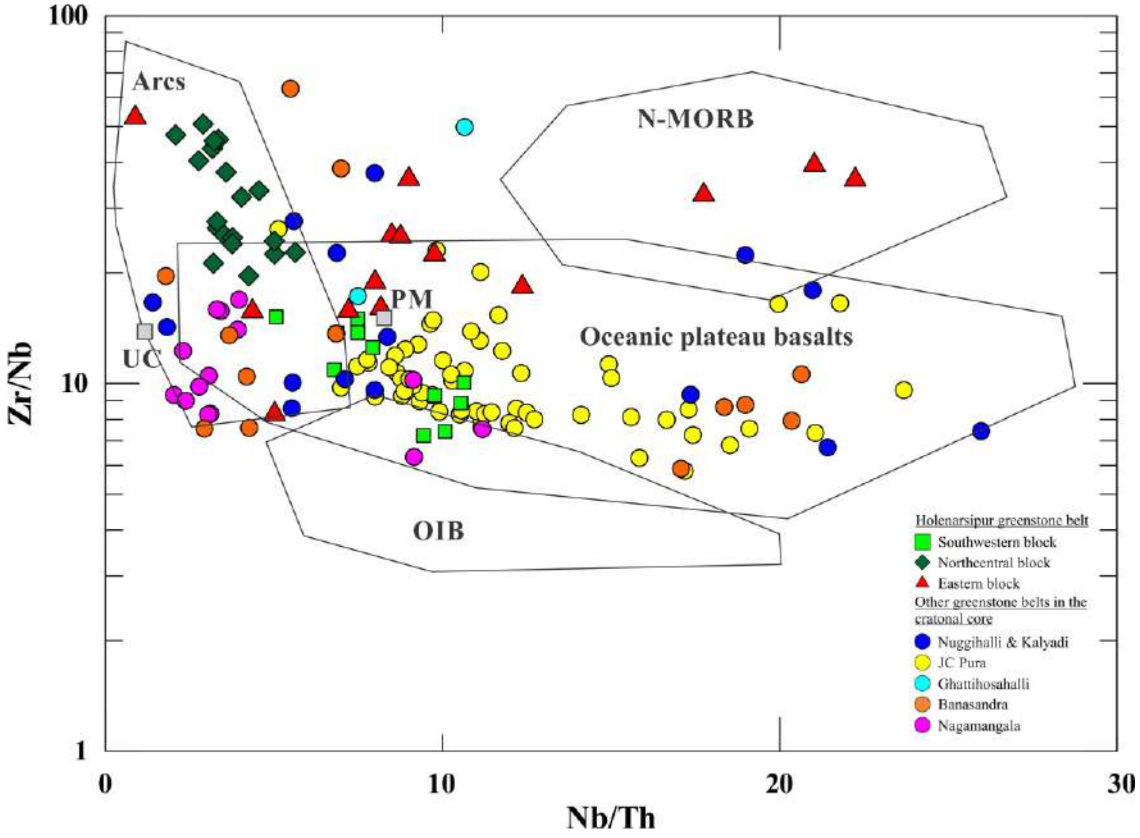
100
10
1
0
10
20
30
Zr/Nb
Nb/Th
Arcs
N-MORB
PM
UC
Oceanic plateau basalts
OIB
Holenarsipur greenstone belt
Southwestern block
Northcentral block
Eastern block
Other greenstone belts in the cratonal core
Nuggihalli & Kalyadi
JC Pura
Ghattihosahalli
Banasandra
Nagamangala

Fig. 8e

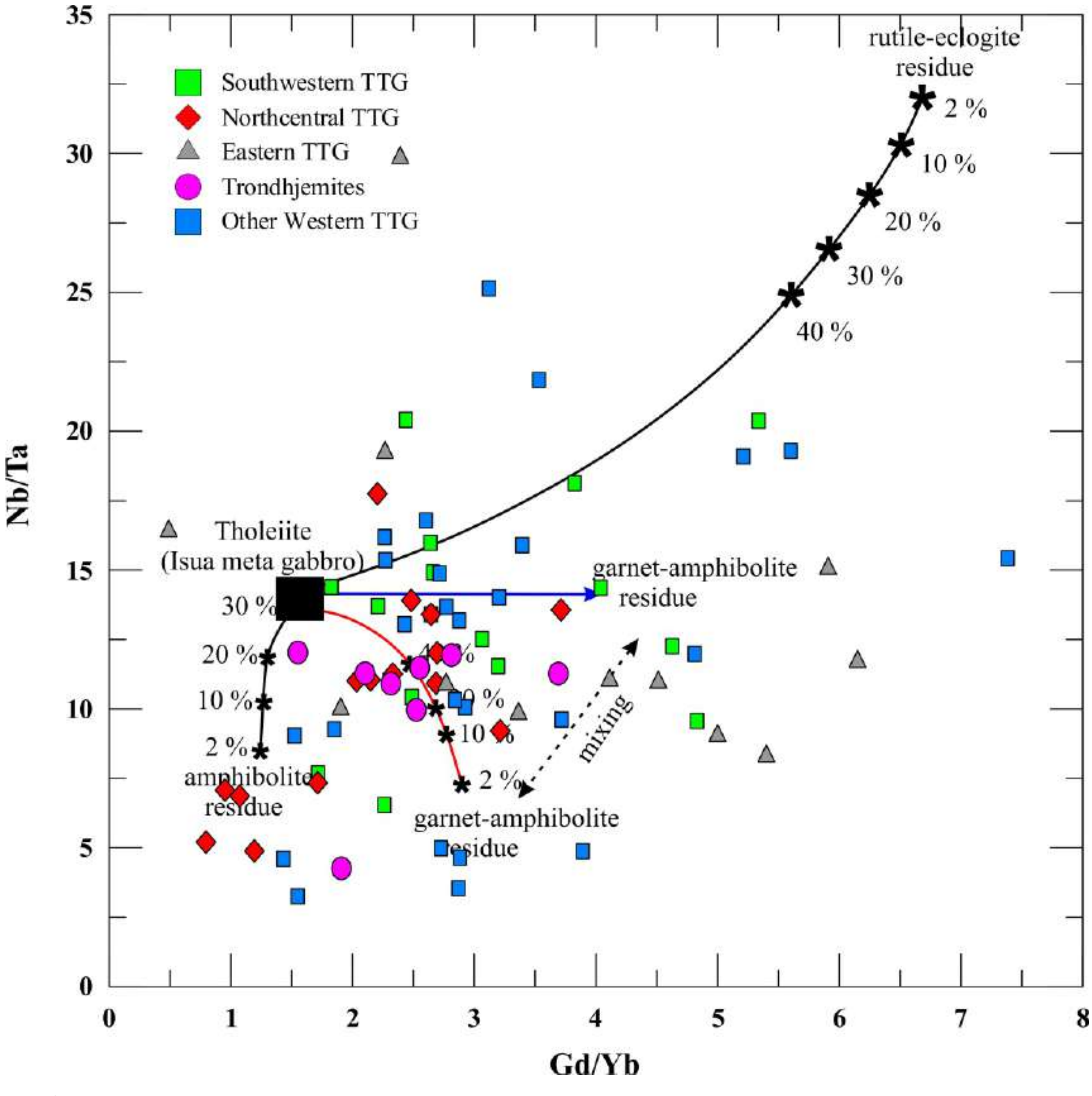
35
30
25
20
15
10
5
0
0
1
2
3
4
5
6
7
8
Nb/Ta
Gd/Yb
Southwestern TTG
Northcentral TTG
Eastern TTG
Trondhjemites
Other Western TTG
rutile-eclogite residue
2 %
10 %
20 %
30 %
40 %
Tholeiite (Isua meta gabbro)
garnet-amphibolite residue
30 %
20 %
10 %
2 %
amphibolite residue
40 %
20 %
10 %
2 %
garnet-amphibolite residue
mixing

Fig. 9a

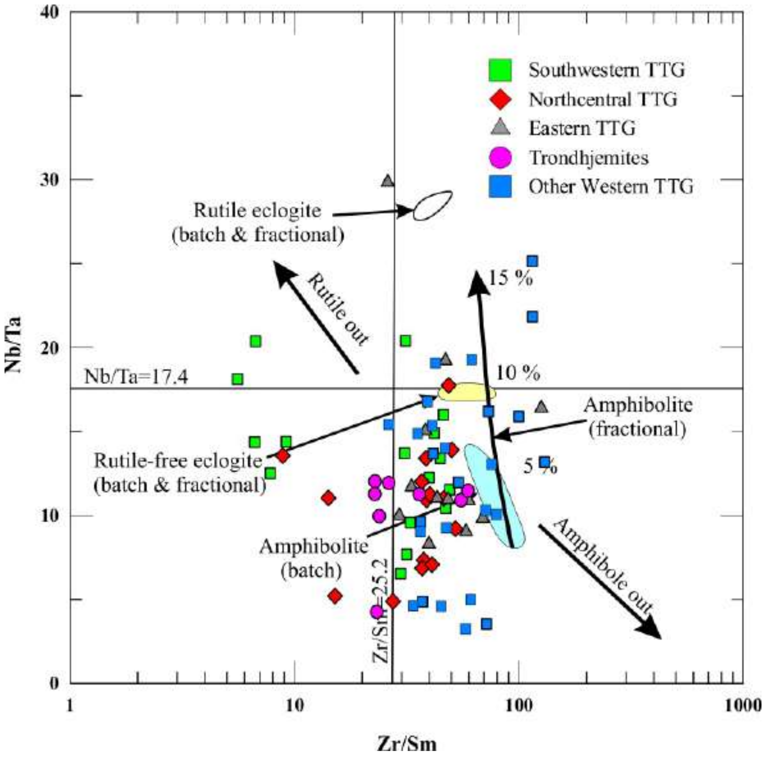

Southwestern TTG
Northcentral TTG
Eastern TTG
Trondhjemites
Other Western TTG
Rutile eclogite
(batch & fractional)
Rutile out
15 %
10 %
5 %
Nb/Ta=17.4
Amphibolite
(fractional)
Rutile-free eclogite
(batch & fractional)
Amphibolite
(batch)
Zr/Sm=25.2
Amphibole out
Nb/Ta
Zr/Sm
0
10
20
30
40
1
10
100
1000

Fig. 9b

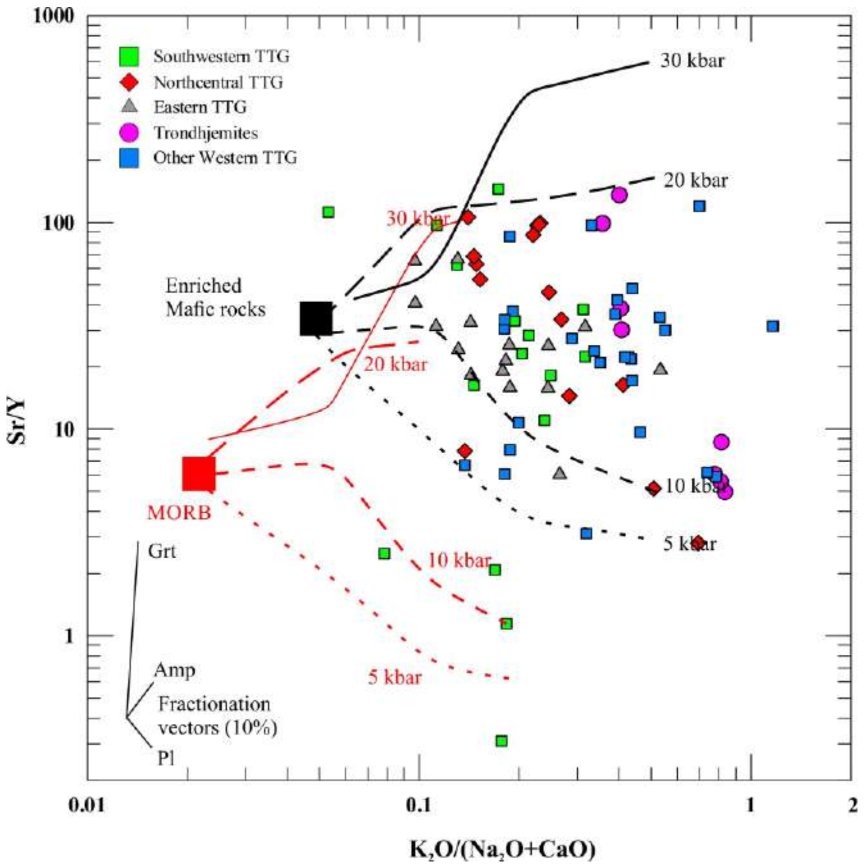

Southwestern TTG
Northcentral TTG
Eastern TTG
Trondhjemites
Other Western TTG
30 kbar
20 kbar
10 kbar
5 kbar
30 kbar
20 kbar
10 kbar
5 kbar
Enriched
Mafic rocks
MORB
Grt
Amp
Fractionation
vectors (10%)
Pl
Sr/Y
$K_2O/(Na_2O+CaO)$
1000
100
10
1
0.01
0.1
1
2

Fig. 9c

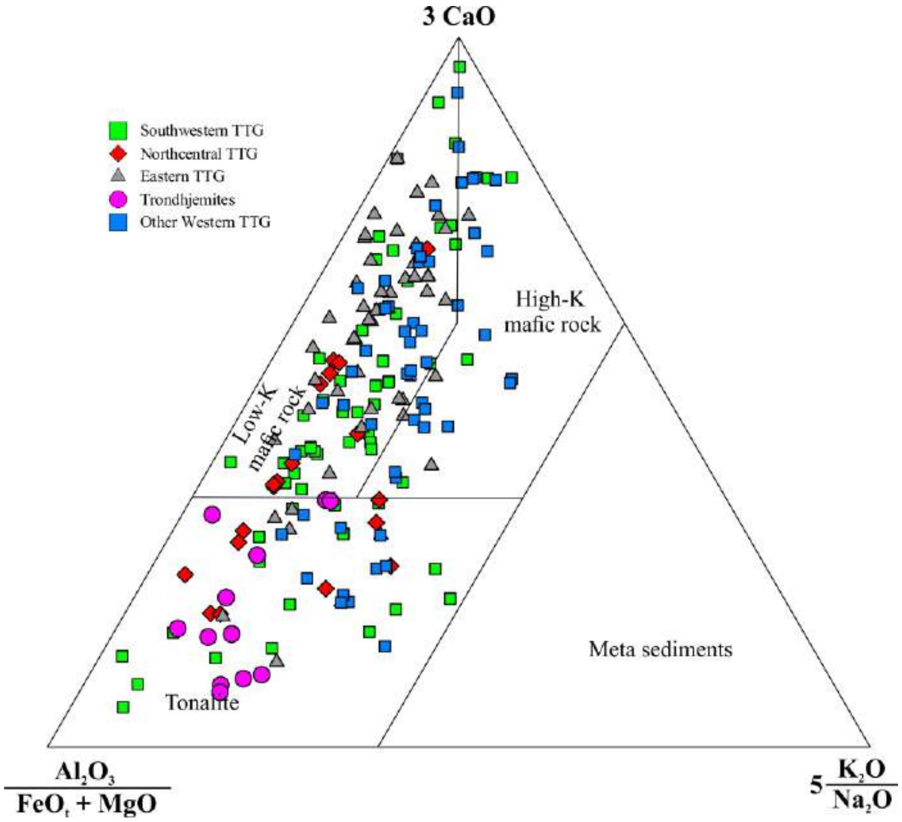

3 CaO
Southwestern TTG
Northcentral TTG
Eastern TTG
Trondhjemites
Other Western TTG
High-K mafic rock
Low-K mafic rock
Meta sediments
Tonalite
$\frac{Al_2O_3}{FeO_t + MgO}$
$5\frac{K_2O}{Na_2O}$

Fig. 9d

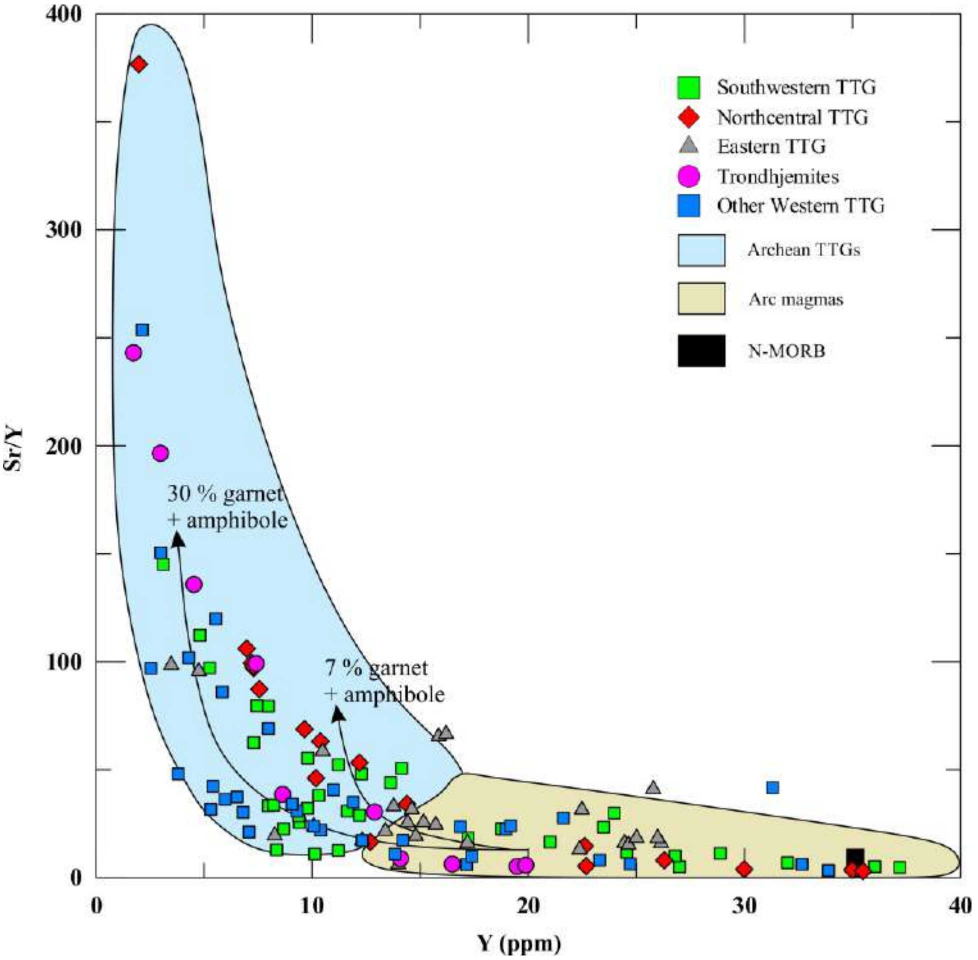

Southwestern TTG
Northcentral TTG
Eastern TTG
Trondhjemites
Other Western TTG
Archean TTGs
Arc magmas
N-MORB
30 % garnet + amphibole
7 % garnet + amphibole
Sr/Y
Y (ppm)
400
300
200
100
0
0
10
20
30
40

Fig. 9e

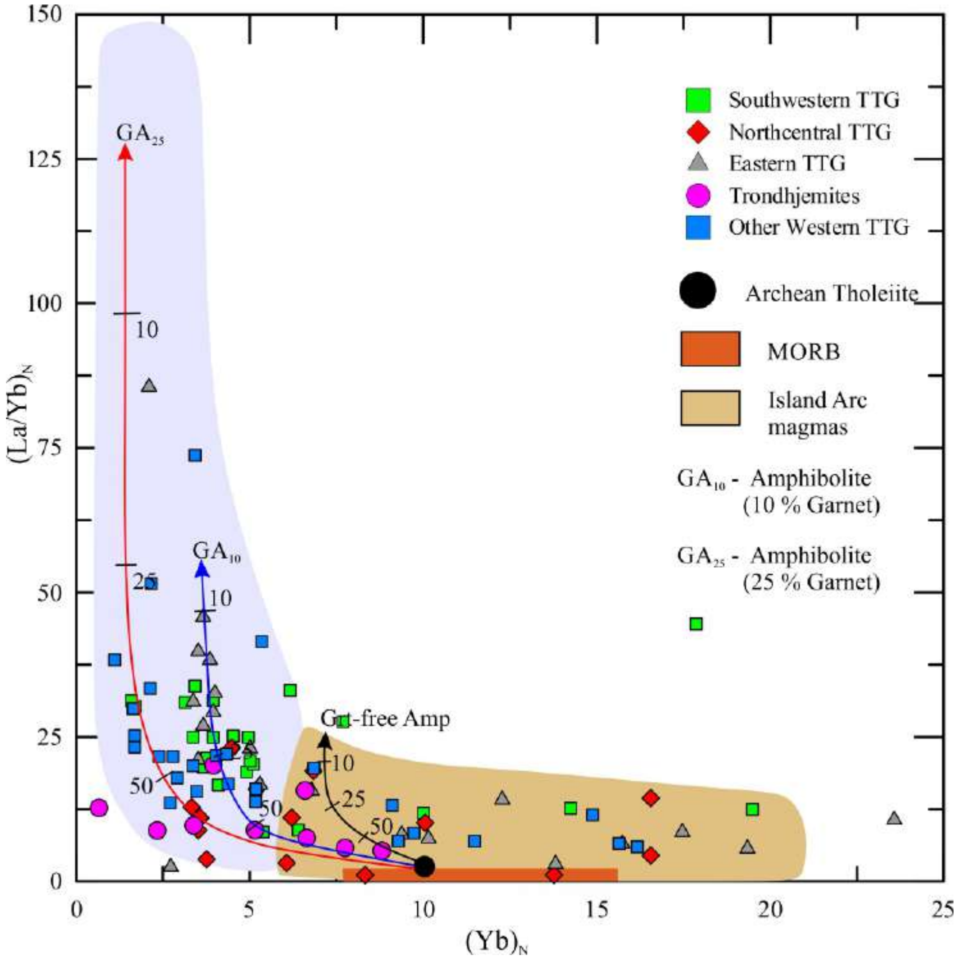
(La/Yb)$_N$
(Yb)$_N$
0
5
10
15
20
25
0
25
50
75
100
125
150
GA$_{25}$
GA$_{10}$
Grt-free Amp
10
25
50
10
50
10
25
50
🟩 Southwestern TTG
🟥 Northcentral TTG
▲ Eastern TTG
● Trondhjemites
🟦 Other Western TTG
● Archean Tholeiite
MORB
Island Arc magmas
GA$_{10}$ - Amphibolite (10 % Garnet)
GA$_{25}$ - Amphibolite (25 % Garnet)

Fig. 9f